SPRINGER LABORATORY

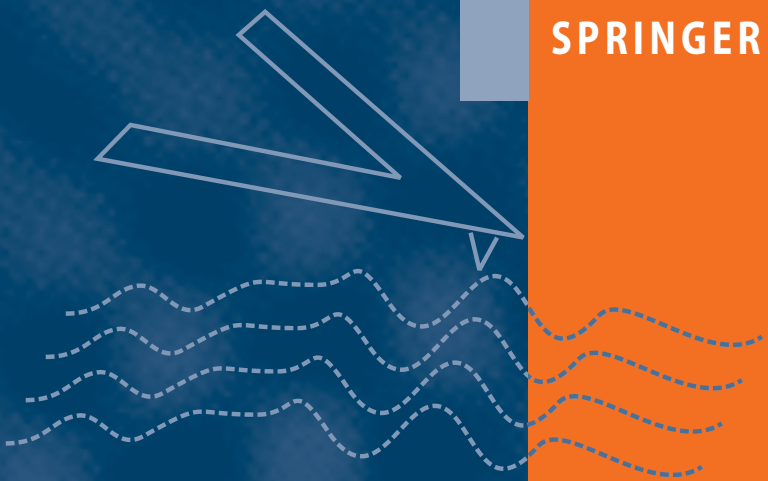

H. Schönherr · G. J. Vancso

Scanning Force Microscopy of Polymers

Springer

SPRINGER LABORATORY

Springer Laboratory Manuals in Polymer Science

Pasch, Trathnigg: HPLC of Polymers
ISBN: 3-540-61689-6 (hardcover)
ISBN: 3-540-65551-4 (softcover)

Mori, Barth: Size Exclusion Chromatography
ISBN: 3-540-65635-9

Pasch, Schrepp: MALDI-TOF Mass Spectrometry of Synthetic Polymers
ISBN: 3-540-44259-6

Kulicke, Clasen: Viscosimetry of Polymers and Polyelectrolytes
ISBN: 3-540-40760-X

Hatada, Kitayama: NMR Spectroscopy of Polymers
ISBN: 3-540-40220-9

Brummer, R.: Rheology Essentials of Cosmetics and Food Emulsions
ISBN: 3-540-25553-2

Mächtle,W., Börger, L.: Analytical Ultracentrifugation of Polymers and Nanoparticles
ISBN: 3-540-23432-2

Heinze, T., Liebert, T., Koschella, A.: Esterification of Polysaccharides
ISBN: 3-540-32103-9

Koetz, J., Kosmella, S.: Polyelectrolytes and Nanoparticles
ISBN: 3-540-46381-X

Stribeck, N.: X-Ray Scattering of Soft Matter
ISBN: 3-540-46488-4

Schärtl, W.: Light Scattering from Polymer Solutions and Nanoparticle Dispersions
ISBN: 3-540-71950-2

Khulbe, K. C., Feng, C. Y., Matsuura, T.: Synthetic Polymeric Membranes
ISBN: 3-540-73993-7

Keddie, J. L., Routh, A. F.: Fundamentals of Latex Film Formation
ISBN: 978-90-481-2844-0

Schönherr, H., Vancso, G. J.: Scanning Force Microscopy of Polymers
ISBN: 3-642-01230-3

Holger Schönherr • G. Julius Vancso

Scanning Force Microscopy of Polymers

With 191 Figures and 1 Table

Springer

Prof. Dr. Holger Schönherr
Universität Siegen
Physikalische Chemie
Adolf-Reichwein-Str. 2
57068 Siegen
Germany
schoenherr@chemie.uni-siegen.de

Prof. Dr. G. Julius Vancso
University of Twente
MESA$^+$ Institute for Nanotechnology
Materials Science and Technology
of Polymers
P.O. Box 217
7500 AE Enschede
The Netherlands
g.j.vancso@utwente.nl

ISBN 978-3-642-01230-3 e-ISBN 978-3-642-01231-0
DOI 10.1007/978-3-642-01231-0
Springer Heidelberg Dordrecht London New York

Library of Congress Control Number: 2009943835

Cover design: WMXDesign GmbH, Heidelberg, Germany

Printed on acid-free paper

Springer is part of Springer Science+Business Media (www.springer.com)

Springer Laboratory Manuals in Polymer Science

Preface

Scope of the Book

Synthetic and natural polymers exhibit a complex structural and morphological hierarchy on multiple length scales [1], which determines their performance. Thus, research aiming at visualizing structure and morphology using a multitude of microscopy techniques has received considerable attention since the early days of polymer science and technology. Various well-developed techniques such as optical microscopy and different forms of electron microscopy (Scanning Electron Microscopy, SEM; Transmission Electron Microscopy, TEM; Environmental Scanning Electron Microscopy, ESEM) allow one to view polymeric structure at different levels of magnification. These classical techniques, and their applications to polymers, are well documented in the literature [2, 3].

The invention of Scanning Tunneling Microscopy (STM) inspired the development of Atomic Force Microscopy (AFM) and other forms of scanning proximity microscopes in the late 1980s [4, 5]. AFM, unlike STM, can be used to image nonconducting specimens such as polymers. In addition, AFM imaging is feasible in liquids, which has several advantages. Using liquid imaging cells the forces between specimen and AFM probe are drastically reduced, thus sample damage is prevented. In addition, the use of water as imaging medium opened up new applications aiming at imaging, characterizing, and analyzing biologically important systems.

When used as imaging tool to visualize surface topography, AFM is capable of covering a very broad range of magnifications, from several nanometers to over 100 micrometer scan sizes. This allows one to visualize structure from molecular lattice imaging to morphological superstructures (exposed at the specimen surface). In some cases, even single macromolecules (especially biomacromolecules) can be imaged.

The AFM probe tip interacts via various mechanisms with the sample surface, including simple quasi-static and dynamic normal and lateral forces. These (and other) interactions depend on local physical properties of the sample, on the scale of the probed area. Tribological, viscoelastic, and microhardness mechanical properties can be probed under (more or less) controlled environmental conditions.

Depending on the interactions measured between probe and sample, and on the control of the imaging parameters (e.g. feed-back signals), many different so-called "imaging modes" exist. With substantially refined, robust commercial temperature control systems at hands it is currently possible to interrogate polymers in temperature-dependent studies of structure. For polymers, a particularly interesting possibility is to map surfaces based on contrast and local variation in thermal properties such as melting temperature range, transition enthalpies, and thermal conductivity.

A clear trend in instrumental development is to increase the scanning speed (and at the same time retain sensitivity) and to control the imaging environment. In addition to a (static) visualization and characterization of structure and morphology, and to quantitative measurements of (surface) physical properties, monitoring of dynamic, time-dependent phenomena, such as thermal transitions, swelling, and chemical reactions, receive increasing attention. Functionalization of AFM probes by various chemical groups allows one to control local chemistry and obtain chemically specific signals, which opens up the possibility of analysis and characterization of functional group distributions at polymer surfaces. An important aspect regarding this chemically sensitive adhesion map imaging is the ability of AFM to study on the nanoscale (single asperity) adhesion contact mechanics. These abilities are being enhanced using recently introduced advanced AFM modes, such as modes that exploit imaging at higher harmonics.

In this volume, we treat AFM of synthetic as well as natural and biological macromolecular materials. The focus is, nevertheless, laid on the materials science and technology aspect, i.e., biological function and biology-related issues are left out. Instead, morphology and structure imaging, surface properties, nanoscale mechanical properties, and practically relevant processes (phase transitions) for typical laboratory and industrial applications constitute the bulk of the treatment.

The above list represents the use of scanning proximity techniques in analysis and characterization, which is the focus targeted for this volume. In addition to the use of AFM and related scanning proximity approaches in analysis and characterization, these methods have become key enabling technologies in controlled manipulation of matter for nanotechnology. Although this is a field with extraordinary potential for the future, we decided to focus on the practical, analytical, and characterization aspects of AFM when used in conjunction with polymers.

To whom is this Volume Written?

Our primary target is the readership of laboratory scientists, including industrial researchers and academic personnel (graduate students and postdoctoral researchers) working on the lab floor level. The common need for this target audience is a self-containing volume, which they can use to accompany their instrument user's manual (whatever instrument they are using) when engaged in polymer research (surface science, analysis, and characterization as described above). "Self-containing" means, in our vision, that the book does *not* go in depth of physical derivations, but discusses only the final results of the fundamentals relevant for understanding.

This was done in a didactically clear and easily understandable way with many graphical representations and visuals. Such sections promote the understanding of the actual physical processes and phenomena involved when using AFMs. Thus, the possible misinterpretation of observed *apparent* features or contrast differences, which are still too frequently found in the literature, may be avoided. To this end, we also introduce and discuss typical applications by using explicit case studies, where we focus on the routine procedure, on limitations, and on eventual potential for future expansions for the particular applications.

The book, however, will be useful also for managers for their decision-making and project management activities. We believe that the volume can contribute to an improved ability to make decisions regarding "feasibility and doability" of experiments and particular projects, and to help to judge the time involvement necessary to complete given tasks more realistically. Hence for this group, an ongoing systematic, continuing reading of relevant subjects, without being confronted with every – perhaps unnecessary – detail is important, which will be dealt with in this volume.

Acknowledgments

Inspiration: Helmut Ringsdorf (Johannes Gutenberg Universität Mainz, Germany), Curtis W. Frank (Stanford University), late James E. Guillet (University of Toronto, Canada), Hans-Joachim Cantow (University of Freiburg, Germany), Ivan Tomka (ETH Zurich, Switzerland)
Discussions: David. N. Reinhoudt (MESA$^+$ Institute for Nanotechnology, Twente University, The Netherlands), Jurriaan Huskens (MESA$^+$ Institute for Nanotechnology, Twente University, The Netherlands), Dr. Sergei Magonov (Agilent Technologies, USA)
Data, images & recipes: A. Bittner (MPI Metallforschung Stuttgart), Alice P. Gast (MIT), Poe Ratanabanangkoon (Stanford University), Joe M. Johnson (Stanford University), Steve G. Boxer (Stanford University), Willy Wiyatno (Stanford University), Robert M. Waymouth (Stanford University), Larry E. Bailey (Stanford University), Curtis W. Frank (Stanford University), Kenichi Morigaki (Institute of Advanced Industrial Science and Technology (AIST) Midorigaoka, Ikeda, Japan), Wolfgang Knoll (Austrian Science Center), Anasys Instruments Inc, VEECO Metrology Inc.
Photographs, Microscopy: Clemens J. Padberg, Ewa Tocha, Anika Embrechts, Joost Duvigneau
Administrative support: Genevieve Rietveld
Corrections, proofreading: Dorina Trifonova-van Haeringen, Sissi de Beer, Ewa Tocha, Hong Jing Chung, Davide Tranchida
Financial Support: The authors wish to thank the Netherlands Foundation for Scientific Research (NWO-CW) for the generous financial support since 1996.

References

1. Woodward AE (1989) Atlas of polymer morphology. Hanser Gardner, Ohio
2. Sawyer LC, Grubb DT, Meyers GF (2008) Polymer microscopy: characterization and evaluation of materials, 3rd edn. Springer, Berlin
3. Hemsley DA (ed) (1989) Applied polymer light microscopy. Elsevier Applied Science, Georgia
4. Magonov SN, Whangboo MH (1996) Surface analysis with STM and AFM: experimental and theoretical aspects of image analysis, Wiley, New York
5. Colton RJ, Engel A, Frommer JE, Gaub HE, Gewirth AA, Guckenberger R, Rabe J, Heckl WM, Parkinson B (1998) Procedures in scanning probe microscopies, Wiley, New York

Contents

Part II Case Studies: Macromolecules, Polymer Morphology and Polymer Surface Properties by AFM

Part I
Principles: Theory and Practice

1 Physical Principles of Scanning Probe Microscopy Imaging

Abstract

Microscopic methods have been among the important tools in the study of synthetic and natural polymers and have greatly helped to unravel details of the rich and sometimes very complex structural and morphological hierarchy that polymers display on multiple length scales. Because of the close relation between performance of polymeric materials and their hierarchical structures, as well as because of the continuing strive toward the mesoscopic and nanoscopic size regime in modern technology, high-resolution analysis tools are still becoming more and more important. In particular, scanning probe microscopy has become a prominent technology in this respect. The different atomic force microscopy (AFM) techniques relevant for polymers have many basic features in common, which will be introduced in the first part of this chapter on the theory of AFM. The practical aspects of AFM operation are highlighted in the second part of this chapter. Specific examples, including a large number of hand-on examples, follow in part II of the book.

1.1 Introduction

The well established family of microscopy techniques that includes among others polarized optical microscopy (OM) [1] and various electron microscopies [2] was complemented in the late 1980s by newly developed scanning proximity probe microscopy techniques [3]. Among these techniques, atomic force microscopy (AFM) in particular has successfully complemented the traditional techniques for studying simultaneously polymer morphology and surface properties. Compared to scanning tunneling microscopy (STM), which is inherently limited to conducting samples, AFM is more generally applicable. A much broader range of materials, including insulators, such as most polymers, can be directly studied. AFM and related approaches can be considered to be unique techniques that provide topographical information in 3D with high spatial resolution over lateral length scales of $>100\mu m$ down to nanometers. Different modes allow one to image with material-specific

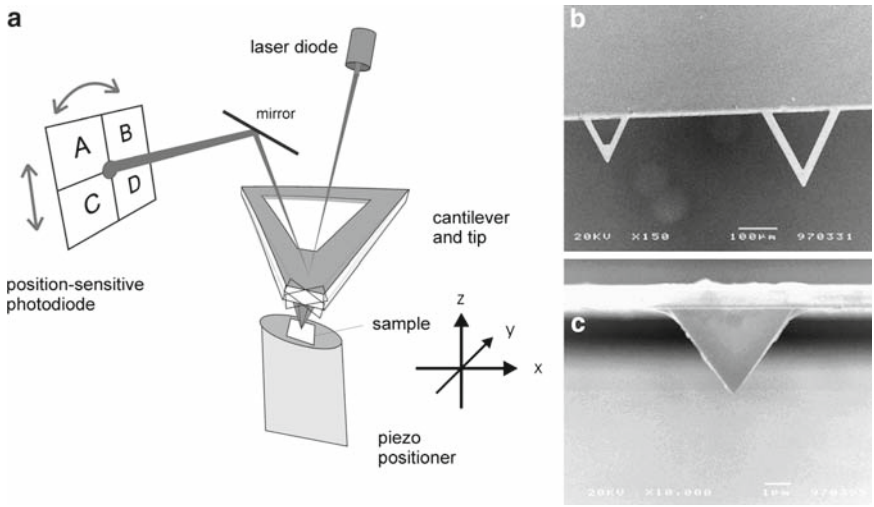

Fig. 1.1 (a) Schematic diagram of contact mode AFM and SEM images of (b) V-shaped AFM cantilevers and (c) tip. The basic elements of transducer (piezo positioner), cantilever and tip assembly, and ultrasensitive force detection system (optical beam deflection/photodiode detector) are common for most AFM techniques, while details may differ (reproduced with permission from [4])

contrast, e.g., based on differences in adhesion, friction, or elasticity, thus enabling high-resolution mapping of composition in heterogeneous systems.

In AFM, a sharp scanned probe collects localized information. Typically, the proximal probe and the sample surface are in contact and the corresponding data are collected, while probe and sample are mutually displaced (Fig. 1.1). Among the various modes utilized, contact mode (CM) AFM and intermittent contact (tapping) mode are most prominent. In CM–AFM, the deflection of a cantilever to which the tip is attached is monitored, while in intermittent CM the tip−cantilever assembly is resonating and the amplitude of the cantilever is monitored to extract the surface profile.

1.2 The Physical Principles of Atomic Force Microscopy

AFM connects the nanometer and micrometer length scales utilizing a sharp probe tip that senses interatomic forces acting between the surface of a sample and the atoms at (or near) the apex of the tip. Variations of these forces as a function of the tip apex (x,y,z) position with respect to the atomic arrangements of the specimen surface are the basis of imaging. Because of the decaying interaction forces acting as a function of increasing distance between interacting bodies, it is usually the apex and its vicinity, which dominate interaction forces. Thus, it is usually sufficient to approach the tip and its surroundings with a hemisphere, or a parabolically shaped

apex, and consider its interaction with a plane (specimen). A basic understanding of interatomic and intermolecular forces as a function of distance among interacting bodies is essential in the practice of AFM. Without this, it is difficult to interpret force–distance curves, to tune operating conditions in the CM, and to optimize imaging conditions. For a proper understanding of hysteretic force–distance curves, a description of the processes taking place when the tip approaches the sample, jumps into contact, and is withdrawn should be discussed. To this end, we shall use a simple analytical expression as developed by Sarid [5].

Depending on the modes of operation, the tip is actuated, and the surface–tip forces are measured, utilizing different modes of operation (so-called imaging modes). In CM, imaging cantilever bending (up or down) caused by interatomic forces is observed. Following proper calibration of the cantilever spring constant, the bending is converted to force. This necessitates a short introduction into static cantilever beam theory. *Hence, we shall summarize the physics of the relevant calibration techniques.*

In tapping (or intermittent contact) mode imaging, the tip is driven by an oscillator near its resonance frequency. For a proper understanding and tuning of image contrast, image contrast inversion, height, amplitude, and phase imaging, the basics of the physics of simple, linear, and damped harmonic oscillators are needed. Finally, a recent development by Veeco, the so-called HarmoniX TM imaging, utilizes asymmetrically attached tips with respect to the cantilever symmetry axis for capturing the basic and higher harmonic vibration modes. This new instrument carries a great promise for simultaneous capturing of surface morphology, mechanical performance, and mapping of surface chemical groups at high frame capture speed. In view of the great potential of this technique, primarily for studies of soft condensed materials (e.g., polymers) we close the chapter with a short account of the physical principles of this imaging mode.

1.2.1 Forces Between Atomic Species and Surfaces of Solids

Intermolecular and surface forces are treated in detail in the excellent book of Israelachvili [6]. We shall use some of the treatments of Israelachvili, as well as one of our earlier reviews discussing imaging and imaging forces with chemical specificity [7].

In the last 40 years, techniques to directly measure surface forces and force laws (force vs. separation distance between surfaces) have been developed such as the surface forces apparatus (SFA) [6] and AFM. Surface forces are responsible for the work required when two contacting bodies (such as an AFM tip in contact with a solid surface) are separated from contact to infinite distance. Although the physical origin of all relevant surface forces can be derived from fundamental electromagnetic interactions, it is customary to group these in categories based on characteristic features that dominate the relevant physical behavior. Thus, one speaks of ionic (monopole), dipole−dipole, ion−dipole interactions, electrostatic multipole forces (e.g., quadrupole), induced dipolar forces, van der Waals (London dispersive) interactions, hydrophobic and hydrophilic solvation, structural and hydration forces,

steric and fluctuation forces, etc. (see [6, p. 28]). Leaving out London dispersive forces, which are always present (hence called nonspecific) one speaks of molecule-specific (specific) interactions for the remainder of the cases. For example, strong dipole−dipole interactions occur when a H atom bonded to an electronegative atom in a molecule interacts with the lone pair of a nearby atom bonded to another molecule. The complementarity here is obvious such as in ligand−receptor (key−lock) or antibody−antigen type interactions for entirely specific pairs of molecular fragments that bind in biological macromolecules (e.g., for biotin and avidin, with an interaction energy of 35kT, which is one of the highest known values for a ligand−receptor system).

The attractive contribution of the typical Lennard-Jones potential varies with the inverse sixth power of the interspecies distance, while the repulsive interactions depend on the inverse twelfth power. By convention, positive energy corresponds to repulsion, and negative energy to attraction. The value of the potential energy for a pair of interacting species at a distance of separation r can be obtained as the integral (i.e., area) under the force−distance curve as shown in Fig. 1.2.

Surface forces acting between mesoscopic or macroscopic bodies can be described by summing up pairwise interatomic (intermolecular) forces for each participating atomic (molecular) pairs within the interacting bodies. Semiempirical

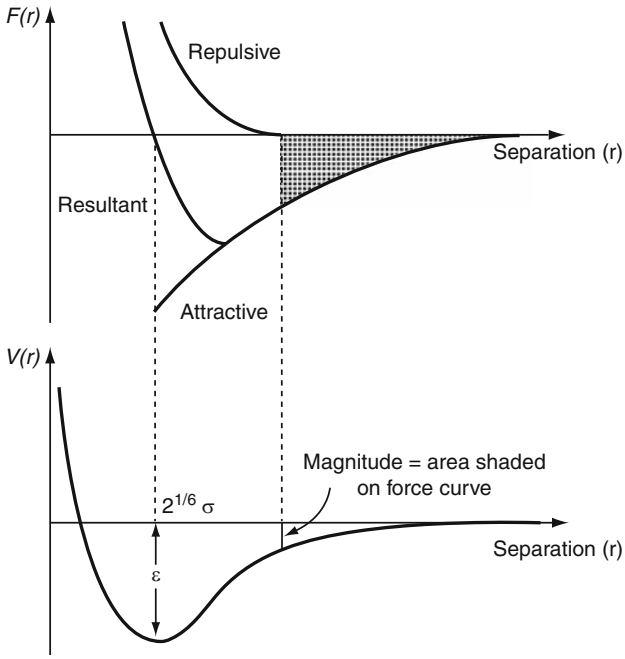

Fig. 1.2 The Lennard–Jones "6–12" two-body potential [potential energy V(r)] and force F(r) for two interacting atoms ("point-like" molecules) as a function of separation distance r. Reproduced with permission from [7]; copyright Springer Verlag

expressions such as the sum of repulsive and attractive contributions described by power law relationships have been proposed (Mie, van der Waals). If the pairwise (two body) potential between two atomic or molecular species (hereinafter species) is described by a potential $V(r)$ as a function of the separation distance, r, between the species, the force $F(r)$ and the potential are related through simple differential (integral) equations:

$$-F(r) = \frac{\mathrm{d}V(r)}{\mathrm{d}r} \quad V(r) = -\int_r^\infty F(r')\mathrm{d}r' = \int_\infty^r F(r')\mathrm{d}r'.$$

The Lennard–Jones (LJ) potential has the following functional form:

$$V(r) = 4\varepsilon\left[\left(\frac{\sigma}{r}\right)^{12} - \left(\frac{\sigma}{r}\right)^{6}\right],$$

where, the potential energy has its minimum value at $r=1.12\sigma$(and not at $r=\sigma$) at the equilibrium intermolecular separation with zero force and ε is the depth of the potential energy well (the minimum value of the $V(r)$ function) at equilibrium separation. The LJ potential is an empirical formula, and does not explain the origins of the acting forces. Other empirical equations (with different exponents) can be used that may give better fits for specific problems, e.g., for H-bonded systems a 12–10 potential results in a more realistic fit with experiments (see [6]).

The two system-specific parameters in the LJ equation encompass σ and ε. If their values, the number density of species within the interacting bodies, and the form/shape of the bodies are known, the mesoscopic/macroscopic interaction forces between two bodies can be calculated. The usual treatment of calculating net forces between objects includes a "pairwise" summation of the interaction forces between the species. Here, we neglect multibody interactions, which can also be considered at the expense of mathematical simplicity. Additivity of forces is assumed during summation of the pairwise interactions, and retardation effects are neglected. The corresponding so-called Hamaker summation method is well described in standard texts and references [5, 6]. Below we summarize a few results relevant for AFM.

We shall review the interaction energy $W(x)$ where x is a characteristic distance for a given rigid-body system (e.g., considering interaction forces between a spherical and a semi-infinite planar object, the separation or gap distance). Considering the interaction energy of a sphere with a half-space with a gap distance d, one arrives at the following formula (if only the attractive contributions to the LJ potential are considered, i.e., it is assumed that $V(r)=-C/r^6$ [6, 7]:

$$W(d) = -\frac{AR}{6d},$$

where, R is the radius of the sphere and A is the so-called Hamaker constant defined as

$$A = \pi^2 4\varepsilon\sigma\rho_1\rho_2 = \pi^2 C\rho_1\rho_2,$$

with the parameters of the LJ potential ($C=4\varepsilon\sigma$) and the number densities of the species 1 and 2, i.e., ρ_1 and ρ_2 in the sphere, and half-space, respectively.

To use the force expression for a sphere and a flat space as determined above, we calculate the force acting between a sphere with a radius of 1μm (e.g., a colloidal probe attached to an AFM cantilever) [8] and the surface at a distance of 1nm from each other. A characteristic value of the constant C in the force expression is obtained as $C=4\varepsilon\sigma=5\times10^{-78}\mathrm{Jm}^6$ in the LJ potential and the number densities of typical species in a usual solid can be approximated by $\rho_i \cong 3\times10^{28}\mathrm{m}^{-3}$ [5].With these values, the Hamaker constant becomes $A=1\times10^{-19}$J, which yields for the force between the sphere and the flat surface a value of 1.6×10^{-8}N (16nN). In AFM experiments the tip radii are much smaller (on the order of 5–50nm) and the tip–sample distance varies (depending on imaging conditions). Typical values of contact forces (at pull-off; see force–distance curves) in AFM range between 10pN and 10nN. For comparison, covalent bonds rupture around 2–5nN [9]; breaking a base pair in DNA requires a force of 10–20pN. In this example, treating the surface forces of an interacting sphere and a flat surface, a gap between the two bodies was assumed.

If brought into contact, the (theoretical) distance assuming an LJ interaction potential would be equal 1.12σ. Elastic deformation of the sphere and the flat surface have not been considered (infinite stiffness was assumed for the bodies). In such cases, the contact ideally is a point contact. However, if the Young's modulus (modulus of elasticity) of one of the bodies (or both) has a finite value, then the contact point becomes a contact circle with a radius "a." The value of the contact radius "a" depends in such cases on the elastic properties of the spheres, on the Young's moduli E_1 and E_2, and on the Poisson's ratios ν_1 and ν_2, of the two contacting materials, respectively. The value of the contact radius "a" for two spheres pressed together can be calculated from the following formula:

$$a^3 = \frac{3}{4}\left(\frac{1-{\nu_1}^2}{E_1} + \frac{1-{\nu_2}^2}{E_2}\right)\frac{R_1R_2}{R_1+R_2}L$$

with the load L pressing the two spheres of the corresponding radii R_1 and R_2, respectively, without assuming surface forces. The "flattening out" of the contact area from a point (infinite stiffness) to a circle is due to elastic deformation under the applied mechanical load [10]. These (and the corresponding) expressions were derived by Hertz, hence the name "Hertzian contact." If one assumes that one of the spheres is a flat surface (say, $R_1=\infty$ and $R_2=R$) and if one of the surfaces has a much larger modulus (virtually rigid, $E_1=\infty$) as compared to the other ($E_2=E$), then the contact radius can simply be written as

$$a^3 = \frac{3}{4}\left(1-\nu^2\right)\frac{RL}{E}.$$

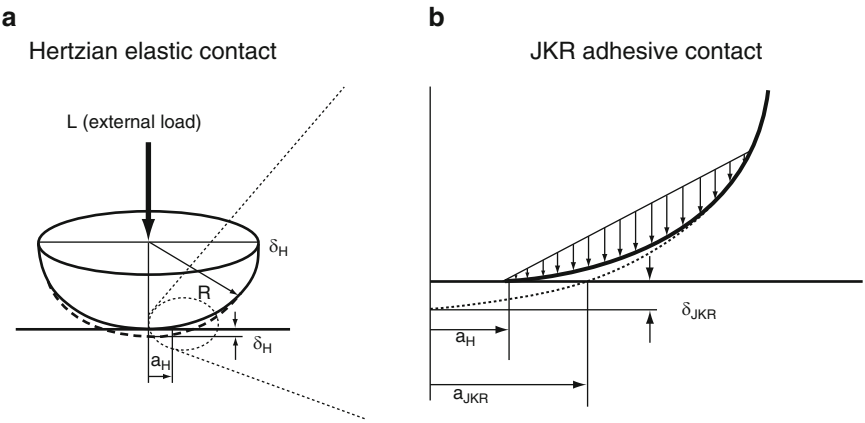

Fig. 1.3 Comparison of elastic Hertzian contact (left) and adhesive JKR contact (right). (a) Hertzian contact: Dashed line (sphere): shape of contacting spherical lens prior to pressing to the flat surface by force L. Hertzian contact profile shown by solid line, with radius under external load L: a_H; (b) JKR contact: Schematic of adhesion force (adhesive "zone" model, forces schematically indicated by vectors) further deforming a spherical lens from Hertzian contact (solid line) to JKR contact (dotted line) with radius a_{JKR}. Reproduced from [7] with permission; copyright Springer Verlag

Hertzian contact mechanics in AFM plays a role in indentation measurements as shown later. However, when surface (adhesive) forces are present, the shape of the contacting spheres in the vicinity of the rim of the contact area will further be deformed. As a result of van der Waals attraction, this additional deformation of the elastic body will pull the two contacting objects closer together and hence will increase the contact radius as compared to the Hertzian value. It was Johnson, Kendall, and Roberts (JKR) who described the area of contact of two spheres including surface energy under the combined external load and the load of adhesion forces [10]. Figure. 1.3 [7] shows the contacting geometry for an infinitely stiff (rigid) surface and an elastic sphere for the Hertzian (dashed line) and JKR (solid line) contacts, respectively.

Near the contact, the vertical arrows at the dashed contour schematically represent the surface forces which cause an additional deformation of the elastic sphere thus increasing the contact radius from a_H (Hertz) to a_{JKR} (JKR). The contact radius for the JKR model is a function of the external load, the work of adhesion, the radius of the contacting sphere (or the reduced radii of the contacting spheres, if two spheres are in contact) and the elastic constant K (a combination of the Young's moduli and the Poisson's ratios of the contacting materials), defined as

$$\frac{1}{K} = \frac{3}{4}\left(\frac{1-{v_1}^2}{E_1} + \frac{1-{v_2}^2}{E_2}\right).$$

The JKR contact radius becomes

$$a^3{}_{\mathrm{JKR}} = \frac{R}{K}\left[L + 3\pi W_{132}R + \left(6\pi W_{132}RL + (3W_{132}\pi R)^2\right)^{1/2}\right],$$

where, W_{132} is the work of adhesion between two bodies (in a third medium). The value of a_{JKR} can only become zero (at the rupture of contact) if the normal force is negative, i.e., if the contacting sphere is pulled up (away from the flat). In this case, a physical solution can only exist if

$$6\pi W_{132}RL \leq (3W_{132}\pi R)^2.$$

When the contacting sphere is about to "jump off," the force that is necessary to separate the sphere from the flat plane, L_{pf} is written as

$$L_{\mathrm{pf}} = -\frac{3}{2}(W_{132}\pi R).$$

For the Hertzian contact, no force is needed to pull away the contacting sphere from the flat plane in excess of the weight of the sphere. However, for the JKR contact, due to adhesion forces, this does not hold. The value of the nonzero pull-off force represents the adhesion of the contacting sphere with the flat plane. Strictly speaking, this force corresponds to adherence of the surfaces as energy dissipation, surface relaxation, etc. also influence its value. It should be stressed that the value of the JKR pull-off force only depends on the sphere (lens) radius and the work of adhesion in the medium in which the JKR experiment is conducted. Thus, the contact area and mechanical properties for true JKR contacts do not play a role for its value. All the above considerations for contact mechanics were based on pairwise additivity of molecular forces.

The role of the medium, in which contacting and pull-off are performed, has been mentioned but not considered so far. However, the surroundings obviously influence surface forces, e.g., via effective polarizability effects (essentially multi-body interactions e.g., by the presence of a third atom and its influence via instantaneous polarizability effects). These effects can become noticeable in condensed media (liquids) when the pairwise additivity of forces can essentially break down. One solution to this problem is given by the quantum field theory of Lifshitz, which has been simplified by Israelachvili [6]. The interaction is expressed by the (frequency-dependent) dielectric constants and refractive indices of the contacting macroscopic bodies (labeled by 1 and 2) and the medium (labeled by 3). The value of the Hamaker constant A_{total} is considered as the sum of a term at zero frequency ($\nu = 0$, dipole–dipole and dipole–induced dipole forces) and London dispersion forces (at positive frequencies, $\nu > 0$).

$$\begin{aligned} A_{\mathrm{total}} &= A_{\nu=0} + A_{\nu>0} \\ &\approx \frac{3}{4}kT\left(\frac{\varepsilon_1 - \varepsilon_2}{\varepsilon_1 + \varepsilon_2}\right)\left(\frac{\varepsilon_2 - \varepsilon_3}{\varepsilon_2 + \varepsilon_3}\right) + \frac{3h\nu_{\mathrm{e}}}{8\sqrt{2}} \\ &\quad \times \frac{(n_1{}^2 - n_3{}^2)(n_2{}^2 - n_3{}^2)}{(n_1{}^2 + n_3{}^2)^{0.5}\left[(n_1{}^2 + n_3{}^2)^{0.5} + (n_2{}^2 + n_3{}^2)^{0.5}\right]}. \end{aligned}$$

Here, ν_e is the main electronic absorption frequency in the UV, typically around $3\times10^{15}s^{-1}$ [6]. An analysis of the above equation shows some interesting consequences. A close match between the dielectric constants of the interacting bodies leads to diminishing values of the first term. The second term (determined by the refractive index values) shall then play the dominant role in the surface forces in this case. This effect can be utilized in "force spectroscopy" to maximize pull-off forces. On the other hand, interaction forces can also be minimized by a proper choice of the medium. Both these aspects will be important later for AFM-based force spectroscopy.

Finally, we note that several other contact mechanics theories have been put forward, which are not described in detail in this contribution. The most important ones of these theories for AFM applications include the Derjaguin–Muller–Toporov (DMT), the Burnham–Colton–Pollock (BCP), and the Maguis mechanics [11, 12]. These theories differ in the assumptions (and limitations) and yield different expressions for the pull-off force. For example, the DMT theory, which assumes that long-range surface forces act only outside the contact area (as opposed to JKR, where adhesion forces only inside the contact area are assumed), predicts a pull-off force of $-2\pi RW$.

1.3 Modeling the AFM Force–Distance Curve: Interactions Between Tip and a Planar Half-Space

Subsequently, we treat the dynamics of tip–sample approach using a sphere with a radius R representing the tip; a Hookean spring beam with a spring constant k representing the cantilever, and a flat specimen. Interatomic interaction forces are described by the Lennard–Jones 6–12 potential, neglecting Kasimir forces (retardation effects). We describe the total potential energy of this system as a function of cantilever–surface distance. We give further a relationship between cantilever bent (forces acting on the cantilever) and the distance of the cantilever from the surface. Details of this treatment and the main results can be found in [5].

Using the notations in Fig. 1.4, we shall first describe the total potential energy as a function of "u." Then, we express the cantilever deflection "z–u" at different cantilever–surface distance "u."

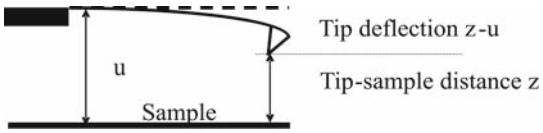

Fig. 1.4 The position of the cantilever in the scheme without interaction forces is horizontal, and the distance from the sample surface is equal to "u" (dashed line; in experiments not necessarily parallel with the sample surface plane). In the presence of (attractive) interaction forces, the cantilever will bend "downwards" with a deflection (measured at the free end of the cantilever) equal to z – u. Neglecting the tip vertical size, this results in a tip−sample distance of "z"

The total potential energy is equal to the sum of the stored elastic energy of the bent lever and the intermolecular energy for the tip–sample surface (intermolecular energy between a sphere and a flat half-space):

$$W_{\text{total}} = W_{\text{t}} = \frac{1}{2}k(z-u)^2 + F_0\sigma\left[\frac{\sigma^7}{210z^7} - \frac{\sigma}{z}\right],$$

where, the constant F_0 can be written as $F_0 = \frac{2}{3}\pi^2\varepsilon\rho_1\rho_2\sigma^4 R$.

Here, ε and σ are the Lennard–Jones parameters, ρ_1 and ρ_2 are the number densities of atoms in the sphere (representing the tip) and the semispace, respectively, and R is the radius of the sphere replacing the tip.

The five potential energy curves shown in Fig. 1.5 show two energy minima at different deflections. The absolute minimum (curve for the smallest u value) corresponds to the stable equilibrium. For the largest u value (largest cantilever−sample distance) the absolute minimum is broad and is around 3nm deflection. A sharp local minimum can be seen at ca. 0.2nm distance. For the lowest cantilever–sample distance shown, the situation becomes reverse: the sharp minimum at low tip–sample distance (at ca. 0.2nm) becomes the absolute minimum. For intermediate cantilever−sample distances two minima can be observed: a broad at higher deflection, and a sharp at smaller deflection values. The existence of these two minima results in a hysteretic cantilever deflection vs. tip–surface distance curve (see Fig. 1.6).

The hysteretic behavior can be understood based on the potential energy function shown on Fig. 1.5. For large u values, the force (derivative of the potential energy) is zero [in position (1)]. When approaching the sample surface, we decrease the value of u, and the cantilever would bend with decreasing u more and more toward the sample surface; i.e., the value of z is getting smaller with decreasing u. This results in a decrease in the z–u value [compare (1), (2), and (3) in Fig. 1.6]. In point (3), i.e., at the corresponding u value, the sharp energy minimum at ca. 0.2nm distance

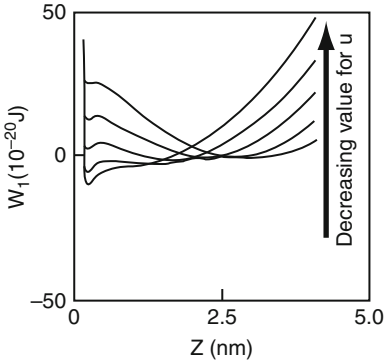

Fig. 1.5 Total potential energy of a spherical tip−planar sample system as a function of tip−sample distance for five different cantilever−surface distance values (u = 1.0, 1.5, 2.0, 2.5 and 3.0 nm). Reproduced from [5] with permission, copyright Oxford University Press

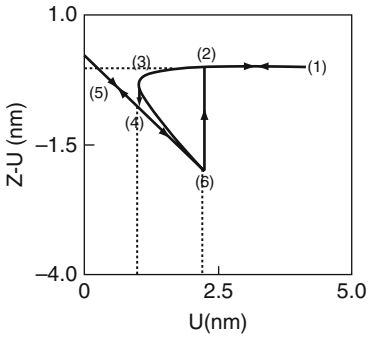

Fig. 1.6 Cantilever deflection (z – u) as a function of the tip−surface distance. The cantilever deflection is proportional to the force acting on the tip. A hysteretic behavior is clearly visible. Reproduced from [5] with permission, copyright Oxford University Press

(see Fig. 1.5) becomes the absolute minimum, and the tip jumps into this energy state, resulting in a tip−surface contact [point (4), snap on]. Upon further decrease of u of the tip [to point (5) and beyond] the deflection $z–u$ (i.e., the force the tip exerts on the surface) will increase linearly (Hookean deflection). When the cantilever is subsequently withdrawn, first the contact between sample and tip is maintained [from (5) to (4) and beyond]. In position (4), the potential energy of the cantilever–tip/sample surface system is still in the sharp minimum and around 0.2nm (Fig. 1.5). Upon further withdrawal (further increase of u) the tip would have to "jump" out into the broad energy minimum (when this becomes deeper as compared to the small distance sharp minimum). However, this requires passing the energy barrier separating the two minima (rolling out from the sharp minimum to the broad minimum), i.e., there is a bistable region present for the corresponding cantilever−sample distances. Rolling out to the broad minimum will take place at point (6), which corresponds to a snap off of the tip from the sample surface. Hence, a clear hysteretic behavior of the force (which is proportional with z – u) vs. tip (or cantilever) distance can be observed when approach and withdrawal are compared. This is a result of the adhesive intermolecular forces between tip and sample. We note that the hysteresis depends on the cantilever stiffness, for stiffer cantilevers the snap-on jump will be shifted to smaller u values. For strong enough cantilevers, the snap-on can even disappear. Surface chemical composition, surface free energy, contamination, roughness, thin condensed water layers, etc. can change this behavior, yet the force curve hysteresis, snap-on, and pull-off as shown in Fig. 1.5 illustrate ideal force−distance curves that one captures in a typical CM operation.

1.4 Static Theory of Deflected Cantilever Beams

A cantilever is a beam, which is supported (clamped) into a substrate only at one end. It can be statically loaded, e.g., at its free end (see Fig. 1.7). This load will deflect the lever, bending it toward the direction of the load. The deflection at a given

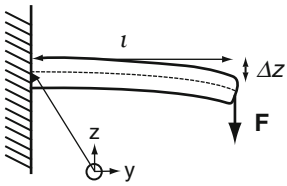

Fig. 1.7 A cantilever beam bending around the x-axis (the origin of the Cartesian reference system shown is offset for clarity). The dashed line is the so-called neutral line exhibiting no compression (or expansion) of the bent cantilever with respect to the original length l. Above the neutral line the cantilever expands, and below contracts due to volume stresses

distance away from the clamped end can be expressed as a function of the cross sectional profile, beam material modulus, and magnitude/point of attack of the force. Here, we focus on simple cases, e.g., assume a beam loaded at its free end, and assume a homogeneous cross section and isotropic, homogeneous beam material. We further assume small deformations. What we seek for is a deflection of the free end. In AFM, this deflection (usually measured by *optical* beam techniques) is used in combination with the spring constant of the cantilever to express the force we measure. In a simplistic picture, the integrated AFM cantilever–tip system bears an analogy to a stylus with a finite mass attached to a (vertical) spring deformed under its weight.

Cantilevers in AFM function as force transducers converting unknown force to measurable deflection. The value of the unknown force can then be expressed by Hookean mechanics following spring constant calibrations. In addition to static point loads, cantilevers can also be vibrated, e.g., by an oscillation piezo to which the fixed end of the beam is attached (or by other approaches). Excitation frequency, oscillation amplitude, and phase relationships are variables that govern dynamic tapping (intermittent contact) imaging. This problem will be discussed in the next section.

In equilibrium, the sum of all forces and torques are zero. For bent levers, rotational equilibrium should be considered, which is related to the so-called area moment of inertia. The area moment of inertia (I) measures the beam's ability to resist bending. The larger its value, the less the beam will bend.

The area moment of intertia I can be written as

$$I = \iint z^2 \mathrm{d}x\mathrm{d}y.$$

The beam spring constant k has the form

$$k = 3\frac{EI}{l^3}.$$

For beams with rectangular cross section the area momentum is described by

$$I_\mathrm{r} = \frac{ad^3}{12},$$

where, a is the width (in the x direction) and d is the thickness (in the z direction) of the lever; and for cylindrical beams with a diameter d

$$I_c = \frac{\pi d^4}{64}.$$

Thus, the deflection of a rectangular beam under force F, for small (Hookean) deformations has the following form:

$$\Delta z = \frac{F}{k} = F\frac{4l^3}{Ead^3}.$$

This is the basic formula for beam deflection and it shows that the beam stiffness is proportional to the third power of the beam thickness, linearly proportional to the beam width and proportional to the negative third power of the beam length. A good treatment of beam mechanics can be found in [13] and in http://www.efunda.com/formulae/solid_mechanics/beams/theory.cfm.

1.4.1 Vibrating Cantilever Beams

In force microscopy, understanding and describing cantilever resonance (forced, damped resonating lever) plays an important role for intermittent contact (tapping mode), force modulation, phase imaging, HarmoniX imaging, etc. In order to introduce forced oscillation of cantilevers, we first briefly recapitulate the physics of a freely vibrating spring−mass system, and then introduce driven oscillators, and damped, driven oscillators. For a thorough introduction, the reader should consult textbooks in classical mechanics, such as [14]. We complete this part with a brief account on the basics of HarmoniX operations.

In the treatment of a linear harmonic oscillator, we assume that a mass m, attached to a spring with a spring constant k is freely vibrating without loss of energy in the vertical (z) direction (see Fig. 1.8).

In equilibrium, the spring force $-kz$ must be equal to the acceleration force (Newton's second law), i.e.,

$$m\frac{\mathrm{d}^2 z}{\mathrm{d}t^2} + kz = 0.$$

The free natural angular frequency of the vibrating motion is defined as $\omega_0 = \sqrt{\frac{k}{m}}$.

The solution of this classical differential equation becomes

$$z(t) = A\sin(\omega_0 t + \varphi)$$

with φ as the phase angle, and A as the vibration amplitude.

The oscillation frequency f_0 is defined as $f_0 = (1/2\pi)\omega_0$ and the oscillation period T_0 is $T_0 = 1/f_0$.

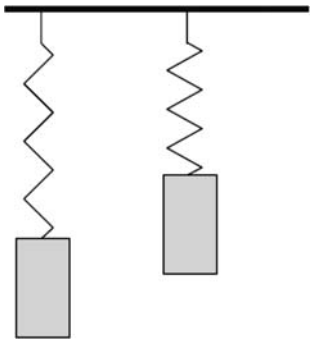

Fig. 1.8 Vibrating mass-spring system

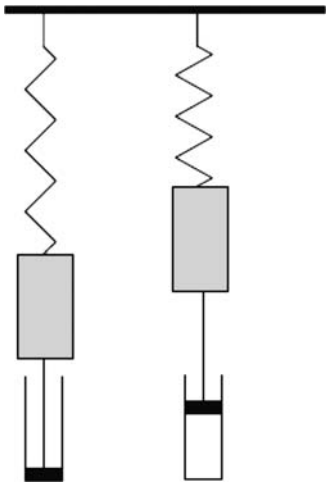

Fig. 1.9 Vibrating mass-spring system with damping

If the oscillation is damped by friction (viscous element, dashpot in Fig. 1.9), then an additional force describing the damping must be added to the equation of motion, which becomes:

$$m\frac{\mathrm{d}^2z}{\mathrm{d}t^2} + b\frac{\mathrm{d}z}{\mathrm{d}t} + kz = 0,$$

where, damping force, resulting in energy dissipation, is proportional to the instantaneous vertical speed. The resonance frequency becomes:

$$\omega_\mathrm{r} = \frac{\sqrt{\omega_0^2 - 2b^2}}{2\beta} \text{ with } \beta = \frac{b}{2m}.$$

As there is energy dissipation, without restoring energy the vibration would taper off. In order to maintain the vibration, energy must be pumped into the system, i.e., motion must be forced. In force microscopy, this can happen in various ways. The cantilever beam can be attached to a vibrating bimorph at its base, which consists of a piezoelectric ceramic stub sandwiched between two metals, serving as electrodes. When a voltage is applied to the metals, the bimorph will bend, or vibrate, with a given vibration amplitude. The lever can be vibrated by vibrating the sample underneath via variation of intermolecular forces acting on the tip (sample-driven lever, see [5]), and by driving the tip (e.g., using magnetic tips and an oscillating magnetic field).

We shall first summarize the motion of the damped forced oscillator, which includes a force contribution driving the motion and supplying energy to the vibrating system.

$$\Sigma F = m\frac{\mathrm{d}^2 z}{\mathrm{d}t^2} = F_{(\mathrm{spring})} + F_{(\mathrm{damping})} + F_{(\mathrm{driving})} = -kz - b\frac{\mathrm{d}x}{\mathrm{d}t} + F_0 \cos(\omega t),$$

i.e., the oscillator is driven by a periodic force having an angular frequency ω (which is adjustable) and an amplitude F_0. The damping of oscillations resulting from friction is counteracted by supplying the system with energy from an external source at a supply rate which is equal to the energy absorption rate of the damping medium (driven, damped osscilator). Resonance occurs when the amplitude of a driven and damped oscillatory system is at a maximum. This resonant frequency depends on the driving frequency ω, and the damping coefficient b (Fig. 1.10).

The solutions to the differential equation of a driven, damped harmonic oscillator include the amplitude and the phase as a function of the reduced angular

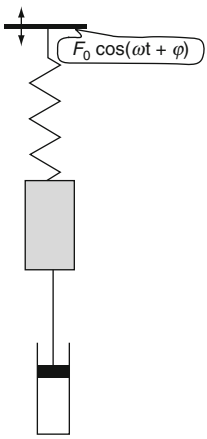

Fig. 1.10 Illustration of a forced mass-spring oscillator. The left end of the spring is wiggled back and forth with an angular frequency ω and a maximum amplitude F_0. Damping is proportional to friction, i.e., to negative velocity

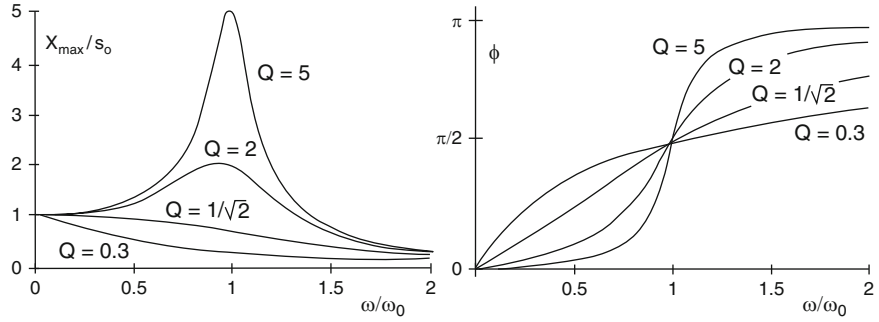

Fig. 1.11 Qualitative plots of solutions (normalized damping amplitude and phase shift) for a damped, driven oscillator as a function of the relative frequency ratio. In-phase vibrations correspond to a phase shift of zero, while out-of-phase means a phase shift of 180° (πradian). With increasing quality factor (decreasing damping) the resonance becomes sharper

frequency of the excitation; i.e., ω/ω_0. Depending on the parameters, a resonance of the amplitude at excitations around the natural eigen frequency can be observed. The sharpness of the resonance is usually described by the so-called quality factor of the oscillator. For subsequent considerations, the quality factor, Q, of an oscillator is defined as its resonance frequency divided by the width of the resonance. High Q factors mean high resonance frequencies with corresponding narrow resonance widths. The higher the Q value, the more stable is the oscillator, for a high Q means that an oscillator will operate close to its natural resonance frequency (Fig. 1.11). There is a relationship among the quality factor, the damping coefficient, and the resonance frequency, written as:

$$b \approx \frac{m\omega_0}{\sqrt{Q^2 + \frac{1}{2}}}; \frac{m\omega_0}{Q},$$

$$Q \approx \frac{\omega_0}{\Delta\omega}; \frac{m\omega_0}{b} = \frac{\text{Energy stored}}{\text{Energy dissipated}}.$$

The simple textbook solution of a harmonic damped oscillator becomes complex when the vibrating tip interacts with the surface of a sample, e.g., in tapping mode AFM. Although the different imaging modes and the experimental observables may vary, the underlying physics is similar. Amplitude and frequency modulated AFMs are most commonly used, labeled by AM–AFM (amplitude modulation or tapping) and FM–AFM. For a detailed review of this topic several reviews are available, e.g., [15].

The differential equation of motion of a damped oscillator, which interacts with the surface via a weak tip–sample force F_{ts}, can be written by adding tip–sample interactions (weakly perturbed oscillator).

$$m\ddot{z} + kz + \frac{m\omega_0}{Q}\dot{z} = F_{\text{ts}} + F_0 \cos(\omega t).$$

The solution depends on the interaction forces, including long range attractive interactions, contact and short range repulsion forces, JKR forces, etc. The relevant parameters include the (driving) frequency, the phase, and the amplitude of the oscillation (Fig. 1.12).

The oscillation amplitude A is the primary variable in AM–AFM. Its representation as a function of the average tip–surface separation d is called amplitude curve. The numerical solution of the weakly perturbed oscillator shows in some situations two different solutions for the vibration amplitude, a low (L) and high amplitude (H) solution. If the tip–surface separation and the external parameters are unchanged, the initial conditions will determine which solution is realized.

For a weakly perturbed, harmonic damped driven oscillator, the resonance is shifted on the frequency scale depending on the sign of the interaction forces (Fig. 1.13). The availability of analytical expressions facilitates the applications of the weakly perturbed harmonic oscillator models for AM–AFM. Such harmonic models may be useful to illustrate the concepts used in AM–AFM well enough; however, in most practical imaging cases, they do not describe the experiments [15].

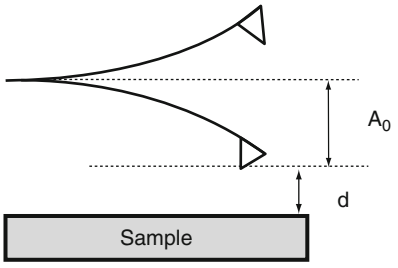

Fig. 1.12 Tip–sample distance d and free vibration amplitude A_0. When the tip approaches the surface, the value of A_0 will decrease. In tapping, the tip "touches" the surface at each cycle, which changes the oscillation amplitude to A. The setpoint at which images is done is defined as A/A_0

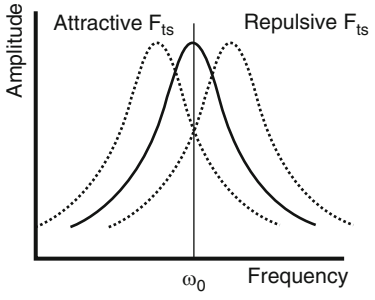

Fig. 1.13 Resonance curve shifts for vibrating lever as a function of attraction, or repulsion

In a tapping experiment, the cantilever is vibrated at a given fixed frequency ω (either at resonance or slightly off resonance) and the amplitude and phase are measured. Further parameters include the free oscillation amplitude and the distance of the "bottom" (close) amplitude from the sample. Depending on the nature of interactions, the resonance curve gets distorted. Based on energy balance and dissipation arguments (which also account for nonlinear oscillation behavior), a unified theory has been offered by Garcia and coworkers, which not only describes the weakly perturbed, harmonic, but also the coupled nonharmonic oscillator relevant for most practical imaging conditions [16].

The first argument to consider energy dissipation in place of mass point systems was put forward by Cleveland et al. [17] (Fig. 1.14).

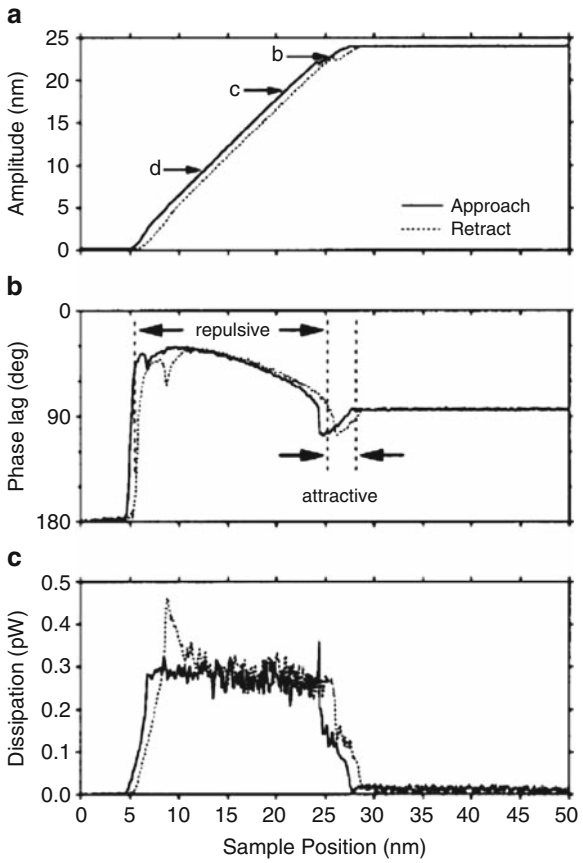

Fig. 1.14 The amplitude, phase, and powder dissipation of the resonating cantilever measured as a function from the sample surface (d) according to Cleveland et al. The sample first was approached and then withdrawn. (Data obtained using Si cantilever/tip tapping on Si wafer.) Reproduced with permission from [17]

The results demonstrate the relationship between the phase angle and energy dissipation. From a physics point of view, the action of attractive and repulsive, nonlinear tip–surface interactions contribute to the coexistence of two stable oscillation states in AM–AFM. The jump in the amplitude curve corresponds to transition from the attractive to the repulsive regime, near point *b*, where the phase changes sign. This will later be important for interpretations of phase images.

Phase contrast in AM AFM can be observed primarily due to inelastic contributions and some elastic ones (topography, contact–noncontact transitions, and variation of elasticity if dissipative channels are present). Attractive (low amplitude, L branch) and repulsive (high amplitude, H branch) regimes are shown below (Fig. 1.15 and 1.16).

The unified theory by Garcia et al. considers the cantilever–tip system as a driven anharmonic oscillator with damping, and averages over the oscillation period are considered. This approach allows one to express tip–surface conservative and dissipative forces in terms of observable features such as amplitudes or phase shifts.

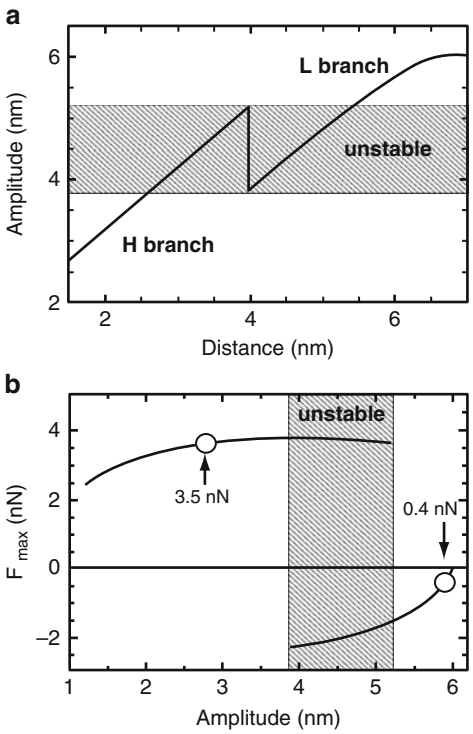

Fig. 1.15 (a) Theoretical amplitude curve as a function of sample−tip distance (d). The shadowed region corresponds to unstable behavior. (b) Corresponding force maximum as a function of the damped amplitude. Adapted from [15] with permission by Elsevier

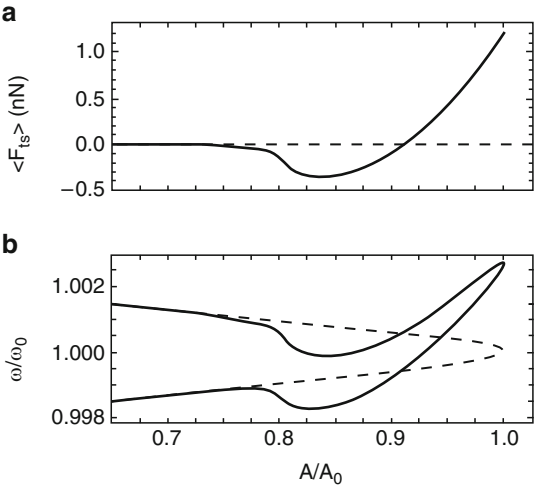

Fig. 1.16 Average tip−sample force and oscillation frequency as a function of reduced amplitude (setpoint). The dashed resonance corresponds to a damped driven oscillator without sample−tip interactions. Reprinted from [16], copyright American Physical Society

Variations of surface topography alter the tip–surface distance and will result in an instantaneous change of the amplitude. A feedback mechanism in imaging will keep the amplitude constant by adjusting the vertical z position of the sample holder to compensate for the topography. This feedback signal will give a topographic image of the surface. When the phase lag is also detected, (phase imaging) the phase signal will provide information about the energy dissipation that can be related to composition. Phase contrast can be observed primarily because of inelastic contributions such as surface adhesion hysteresis, viscoelastic dissipation, and long-range hysteresis.

The average value of F_{ts} as a function of the reduced amplitude is shown in Fig. 1.16 featuring attractive (negative) and repulsive (positive) forces. The normalized resonance curve (solid line) deviates from the forced harmonic oscillator behavior and exhibits a shape that resembles the force. For small amplitudes, the tip does not "reach" the surface and $F_{ts} \cong 0$. For higher amplitudes, the attractive forces increase, and reach a minimum (mechanical contact). For further increase of the amplitude, the share of the repulsive forces increases and eventually they become dominant. Attractive forces shift the resonance curve to frequencies lower than the free resonance, while repulsive forces cause a shift to higher frequencies. This peculiar shape results in certain operating frequencies in three amplitude values as solution (instability). This unifying theory of imaging by Garcia et al. and its subsequent detailed analyses serve as physical basis for AM–AFM for interacting systems.

The dissipated energy, which is the difference between the externally supplied energy and the energy dissipated by the medium, can be written as [15, 17]

$$E_{\text{diss}} = E_{\text{ext}} - E_{\text{med}} = \left(\sin\varphi - \frac{A}{A_0}\right)\frac{A}{A_0}\frac{\pi k {A_0}^2}{Q}.$$

Obviously, the phase signal φ is determined by the dissipated energy. A nice recent highlight of phase imaging for soft matter can be found in [18].

Finally, we mention that the recent HarmoniX imaging by Veeco holds the promise of significantly enhancing composition specific and material phase contrast due to the a special asymmetric attachment of the microfabricated tip off the cantilever axis. The related torsional vibrations have a high-frequency bandwidth and hence, they can respond to high-frequency forces and are more sensitive at the same time because of the special asymmetric cantilever–tip geometry. It is expected that this development will result in additional development of quantitative materials characterization at high speed [19].

References

1. Hemsley DA (1989) Applied polymer light microscopy. Elsevier Applied Science, London
2. Sawyer LC, Grubb DT, Meyers GF (2008) Polymer microscopy: characterization and evaluation of materials, 3rd edn. Springer, Berlin
3. Binnig G, Quate CF, Gerber C (1986) Phys Rev Lett 56:930
4. Schönherr H (1999) From functional group ensembles to single molecules: scanning force microscopy of supramolecular and polymeric systems. Ph.D. Thesis, University of Twente, Enschede, The Netherlands
5. Sarid D (1991) Scanning force microscopy with applications to electric, magnetic and atomic forces. Oxford University Press, Oxford (ISBN 0–19–506270–1)
6. Israelachvili J (1992) Intermolecular and surface forces. 2nd edn. Academic, London
7. Vancso GJ, Hillborg H, Schönherr H (2005) Chemical composition of polymer surfaces imaged by atomic force microscopy and complementary approaches. Adv Polym Sci 182:125–129
8. Ducker WA, Senden TJ, Pashley RM (1991) Direct measurement of colloidal forces using an atomic force microscope. Nature 353(6341):239–241
9. Grandbois M, Beyer M, Rief M, Clausen-Schaumann MH, Gaub HE (1999) How strong is a covalent bond. Science 283(5408):1727–1730
10. Johnson KL (1985) Contact mechanics. Cambride University Press, Cambridge
11. Cappella B, Dietler G (1999) Force-distance curves by atomic force microscopy. Surf Sci Rep 34(1–3):101–104
12. Butt H-J, Cappella B, Kappl M (2005) Force measurements with the atomic force microscope: Technique, interpretation and applications. Surf Sci Rep 59 (1–6):151–152
13. Hibbeler RC (2003) Mechanics of materials. Pearson Prentice-Hall, Singapore

14. Kibble TWB, Berkshire FH (2004) Classical mechanics. Imperial College Press, London
15. Garcia R, Perez R (2002) Dynamic atomic force microscopy methods. Surf Sci Rep 47:197–301
16. Paulo AS, Garcia R (2002) Unifying theory of tapping-mode atomic-force microscopy. Phys Rev B 66, 041406(R)
17. Cleveland JP, Anczykowski B, Schmid AE, Elings VB (1998) Energy dissipation in tapping-mode atomic force microscopy. Appl Phys Lett 72 (20):2613–2615
18. García R, Magerle R, Perez R (2007) Nanoscale compositional mapping with gentle forces. Nat Mater 6(6):405–411
19. Sahin O, Magonov S, Su C, Quate CF, Solgaard O (2007) An atomic force microscope tip designed to measure time-varying nanomechanical forces. Nat Nanotechnol 2(8):507–514

2 Atomic Force Microscopy in Practice

Abstract

Imaging with an AFM requires an appropriate preparation of the sample as well as of the force microscope for the planned experiment. In this chapter, the basic steps to prepare an AFM setup for a standard contact mode and for intermittent contact (tapping) mode AFM operation will be briefly treated. In addition, practical hints regarding the selection of probes tips, sample preparation, choice of operation modes, and imaging media are provided. Finally, tip modification procedures, calibration issues (spring constant, scanner, photodetector, etc.), general guidelines for AFM laboratories, as well as data evaluation and handling will be very briefly treated.

2.1 Assembling of AFMs for Operation

Assembling different brands and types of force microscopes requires naturally instrument and mode-specific steps and may differ in particular details due to practical peculiarities. On the basis of two common AFM modes, a scanned sample AFM (such as a Digital Instruments/VEECO multimode) and a tip scanning stand alone AFM (such as a Molecular Imaging Pico SPM), the overall principles and basic steps will be introduced in this chapter. These can be generalized to within the limitations of the particular type of AFM the reader is using. We recommend strongly to consult the corresponding manuals.

2.1.1 Scanned Sample AFM (Contact Mode)

The typical scanned sample AFM scanning unit consists of the following parts: a base, a scanner, and an optical head, in which a holder for the cantilever is mounted (Fig. 2.1). In addition, a probe tip/cantilever and sample, which will be mounted on a metallic sample puck, are required. Careful handling of the sensitive equipment (avoid shock, mechanical stress on the cables, temperatures above 40°C, high humidity for the scanner, etc.) is a prerequisite for this work. We recommend wearing

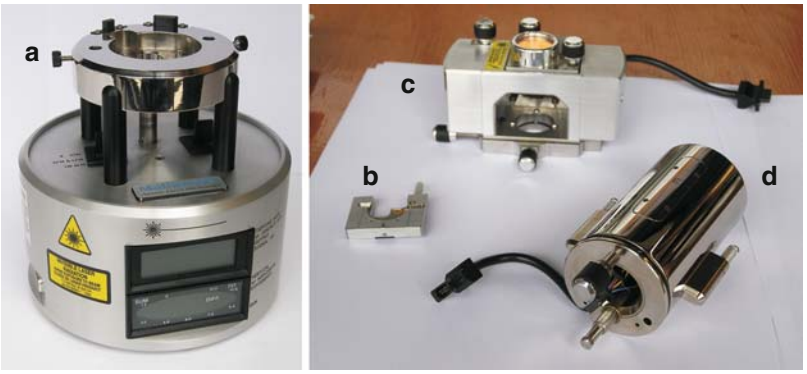

Fig. 2.1 Photographs of the essential components of a sample scanning AFM: (**a**) scanner base, (**b**) cantilever holder, (**c**) optical head, and (**d**) scanner of a typical scanned sample AFM

typical unpowdered lab gloves (made from latex, polyurethane, etc.) to prevent possible contamination of the instrument and samples with fingerprints. In addition, we recommend consulting the manuals for risks of electric shock if cables are not properly used, if there is exposure to laser light, etc., as applicable.

The sample (mounted on a metallic sample puck) is attached to the scanner, which will later position the sample in all three spatial directions. The optical head comprises the cantilever–tip assembly in a special holder, as well as the optics (laser and photodetector) of the beam-deflection detection scheme. The base contains electronic circuitry and is the interface between controller and actual force microscope. It also serves as physical holder for the scanner and may include a stepper motor, which is used for the coarse and fine approach between tip and sample (see below).

The manual assembly can be divided into four basic steps:

Route (a)

1. Mounting of the cantilever in its holder
2. Mounting of the scanner on the base
3. Securing the cantilever holder in the optical head
4. Mounting of the optical head/cantilever holder assembly to the scanner

Alternatively, one can follow

Route (b)

1. Mounting of the cantilever in its holder
2. Mounting of the scanner on the base
3. Mounting of the optical head to the scanner
4. Securing the cantilever holder in the optical head

These steps are identical for contact mode (CM) and intermittent contact (tapping) mode operation, except for the choice of the cantilever. As discussed in more detail below (Sect. 2.2), CM levers for experiments in ambient conditions are relatively soft (with a cantilever spring constant k_c between ~0.05 and ~1.00 N/m), while tapping mode probes are stiffer (k_c ~10–100 N/m). For tapping mode operation in liquids, such as water, CM levers are used.

First, the cantilever is mounted in its holder. Care has to be taken to hold the cantilever chip gently with the tweezers on the side, as shown schematically by the arrows in Fig. 2.2a). Contact of the tweezers with the lever (and potentially the tip) must be avoided; in addition, the chip should always reside with its bottom part on the sample preparation table. If the chip flips over (e.g., because it has been dropped while handling it with the tweezers), one has to assume that the tip may be damaged,

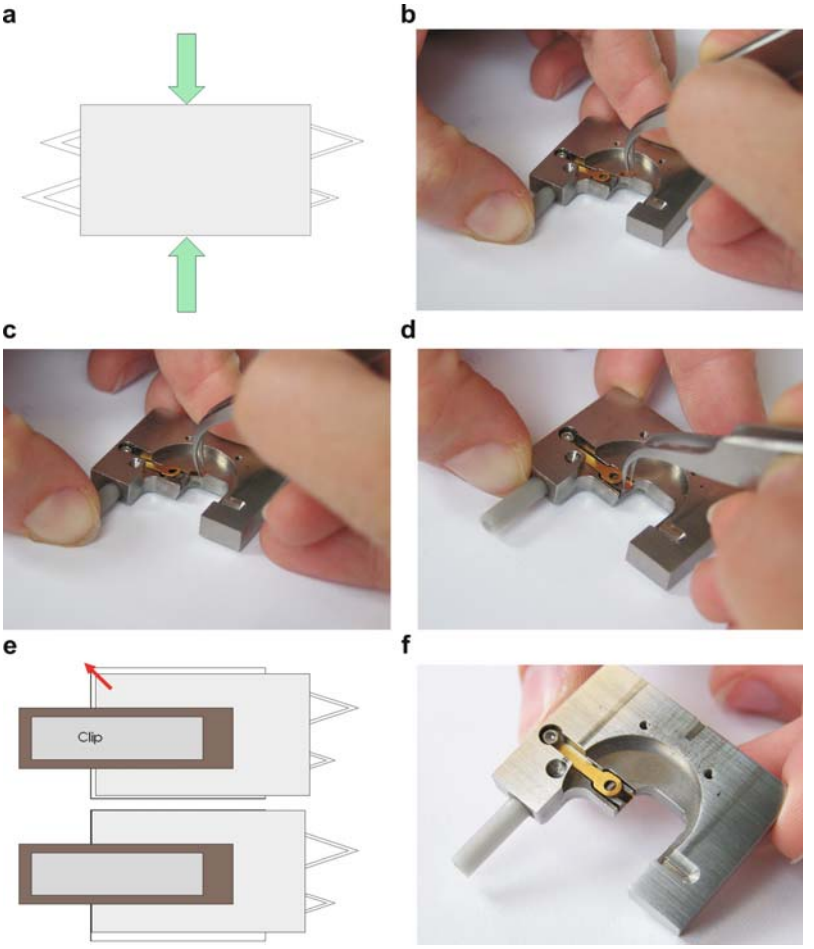

Fig. 2.2 Stepwise mounting of the cantilever into the cantilever holder (details: see text)

even though the cantilever may still be visibly unimpaired (as viewed, e.g., through an eyepiece or an optical microscope).

To open the brass clip of the cantilever holder, the holder is pressed against the table. Then the chip is slid carefully under the clip and the load is released. One should gently push the chip to the end of the "mold," preferably in plane-parallel contact with the sidewall, to avoid possible movement at a later stage.

To start the assembly of the AFM head, the safety screw on the scanner is removed (Fig. 2.3a) and the scanner is mounted carefully on the base (Fig. 2.3b). The stepper motor is slowly moved "up" (using the toggle switch, Fig. 2.3c) to make sure that the hexagonally shaped screw and the fitting on the base match.

Once the scanner sits tightly on the base, it is secured by inserting the safety screw from below (Fig. 2.4a). Subsequently, the scanner cable is carefully inserted into the corresponding plug on the base (Fig. 2.4b).

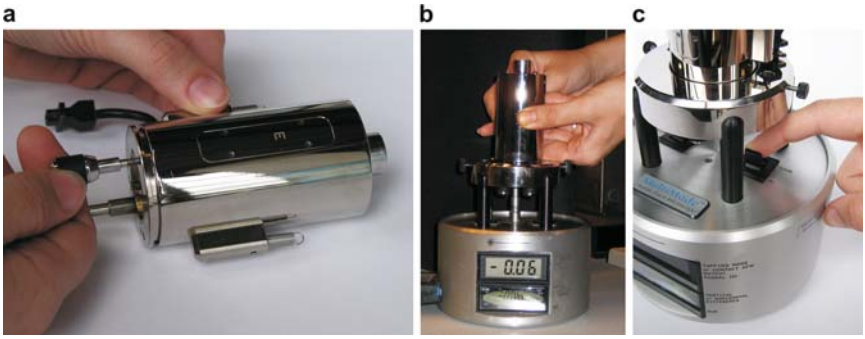

Fig. 2.3 Stepwise mounting of piezo scanner: (**a**) removal of the safety screw; (**b**) placement of scanner on the base; (**c**) operation of the stepper motor (details: see text)

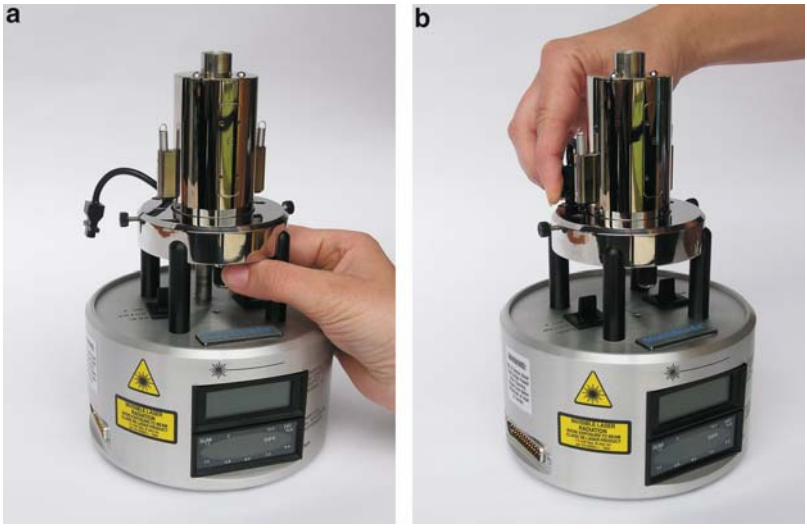

Fig. 2.4 (**a**) Securing the scanner's safety screw; (**b**) insertion of scanner cable into base

To mount the optical head onto the scanner/base assembly, there are two alternative options:

One can (1) first mount the head, followed by insertion of the cantilever holder and securing the cantilever holder screw on the backside (*Route b*, Fig. 2.5), or (2) vice versa, i.e., the holder is secured before the head is mounted (*Route a*, Fig. 2.6). In both cases, the head should be lowered carefully onto the three metal balls on the scanner; holding the head tightly with one hand, the springs on both sides of the scanner are slid over the corresponding metal pins so that they securely hold the optical head in place. *Careful*: Hold the head tightly, especially if only one spring is attached and make sure that the springs are properly attached before release of the grip on the optical head. Otherwise, the head may fall off the scanner and will likely be damaged. Once the head is secured, the scanner cable should be inserted into the corresponding plug on the base.

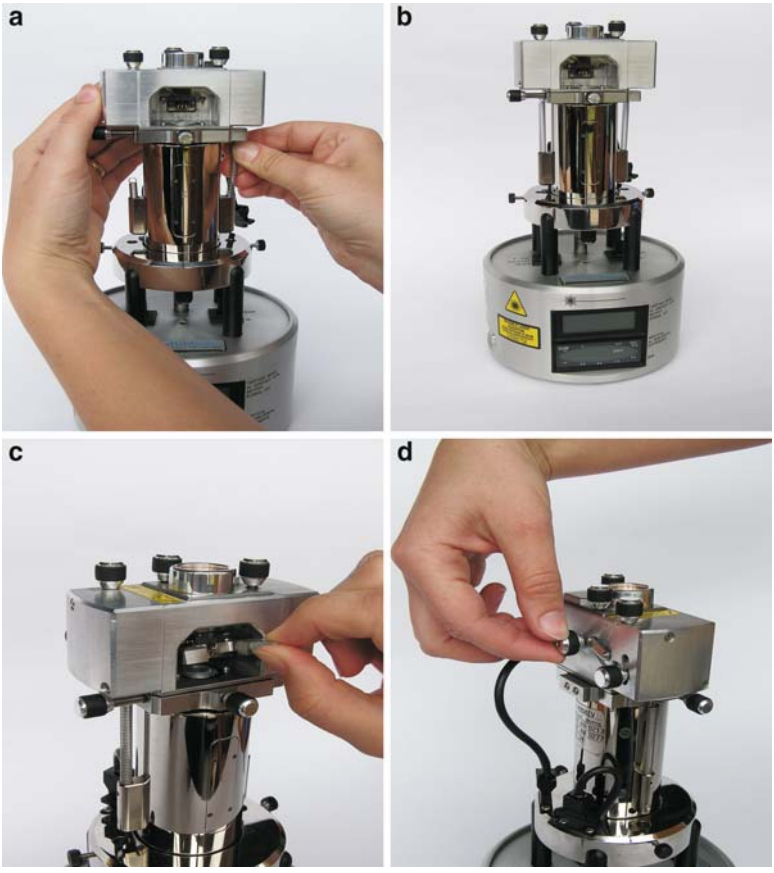

Fig. 2.5 Essential steps of mounting the optical head: (**a**) Mounting of the optical head and securing of the springs; (**b**) optical head mounted on the scanner; (**c**) insertion of cantilever holder into optical head; (**d**) fixation of cantilever holder

Once the optical head, scanner, and base have been assembled and the cables of the scanner and the optical head have been attached, the base can be connected to the controller, following the specifications and instructions of the manufacturer. Care has to be taken that the controller is *not* running and is *not* sending high-voltage signals to the scanner.

To prepare the AFM setup for an experiment, the laser must be aligned, followed by the adjustment of the photodiode position, the mounting of the sample, and finally the crude and fine approach of the tip toward the sample surface.

The laser light position can be altered by turning the screws of the laser stage (Fig. 2.7). To detect where the laser light is being focused and where the reflected beam is directed to, a piece of paper can be inserted into the path of the beam (see

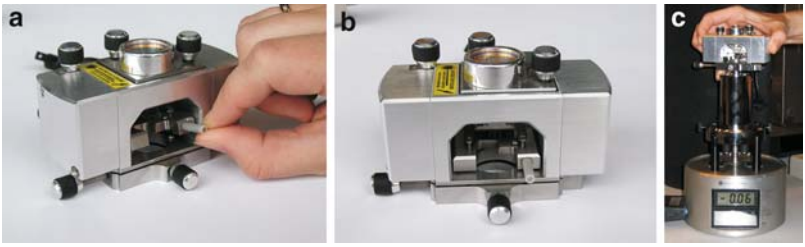

Fig. 2.6 (**a**) Insertion of cantilever holder; (**b**) premounted cantilever holder (the holder has been fixed by tightening the corresponding screws, compare Fig. 2.5d); (**c**) mounting of cantilever holder/optical head assembly onto the scanner

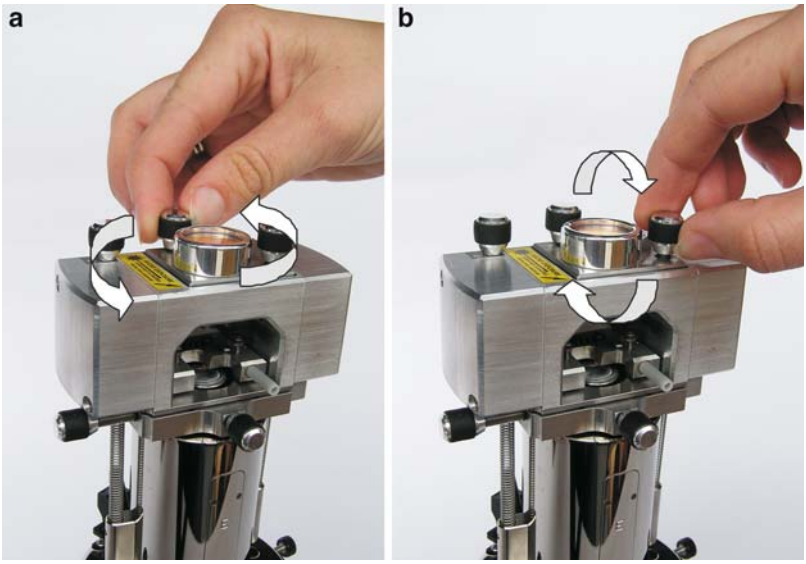

Fig. 2.7 Adjustment of laser light position and alignment via laser stage screws

below). However, please be careful: do not touch the mirror; also never insert reflective objects such as tweezers into the optical path, as laser light may be reflected into the unprotected eye.

An alternative method is to hold the head firmly in one hand and to guide the laser light onto a piece of paper on the table. For this, the head must be detached from the base by carefully removing the springs that secure the head (see above). Instead of analyzing the reflected light from the cantilever, which reaches the photodiode, the blocking of the incident beam is monitored.

The laser light is first directed downward onto the metallic top of the piezo scanner. The laser is reflected and scattered on the rough metal surface, which is easily detected by the eye. As shown schematically in Fig. 2.8a, the laser light spot discernible on the metal is moved to the right using the screws on the laser stage. Once the laser light hits the cantilever substrate, the intense spot on the metal due to reflection/scattering is no longer visible. Subsequently, the laser stage is moved in the opposite direction (corresponding to a movement of the laser spot to the left) such that the laser spot becomes detectable again. This means that the laser light is reflected at a position indicated by the faint spot in Fig. 2.8a, i.e., somewhere on the vertical (dashed) line.

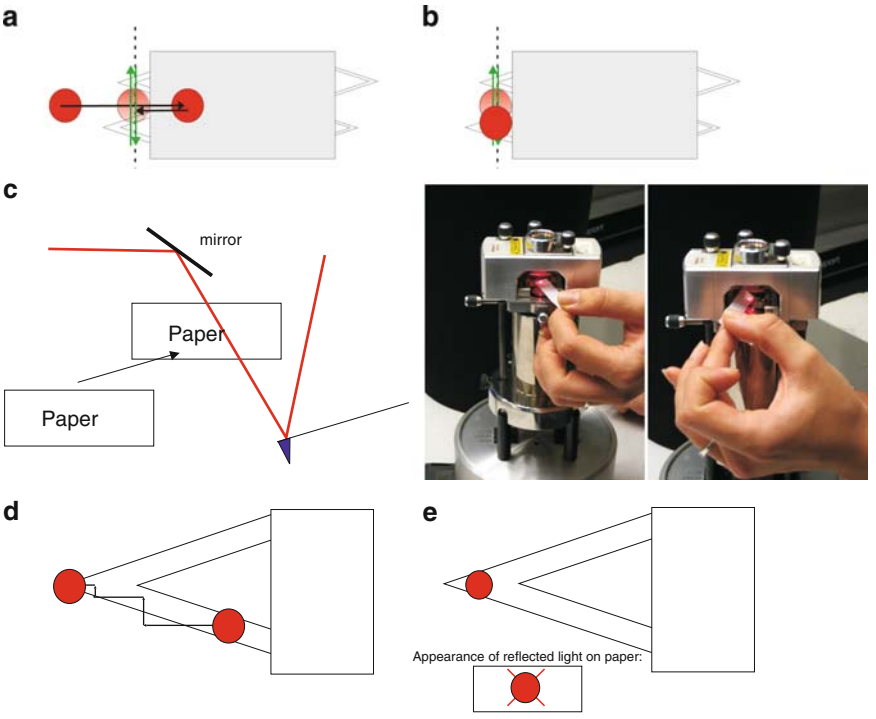

Fig. 2.8 Stepwise process of laser alignment using the paper method (details: see text)

Now we move the spot (using the laser stage) up and down (Fig. 2.8b). If the laser light is reflected off the cantilever, the intensity of the light reflected from the metal is reduced, which can be seen again easily by bare eye. The part of the reflected intensity that is missing is directed toward the mirror and the photodiode (Fig. 2.8c). As mentioned, the reflected beam can be detected conveniently using a piece of paper.

The aim of the paper insertion is to detect the light reflected off the cantilever, as shown below. To properly position the paper to be able to detect the reflected laser light, the piece of paper is first moved into the incident beam. A sharp laser light spot can be easily detected. Subsequently, the paper is moved to the left into a position where the incident light is no longer blocked by the paper. If the alignment procedure according to Fig. 2.8a, b has been successfully carried out, we can observe the reflected laser light as a spot on the paper once we unblock the incident beam.

Having located the reflected laser light, we move the spot in an iterative manner to the end of the cantilever (shown in Fig. 2.8d). While we monitor the reflected laser light on the paper, the spot is moved using the laser stage to the left hand side. If the intensity decreases, the laser stage is moved in the vertical direction (up or down, as required). Continued movement to the left and correction in the vertical direction will ultimately result in a laser spot position on the very end of the cantilever. Reflection from the cantilever edges may result in the appearance of the spot with two diagonal lines, as shown in Fig. 2.8e. For optimized imaging, the spot is moved slightly to the right to ensure a spot on the paper with a well-defined appearance that is devoid of any stray light.

After aligning the laser, the mirror position is turned such that the reflected laser light is directed onto the photodiode (Fig. 2.10a). A maximized sum signal shows a good position (Fig. 2.9). Subsequently, the spot is centered on the photodiode by moving the diode in the vertical and lateral direction such that the corresponding difference signals (see Fig. 2.9) are ∼0.

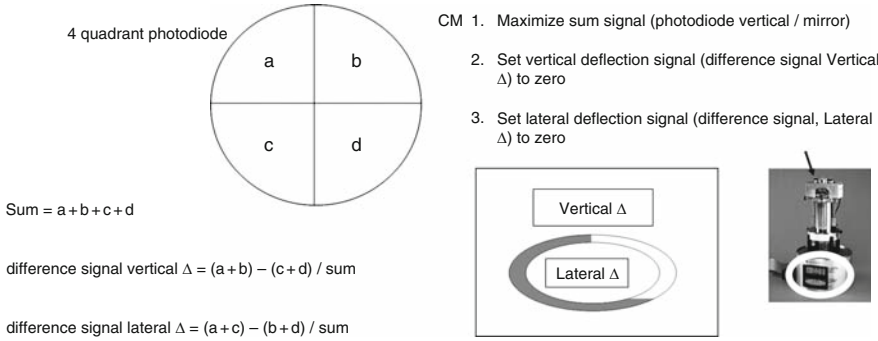

Fig. 2.9 Schematic of photodetector and differential output signals. The top LCD display shows the vertical deflection signal and the lower panel the lateral signal, while the sum signal is displayed as a bar in the ellipse on the lower part of the round display (see schematic)

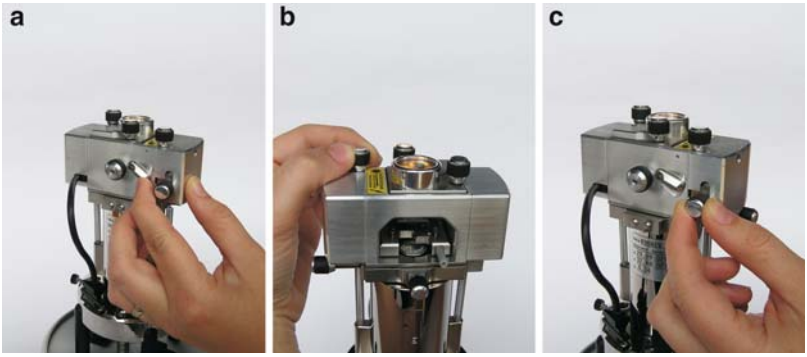

Fig. 2.10 Adjustment of mirror and photodetector position: (**a**) optimizing the mirror position; adjustment of (**b**) vertical and (**c**) lateral photodiode positions

The adjustment of the mirror rotation angle and the vertical and lateral positions of the photodiode are shown in Fig. 2.10.

To prepare the set up for an experiment, the sample should be mounted. For this purpose, we remove optical head, after driving the stepper motor upward to protect the tip and the sample from unintended contact. The sample (mounted to the sample puck; see Sect. 2.2.2) is placed on the piezo scanner in center position. Finally, the optical head is placed again carefully on scanner (please ensure that the tip is far from the sample) and, *with utmost care*, is secured with the springs (for warning: see above).

The set up is now in principle ready to start an experiment. The coarse approach is carried out to position the tip close to (but not in contact with) the sample surface. Using an eyepiece, the cantilever can be viewed from the side (or alternatively one can use a top-view CCD camera for this purpose). With the eyepiece, we locate the reflection of the laser light on the cantilever and its reflection (mirror image) on the sample (red spots). Using the stepper motor, we lower the optical head until the spots are close; however, we still want to clearly be able to detect a gap between the spots. In older scanner types, the optical head is lowered by using the stepper motor for one pod of a tripod, while the other two are lowered manually using the corresponding screws. In this case, it is essential that the head is lowered such that it stays leveled at all times.

With a top-view CCD camera, we bring the camera in focus on the cantilever and then on the sample surface. Subsequently, we move the focal plane upward. Using the stepper motor, we lower the optical head until cantilever becomes sharp in focus. Following both approaches, the tip is now $<$ several 100 μm away from the surface.

The fine approach for CM is carried out by the controller in an automated fashion. Before this approach and the start of the experiment are explained, the photodiode position must be adjusted. The position of the photodiode is changed such that the lateral deflection signal is set to 0.0 V and the vertical difference signal is offset to –2.0 V. The vertical deflection setpoint is entered as 0.0 V in the computer menu. Upon contact with the surface as a consequence of a lowered

optical head, the cantilever will bend upward (resulting in a more positive photodiode signal). By choosing the offset of –2.0 V, we limit the descent of the head and the tip to the vertical deflection setpoint of 0.0 V (i.e., upon lowering the tip, the controller will start scanning with active feedback loop control once the deflection signal reads 0.0 V).

Before the scan is started, the sensitivity of the feedback loop is adjusted by a default setting of the gains: integral gain: 2.0; proportional gain: 2.0; differential gain: 0.0. The tip and sample are protected against damage by opting for a small initial scan size (e.g., 1 μm) and a low scan rate (3.0 Hz). If all these parameters have been adjusted and the vertical deflection signals have been checked, we can start the scan by pressing the "engage" button.

During the descent of the tip, we closely monitor both vertical and lateral deflection signals on the LCD panels. Some variation of these signals (flickering) due to interference effects is typically observed. Upon descent, the vertical deflection signal may change monotonically, in particular for soft cantilevers for decreasing tip−sample separation distances close to physical contact. This cantilever deflection is caused by long-range forces, such as electrostatic forces, between surface and tip. By contrast, the lateral signal should *not* change monotonically. Unless tip and sample (or some protruding parts of the cantilever holder and the sample) are in contact, the lateral signal can only show the mentioned variations. If the lateral deflection signal changes its value monotonically, the engagement procedure must be stopped immediately and the tip/cantilever assembly and sample roughness must be checked to prevent unwanted contact.

The stepper motor of the AFM will reduce the tip−sample separation distance until the actual value of the vertical deflection and the chosen setpoint (0.00 V) coincide. Once the values are equal, the descent stops and the scan starts automatically according to the preset parameters.

Successful tip engagement on the surface is characterized by a jump of the vertical deflection signal from some negative value to 0.00 V differential signal. The force with which the tip engages depends on the magnitude of the jump. If the jump is not noticeable, the upward deflection of the lever as a result of long-range forces may have been such that the differential signal reached 0.00 V without the tip reaching physical contact with the surface. This situation is called, "false engagement." It can be faithfully identified by choosing a higher setpoint value for the feedback loop, e.g., +1.00 V, which corresponds to higher imaging forces. Only if the surface is within reach of the z travel of the piezo scanner, will an image be obtained, the difference signal show a value equal to the setpoint value, and the scanner's z center position (indicated on the AFM image panel) stay within the max/min limits. If the z center position goes out of limits, the piezo is fully extended; however, it cannot reach the setpoint value. Thus, no physical contact between tip and sample had been established. In this case, the tip is withdrawn *once* from the surface (using the appropriate software command), the vertical deflection value is set again to −2.00 V, and the engagement procedure is started again. Depending on the tip−sample forces and the cantilever spring constant, this procedure needs to be repeated several times.

After successful engagement, the gains must be adjusted and the imaging force (i.e., the setpoint) should be minimized. The adjustment of the gains, which regulate the sensitivity of the feedback loop and thus the accuracy with which the controller maintains the constant force value, is best done by analyzing the height and deflection signals in the so-called scope mode. The scope trace and retrace correspond to the currently captured signals for one scan line (back and forth). By increasing the gains in small increments, we aim at a minimized error (i.e., deflection) signal as we operate the AFM in constant force mode. Too low gains result in inadequately maintained setpoint value, i.e., imaging force, and thus a "height" image that does not represent topography of the scanned sample. In fact, at very low gains, the cantilever bends when the tip encounters high features and the image conditions represent "constant height" conditions. In this case, the deflection signal shows pronounced contrast (Fig. 2.11a). For increased gains (Fig. 2.11b), the height image displays the expected profile, however, the residual deflection at the edges shows that the force is by no means kept constant. With appropriate gains, the deflection contrast is vanishing, except for locations with steep changes in topography, while the height image (that displays the z-travel of the piezo required to maintain a constant setpoint force) shows an adequate profile (Fig. 2.11c). If the gains are set too high, the piezo scanner will show clearly discernible uncontrolled feedback (overdrive) seen as overshoot at steep topographic features or even oscillations (Fig. 2.11d, e). Depending on the magnitude and frequency, this unwanted feedback can be audible.

The gains do require adjustment if we alter the scan rate, the scan size, and the setpoint, i.e., the imaging force. It is particularly important to remember that both scan size and rate influence the tip velocity, i.e., if the scan size is increased, the rates should be decreased correspondingly if the feedback loop should operate with a similarly negligible error. Thus, the force and parameter settings that were optimized for a scan size of 1×1 μm^2, cannot be the same for a scan size of 10×10 μm^2 at constant scan rate, as the tip velocity is increased by a factor of 10.

The appropriate force setting is performed in the force−distance mode (Fig. 2.12; for details see also Sect. 4.1 in Chap. 4). In this mode, the deflection of the cantilever is monitored as a function of sample/piezo position, while the tip is brought periodically in and out of contact with the sample surface. The measured cantilever deflection z can be converted to the corresponding force F, by applying Hooke's law, if the spring constant of the lever k is known ($F = k\,\Delta z$).

The adhesion between tip and sample is characterized by the so-called pull-off or pullout force, which corresponds to the jump in deflection (force) in position 5 in Fig. 2.12. When performing an AFM scan, this force will pull tip and surface together. In addition, the tip may apply an extra force (load) on the surface, depending on the preset value of the setpoint force. The imaging force is the sum of this load and the contribution of adhesion (Fig. 2.13). By reducing the load, the imaging force is reduced as well. However, the pull-off force represents a limit below which stable imaging is not feasible. One may work against the adhesion by selecting a negative load; however, once the tip pulls off the surface, the feedback loop will cause a full retraction of the piezo as the setpoint value is smaller than the

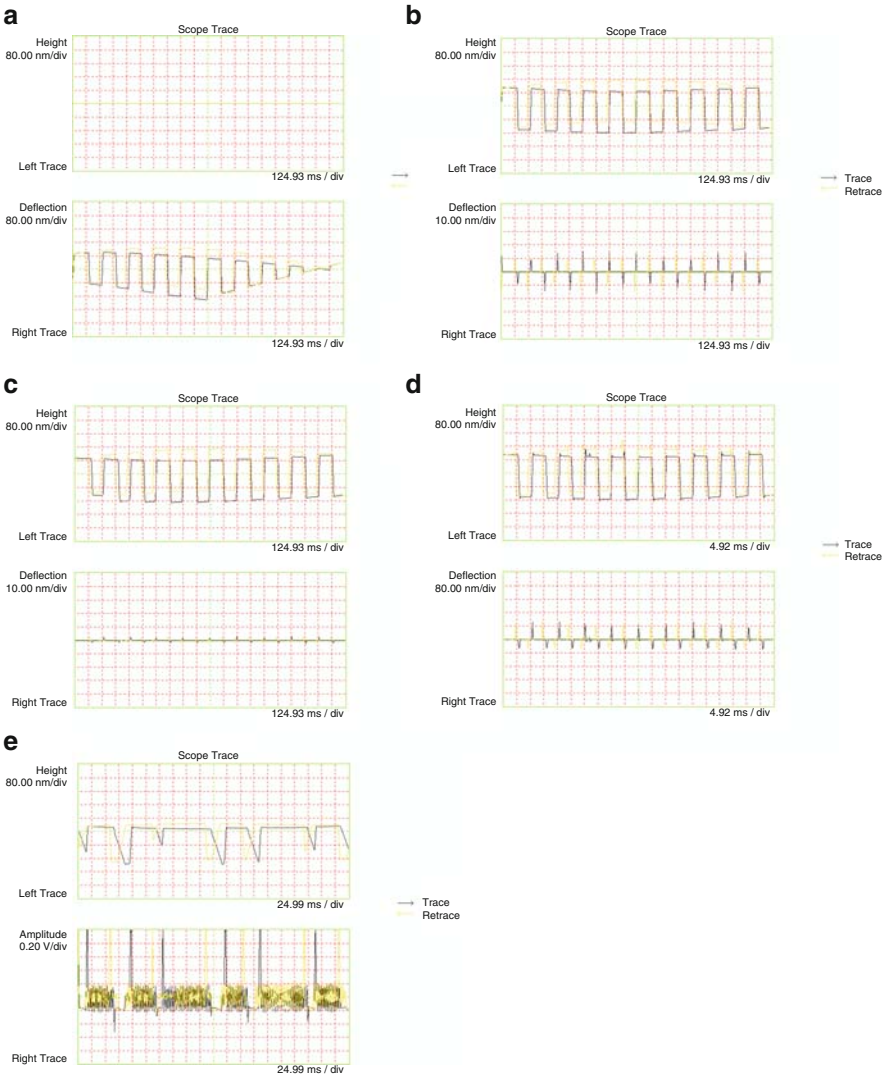

Fig. 2.11 Scope traces for TM–AFM height and amplitude images recorded for different gain settings (details see text)

actual deflection signal (which corresponds to the signal of the now freely suspended lever). In addition, the magnitude of the adhesive forces depends on the radius of the particular tip used (Sect. 4.1 in Chap. 4).

The magnitude of the pull-off force also depends on the imaging medium as intermolecular forces may depend on the medium (Chap. 1) and since in ambient conditions water may condense at the tip−surface contact, giving rise to the well-known capillary forces. Thus, by performing experiments in liquid media, such as

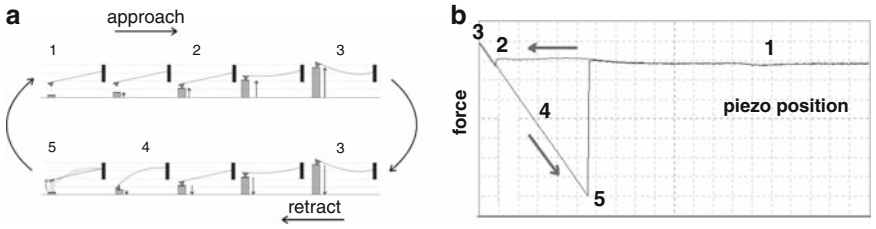

Fig. 2.12 (**a**) Measurement of force–distance curves (schematic representation). The sample is approaching the tip (1); at some distance the gradient of the force overcomes the cantilever spring constant and the tip jumps into contact (2); further movement up causes a deflection of the cantilever (3), during the retraction the tip sticks usually much longer (4) and snaps off, when the spring constant overcomes the force gradient (5). (**b**) Corresponding output: force–displacement plot. Reproduced with permission from [1]

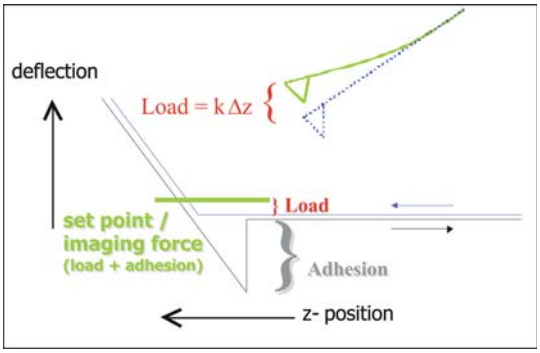

Fig. 2.13 Schematic of force displacement curve and relation of load, adhesion (pull-off force), and imaging force on the one hand and setpoint on the other hand

water, or in dried gas atmosphere, the often overwhelming contribution of capillary forces can be avoided or reduced.

Once all imaging parameters are set, data can be acquired and captured. It is important to note that the data may depend on the actual settings (force, scan velocity, feedback loop quality, etc.); therefore, one should note these parameters independently. The data displayed on the screen is typically planefitted to be readable (in case the sample plane does not coincide with the horizontal $x, y = 0, 0$ plane of the scanner, the image would appear tilted and flat surfaces would appear in saturated colors; compare also Sect. 2.2.7). A line-by-line planefit is most often utilized. Here, the data of each captured scan line is normalized by subtracting a first order polynomial fit from the particular line. The captured data, however, should be captured without planefit in order to facilitate meaningful analysis at a later stage (Sect. 2.2.7).

A final remark refers to the z center position of the scanner. Because of thermal and other expansions, e.g., as a result of temperature equilibration, especially on

rougher samples, the z center may go out of limits. For samples with excessive roughness or pronounced sample tilt, this may occur, depending on lateral scan size, right after engaging the tip. Z center out of limits means, as alluded to above, that the scanner/feedback loop cannot reach the setpoint value. In case of a fully extended scanner, this is of no consequence other than the absence of AFM data; however, in the situation of a fully retracted piezo, the tip must be immediately withdrawn to avoid sample and probe damage.

2.1.2 Stand Alone AFM (Contact Mode)

The steps for setting up a stand alone (tip scanning) AFM are very similar to those for CM. Again, each AFM brand has its own peculiarities, but the general features are very similar. In Fig. 2.14, the entire set up of a stand alone microscope, including transparent environmental chamber, is shown. In the following pages we quickly summarize the basic steps of assembly, keeping in mind that the conceptual differences to the previous paragraphs are minor.

The individual parts are shown in more detail in Fig. 2.15.

Mounting the cantilever to the scanner requires (in addition to the scanner, the cantilever, and tweezers) a special tool to release the force of the clamping mechanism (clip, compare Fig. 2.16a). The tool lifts up the clip as shown below in

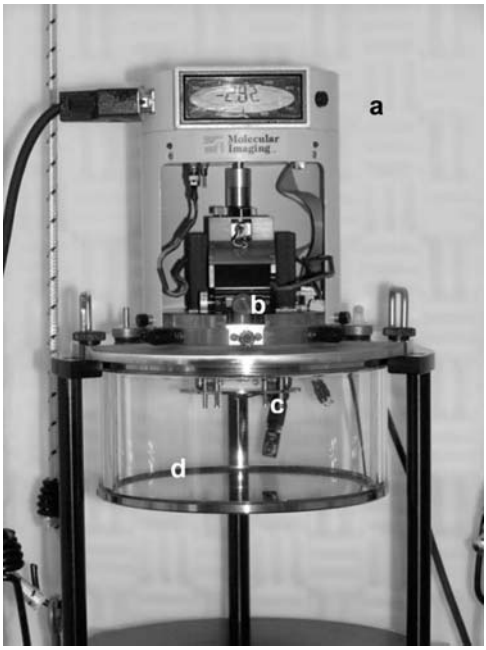

Fig. 2.14 Fully assembled stand alone AFM comprising (**a**) the base (incl. LCD display), (**b**) scanner and photodetector, (**c**) sample, and (**d**) environmental chamber

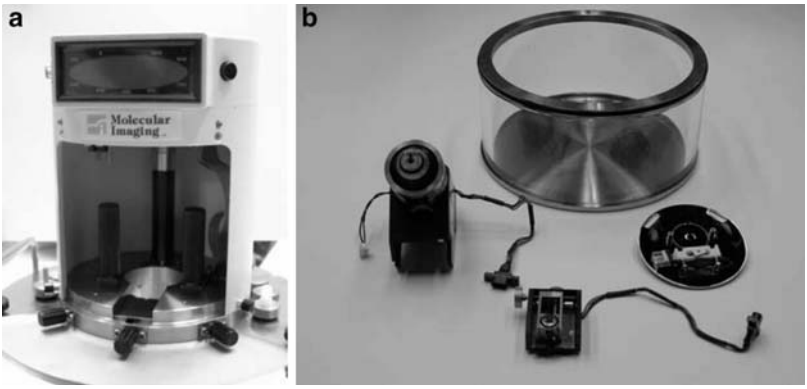

Fig. 2.15 (**a**) AFM base and (**b**) scanner, photodetector, sample mount (*front left to right*), and environmental chamber (*back*)

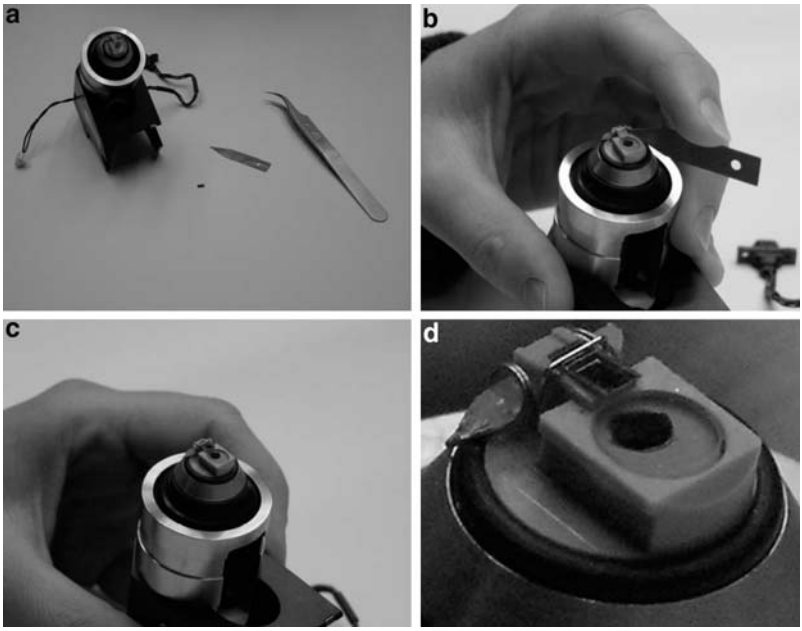

Fig. 2.16 Insertion of probe as described in the text

Fig. 2.16b. The cantilever chip can be inserted gently under the lifted clip, aligned with the shape of the holder, followed by releasing the clip.

First, the scanner (incl. the previously mounted cantilever/tip) is inserted upside down into the base (Fig. 2.17). Subsequently, the scanner cable is attached.

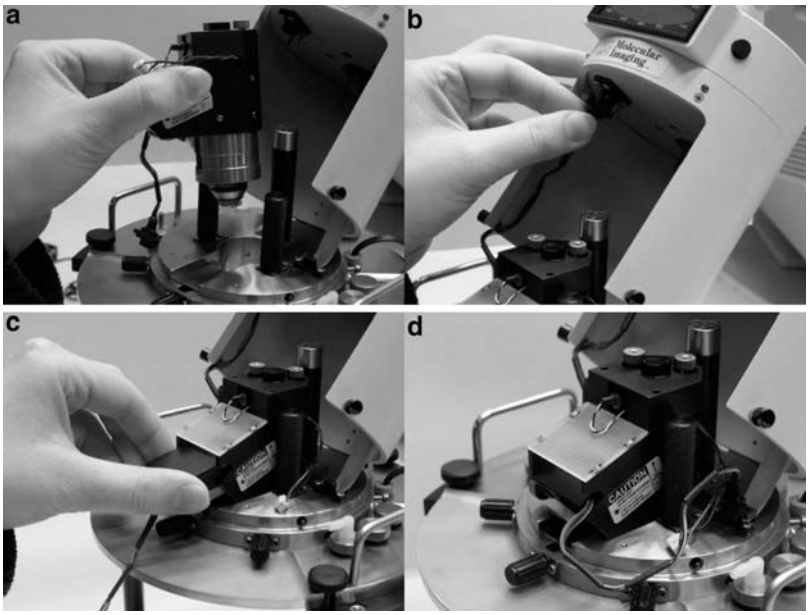

Fig. 2.17 (**a**, **b**) Mounting of scanner; (**c**, **d**) attachment of photodiode

Fig. 2.18 Mounting of sample

The separate photodetector is mounted subsequently as depicted in panel (c) in the scanner side port and connected to the base through the cable.

The sample is immobilized on a metallic sample puck (see arrow) on the sample holder plate (Fig. 2.18a). This plate is finally attached from below as shown by several screws. Care has to be taken not to touch the probe tip as a result of inadequate screw positions.

The laser is adjusted by turning the corresponding screws on the laser stage (Fig. 2.19), similar to the procedures described for the scanning sample AFM. The laser alignment can be checked by visual inspection of the laser light as it is reflected on a sheet of paper below the base. Panel (b) shows the situation in which laser light does not reflect off the cantilever (round spot), while in panel (c) a typical reflected spot can be recognized. In addition to the paper, the reflected light is seen on the

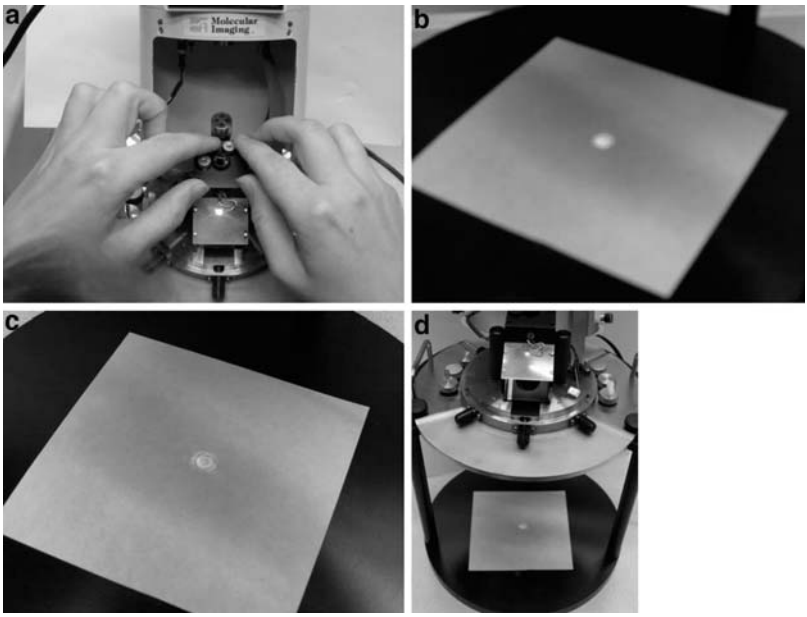

Fig. 2.19 Laser alignment: (**a**) Adjustment of laser stage by laser stage screws; (**b**) laser light reflected off a piece of paper for off cantilever position; (**c**) same for on cantilever position; (**d**) in addition, the spot can be analyzed on the reflection on the scanner window

scanner (Fig. 2.19) window (panel d). If the laser light reflected off the cantilever reached the photodiode, a maximized signal is indicative of an appropriate alignment. The differential deflection signal is read as an Arabic number directly from the LCD display, as shown in Fig. 2.14, while the sum signal is displayed in the ellipse on the lower part of the display. The display can be switched to the lateral deflection signal by using a small switch (Fig. 2.19).

The protocol and settings for the engagement process and the imaging are essentially identical to the procedures discussed earlier and we refer here only to this section and the corresponding manuals (if applicable).

2.1.3 Intermittent Contact (Tapping) Mode

The prime differences among the different AFM modes, such as CM (discussed above) and intermittent CM, as elucidated in the following section, are the feedback parameters and the choice of the cantilever. For intermittent contact (tapping) mode AFM, a stiff cantilever (k typically 10−50 N/m) with a resonance frequency of 100−400 kHz is chosen. The cantilever, which is inserted in an identical manner as for CM into the cantilever holder, is excited to vibrate by an integrated piezo actuator. Instead of deflection (contact force), the amplitude of the forced oscillating lever is detected, analyzed, and utilized in the feedback loop (Fig. 2.20).

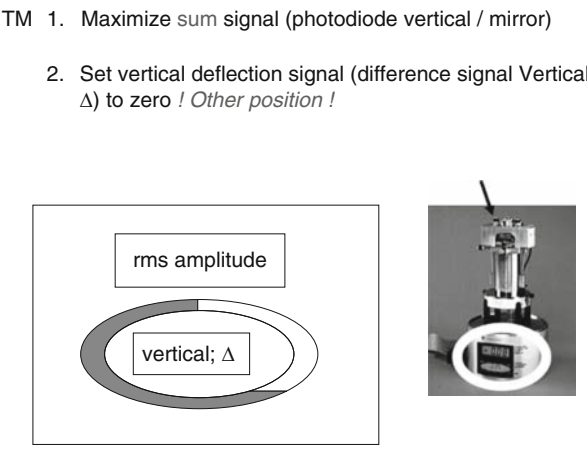

Fig. 2.20 Schematic of adjustment of photodiode signals for TM. Note that the LCD display shows a different signal compared to contact mode

Practically speaking, the laser alignment is performed for CM; then the base is switched with a toggle switch (DI multimode) to tapping mode. This changes the LCD display information.

A first difference compared to the details of CM operation is noticed when the cantilever has been inserted and the laser positioned such that the reflected light is centered on the photodetector: one has to locate the resonance frequency and set an appropriate excitation frequency. This procedure is called cantilever tuning. We strongly suggest not to use the built-in automated routine, but to perform this simple operation manually.

For this purpose, the cantilever tune menu is opened and a frequency sweep is performed. From the probe manufacturers data sheet, the resonance frequency is approximately known, e.g., 300 kHz. Hence, we excite the lever with low power (drive amplitude 25 mV) and sweep the frequency for ± 30 kHz around the expected resonance frequency of 300 kHz. In advanced AFM set-ups, the resonance frequency may also be independently determined before the tuning by a thermal tune (please consult the corresponding manual for details; the procedure is globally reviewed in Sect. 2.2.5).

The amplitude of the cantilever should display a maximum at the resonance frequency $f_{\max}$. If this is not found, the sweep width (in case the resonance frequency lies outside the scanned range) and subsequently drive amplitude may be increased (in case the amplitude is too small to be detected) (Fig. 2.21).

After the resonance frequency has been localized, we set the operation frequency to $f_{\max}$ or to the frequency at which the amplitude is $\sim 85\%$ of the maximum amplitude $A_{\max}$. This latter choice has been shown to be beneficial to reduce the imaging forces. Subsequently, the phase signal is zeroed (the phase lag between excitation vibration and cantilever reaction is set to zero) and finally the amplitude is

Fig. 2.21 Amplitude *A* (curve with maximum) and phase response of TM–AFM cantilever

adjusted. This can be done by setting a particular drive amplitude in order to reach a chosen (cantilever) amplitude. The exact value of the amplitude is chosen depending on the nature of the sample (for details: see the corresponding hands-on example). As a rule of thumb, we can state that the cantilever amplitude should be as low as possible to ensure smallest possible peak forces; for glassy samples imaged in ambient air, it can be as low as 25 nm (DI multimode: ca. 0.5 V), while for viscoelastic samples and polymers, above T_g higher amplitudes (up to 200 nm; 4.0 V) may be required to overcome tip−sample adhesion. During the experiments, the appearance of the images and the constant small value of the deflection signal are good indicators for appropriate tapping. If the amplitude is too small, the tip cannot overcome the attractive interactions and remains pinned on the surfaces, while the sample is being scanned. Hence, the stiff probe is dragged over the surface, resulting in (1) sample damage and (2) useless AFM data.

Occasionally the resonance peak looks unsymmetric or distorted; it is also possible that multiple peaks are observed in the frequency scan. These ill-shaped peaks are either the result of an ill-behaved resonance due to misfabrication of the lever; however, often the coupling of the excitation vibration of the incorporated piezo oscillator and the cantilever chip are responsible. The reader is encouraged to remove the cantilever holder and subsequently the cantilever chip from the holder; the cantilever is then placed again into the holder and secured with the corresponding clip. If this change in position and clamping in the holder does not help, the reason for the unsymmetric resonance may be indeed the particular cantilever. As long as the resonance peak can be identified and the slope of the resonance peak is steep enough, the lever may still be used for imaging.

Before the AFM experiment is started, the scan parameters must be adjusted. First of all the tapping AFM menu must be chosen; compared to CM, there are a number of changes: the scan rate must be reduced (max. 1.0 Hz) and the gains are typically set to lower values (integral gain: 0.5; proportional gain: 1.0; differential gain: 0.0).

The manual tip−sample approach should be carried out with extra care to avoid unintentional tip−sample contact. Most tapping mode levers are made of silicon, which is brittle. Therefore, tip-sample contacts may easily lead to tip damage.

The engagement procedure is simplified compared to CM since the stiff tapping mode levers do not bend as a result of long-range forces. However, it is still advisable to monitor the amplitude signal on the LCD display. The actual setpoint value is determined (during the preengage check) and preset by the AFM controller (using a particular software routine). If the amplitude happens to drop to zero before the surface has been reached, the descent must be aborted. Likely, there has been contact between the sample and the tip/cantilever/holder resulting in the complete damping of the forced oscillation.

False engagement is also possible in tapping mode and can be attributed to damping of the cantilever vibration by the air cushion in between tip and sample. Similar to CM, there is a simple check whether the probe is really engaged: The setpoint is *lowered* slightly (corresponding to *increased* amplitude damping and hence *increased* forces). *Please be aware that the sign of the change is opposite to contact mode!* If the surface is within reach of the *z*-travel of the piezo, an image will be displayed and the amplitude display will show the setpoint value (rms voltage). In addition, the scanner's *z* center position will show a value between max/min. In case of false engagement, detected by a *z* center position out of limits and an rms amplitude value unequal to the setpoint, we withdraw the tip once and restart the engagement procedure.

After successful engagement, the gains must be adjusted and the imaging force should be minimized (i.e., the setpoint maximized, see above). The adjustment of the gains is performed best in the scope mode. By increasing the gains in small increments, we aim at a minimized error (i.e., amplitude) signal since we operate the AFM in constant amplitude mode. If the gains are set too high, the piezo scanner will show clearly discernible uncontrolled feedback seen as oscillations. These are first recognized in the amplitude and phase images.

It is not advisable to adjust the amplitude setpoint settings in the amplitude−distance mode (Fig. 2.22). Here, a too high damping that would be present when the

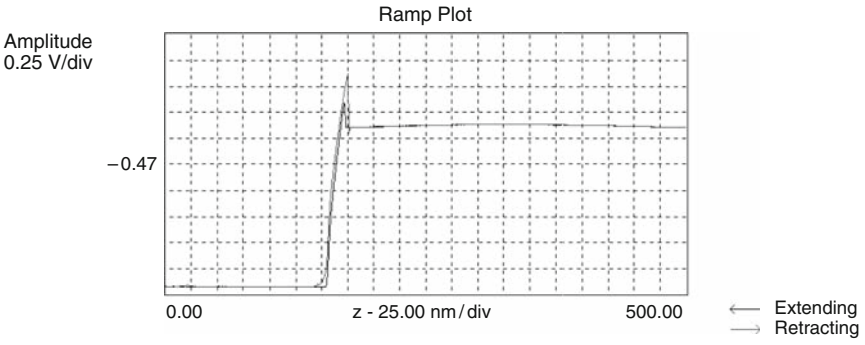

Fig. 2.22 Typical tapping mode amplitude–distance curve

entire curve is recorded, as shown in the figure, may result in tip damage. In this mode, the amplitude of the cantilever is monitored as a function of sample/piezo position, while the tip is brought periodically in and out of contact with the sample surface.

Instead, it is advisable to follow an alternative strategy. We will first determine the rms amplitude of the freely forced oscillating lever. This is done by selecting a setpoint higher than the amplitude adjusted during tuning. This setpoint value cannot be reached by the AFM controller/set-up; the feedback loop will retract the sample in order to minimize the damping; yet even after full retraction to its minimum length, the actual rms amplitude is still below the chosen setpoint value. However, the value is displayed on the LCD display and can be noted. As a setpoint for imaging, we may now choose a value that corresponds to 90%, or less, of that value. Setpoint ratios of ~0.90, ~0.75, and ~0.4 have been attributed to soft, intermediate, and hard tapping conditions, respectively by Magonov et al. [2].

2.2 Practical Issues of AFM Operation

2.2.1 AFM Cantilevers, Tips, and Their Characteristics

For different modes and purposes, there are special AFM probes (cantilevers and tips). These differ in terms of their geometry, dimensions, force constants, resonance frequencies, tip position, shape and radius, material, etc. There are numerous commercial sources and we refer to these for finding the appropriate probes for the given experiment and sample. It is also clear based on the rudimentary treatment of tip−sample interactions (Chap. 1) and the basic AFM features that the attainable information and resolution are in many cases dictated by the properties and characteristics of the probe tip. The tip physically interacts with the surface and its sharpness and aspect ratio, for instance, determine the degree of convolution in imaging small features or the limited success in the visualization of small pores (Fig. 2.23).

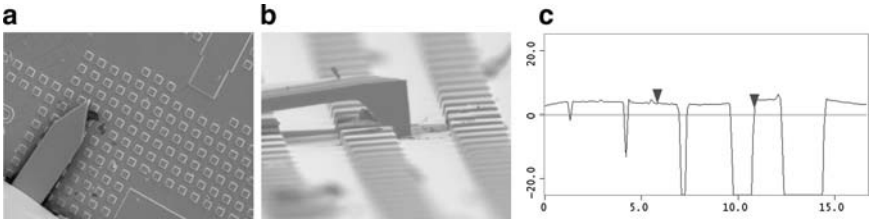

Fig. 2.23 (**a**) Top-view and (**b**) side-view SEM image of probe tip in contact with a patterned elastomer sample. (**c**) Section of an AFM micrograph of micro- and nanopores of identical depth fabricated in silicon showing the limited ability of the tip to penetrate into the pores

AFM cantilevers and tips can be differentiated based on some central characteristics that are summarized below.

Material	*Geometry*
Silicon	Single beam cantilever
Silicon nitride	V-shaped cantilever
Metal or diamond coated levers and tips	Tip shape: pyramidal (opening angle, aspect ratio)
Diamond tips	Inclination angle of tip
Chemically functionalized probe tips	Tip position on cantilever
etc.	Oxide sharpened
Special properties	etc
Conducting	*Relevant physical parameters*
Actuated	Length
Thermal sensor equipped	Width
Chemically distinct coating	Thickness
etc.	Spring constants
	Resonance frequency
	Tip radius
	etc

2.2.1.1 Contact Mode Cantilevers and Tips

Electron micrographs of typical levers and tips are shown below to illustrate some representative examples and dimensions (Fig. 2.24).

Because of misalignment in the production process, the tip may not always be situated symmetrically on the long cantilever axis. This type of error in tip position may lead to erroneous readings of deflection as vertical and torsional deflections are coupled (Fig. 2.25).

Intermittent contact (tapping) mode probes are depicted in Fig. 2.26, while special AFM probes are shown in Fig. 2.27.

2.2.2 Sample Preparation

One notable difference of AFM in comparison with electron microscopy is the ease of sample preparation. There is no need for conductive coatings, thin sections, etc. This means that any polymer sample can in principle be analyzed by AFM, provided the part fits into the corresponding microscope. There are also stand alone AFM models that can operate on any large macroscopic surface, such as an airplane wing, to perform local analysis.

However, since AFM measures topographic and other information using a sharp tip with typical dimensions of several micrometers, opening angles of $<20°$ to $>35°$, and radius of curvature of 5−50 nm (or larger), sample roughness is a crucial issue. This is also true because of the limited z-travel of most common piezo transducers, which limits the difference between the highest and lowest point on the scanned

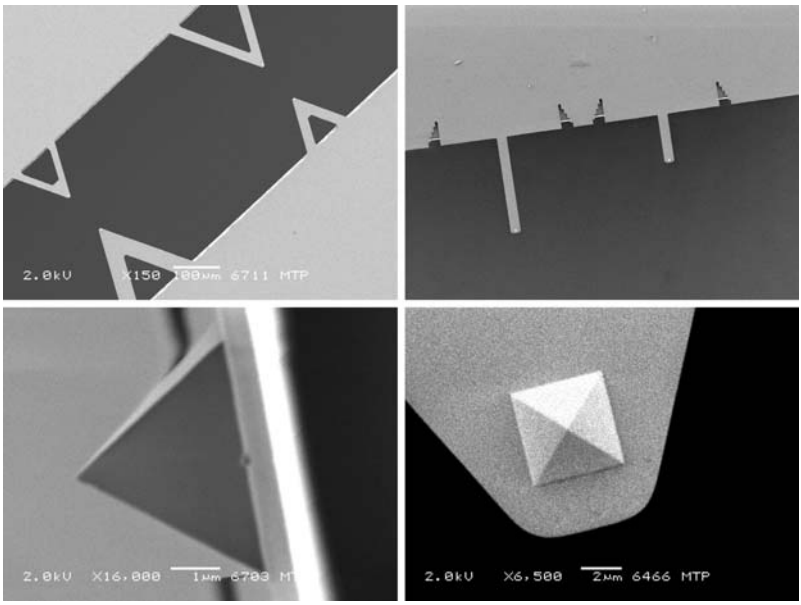

Fig. 2.24 SEM images of CM cantilever (V-shaped and single beam) and microfabricated tips

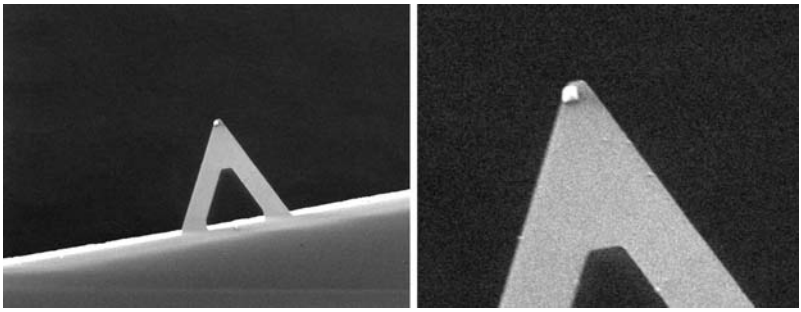

Fig. 2.25 SEM image and digital zoom of misfabricated CM cantilever: the microfabricated tip is located off the central axis of the lever

surface to several micrometers. Pronounced roughness in excess of the z-travel or in conflict with the physical shape of the probe may result in heavily convoluted images (see e.g., Figs. 2.42 and 2.43). Therefore, sample preparation should provide smooth sample surfaces with low roughness.

For polymers, we can differentiate different sample preparation procedures that aim at providing smooth films or surfaces or at exposing the interior of bulk samples at a specimen surface.

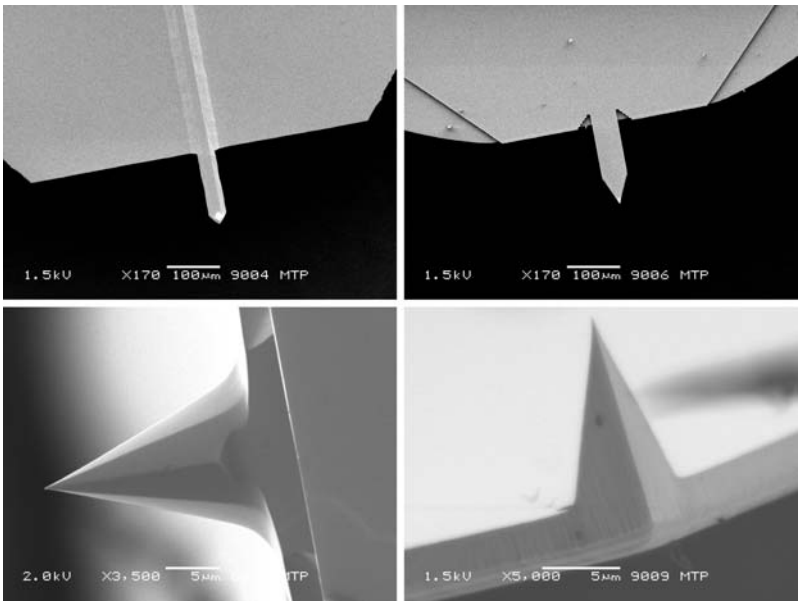

Fig. 2.26 SEM images of different TM cantilevers and microfabricated tips

In solvent casting, a thin film is prepared on a solid substrate by casting a solution of polymer onto the substrate, followed by evaporation of the solvent. Thicker films with some control over film thickness can be prepared. Enhanced control over thickness is achieved in the so-called doctor-blading approach, where the thickness of a viscous polymer solution is adjusted down to the 10 nm range by removing excess solution using a knife (the knife−substrate spacing is controlled).

Spin-coating exploits centrifugal forces and rapid evaporation of the solvent to prepare films with controlled thickness and roughness. Here, a polymer solution is deposited on a cleaned substrate, which is spun with high velocity around its central axis. The solution spreads and is spun off the substrate, leaving a film behind. The thickness can be controlled by the polymer concentration ($d_{\text{film}} \propto$ conc.) and the rpm ($d_{\text{film}} \propto \sqrt{\text{rpm}}$).

The interior of bulk samples can be revealed by fracture, freeze fracture, or (cryo-/ultra)microtoming. These techniques are well established in electron microscopy and require substantial training to ensure that the knives used do not introduce scratches and other artefacts. Unlike in SEM or TEM analysis, however, it is very well possible to analyze the trimmed specimen instead of the very thin sections removed (cryofacing). This loosens the constraint of ultrathin sections in many applications. Care has to be taken that the sample to be imaged is not significantly thicker or thinner than the calibration grating used for scanner calibration (see Sect. 2.2.5)

Crucial for all AFM experiments, independent of the sample preparation method and also in the absence of any sample preparation, is the firm attachment of the

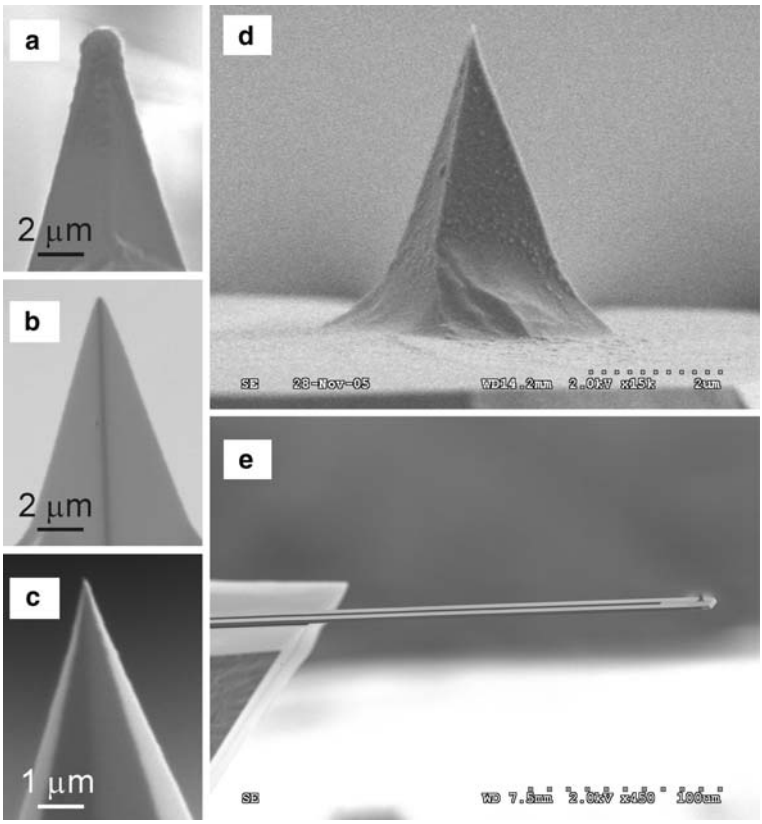

Fig. 2.27 SEM images of different specialized AFM probes: (1) tips of widely different radii (**a**) 870 nm, (**b**) 150 nm and (**c**) 20 nm; (**d**, **e**) thermal probe and tip (images courtesy Anasys Instrument Inc.)

corresponding samples to the AFM sample holder. Many AFM types rely on ferromagnetic metallic pucks that are attached to a strong magnet on the scanner.

Samples in the form of freestanding polymer films, sections, microtomed specimens, or substrate-supported sample must be *firmly* attached to the sample pucks. In some cases, samples may be deposited straight onto the pucks, such as for instance polymer colloids. A second requirement for attachment is that the sample specimen's surface is exposed in a flat and leveled fashion in order to reduce possible shortcomings of the scanner maximum z travel.

Double-sided sticky tapes are popular for the attachment of samples. Various brands and types are available. For many routine measurements conventional tape is sufficient; however, some thicker variants may lead to problems when pressure is exerted to fix the samples, since the tape will relax and hence cause substantial drift in the AFM image. A similar effect may be present as a result of thermal expansion, when a "cold" AFM is operated with high resolution in the first hour(s)

of operation. Among the many parts that may contribute to the drift, the sticky tape is one. Particular problems with tape have been observed for measurements in liquid media (compare Sect. 3.3).

Alternatively, different types of glue, including epoxy or cyanoacrylate-based glues, can be used. Care has to be taken to avoid sample contamination. In particular, cyanoacrylates must not be covered during curing as they outgas material that deposits on the sample if covered.

2.2.3 Choice of Operation Modes and Suitable Imaging Environments

The choice of operation modes and, if applicable, suitable imaging environments depend on many factors, including the type of polymer system to be analyzed and the type of information that is required. Biologically relevant materials or effects that are intrinsic to the liquid−solid interface, for instance, require, of course, AFM under liquid. For a number of experiments, these almost trivial considerations dictate the choice and we refer to the hands-on sections in the corresponding chapters for more detailed information.

2.2.3.1 Contact Versus Tapping Mode

One central concern with routine AFM on polymers is the presence of shear forces that occur in CM. These forces are a result of friction between AFM probe tip and the polymer sample and may deform and plastically modify the polymer surface. This has been observed even for glassy materials, such as PS, when imaged at ambient conditions (see Sect. 3.2.3 in Chap. 3; Fig. 3.16). In addition to sample damage, the tip may be affected by adhering particulates or, even worse, by wear. These phenomena limit the resolution dramatically and may result in unwanted artefacts (excessive tip imaging). Thus, minimized imaging forces are essential, and this may require the operation under a suitable liquid to eliminate capillary forces.

For many fragile materials and research/practical questions, intermittent CM is preferred as the lateral forces are practically avoided. Thus, sample damage or deformation is circumvented. However, despite the absence of shear forces, too high amplitudes or too low setpoint ratios may lead to damage of the sample or the tip as well.

2.2.4 Tip Handling and Modification Procedures

Since the sharpness of the probe tip determines the attainable resolution in many cases, it is crucial that the AFM tips are handled with utmost care. In many laboratories, it is not practical to quantify the sharpness of all individual tips because this is a time consuming and challenging task. However, the sharpness of commercially available tips often varies even on the same wafer and among nominally identical probes.

Tips should be handled as described in Sect. 2.1.1 and any uncontrolled contact of the tip with any surface (i.e., without proper piezo/system feedback) must be avoided. After longer storage times (e.g., on poly(dimethyl siloxane)-based adhesive layers) or for certain experiments, cleaning of tips is necessary.

CO_2 snow cleaning, immersion in organic solvents, the use of UV–ozone or plasma cleaners, and strong oxidizing solutions have all been reported. Care must be taken that the probes do not touch any object unintentionally (e.g., while venting a plasma cleaner chamber) and that the reflective metal coating (if applicable) is not damaged. For many routine experiments, a simple solvent cleaning is sufficient. This is done by immersion of the cantilever chip with tweezers into a solution of high purity toluene followed by drying in a gentle stream of nitrogen (this must be done with proper safety clothing and under proper ventilation; please refer to standard chemistry literature for safety precautions).

Organic thin film (monolayer) coatings can be applied on oxide or metal (typically gold)-coated probe tips following recipes for self-assembled monolayer depositions that were adjusted for AFM probe technology. These probes are also commercially available and are useful to ensure known surface chemistry, to immobilize molecular species for assessing specific interactions, or to enable enhanced imaging conditions.

2.2.5 Calibration Issues

The AFM scanners are calibrated by imaging a grating of defined spacings (Fig. 2.28a). Closed loop systems require only an occasional check of the calibration of the capacitive sensors; open loop scanners, however, require, in particular for the x, y calibration, a regular (monthly) check and calibration. For a typical AFM system, the deviation should not exceed 5%; otherwise a calibration is needed. Based on the images acquired on the gratings, automated calibration routines correct altered x, y, and z sensitivities, scanner bow effect (Fig. 2.28b), etc.

The calibration of the z direction must be carried out, as already mentioned, on a calibration specimen that possesses identical height as the samples to be analyzed. For open loop tube scanners the calibration was reported to depend on the sample height [3], which is easy to see considering that the tube deforms such that a point on the sample surface travels on the surface of a sphere. Changing the radius of the sphere results for a given angular change in an altered path on the surface of the sphere, i.e., if the sample is thicker than the calibration grating for z calibration, lateral distances will be underestimated and vice versa.

A central question is often “how sharp is the tip?” Together with tip aspect ratio, opening angle, and tip inclination angle (taking into account that the cantilever is mounted under an angle), this defines in many circumstances the resolution.

Direct imaging with SEM or TEM can provide access to the required information (see Sect. 2.2.1). In addition, there are specially designed gratings that possess features, such as tips, that are sharper than the probes used. By scanning these features, one obtains convoluted AFM images (the information in the image is in parts due to the tip and its shape and size, and in parts due to the grating).

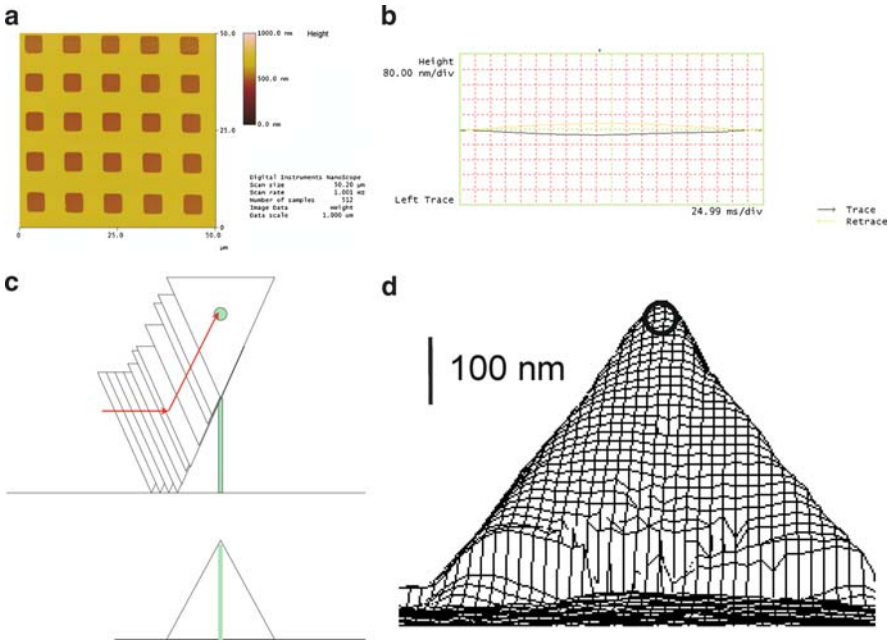

Fig. 2.28 (**a**) Contact mode AFM height image of a calibration grating. (**b**) Cross sectional plot of an AFM height image of a flat silicon wafer displaying a pronounced scanner bow effect. This scanner must be recalibrated to correct for this bow. Any data captured should be planefitted accordingly (*see below*) (**c**) Schematic of tip imaging on a hypothetical needle (*top*); the AFM height image will display the shape of the tip itself. (**d**) Image obtained by contact mode AFM on a calibration gratin exposing very sharp tips; the tip radius r determined was 25 nm

Similarly challenging, but nevertheless important in the context of constant experimental conditions (e.g., imaging at the same force) or force mapping, is the calibration of spring constants in CM AFM. The nominal spring constants stated by the suppliers are mere indications and cannot be trusted. This is primarily due to the impact of the cantilever thickness on k_N.

The force constants of *single beam* cantilevers (normal spring constant k_N, torsional spring constant k_φ, and lateral spring constant k_L) can be calculated, assuming levers of constant thickness, based on measured cantilever dimensions, from continuum elasticity mechanics of isotropic solids: [4–6]

$$k_N = \frac{Ewt^3}{4l^3}, \tag{2.1}$$

$$k_\phi = \frac{Gwt^3}{3l}, \tag{2.2}$$

$$k_{\mathrm{L}} = \frac{k_{\phi}}{h^2} = \frac{Gwt^3}{3lh^2} \tag{2.3}$$

with cantilever length l, cantilever thickness t, cantilever width w, tip height h, Young's modulus E, Poisson's ratio v, and shear modulus $G = E/2(1 + v)$.

For Si cantilevers, the material properties (Young's modulus and Poisson's ratio) are known in any crystal orientation [7]. By contrast, the material properties of the Si_3N_4 cantilevers are not well defined and may vary significantly [8] due to differences of the CVD processes [9, 10]. For instance, Young's moduli and Poisson's ratios of Si_3N_4 cantilevers in the range of 120−200 GPa and 0.22−0.27, respectively, have been reported.

Procedures for the reliable calibration of normal forces (i.e., k_{N}) are well established. Several methods can be used, such as the thermal fluctuation method [11–13], the reference lever [14], or the added mass technique [15]. We will mention in the following the thermal noise and the reference lever methods in some detail.

The sensitivity of the optical deflection detection system is easily calibrated by recording an *f–d* curve on a stiff substrate, e.g., a glass slide or a piece of silicon. The slope of the hard wall contact region in this photodetector – piezo displacement plot must be unity, as for the movement of 1 nm in z direction the tip and cantilever move upwards 1 nm as well. This function is typically implemented in the AFM software (Fig. 2.29).

Next comes the calibration of the cantilever spring constant in order to be able to relate the measured deflection to force using Hooke's law. Even though the force constants of *single beam* cantilevers can be calculated, assuming levers of constant thickness, based on measured cantilever dimensions, and even though the suppliers state nominal spring constants, experimental calibration of the spring constant for surface normal deflection k_{N} is necessary.

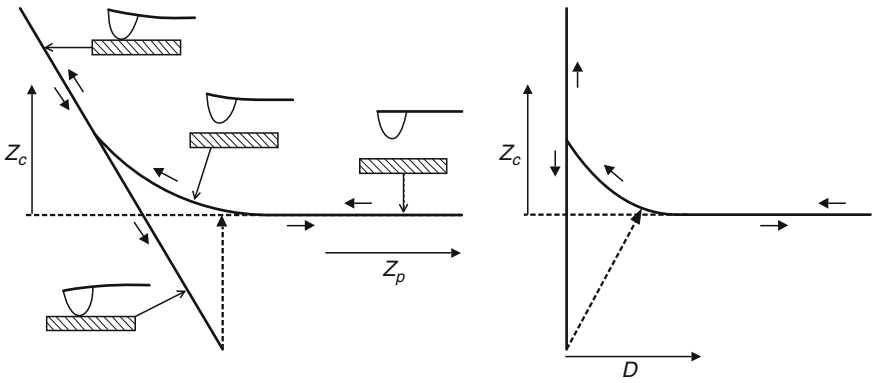

Fig. 2.29 Schematic of a typical cantilever deflection-vs.-piezo height (Z_c-vs.-Z_p) curve (*left*) and corresponding Z_c-vs.-D plot, with $D = Z_c + Z_p$. Reprinted with permission from [16]. Copyright 2005. Elsevier

The most widely used method, as has been proposed by Hutter and Bechhofer, exploits a measurement of the thermal noise of the cantilever. In the model of a harmonic oscillator, the cantilever spring constant k_N is inversely proportional to the mean square deflection due to thermal fluctuations (2.4). In practice, a noise spectrum of the deflection amplitude is recorded after the calibration of the deflection sensitivity. This can be manually done for instruments of some AFM brands by "engaging" in CM using false engagement, (see Sect. 3.2 in Chap. 3), and recording a deflection image. The power spectral density of this image is analyzed. The spectrum shows a peak at the resonance frequency, corresponding to the first vibrational mode. This peak is fitted with a Lorentzian curve and the mean square deflection of the first peak is obtained by integration. Nowadays, the thermal noise calibration method is implemented in modern commercial AFMs; thus these laborious steps and fitting can be circumvented (for details compare AFM manuals).

$$\frac{1}{2}k_c\left\langle \Delta Z_c^2 \right\rangle = \frac{1}{2}k_b T \Rightarrow k_c = \frac{k_b T}{\left\langle \Delta Z_c^2 \right\rangle}. \tag{2.4}$$

As discussed in detail in [16], the appropriate estimation relies on (2.5), in which the effective deflection Z^* (the deflection is read from the instrument after determining the sensitivity from the contact part of a force curve on a stiff substrate) and a correction factor β^* are employed that provide the appropriate relation of the (measured) inclination and the (desired) deflection. The appropriate correction factors β^* for rectangular and V-shaped levers are 0.817 and 0.764, respectively. In the actual software, the numerical values may be different, for instance in DI/VEECO systems, the correction factors (chi^2 correction) should be 1.106 for rectangular and 1.144 for V-shaped cantilevers.

$$k_c = \beta^* \frac{k_b T}{\left\langle Z_1^{*2}(L) \right\rangle}. \tag{2.5}$$

An alternative method relies on the acquisition of *f–d* curves on (1) a stiff substrate and (2) a reference lever with known spring constant. For this method, the reference lever should have a spring constant close to the one that will be calibrated. If we denote the deflection of the cantilever as Z_c and the height of the piezoelectric translator as Z_p (zero is defined for the situation, when the tip just touches the reference cantilever and no deflection has been detected), the spring constant is given by

$$k_N = k_{ref}\frac{Z_p - Z_c}{Z_c} = k_{ref}\frac{1 - Z_c/Z_p}{Z_c/Z_p}. \tag{2.6}$$

Since the spring constant of the reference cantilever k_{ref} is known, k_N can be obtained from the measured slope of the force curve Z_c/Z_p obtained on the reference cantilever in the contact regime (Fig. 2.30).

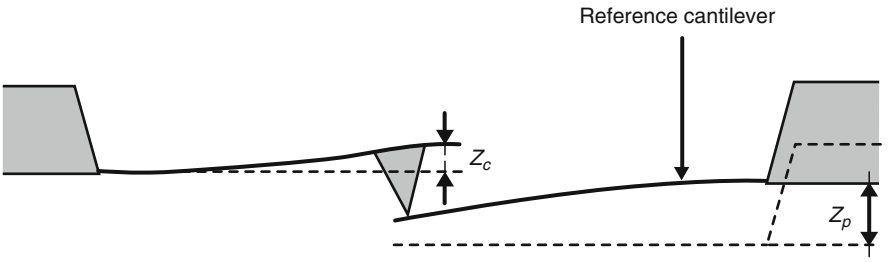

Fig. 2.30 Schematic of cantilever calibration on reference lever. Reprinted with permission from [16]. Copyright 2005. Elsevier

With calibrated detection system and cantilevers at hand, the measurement of adhesive forces can be carried out as outlined in Chap. 4.

By contrast, the calibration of the force constant of a given cantilever and the photodiode sensitivity for measurements of lateral forces remained challenging until recently [17–19]. The conventional calibration techniques proposed for the calibration of LFM can be grouped into (1) reference methods [20] and (2) two-step [8, 21, 22], procedures. The challenges mentioned arise from the fact that the reference methods suffer from systematic errors introduced by contaminations on the reference samples and that a separate calibration of the lateral force constant k_L and the photodiode sensitivity for lateral deflection S_L is hampered by a number of problems. The accuracy of the determined value of k_L is limited because of large errors in the determination of the cantilever dimensions and the uncertainty in the values for Young's moduli and Poisson's ratios for Si_3N_4 (if applicable). The unavailability of a reliable in situ method to calibrate the photodiode sensitivity S_L and its dependence on factors, including laser beam position on the lever, spot size, asymmetry, etc., represent additional complications.

A third group of calibration procedures, the (3) direct (single step) [23–25] techniques avoids (many of) these problems. In particular, the so-called improved wedge-calibration method, in which a tip/cantilever is scanned across a calibration sample with two well-defined slopes (see Fig. 2.31), allows one to calculate the calibration factors with an error of ca. 5% [18].

In the wedge calibration method, a cantilever is scanned across a calibration sample with two well-defined slopes. The friction signal is recorded as a function of the applied load. At a given load L, friction and normal forces (normal force = load + adhesion A) depend on the direction of motion (Fig. 2.32).

It can be shown that relations between measured lateral forces (half width of friction loop $W = (M_u – M_d)/2$) and the friction loop offsets ($\Delta = (M_u + M_d)/2$) for sloped and flat surfaces at a given load (2.7–2.10) can be used to calculate the friction force calibration factor α [nN/V]. M denotes the torsion moment involved, the subscripts u and d denote uphill and downhill scan directions, and the subscripts s and f denote sloped and flat surfaces, respectively.

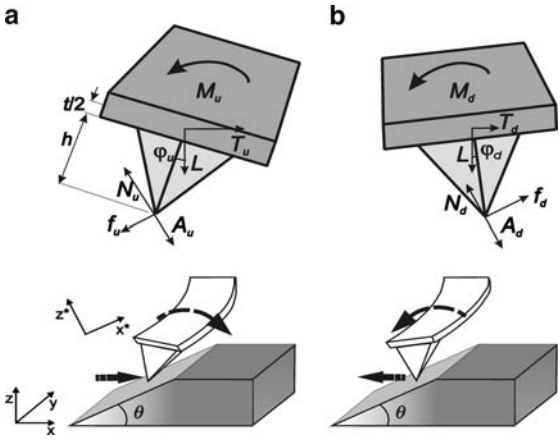

Fig. 2.31 Schematic illustration of cantilever torsion while (**a**) sliding up and (**b**) sliding down on a sloped surface (in the *x* direction). While sliding across a sloped surface with angle θ, the acting forces (the applied load *L*, the horizontal tractive force *T*, the adhesion force *A*, the reaction force from the surface acting on the tip with a component *N* in the surface normal direction and a component *f* (friction force) parallel to the surface) and the torsion momentum *M* are in equilibrium and depend on the direction of motion – uphill and downhill, denoted here with subscripts *u* and *d*, respectively. φ represents the torsion angle of the cantilever, which is proportional to the friction force; *h* and *t* stand for tip height and cantilever thickness, respectively (reproduced with permission from [18]. Copyright 2006 American Chemical Society)

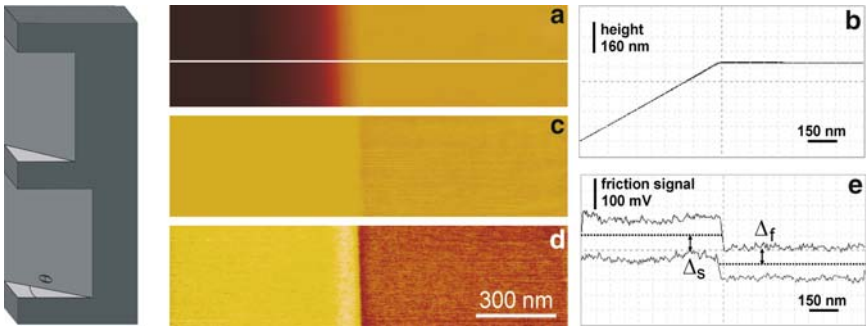

Fig. 2.32 *Left*: Schematic of calibration specimen; *Right*: Example of experimental data measured with a Si_3N_4 tip on both sloped and flat surfaces: (**a**) topography image (vertical scale from *black to white* 800 nm), (**b**) cross section of topography (vertical scale 800 nm), (**c**) difference friction image (trace – retrace, vertical scale 0.5 V), (**d**) off-set of the friction loops (trace + retrace, vertical scale 0.5 V) and (**e**) friction loop corresponding to cross section shown in *panel* (**b**) (the off-sets for sloped and flat surface, Δ_s and Δ_f, respectively, have been marked). Reproduced with permission from reference [18]. Copyright 2006. American Chemical Society

$$\frac{\mu_s(L + A\cos\theta)}{\cos^2\theta - {\mu_s}^2\sin^2\theta} = \alpha W_s \tag{2.7}$$

and

$$\mu_f = \frac{\alpha W_f}{(L + A)} \tag{2.8}$$

$$\frac{{\mu_s}^2\sin\theta(L\cos\theta + A) + L\sin\theta\cos\theta}{\cos^2\theta - {\mu_s}^2\sin^2\theta} = \alpha(\Delta_s - \Delta_f) \tag{2.9}$$

$$\sin\theta(L\cos\theta + A)\cdot{\mu_s}^2 - \frac{\Delta_s - \Delta_f}{W_s}(L + A\cos\theta)\cdot\mu_s + L\sin\theta\cos\theta = 0. \tag{2.10}$$

By solving the quadratic (2.10) for μ_s, two mathematical solutions are provided (for any given load and adhesion). When substituted into (2.7) or (2.8), these yield correspondingly two values of the friction calibration factor α. As α must be identical for sloped and flat surfaces, we obtain μ_f from (2.8). The physical solution stands for μ_s, $\mu_f < 1/tg\theta$. A more detailed description of the wedge calibration procedure can be found in [26, 27].

Thus, in practice we record friction data (images or loops) for both trace and retrace for different setpoints. We also acquire and capture for each setpoint the entire *f–d* curve to calculate the mean pull-off force (= adhesion *A*) and the load *L*. The analysis of the friction data provides the half width of friction loop $W = (M_u–M_d)/2)$ and the friction loop offsets $(\Delta = (M_u + M_d)/2)$ for sloped and flat surfaces for each load, i.e., we measured and calculate the following:

$$A;\ W_{s,\,load}; W_{f,\,load}; \Delta_{s,\,load}; \Delta_{f,\,load}.$$

With knowledge of the inclination angle θ, we can calculate the friction coefficient μ and also the desired calibration factor α as outlined above.

This direct approach allows one to calculate the calibration factors with an error of ~5%. As shown, the approach is not affected by an additional small sample tilt, different feedback settings, and a possible tip position off the central cantilever axis. Only laser light interference and nonspherical tip apex shapes must be taken into account. It is pointed out that the laser alignment of each tip used should *not* be altered throughout the experiments, as this would also introduce relative errors. For a more detailed discussion, the reader is referred to [28].

For measurements in liquid, an additional correction factor that corrects the effect of refraction must be considered. By multiplication with the factor n_{air}/n_{liquid} (*n*: refractive index) one can conveniently rescale the values of lateral photodiode sensitivity obtained in air ($S_L{}^{Air}$) employing, e.g., the improved wedge calibration method using a universal calibration specimen, to obtain the correct value for $S_L{}^{Liquid}$ [29] (Fig. 2.33).

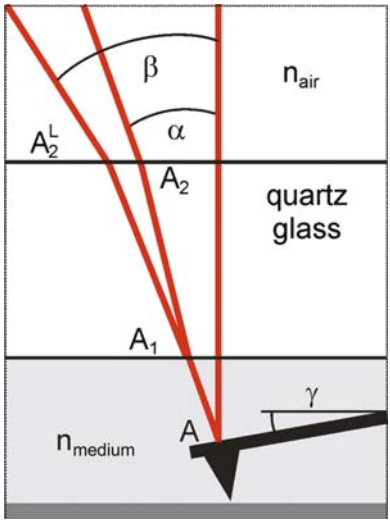

Fig. 2.33 Schematic of effect of refraction: Upon bending the cantilever by an angle δ (not shown in scheme), the light leaves under an increased angle $\beta = 2\delta^L$, instead of leaving the liquid cell under an angle $\alpha = 2\delta$. Reproduced with permission from [29]. Copyright 2007. American Chemical Society

The situation for tapping mode is somewhat simpler, as the resonance frequency is determined for each cantilever at the beginning of an experiment in the conventional tapping mode tune.

2.2.6 General Guidelines for AFM Laboratories

AFM operation requires a minimum of vibrations. These vibrations refer to not only building vibrations, but also vibrations caused by airflow, persons walking in the lab, and equipment, such as personal computers, the AFM controller, etc. To damp out vibrations, AFM scan units are typically placed on passive and/or active vibration damping systems, such as:

Passive: blocks of concrete
Heavy plates suspended from rubber (bungee) cords
Rubber and other antivibration pads
Active: piezo tables
Air tables

Vibrations that are caused by equipment may be transmitted via the corresponding cables. To dampen out vibrations of this sort, cables can be equipped with heavy masses, e.g., metal parts. For sensitive experiments, the placement of the entire AFM scan unit inside acoustic enclosures may be also advisable.

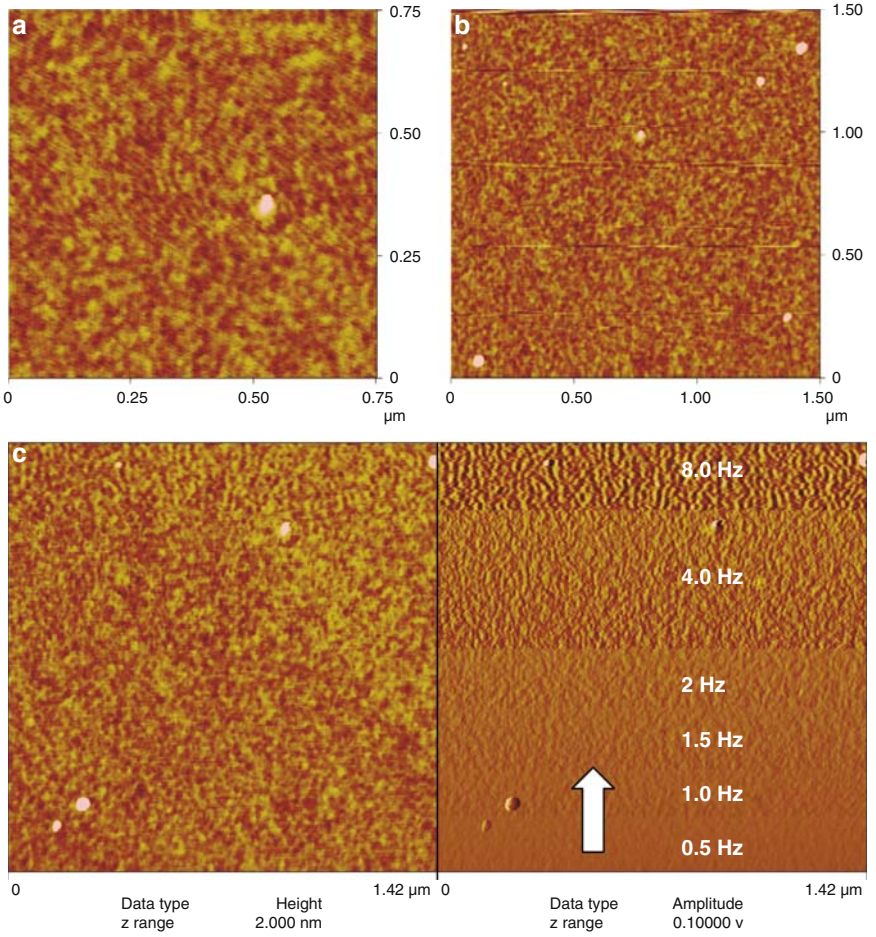

Fig. 2.34 TM–AFM height images displaying (**a**) vibration noise due to insufficient vibration isolation and (**b**) horizontal spikes due to external shocks that were not damped by the isolation system. In *panel* (**c**) an upscan with six different velocities is displayed

In addition, the temperature should be constant, and humidity should preferably not exceed 65% or fall below 10%.

Above, some AFM images are shown that display typical regularly spaced features that are the consequence of vibrations (Fig. 2.34a); in addition, erroneous scan lines due to shock-like vibrations are depicted in panel (b). In addition to vibrational noise, more or less regular features may appear in the images when the scan velocity is set too high. In panel (c) a dual height and amplitude scan is shown (upscan) in which the scan velocity was stepwise increased. The magnitude of the rms amplitude increases as the feedback loop is more and more unable to correct the encountered topographic changes; for the highest scan rate oscillatory-like features are observed.

2.2.7 Data Evaluation

Data evaluation is nearly as important as data acquisition and despite the many good offline options of the various AFM softwares and separate programs, many data published still to date suffer from artefacts introduced in the data processing and evaluation phase. A full account on data treatment, analysis, and evaluation is out of scope of this book; therefore, we will focus on a few selected procedures that are most relevant and can be carried out on most commercial AFM brands *without* other specialized software.

The reader is strongly encouraged to capture and store the data as "raw" as possible, i.e., without planefit, flattening, or filtering. As the data is being altered with most procedures, it is also wise to store processed data in separate files.

Rudimentary data processing is necessary as the captured raw data may suffer from the following shortcomings (reminder: the data displayed on the screen during the AFM scan are already processed data).

One of the problems is the fact that the sample plane and the $x, y = (0, 0)$ plane of the scanner only rarely coincide, hence part of the image is well visible while other parts are above or below the plane displayed. Depending on the level of mismatch, a planefit (first order) levels the image. Higher order planefits remove artefacts related to scanner bow effects. To perform an appropriate planefit, it may be necessary to *include only* certain areas in the calculation of the mean plane. This is the case if large-scale corrugations on a flat film are present that do not reside in the mean plane.

The planefit procedure calculates a single polynomial fit for the entire image and then subtracts the polynomial fit from the image. One differentiates different order of planefitting:

First order planefit removes tilt;

Second order planefit removes tilt and an "arch-shaped" bow;

Third order planefit removes tilt and an "S-shaped" bow.

A second issue is a mismatch between certain scan lines due to various effects, including vertical (Z) scanner drift, image bow, and skips. This effect can be eliminated by the operation called flattening. A first order flattening is a similar operation to the line by line planefit described in Sect. 2.1.1.

Zero order (0) flattening removes the Z offset between each scan line by subtracting the average Z value from every point in the scan line;

First order (1) flattening removes the Z offset between scan lines, and the tilt in each scan line;

Second order (2) flattening removes the Z offset between scan lines, and the tilt and bow (arch shaped) in each scan line.

Third order (3) flattening removes the Z offset between scan lines, and the tilt and bow (S-shaped) in each scan line.

Filtering, such as high pass or low pass filtering, is *not* advisable, unless high resolution imaging is performed and some (e.g., vibrational) noise should be eliminated. Under certain circumstances these filtering operations can indeed alter the vertical scale, which is not wanted.

2.2.7.1 Example: Determination of the Film Thickness of Spin-Coated Films

A spin-coated poly(methyl methacrylate) (PMMA) film on silicon has been scratched using sharp tweezers. This procedure removes the film, but does not damage the underlying silicon wafer. The raw AFM height data are shown in Fig. 2.35a. From the image, it is clear that the sample plane was not exactly horizontal; therefore, a planefit operation was performed. In Fig. 2.35b, we display a zero order planefit, which only moves the center of the image to the zero plane. In Fig. 2.35c, the result of a first order planefit is shown that was done considering the

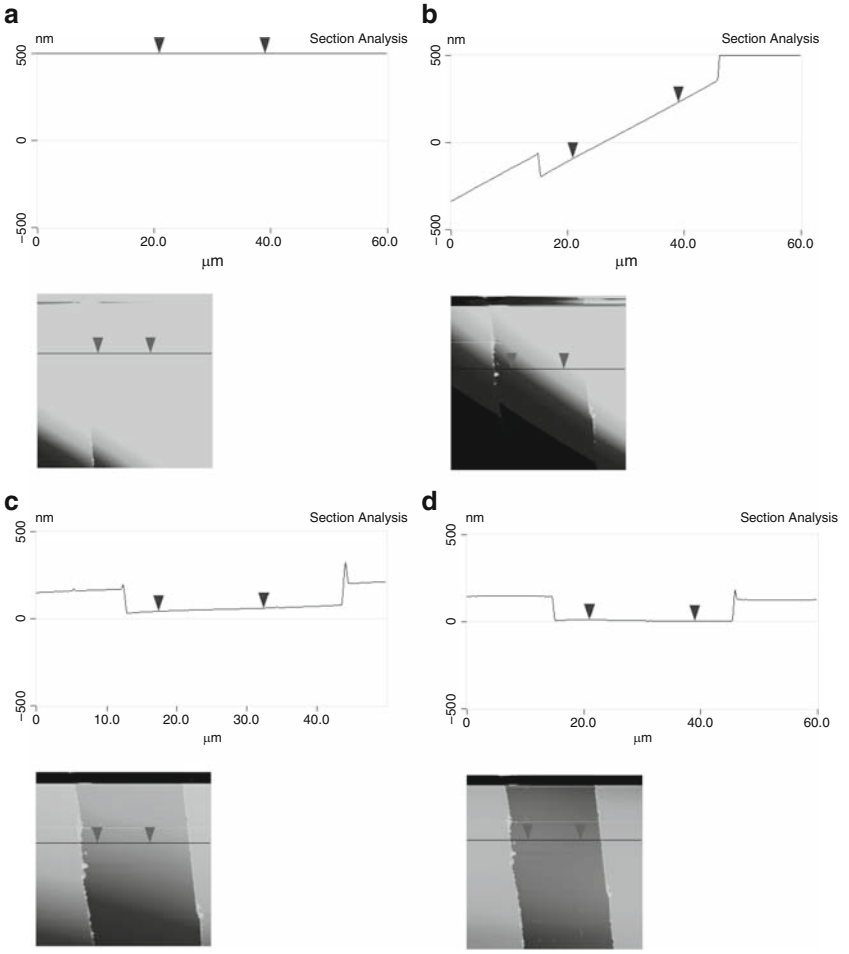

Fig. 2.35 AFM height images and corresponding cross sectional analyses of a PMMA thin film on silicon that was partially removed in the vertical direction (**a**: raw data; **b–d** planefitted data, details see text)

entire scanned image, while in Fig. 2.35d only the areas of the film, but not of the silicon wafer were considered.

The cross sections show the sample tilt (panel b) and the inadequately calculated planefit in panel (c). The clearly discernible slope in the direction of the section analysis may cause errors in height measurements that in turn may lead to erroneous thickness values. Only the data shown in panel (d) displays a cross section with no discernible slope, as would be expected for the sample.

2.2.7.2 Appropriate Flattening

If a flattening is necessary, it must be properly executed: high and low features must be excluded from the analysis (see corresponding software manuals for exact procedures). In Fig. 2.36, an AFM height image of a calibration grating is shown, in which parts of the square shaped depressions were excluded from the calculation (as is advised). In the lower two rows, this has not been done on purpose. As a result, a vertical profile would show elevated areas between the depressions that are an artefact of the data processing.

In the examples discussed above, we have already utilized a common data display format, i.e., the top-view. In this option, the height information is displayed in a color (or gray scale) scheme. Typically the z scale is shown with exaggerated zoom; in the figures shown above the *z*-scale covers over the entire range height values from 0 to 1000 nm over a lateral scan size of $(60\ \mu m)^2$. In addition, the color scale and contrast settings may enhance the subjective contrast and particular

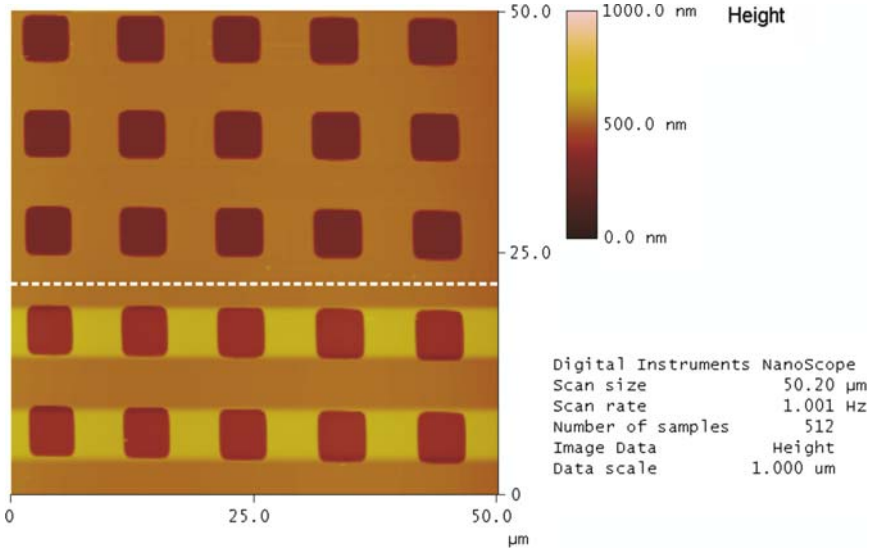

Fig. 2.36 AFM height image in which the *upper part of the image* was properly flattened, while for the *lower parts* the depressions were not excluded from the analysis. The calibration grating is of course devoid of elevated squares (compare also Fig. 2.28a)

features, while small-scale variations in slope for instance may be hidden within one type of gray scale that is without contrast to the eye. Hence, a careful cross-sectional analysis (compare Fig. 2.35) is advisable.

2.2.7.3 Data Display Formats

The data can also be displayed as a 3D plot. Again, the height information is shown with exaggerated scale. The different display formats and the dependence of the "visual appearance" and appeal on the color and contrast settings are exemplified in Fig. 2.37, where the same data (polymeric colloidal particles on a flat silicon wafer) are shown with different z-scales and contrast settings.

2.2.7.4 Data Analysis Tools

Some of the most important data analysis tools are shown for an image of a microphase separated block copolymer film. The tapping mode AFM height data were subjected to a first order planefit to eliminate the effect of sample tilt (Fig. 2.38).

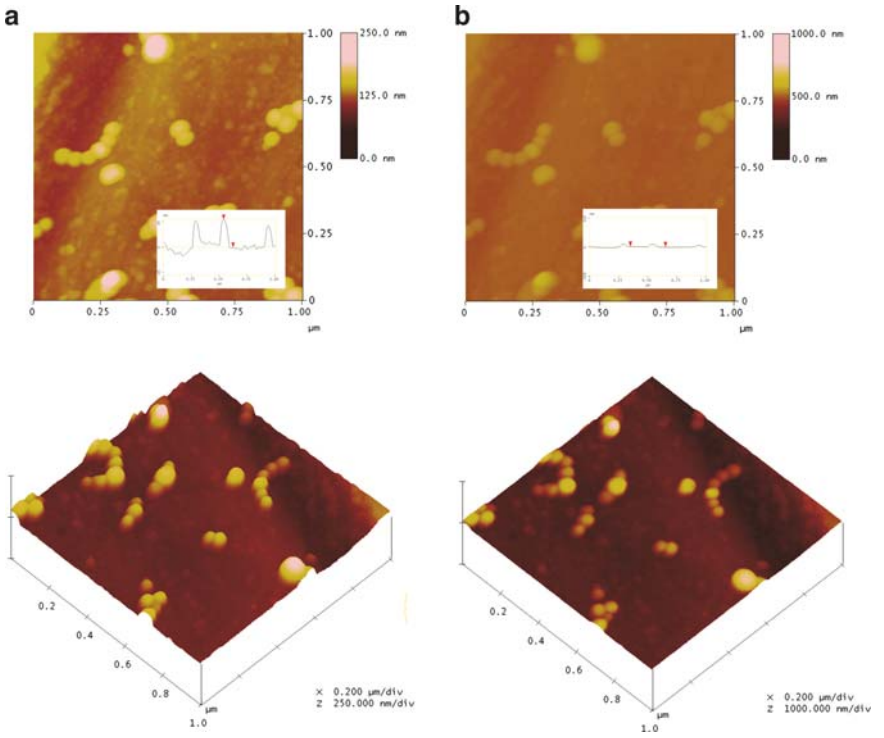

Fig. 2.37 The same AFM height data of colloidal particles displayed with different scales and settings. In *panel* (**b**) the lateral and vertical scales match

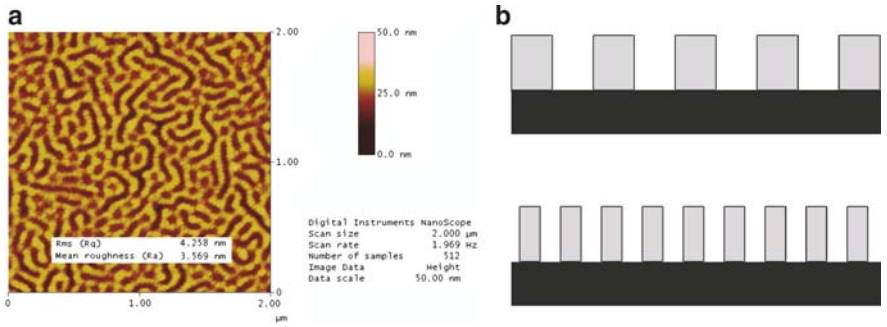

Fig. 2.38 (**a**) TM–AFM height image of block copolymer and calculated R_q and R_A roughness values. The displayed numbers (output of software) possess an unjustified number of decimals. (**b**) Schematic of two surface profiles that exhibit identical R_q and R_A, yet widely different feature size

2.2.7.5 Roughness

The roughness of sample surfaces is often of interest. Different roughness parameters can be calculated based on the acquired AFM data. Most often the *rms* roughness R_{rms} (also denoted R_q) is calculated as the standard deviation of all pixel values from the mean pixel value $\bar{Z}$.

$$R_{rms} = \sqrt{\frac{\sum\limits_{\substack{x=1,N \\ y=1,M}} (Z_{x,y} - \bar{Z})^2}{(N-1)(M-1)}}. \tag{2.11}$$

The R_A roughness value represents the standard deviation of pixel value from the mean plane.

$$R_A = \sqrt{\frac{\sum\limits_{\substack{x=1,N \\ y=1,M}} (Z_{x,y} - \bar{Z}_{x,y})^2}{(N-1)(M-1)}}, \tag{2.12}$$

where N and M are the number of pixels in the x and y directions, and $Z_{x,\,y}$ is the image pixel height with respect to the center plane height $\bar{Z}_{x,\,y}$ for the pixel (x, y).

These and other roughness parameters are discussed in [30]. Caution has to be exercised when comparing roughness data. According to (2.11) and (2.12), the two surfaces shown schematically in Fig. 2.38b possess identical roughness values.

2.2.7.6 Profile (Cross section)

Cross-sectional plots and profiles, as already utilized in many instances above, are very useful to analyze horizontal or surface distances, as well as step heights and

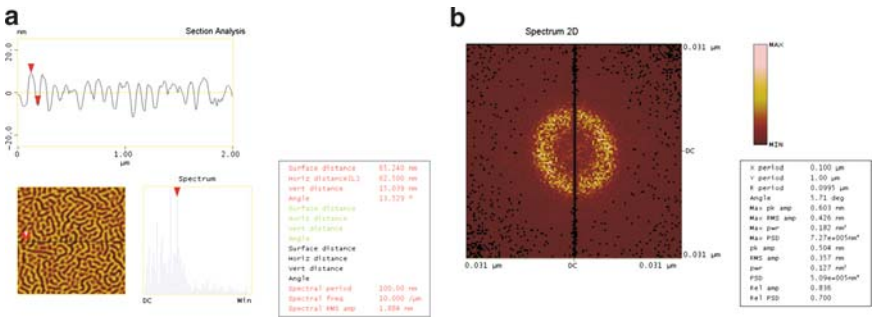

Fig. 2.39 (**a**) Cross sectional analysis of AFM data incl. 1D-FFT analysis along the selected line. (**b**) the 2D-FFT shows the typical periodicity in 2D; the *R* value agrees well with the value obtained from the 1D analysis in *panel* (**a**)

periodicities along one particular line (via a 1D fast Fourier transform (FFT) spectrum). As shown, the corrugation and spacings in a block copolymer film can be directly analyzed. In addition, the spectral period of the 1D-FFT reveals the typical repeat distance along the depicted line. In panel (b), the 2D-FFT that is calculated in a separate analysis, is also shown (Fig. 2.39).

2.2.7.7 Step Height Analysis

The determination of film thicknesses can be carried out, as shown above, by analyzing cross sectional plots. An improved statistics is obtained using a step height analysis. Here, two sets of two lines define certain areas on the two levels of altitude, which are analyzed. Instead of calculating individual height differences, the software estimates the mean difference in height between the areas selected Fig. 2.40.

2.2.7.8 Bearing Analysis

In the bearing analysis, the depths of all pixels of the image with respect to a reference point, e.g., the highest pixel are analyzed. This type of analysis renders the estimation of surface coverages and the estimation of depths possible, either for the entire image or for a selected area. The depth distribution of pixels may for instance reveal the depth levels present. In case of the calibration grating shown in Fig. 2.28a, this would be a bimodal distribution (Fig. 2.41). These data can be deconvoluted using graphics analysis software, similar to a spectroscopic deconvolution. The cumulative distribution depicted on the right hand side aids in the estimation of surface coverage.

There are of course numerous other analysis methods, including grain size, localized depth analyses, etc. The reader is referred to the manuals of the AFM software and to the Appendix for independent analysis software packages.

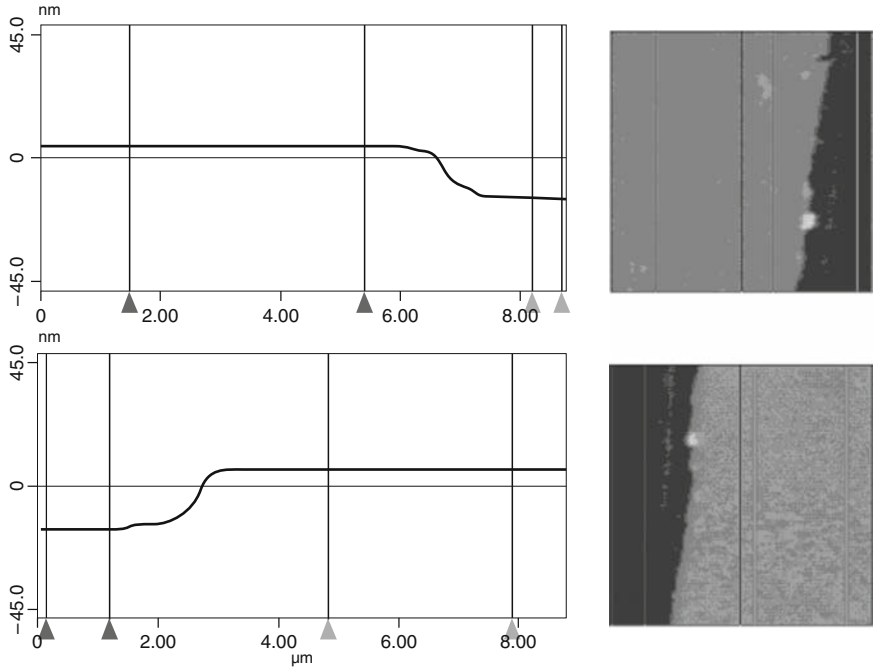

Fig. 2.40 Step height analysis of AFM height images of a thin polymer film prior to and after swelling (step heights of 19.0 and 21.3 nm were measured). Reproduced with permission from [31]. Copyright 2005. American Chemical Society

2.2.8 Typical AFM Artefacts

The possible presence of artefacts in microscopy data is an important aspect, which always has to be taken into account when analyzing the images. "Seeing is believing" is a corollary of the quick, and sometimes over-quick, jump from visual impression to interpretation. Optical illusions are well known to everyone; still no one would question the ability of our visual system to differentiate different objects. In microscopy, however, and AFM and related techniques in particular, the presence of artefacts has led to some reservation to accept the techniques as characterization and analytical techniques, and even brought discredit to the technique(s) in general. This may in parts be attributed to uncritical authors who made or make unsubstantiated claims. However, another part may be due to researchers and readers who shy away from appropriate interpretation of the data; appropriate in the sense of established characterization techniques such as nuclear magnetic resonance (NMR). If the imaging mode, the nature, and extent of tip–sample interactions, as well as possible artefacts, are taken into consideration, and if the instrument and detection scheme are properly calibrated, AFM becomes a reliable *quantitative* surface analysis technique.

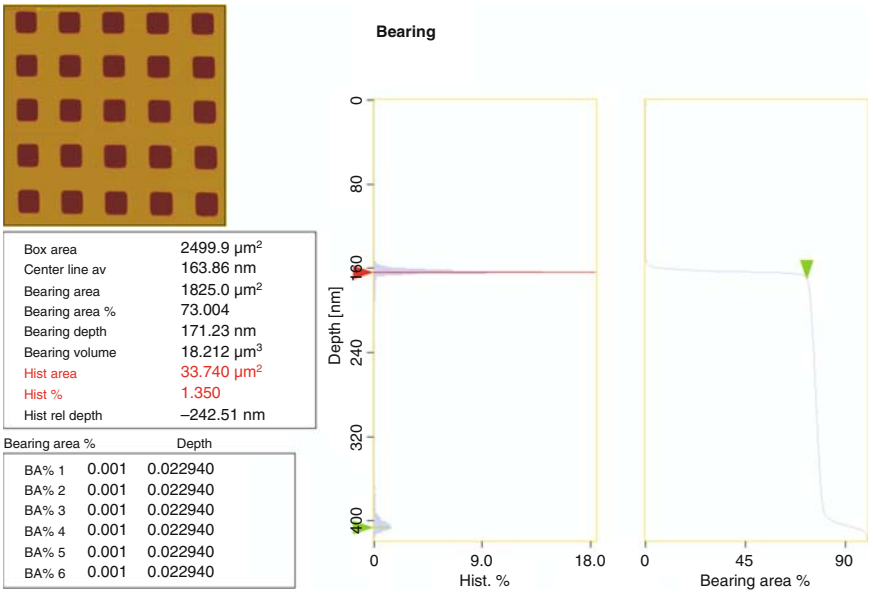

Fig. 2.41 Bearing analysis of AFM height image of calibration grating displaying the depth distribution (*middle*) and the cumulative distribution of depths (*right*)

One limitation of AFM is of course the fact that the data acquired is convoluted with information of the probe tip (size, asymmetry etc.). This phenomenon is called "tip imaging." Strictly speaking all AFM images show this effect, albeit to a different extent. In the philosophical limit of an atomically sharp tip with infinite aspect ratio, the data are not convoluted unless we image single atoms. Depending on the size and geometry of the tip, features appear broader than they are in reality (Fig. 2.42a). In a very simplified model, assuming spherical tip apex and a spherical object, it can be shown how the width is overestimated. Assuming or determining the actual tip shape and dimensions can thus be helpful to deconvolute the data. Typical tip radii are anywhere between a few to several tens of nanometers; thus, for smaller objects and features, this effect must be taken into account. For instance, the individual dendrimers shown in Fig. 2.42b are substantially overestimated in width.

For very high and narrow features it may happen that the image contains practically no information on the objects that was imaged. A mirror image of the tip is observed. As shown in, this is the underlying principle of tip calibration using a standard (Fig. 2.43).

While the tip images, as shown above, do not occur too frequently, unless very rough surfaces are imaged or samples are contaminated, more subtle effects occur very well. In the case of an asymmetry of the probe tip, this is readily recognized, as all "tip images" possess the same orientation. Changing the scan angle does not help to differentiate this kind of artefact from true features, as the actual orientation does not change; only the relative one does change. Thus, the features would all rotate as

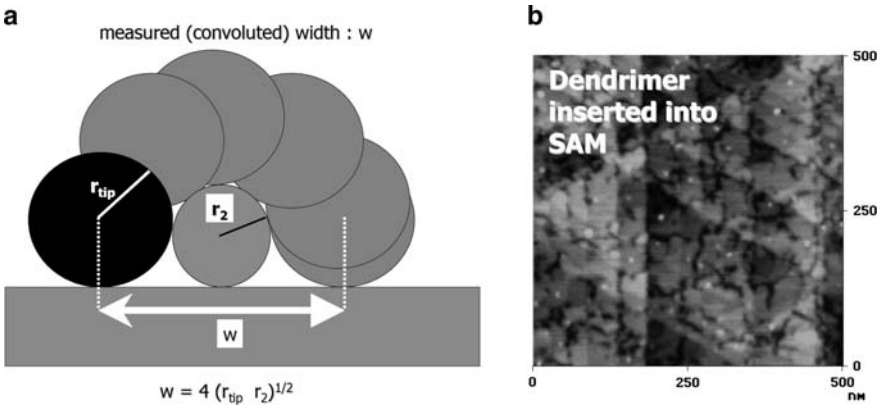

Fig. 2.42 (**a**) Model to quantitatively describe the effect of tip broadening; (**b**) TM AFM height image of dendrimers; while the diameter of dendrimers in solution was determined to be ∼3.5 nm the dimension of each "*dot*" are: height 0.9 ± 0.2 nm, width 23 ± 4 nm). Reproduced with permission from [32]. Copyright 2000. American Chemical Society

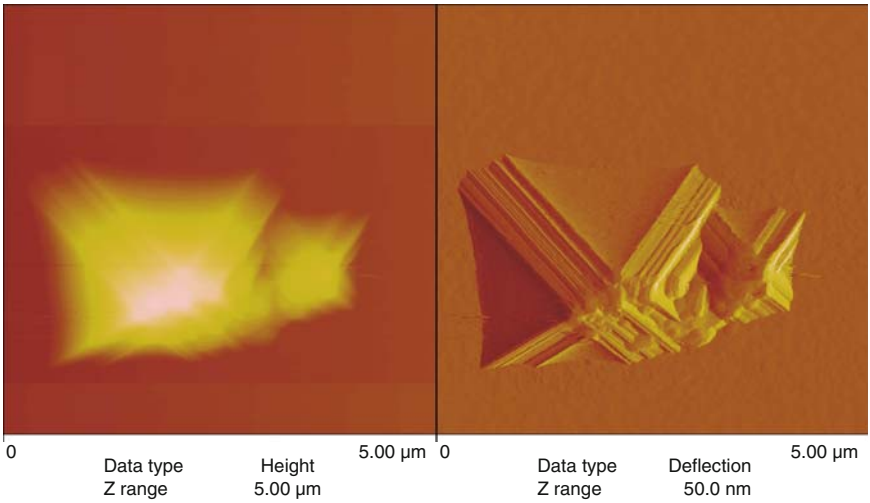

Fig. 2.43 Contact mode AFM and deflection images exhibiting a tip artefact

would the image. To be able to decide whether the triangular features in Fig. 2.44 are real, one would need to manually rotate the specimen relative to the tip.

Similarly clear is the presence of a so-called "double tip" (Fig. 2.45a). Here, the tip exposes two points (sometime in different levels). Again, the features possess typical orientations, as demonstrated nicely below for electrospun polymer fibers (Fig. 2.45). The fibers appear to be double, depending on their orientation.Since two fibers are apparently visible when they are oriented horizontally, while these fibers

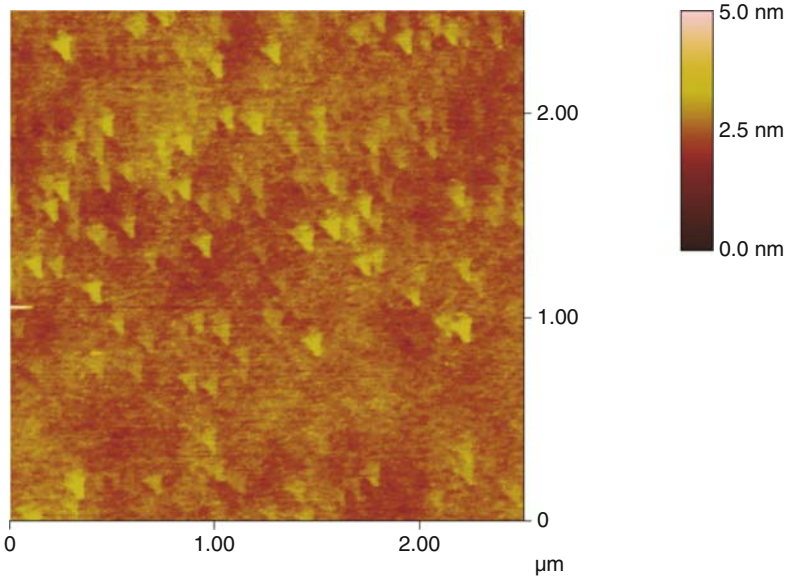

Fig. 2.44 Contact mode AFM image displaying a tip artefact

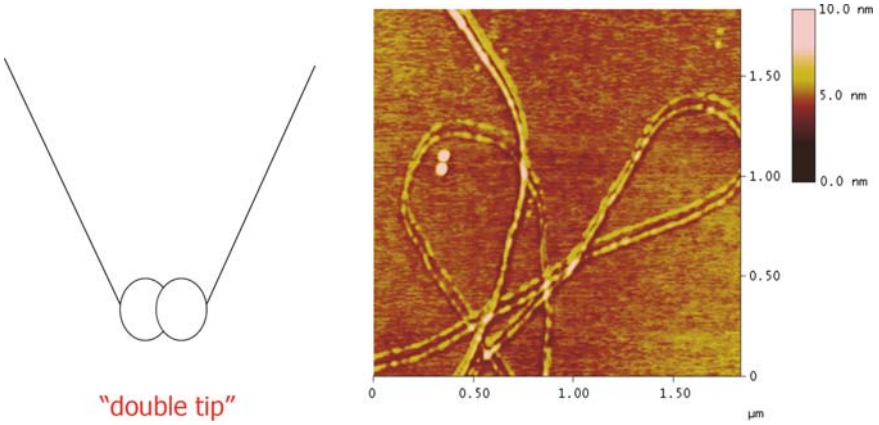

Fig. 2.45 (**a**) Schematic of a double tip; (**b**) AFM height image of electrospun polymer fibers. The appearance of parallel fibers (i.e., a pair of fibers) is highly unlikely on the basis of the orientation dependence of the pairs

seems to merge to one for vertical orientation, the double tip must possess two points that are aligned along the vertical direction.

More difficult is the differentiation of tip convolution effects if there is no hidden symmetry. In the images shown in Fig. 2.46, the tip was altered in the course of an experiment. In fact, the images show the same area of a vertically stretched

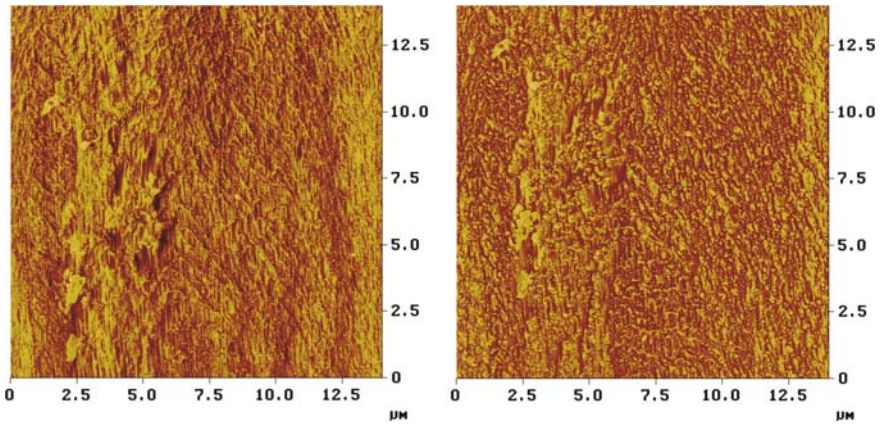

Fig. 2.46 TM–AFM images of the same area of a vertically stretched elastomeric polypropylene as imaged (**a**) with a fresh and (**b**) with an aged tip [33]

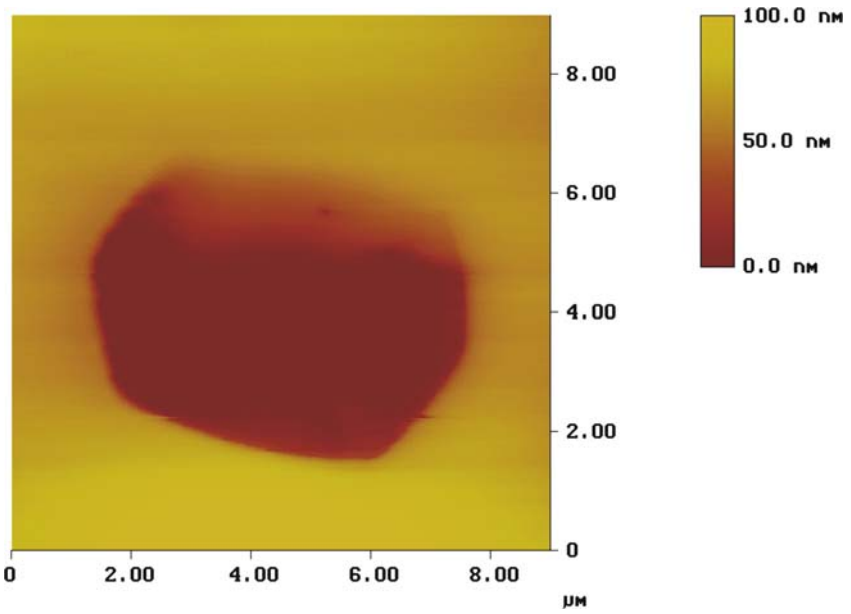

Fig. 2.47 TM–AFM image of a PEO crystal in a melt of PEO. Because of an imaging artefact the crystal appears to be located at a lower depth (Reproduced with permission from [34]. Copyright 2003. American Chemical Society)

elastomeric polypropylene as imaged (a) with a fresh tip and (b) with a likely damaged (broken) or contaminated (by particulates) tip. The images suggest a fibrillar and a grainy texture, respectively.

From these examples, it becomes clear that consistent data acquired with a number of probes may be indeed required to confirm certain results.

Additional important artifacts are related to the effect of the probe tip on the sample specimen. The scanning tip, especially in CM, may result in plastic modification (recognized as vertical ridges (compare Sect. 3.2.3 in Chap. 3; Fig. 3.16). For any experiment, it is hence advisable to zoom out to a larger scan area once in a while to check whether or not the tip has modified the previously scanned area. This can be seen either as altered texture and morphology or as friction or phase images (if applicable).

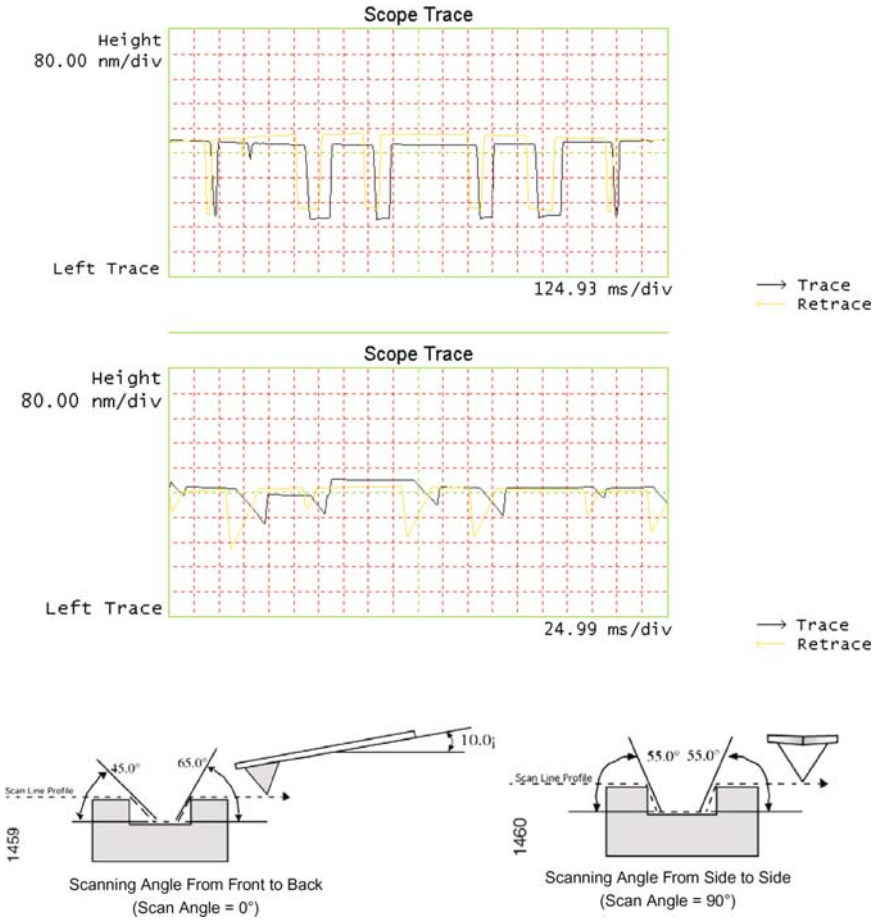

Fig. 2.48 Scope traces (TM–AFM) with high (*upper panel*) and too low (*middle panel*) gains. The mounting angle of the AFM cantilever and the inclination angle of the tip on the cantilever determine the possibility to image steep features, as shown for a silicon nitride CM AFM probe in the *bottom panel* (reproduced with kind permission from the Veeco user manual). As a result of this, the tip's interaction with sidewalls may depend on the direction

The height data obtained depend, as mentioned before, on the quality of the feedback loop (gain setting). In addition, it should not be overlooked that the tip may compress softer areas more than stiffer areas leading to an underestimate of height for the former areas. In tapping mode, the damping may be more pronounced on a soft, sticky, or highly energy dissipative material in some area, thus resulting in an overestimate of the height of these areas with respect to others. An extreme example (not typically observed) is shown in Fig. 2.47, where a poly(ethylene oxide) lamellar crystal has been imaged in the melt. The melt damps the oscillation of the tip/cantilever assembly to such an extend that the melt appears to be at a higher altitude than the crystal (independent images after complete crystallization confirm that the crystal is *not* located inside the melt.

Other artefacts refer to improper scanning conditions and include a halo in the fast scan direction after traversing higher features. If the gains are too low or/and the scan velocity is too high, the tip does not track the surface profile adequately. A comparison of trace and retrace scan (these should overlay well) helps to identify this artefact (Fig. 2.48). The top panel shows the scope trace for an AFM scan of a topographic structure with appropriate gains. The scanner calibration is not optimal as there are (1) a clearly discernible bow and (2) a substantial scan line offset (trace and retrace appear to be shifted). The issue is, however, that in the middle panel the tip did not trace the surface appropriately, as the gains were too low.

Vanishing contrast may be caused by selecting a setpoint that is almost equal to the differential signal for the undeflected cantilever and equal to the *rms* amplitude of the freely oscillating forced oscillator for CM and TM, respectively.

Thermal or instrumental drift (e.g., due to scanner creep in open loop configurations) is a problem that leads to elongated features. As drift is a vectorial quantity (shifted length over time in a given direction) its distorting impact on the image

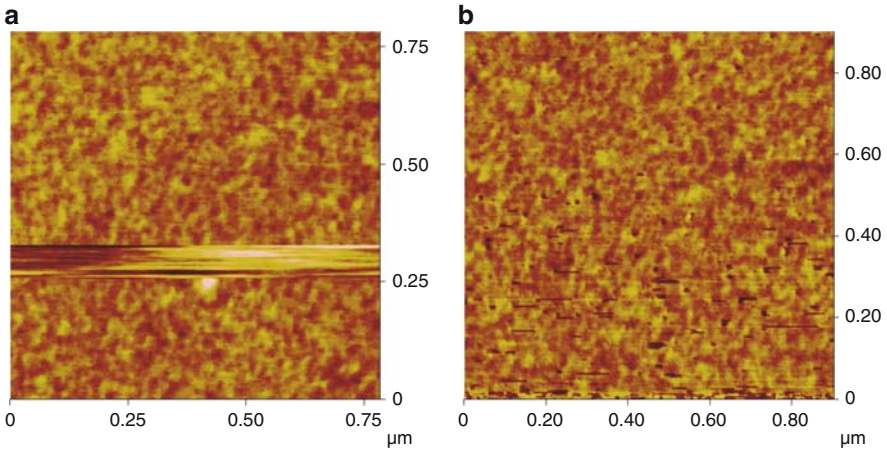

Fig. 2.49 Overview on artefacts in TM–AFM: (**a**) TM–AFM height image of a scan during which the tip temporarily lost contact with the sample surface (setpoint ∼ free oscillation amplitude); *panel* (**b**) displays the bistability effect in intermittent contact mode AFM

depends on relative scan angle and scan velocity. The absence of drift is confirmed if images are captured with disabled slow scan axis (here the scan lines of nominally one and the same line are added on top of each other). Vertical lines indicate the absence of drift; this procedure should be carried out for two different scan angles as the drift direction may coincide with the vertical direction for one angle.

In friction force microscopy, laser light interference may lead to artefacts that are often eliminated by subtracting trace and retrace (after scan line shift correction).

Finally, missing scan lines due to electronic noise, the tip not tracing the surface properly, or the mentioned bistability (in tapping mode, see Chap. 1) may appear. In the later case, one should change the setpoint or the absolute amplitude to exit the region of bistability, while the former line can be removed electronically afterwards (Fig. 2.49).

References

1. Schönherr H (1999) From functional group ensembles to single molecules: scanning force microscopy of supramolecular and polymeric systems. Ph. D. Thesis, University of Twente
2. Magonov SN, Elings V, Whangbo M-H (1997) Surf Sci 375:L385–L391
3. Snetivy D, Vancso GJ (1993) Langmuir 9:2253–2254
4. Landau LD, Lifshitz EM (1986) Theory of elasticity, vol 7. Pergamon, Oxford
5. Albrecht TR, Akamine S, Carver TE, Quate CF (1990) J Vac Sci Technol A Vac Surf Films 8:3386–3396
6. For V-shaped or triangular levers different approximations exist, e.g. the parallel beam approximation: Sader JE (1995) Rev Sci Instrum 66:4583–4587
7. The values of Young's modulus in the [100], [110] and [111] directions are E[100] = 130 GPa, E[110] = 168 GPa, and E[111] = 187 GPa, respectively. Wortman JJ, Evans RA (1965) J Appl Phys 36:153–156
8. Noy A, Frisbie CD, Rozsnyai LF, Wrighton MS, Lieber CMJ (1995) Am Chem Soc 117:7943–7951
9. Kiesewetter L, Zhang JM, Houdeau D, Steckenborn A (1992) Sens Actuator A Phys 35:153–159
10. Schneider D, Tucker MD (1996) Thin Solid Films 291:305–311
11. Levy R, Maaloum M (2002) Nanotechnology 13:33–37
12. Ma HL, Jimenez J, Rajagopalan R (2000) Langmuir 16:2254–2261
13. Butt HJ, Jaschke M (1995) Nanotechnology 6:1–7
14. Tortonese M, Kirk M (1997) Proc SPIE 3009:53–60
15. Cleveland JP, Manne S, Bocek D, Hansma PK (1993) Rev Sci Instrum 64:403–405
16. Butt HJ, Cappella B, Kappl M (2005) Surf Sci Rep 59:151–152
17. Attard P, Pettersson T, Rutland MW (2006) Rev Sci Instrum 77:116110
18. Tocha E, Schönherr H, Vancso GJ (2006) Langmuir 22:2340–2350
19. Pettersson T, Nordgren N, Rutland MW, Feiler A (2007) Rev Sci Instrum 78:093702

20. Buenviaje CK, Ge SR, Rafailovich MH, Overney RM (1998) Mater Res Soc Symp Proc 522:187–192
21. Schwarz UD, Köster P, Wiesendanger R (1996) Rev Sci Instrum 67:2560–2567
22. Liu E, Blanpain B, Celis JP (1996) Wear 192:141–150
23. Feiler A, Attard P, Larson I (2000) Rev Sci Instrum 71:2746–2750
24. Ogletree DF, Carpick RW, Salmeron M (1996) Rev Sci Instrum 67:3298–3306
25. Varenberg M, Etsion I, Halperin G (2003) Rev Sci Instrum 74:3362–3367
26. Ogletree DF, Carpick RW, Salmeron M (1996) Rev Sci Instrum 67:3298
27. Varenberg M, Etsion I, Halperin G (2003) Rev Sci Instrum 74:3362
28. Tocha E, Schönherr H, Vancso GJ (2006) Langmuir 22:2340–2350
29. Tocha E, Song J, Schönherr H, Vancso GJ (2007) Langmuir 23:7078–7082
30. Thomas TR (1999) Rough surfaces, 2nd edn. Imperial College Press, London
31. Feng CL, Zhang Z, Förch R Knoll W, Vancso GJ, Schönherr H (2005) Biomacromolecules 6:3243–3251
32. Friggeri A, Schönherr H, van Manen H-J, Huisman B-H, Vancso GJ, Huskens J, van Veggel FCJM, Reinhoudt DN (2000) Langmuir 16:7757–7763
33. Schönherr H, Wiyatno W, Frank CW, Waymouth RM unpublished data
34. Schönherr H, Frank CW (2003) Macromolecules 36:1199–1208

General Reading

Binnig G, Quate CF, Gerber C (1986) Phys Rev Lett 56:930
Sarid D (1991) Scanning force microscopy, with applications to electric, magnetic and atomic forces. Oxford University Press, Oxford
Wiesendanger R (1994) Scanning probe microscopy and spectroscopy, methods and applications. Cambridge University Press, Cambridge, UK
Miles MJ (1994) In: Spells SJ (ed) Characterization of solid polymers, Chap. 2. Chapman and Hall, New York, pp 17–55
Goh MC (1995) In: Prigogine I, Rice SA (eds) Advances in chemical physics, vol XCI. Wiley, New York
Sawyer LC, Grubb DT, Meyers GF (2008) Polymer microscopy: characterization and evaluation of materials, 3rd edn. Springer, Berlin
Magonov SN, Whangbo M-H (1996) Surface analysis with STM and AFM. VCH, Weinheim
Colton RJ, Engel A, Frommer JE, Gaub HE, Gewirth AA, Guckenberger R, Rabe J, Heckl WM, Parkinson B (1998) Procedures in scanning probe microscopies. Wiley, New York
Meyer E, Overney RM, Dransfeld K, Gyalog T (1998) Nanoscience: friction and rheology on the nanometer scale. World Scientific, Singapore
Magonov SN, Reneker DH (1997) Annu Rev Mater Sci 27:175
Tsukruk VV, Reneker DH (1995) Polymer 36:1791
Sheiko SS (2000) Adv Polym Sci 151:61

Schiraldi DA, Poler JC (2002) In: Mark HF, Bikales N, Overberger CG, Menges G, Kroschwitz JI, (eds) Encyclopedia of polymer science and technology, vol 1, 3rd edn. Wiley, New York

García R, Pérez R (2002) Surf Sci Rep 47:197

Schönherr H (2004) Scanning force microscopy. In: Mark HF, Bikales N, Overberger CG, Menges G, Kroschwitz JI, (eds) Encyclopedia of polymer science and technology, Wiley, New York (doi: 10.1002/0471440264.pst500)

Part II
Case Studies: Macromolecules, Polymer Morphology and Polymer Surface Properties by AFM

3 Visualization of Macromolecules and Polymer Morphology

Abstract

Polymers and their morphology are characterized by a structural hierarchy on different levels, which belong to molecular, nanometer, mesoscopic, micrometer, and macroscopic length scales, respectively. The analysis of the underlying structure by means of scanning force microscopy (SFM) on the relevant length scale, and in particular the interpretation of SFM micrographs, requires some basic concepts of polymer morphology. This chapter reviews some rudimentary concepts of structural hierarchy in polymers and hence lays the ground for the hands-on SFM examples discussed in later chapters.

3.1 Structural Hierarchy in Polymers

It is not the purpose of this monograph to give a detailed discussion into the basic principles of morphology of polymers. Nevertheless, making some introductory remarks here with representative references to the literature seems appropriate, in order to put the individual case studies to be discussed in proper context.

In principle, if the atomic positions in space and the types of atoms in polymeric materials would be exactly known, the structure were fully defined. However, it is obvious that for a kilogram of plastic we do not want to know the position of each atom. Even if we could determine these positions, the huge amount of information would make any corresponding treatment unmanageable and useless. In addition, at different size levels there are typical structural features, which are not necessarily present in other (smaller or larger) size domains. Based on a classification of these characteristic features, one could arrive at a structural description emphasizing, at different size levels, i.e., across the length scales, the typical and representative characteristics of the given length scale. In order to understand structure-property-function relations and to control and design new polymers, macromolecular materials must be considered at the various levels of their hierarchical structure (Fig. 3.1).

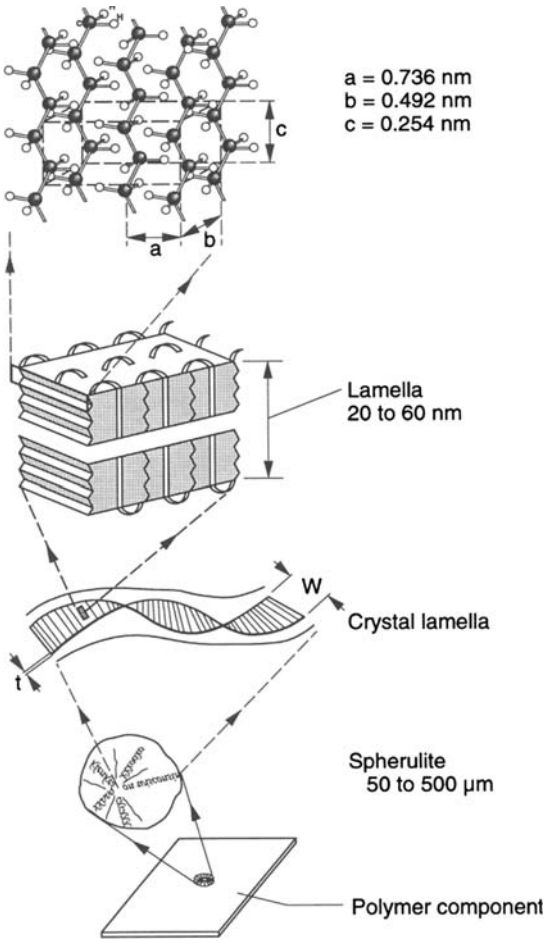

Fig. 3.1 Structural hierarchy in semicrystalline polymers. Reproduced from [1] with permission; copyright: Hanser Verlag. The example is typical for structural organization in semicrystalline polyethylene

At the different levels of this hierarchy, the molecular units, or their aggregates, are embedded within other, larger, structural elements, which may, in turn, be part of even larger units of the increasing size level of structural organization.

We prefer to classify structural hierarchy in five levels including molecular, nanometer, mesoscopic, micrometer, and macroscopic scales (see Fig. 3.1) [1] although sometimes four levels of hierarchy are used including molecular, nanometer, micrometer, and macroscopic scales [3]. Four levels maybe appropriate for amorphous polymers, while five levels are needed for the organization of semicrystalline macromolecular materials.

Various factors influence the structural organization of polymers; the most important one is their thermo-rheological history. Hence, the influence of processing on structure must be separately dealt with. The complex morphology of polymeric materials most of the time cannot be varied just at one level without consequences for the organization at higher levels. Control of structures in multiple dimensions at different length scales (specifically, bottom up, from the nanometer length scale) is a growing and highly topical area of polymer materials science. The ultimate objective of polymer materials research is to design and make materials with complex morphology independently controlled at the various levels of the structural organization to fulfill targeted functions and applications. As we shall see, AFM provides an alternative characterization tool to address questions of structural characterization that have not been possible, or have been notoriously difficult, to tackle prior to the introduction of this technique. Polymeric materials are often not in thermodynamic equilibrium, i.e. their structure at the various levels is kinetically determined. This necessitates the development of in-situ, environmentally controlled AFM approaches to investigate processes in real time.

In the next paragraphs, we briefly review the various levels of structural hierarchy first for single-component homopolymers as the simplest class of macromolecules.

The primary structure of macromolecules is defined as the sequential order of monomers connected via covalent chemical bonds. This structural level includes features such as chain length, order of monomer attachment in homopolymers (head-to-head, head-to-tail placement), order of monomer attachment in various copolymers (block copolymers, statistical and graft copolymers, chemical composition of co-monomers), stereoregularity, isomers, and molecular topology in different branched macromolecules and molecular networks. Structure at this primary level can be manipulated by polymer synthesis [4]. With AFM it is possible to visualize, under certain conditions, single macromolecules (Fig. 3.2) and it is even possible to "manipulate" these (i.e. push with AFM tips). Characteristics of chain-internal

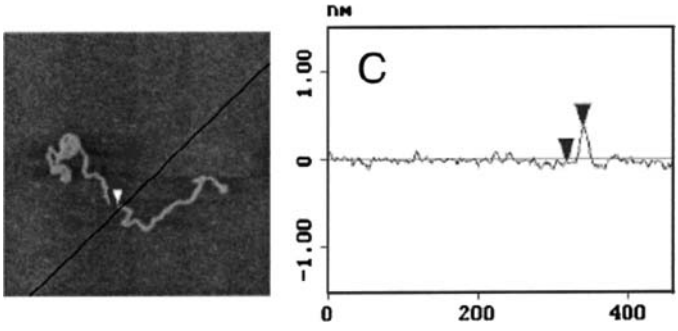

Fig. 3.2 Single chain succinoglycan AFM image on mica in buffer solutions. AFM single chain observations unveiled single chain characteristics, such as end-to-end distance, chain length, chain diameter and chain rigidity (persistence length) as a function of ionic strength. reproduced from [2]; copyright: American Chemical Society

structural details, however, cannot be visualized at present with some exceptions, e.g., helicity [5].

Depending on chain regularity, segments of macromolecules can be organized at the second level of hierarchy (up to a few nanometers) into crystalline unit cells, or into domains with some sort of short-range order in amorphous polymers, when packing in regular crystal lattice is not possible [6]. In polymer crystals, one chain usually belongs to many unit cells as opposed to molecular crystals, where molecules sitting in lattice points thus belong to one (or a few neighboring) unit cells. Packing of groups of atoms in the crystal lattice, including lattice parameters and some features of groups of atoms, making up parts of the polymer chain (methyl, phenylene, etc), can be more or less routinely visualized by AFM (with lattice resolution) depending on specimen preparation conditions, and on the degree of structural order. Corresponding studies may be useful to help decipher polymorphic forms if these coexist within the same specimen.

One must keep in mind that if AFM is used to study molecular packing in crystalline polymers, it is only the top "quasi" 2D surface, which can be visualized. Surface relaxation may change the packing of atoms and groups of atoms with respect to the bulk, hence there is no guarantee that AFM surface images are representative of the equivalent crystal faces within the bulk. In amorphous polymers, short range order (at the level of several segments, or monomer units) may exist although this has been a highly debated issue in polymer physics. AFM is not well suited to study short-range order in amorphous polymers with molecular resolution, although indirect information (surface roughness and fractal structures) may hint at the existence of segmental short range order.

The next level of hierarchy in crystalline polymers is in the range of 10–100 nm, where polymer chains organize themselves in lamellar crystals that are made up by macromolecules folded in a multiple fashion upon themselves. The thickness of these crystals is determined by undercooling conditions, hence its value is not a parameter associated with thermodynamic equilibrium. Lamellar crystals, their folding surfaces, their possible granular structures, fold domains, and their boundaries are features that can be imaged by AFM. There are intensive discussions in the literature whether nucleation and growth in polymer melt crystallization occurs via the fusion of mesomorphic, granular crystalline layers, which form pre-crystalline aggregates, or in one-step nucleation processes [7] and the reader is referred to a recent monograph [8] regarding details. In-situ hot-stage AFM is a technique, which is well suited for high-resolution studies of structure formation at the lamellar level and lamellar organization, including the investigation of the possible presence of pre-crystallization aggregates. Thus, this technique may help solving outstanding issues in theories of polymer crystallization.

In liquid-crystalline (LC) polymers rigid-rod chains possess in the bulk orientational order over length scales from the nanometer to the micrometer range. Corresponding domains and domain defects can be visualized by AFM. For main-chain LC polymers, it is not straightforward to define a distinct level of structural hierarchy in the range of lamellar thicknesses, although (depending on thermo-rheological conditions) microfibrils may form with diameters in this size domain.

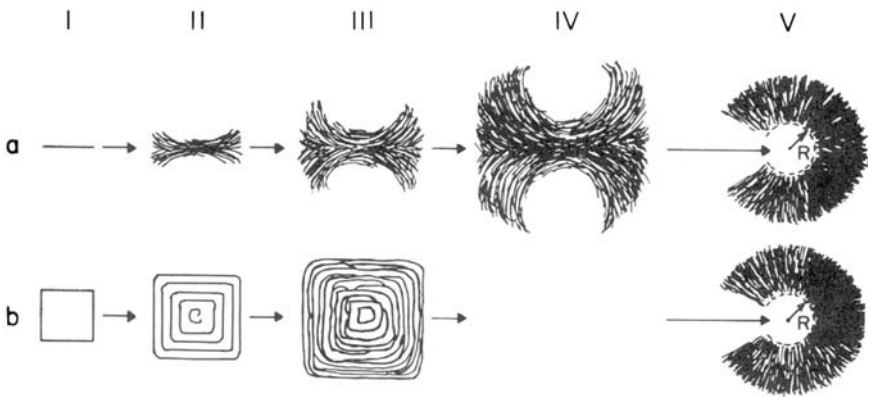

Fig. 3.3 Schematic development of a spherulite via three-dimensional organization of a hedritic core. *Top row*: edge-on lamellar view; *bottom row*: top view. In this example it is assumed that the lamellae are *square-shaped*. Adopted from [9]

In liquid-crystalline polymers, order may include packing of mesogenic, rigid side chains. Correspondingly, terrace-like (layered) morphologies can form in size-domains, which are in the range of typical lamellar dimensions. These can easily be visualized by AFM.

Lamellae in semicrystalline polymers at the next level of hierarchy organize themselves in spherulites, hedrites (which can be considered as immature spherulites) (Fig. 3.3), in trans-crystalline morphologies, cylindrical crystals, etc. These entities may have dimensions in the range between hundred(s) of nanometers to tens of millimeters. The final level of structure in semicrystalline, as well as in amorphous polymers are polymeric products which exhibit shape, and texture. During processing, the usually statistical special arrangement of the different structural entities within the structural hierarchy may become oriented i.e., characteristic textures may form. For example, lamellae may orient in preferred directions depending on the direction of processing and machining. A given type of deformation results in typical characteristic types of preferred orientation (uniaxial, planar, biaxial, etc.). Such textures introduce direction dependence (anisotropy) of physical properties, which obviously influence performance. If the structural features can be imaged which arrange anisotropically during processing, then obviously AFM imaging can yield valuable information about the special arrangement of the structural entities.

Questions which may raise interest in AFM applications are often related to the three dimensional organization of the structural subunits (lamellae) within these larger hierarchical entities and details of the morphology which demand high resolution or phase-specific contrast. It is still a challenge in polymer morphology research to decipher how nature organizes inherently flat (quasi-two-dimensional) building blocks to form three-dimensional spherulites. Several monographs deal with the related problems. At this point, the reader is referred to some very useful

references. The classical reference on crystalline polymers, their crystal structure, morphology, defects, crystal nucleation, growth and annealing, and melting phenomena is in the three-volume series of [10]. The modern book of Allen and Thomas [11] is an excellent text, which presents the fundamentals of the structure of materials in a consistent way, emphasizing generic aspects, including glasses, crystals, and liquid crystals. The authors of this text aim at common viewpoints for discussing polymeric, metallic, and ceramic materials. A most recent and excellent reference describes in a concise fashion the state-of-the-art regarding crystallization; i.e., how crystallinity develops in crystallizable macromolecular materials [12]. The author of this work attempted to complement the literature in areas, which received less attention in books, whenever it was necessary. The new edition of the most useful work of Sawyer, Grubb and Meyers [13] includes not only a detailed description of the basics of the most relevant microscopy techniques (with some information on AFM), but it also describes specimen preparation techniques which can be used also in AFM research, discusses polymer applications with very good examples, and describes problem-solving strategies. Finally, an excellent collection of examples of polymer micrographs obtained with different techniques can be found in [14].

Thus far, we have only considered simple, single-component homopolymers. Obviously, if copolymers are considered, interactions within the bulk of the different comonomers can result in different, more complex forms of structural organization. An interesting example is the class of block copolymers (diblock, triblock, multiblock, etc.) where thermodynamic phase separation (resulting from immiscibility) can introduce regular microphase-separated structures. The size, repeat length, and packing symmetry of these phase-separated structures can be controlled by controlling the overall chain length and the relative block lengths. If one of the blocks can crystallize, corresponding crystalline hierarchies (lamella, unit cell) can form within one type of the phase-separated domains. Block copolymers have created tremendous interest as via chemistry their structural organization can be controlled in different dimensions. Polymer chemistry is just at the beginning of controlling the primary chemical composition in (simple) block copolymers by choosing appropriate synthetic procedures. Thus, a thorough understanding of the complex microphase-separated morphologies is of prime importance. As in block copolymers, the different phases often exhibit different mechanical (and adhesion) properties, different AFM imaging modes that are sensitive to the corresponding (mechanical and surface adhesion) contrast (e.g., phase imaging) can be very useful.

Product development, quality assurance, and performance testing often bring materials to failure and study the corresponding fracture and failure mechanisms. In the process, often characteristic morphologies form which can also be studied by AFM. It must be noted that AFM is not very well suited to study sharp features and rough surfaces. Yet failed surfaces, cracking, and fibrillation often include features the formation of which can be better understood if imaged with high-resolution AFM. Interestingly, deformation and failure mechanisms in amorphous (glassy) polymers can also be described on four levels of structural hierarchy. For example, if brittle, glassy polymers failure begins with crazing which is accompanied by the

formation of fibrils with a diameter on the order of 20 nm (second level of structural hierarchy). The stability of the micro fibrils depends on the primary chemical structure of the chain (e.g., chain chemical composition). If the micro fibrils fail, a crack opens between the two supporting sides of the fibrils and propagates to result in failure. Typical crack sizes have dimensions characteristic for the third level of the hierarchy (micrometer range). The part which fails is at the fourth size level of organization. To prevent crack propagation the impact energy can be dissipated by added elastomers, materials design (deformation of voids deliberately introduced), or properly distributed fillers (in semicrystalline polymers) which promote energy absorption by plastic flow of crystalline ligaments forming between the filler particles. AFM can be a valuable asset for looking at the second level processes and features in these multicomponent materials. Fillers in heterogeneous engineering materials often have dimensions less than 100 nm, such as carbon black and silica in filled elastomers. The primary particles in silica-filled rubber, for example, have typical sizes in the 10 nm range. The distribution of filler and the related morphology in these rubber materials, which determines product performance, can be efficiently studied by AFM.

Blends, composites, and heterogeneous systems (e.g., mixtures of polymers and impact modifiers, etc.) constitute technologically very relevant groups of engineering polymers. In blends, phase separation occurs due to incompatibility of the components but there are no connectivity constraints (in contrast to block copolymers where the immiscible parts are chemically connected), which can result in equilibrium morphologies. Hence, blend microstructures strongly depend on the forming conditions (Fig. 3.4). AFM can be useful for elucidating microstructure also

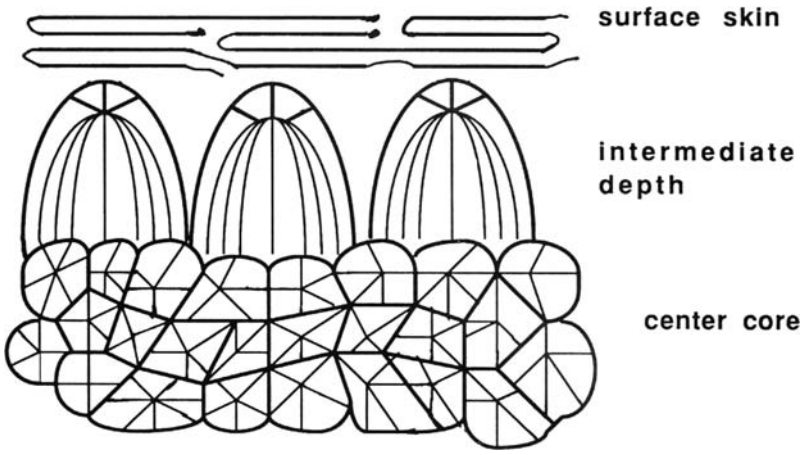

Fig. 3.4 Possible effects of processing (injection molding) on the microstructure of a semicrystalline polymer. In contact with the mold wall (which is assumed to be perpendicular to the plane of the scheme) a surface skin morphology is formed. An isotropic microstructure can be observed in the "center core" interior. Adopted with permission from [15]

for these materials, especially if it is used in imaging modes, which exhibit material-specific contrast.

Nature uses 20 normal amino acids and assembles them in given sequences in nucleic acids and tens of thousands of proteins in a predetermined fashion, resulting in the most complex structures with a wide variety of functions [16]. Even though polypeptides, polynucleotides, and polysaccharides are also linear polymers, at the same time they are also copolymers in which the individual neighboring (and distant) comonomers can interact with each other. Such biomacromolecules have been traditionally the subject of biochemistry. In biochemistry, one usually considers four levels of structural hierarchy, but these are quite different from the four levels of simple, synthetic polymers. One usually considers the sequential order in the corresponding complex copolymeric biomacromolecules as the primary structure. Nature prefers unique (monodisperse) chain lengths for the different biomacromolecules, as well as head-to-tail arrangements. Due to conformational constraints and intrachain interactions, biomacromolecules organize at the next level (secondary structure) in helices and other conformationally ordered segments of portions (residues) of the chain. The residues are further organized in three-dimensional arrangements at the third level (tertiary structure). Independent tertiary units can then organize at the fourth level in quaternary structures via noncovalent association. These structures may either be disordered (e.g., a ribosome) or ordered (textured) arrangements, e.g., tobacco mosaic virus. Quaternary structures may be considered as the "biological equivalents" of a synthetic polymeric product (part) with a structural or functional role.

The structural hierarchy of a thermotropic polyester fiber, depicted in Fig. 3.5, resembles, to some extent, the typical organization of tendon, which functions as the connecting fibrous link between muscle and bone and is "designed" by nature to take up uniaxial stresses. At the lowest level of structural hierarchy in tendon (see Fig. 3.6) one finds the tropocollagen molecule, which is a triple helix of protein chains (primary molecular structure). The primary amino acid sequence in collagen may differ, which is the basis for dividing up collagen into different types. These are organized in micro fibrils (3–4 nm), sub fibrils (20–30 nm), fibrils (50–500 nm, with lateral, banded periodic structure of 64 nm periodicity that can crimp when the fiber is not under tension), and vesicles that make up the final tendon. Nature has designed this fiber hierarchy to achieve optimum performance under uniaxial stress. Such structures can serve as objectives also for man-made efforts to mimic nature and achieve optimum performance for functions which have been optimized in natural biomaterials during the phylogenesis (Fig. 3.7).

It is beyond the scope of this book to go into further details of comparing structural organization in synthetic and biological macromolecules. We cannot resist noting however, that one may consider as the ultimate goal of polymer materials chemistry to synthesize exact and accurate structures of the appropriate monomers in well-defined systems to achieve required functions. Differences in properties and function between man-made polymer parts and biomaterials made up of natural biomacromolecules may well be related to differences in their primary structure and architectural control. Proteins and nucleic acids are precisely defined in their

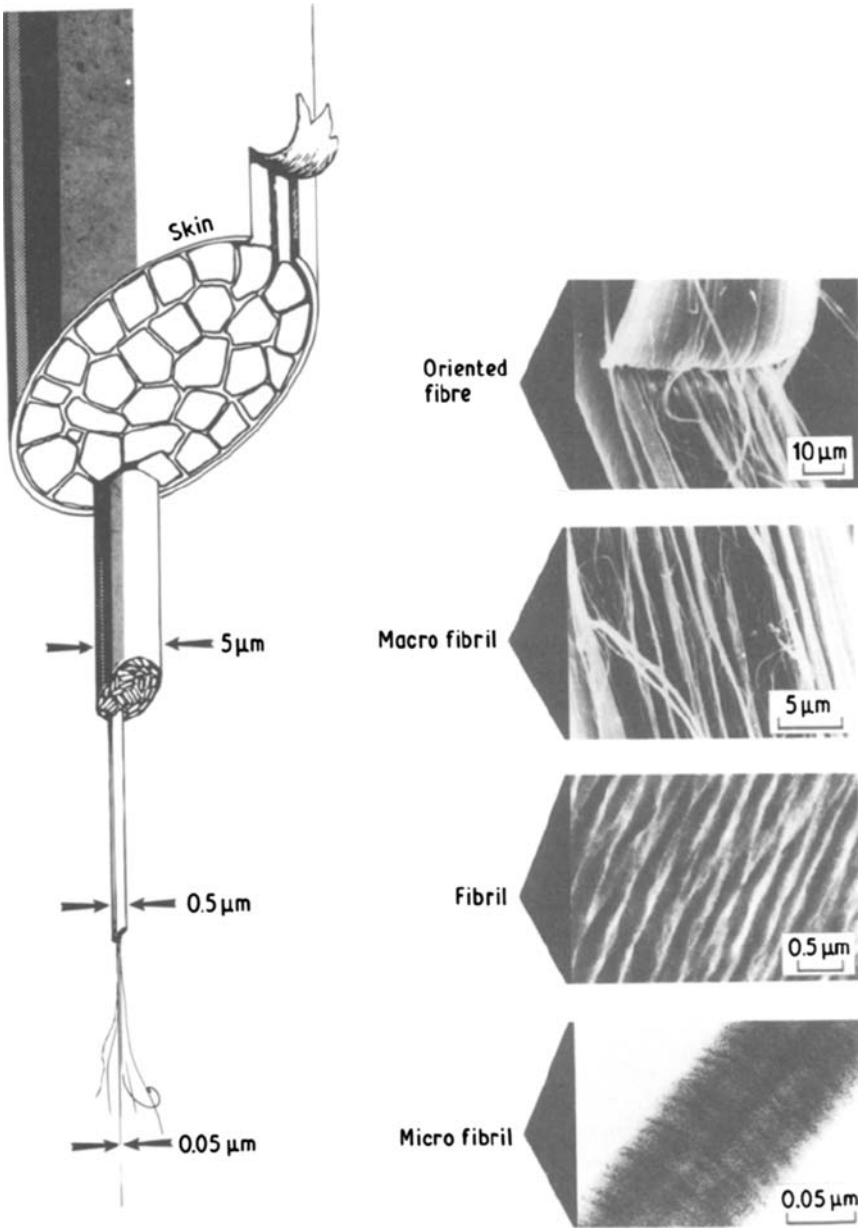

Fig. 3.5 Structural hierarchy in liquid-crystalline fibers. The mechanical performance of highly oriented polymers can approach the ultimate theoretical properties at high degrees of elongation. Anisotropic, rod-like macromolecules, like aromatic copolyesters composed of 2,6-naphthyl and 1,4 phenyl units, often form oriented structures, which can exhibit liquid crystallinity. Extensive structural studies of fibers of these oriented copolyesters showed a hierarchical structure like the one depicted in this Figure. In aramids (Kevlar or Twaron) similar structures may exist. Adopted with permission from [17]

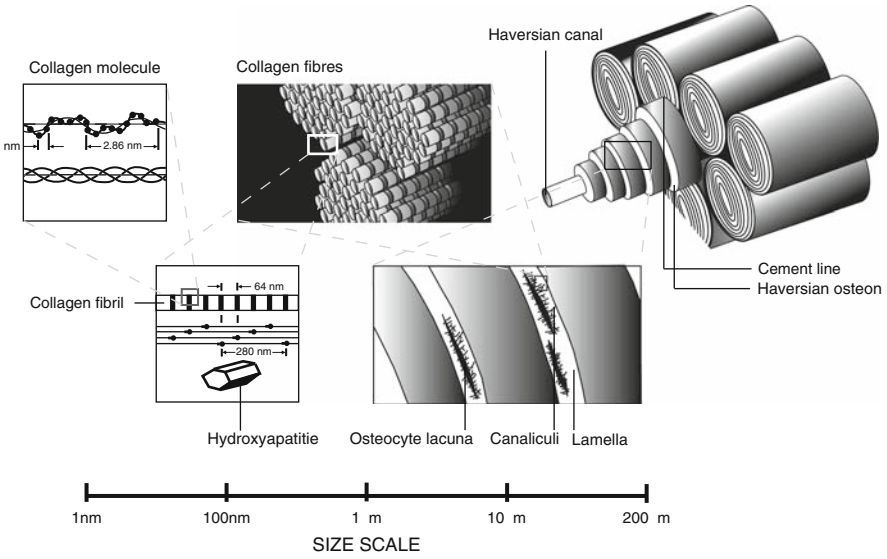

Fig. 3.6 Hierarchical structure in human bone across the length scales. Concept adopted from [18]

primary chemical structure, exhibit head-to-tail connections only, possess controlled stereochemistry, have mono disperse length distributions for a given sort of biomacromolecule, and each biomacromolecule has the same structure within the corresponding natural biomaterial. This can be contrasted with the heterogeneous primary structure within a plastic part, made of synthetic macromolecules.

Recent synthetic achievements allow chemists to synthesize block-copolypeptides with control of chain length, and monomer sequence distribution using transition metal-based initiators for controlled polymerizations [19]. These polymers, which often exhibit intriguing structural hierarchy and self-assembly, bridge the gap in their complexity between "true" biomacromolecules and simple synthetic "conventional" polymers concerning their complexity. Another promising approach encompasses a biomimetic route and uses microbial expressions of artificial genes to synthesize well-defined target structures. AFM again can play an important complementary function as a characterization tool to also investigate these corresponding structures.

While the borders of the hierarchical classification of structure and morphology are somewhat arbitrary and the definitions are not always unambiguous, it must be clear that these are unifying structural aspects that are present in the organization of both man-made and natural polymers. In addition to solving particular, individual structural problems (e.g., in commercial product development), it is hoped that AFM and the related scanned probe techniques will make significant contributions to elucidate the general concepts in a structural order and help reach an ultimate understanding of the underlying scientific principles of structure formation.

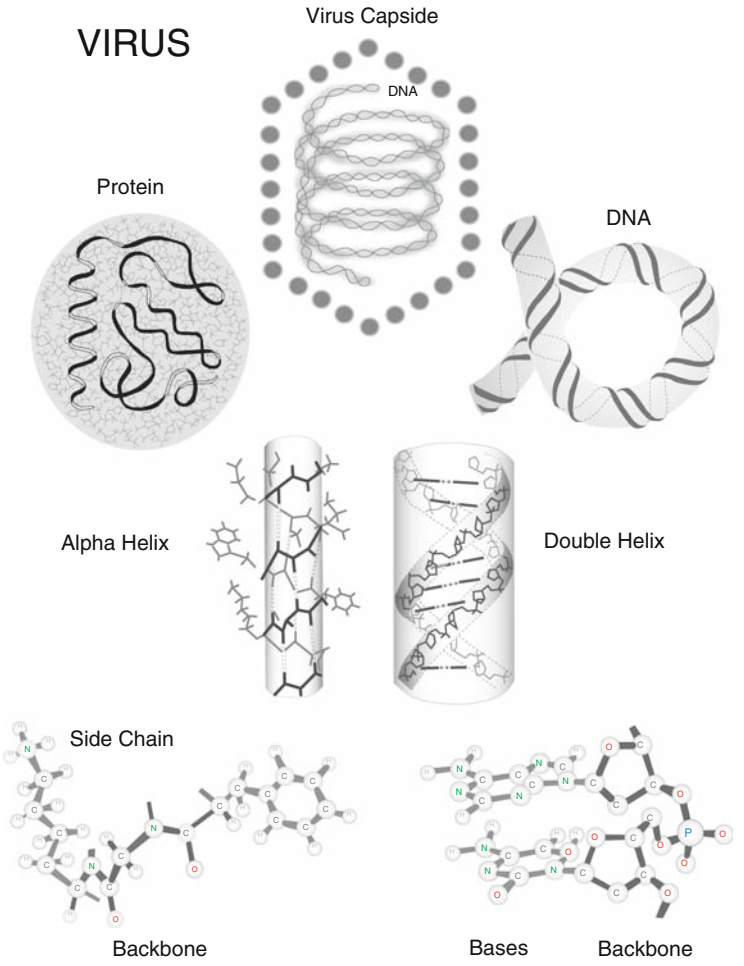

Fig. 3.7 Structural hierarchy in viruses. Adopted from [16]

3.2 Single Component Systems

3.2.1 Visualization of Single Macromolecules

Individual macromolecules can be visualized by AFM in various modes. Owing to the limited true resolution of common AFM tips, the many degrees of freedom of individual polymer chains, and the deformation of the flexible macromolecules by the AFM tip, it is often very difficult to obtain accurate physical information regarding polymer chain conformation, true size etc. However, in some cases AFM can indeed provide information on single macromolecules, which allows one to analyze the conformation or even the motion of macromolecules, as well as to probe interactions and mechanical properties.

The visualization of individual macromolecules demonstrates the potential of AFM methodologies to interrogate soft condensed matter at the level of the fundamental constituents. There are many examples of imaging single DNA and related biologically relevant shape-persistent macromolecules [20], but these will be treated in Sect. 3.3. Here we will focus on man-made artificial polymers and macromolecules, including dendrimers. The literature of AFM studies on shape-persistent macromolecules has been reviewed by Sheiko and Möller and the reader is referred to this paper for further reference [21].

Isolation of the molecules can be achieved, e.g., by adsorbing polymers in very low concentrations on suitable substrates. If clustering of the molecules can be avoided and the adhesion energies are sufficiently high, imaging of individual molecules by AFM methods, and here, in particular, intermittent contact or tapping mode AFM, is possible. Contact mode AFM is less advisable, since due to lateral forces the tip tends to displace and transfer molecules across the sample. The first example of a successful imaging of the conformation of a flexible polymer was reported by Kumaki et al., who studied PS-*b*-PMMA on mica (Fig. 3.8) [22].

In many cases the appearance of a single flexible polymer chain molecule (polymer coil) can be described as a "blob" (Fig. 3.9). The considerations made in Chap. 2 show that the convoluted images obtained are dominated in most cases by the shape and size of the tip apex. Thus, the size (width) of the macromolecule is seriously overestimated.

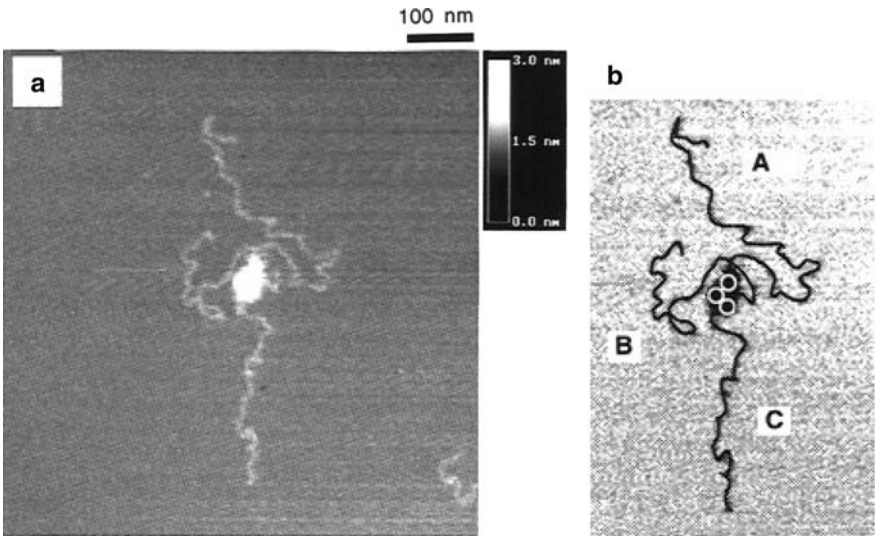

Fig. 3.8 (**a**) AFM image of a PS-*b*-PMMA monolayer deposited on mica (*left*). (**b**) Schematic representation of a possible molecular conformation. The curvilinear lengths of the lines are A, 549; B, 403; C, 314 nm. The end-to-end distances are A, 122; B, 73, C, 189 nm. Reproduced with permission from [22]. Copyright 1996. American Chemical Society

The height may also deviate from the true height of the molecule in case of high compressive forces (flattening of the macromolecule), shifts in resonance frequency owing to different interactions between tip and substrate compared to tip and polymer, or a violation of the basic assumption of the corresponding imaging mode (Chap. 2). Further, it must be taken into account that the immobilization can affect the dimensions of the molecule (i.e., the molecule may spread on a wetting surface).

Dendrimers are well suited to illustrate the effect of image convolution, as well as flattening of adsorbed macromolecules, owing to their well-defined chemical structure. For the third generation dendrimer shown schematically in Fig. 3.10, the corresponding TM-AFM height images show features with a typical height of 1.0 ± 0.2 nm and a width of 18 ± 4 nm. As an upper limit of the size of the

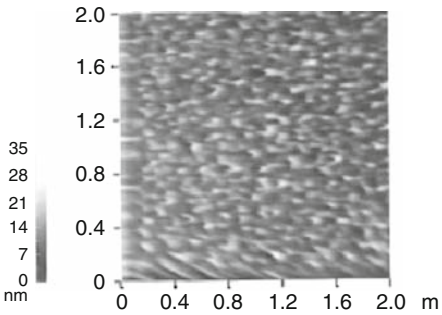

Fig. 3.9 The topography of water-soluble surface-graft 2-(dimethylamino)ethyl methacrylate chains on a poly(ethylene terephthalate) film imaged by CM-AFM. Reproduced with permission from [23]. Copyright 1997. American Chemical Society

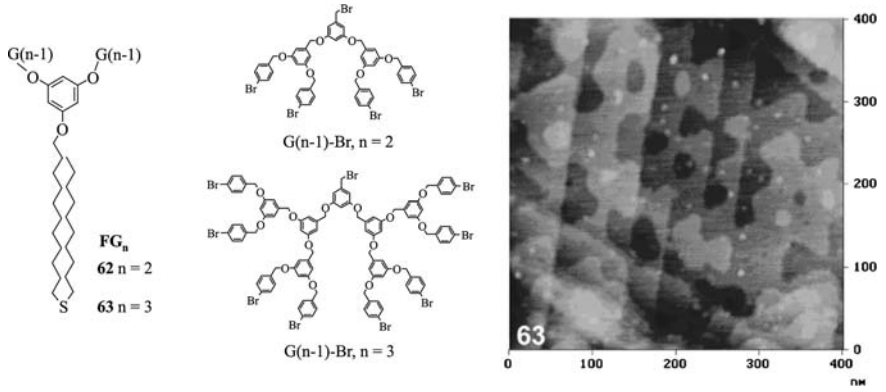

Fig. 3.10 Structure of dendrimers inserted in a self-assembled monolayer on Au(111) (*left*) and TM-AFM height image acquired in air (z-scale: 3 nm). Reproduced with permission from [24]

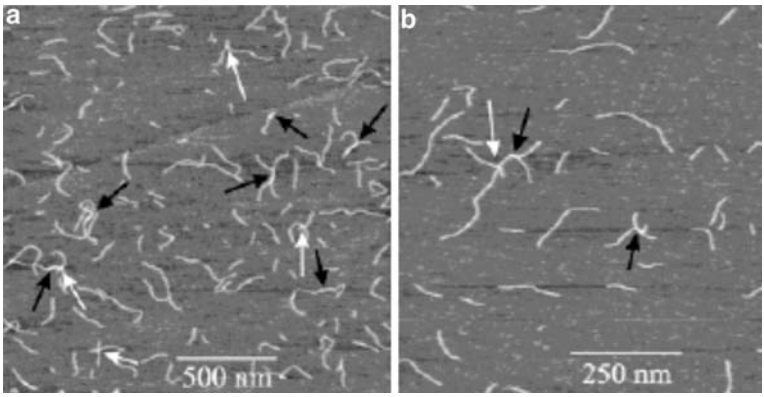

Fig. 3.11 TM-AFM height image of a PIC-Ni sample. Film prepared from a chloroform solution containing (**a**) 0.01 and (**b**) 0.001 g/L of PIC-Ni. *White arrows* indicate intersections of separate chains and *black ones* mark segments consisting of intercoiled chains. Z range: h = 2 nm. Reproduced with permission from [25]. Copyright 2002. American Chemical Society

dendrimer, the all-extended conformation in one plane can be approximated as $<$ ca. 4 nm. While the width is overestimated by a factor of $>$ 4, the measured height of 1.0 nm suggests significant flattening of the macromolecule.

The limitations mentioned are often less severe for stiff, shape-persistent molecules [21] and, for instance, polyelectrolytes as shown in the case studies. An example, which clearly displays individual chains of stiff poly (isocyanodipeptides) (PICs) and their different conformations in films on mica, is shown in Fig. 3.11.

Hands-on Example 1

Visualization of Poly(ethylene imine) (PEI) Adsorbed on Mica

Sample Preparation: Diffusion Controlled Adsorption from Solution

In this experiment we follow a procedure adapted from Pfau, Schrepp and Horn [26]. Commercial PEI with a molar mass between 30 and 1,000 kD is dissolved in water (buffer with pH 4, 1 mM KCl) to yield a solution of 1 to 10 ppm concentration. The latex spheres are separated from the solution and precipitated by centrifugation onto a mica surface fixed at the bottom of the centrifugation tube. Finally, the water is decanted and the samples are dried in air. Alternatively, drops of the solution are placed onto freshly cleaved mica substrates which are rinsed with pure Milli-Q water after several minutes. Subsequently the samples are dried in air.

TM-AFM Visualization of PEI Molecules

The mica substrates are glued to the sample holder using double-sided pressure-sensitive adhesive. An equilibration period of several hours may help to minimize the drift caused by the relaxation of the adhesive.

Standard tapping/intermittent contact mode set-up*: A TM cantilever with a spring constant of ca. 50 N/m and a resonance frequency of ca. 300 kHz is inserted into the cantilever holder. The laser is aligned, the photodiode is moved such that the laser spot is centered, and the excitation frequency and amplitude are adjusted to v at 0.85* A_o *and 100 nm, respectively. The engagement procedure is carried out as described in Chap. 2. After successful engagement the operation point is adjusted to minimum imaging forces by increasing the setpoint as close as possible to the rms amplitude of the freely vibrating cantilever. This can be achieved by increasing the setpoint to the point, where the tip can no longer trace the surface. The rms amplitude signal* A_0 *can be read from the display. Then the setpoint amplitude is adjusted to* $\sim 0.9\ A_0$ *to 0.95* A_0*. If the tip loses track of the surface during scanning, the setpoint must be slightly reduced. Next the scan size is increased stepwise while the gains are optimized accordingly, which corresponds to the vanishing contrast in the amplitude image.*

Images of the adsorbed PEI can be captured at different scan sizes $< 500 \times 500\ nm^2$. The choice of the scan rate is a trade-off between optimized feedback loop and the effect of instrumental drift. In the dual height and phase images shown in Fig. 3.12 individual molecules, as well as clusters, can be differentiated. The quantitative analysis of the observed features together with results from a series of experiments with a systematic variation of the charge density led to the

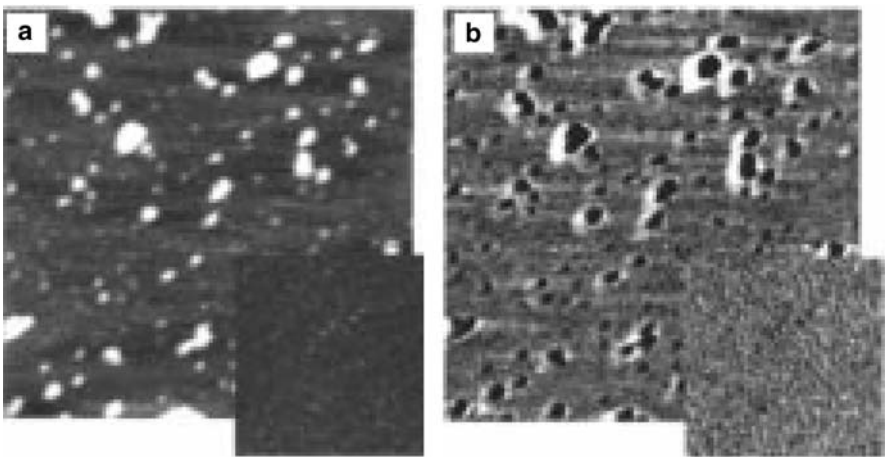

Fig. 3.12 TM-AFM height ($400 \times 400\ nm^2$) (**a**) and phase contrast (**b**) pictures acquired simultaneously on 150 kD PEI adsorbed onto mica. The *z* range in the height image is 2 nm, and the range of phase shifts is 5°. The *insets* in **a** and **b** show corresponding height and phase images of mica incubated with 1 mM KCl buffered at pH 4 but without polymer. Reproduced with permission from [26]. Copyright 1999. American Chemical Society

conclusion that individual molecules have been resolved [26]. Furthermore, a model, which describes the adsorption of PEI and its changed conformation, has been proposed [26].

Hands-on Example 2

Visualization of Poly(amidoamine) Dendrimers Adsorbed on Mica

Sample Preparation: Spincoating

The second illustrative example deals with the imaging of individual dendrimer molecules of a different generation on mica. This procedure is adapted from the work in the group of Tomalia [27]. Ethylenediamine (EDA) core poly(amidoamine) dendrimers (generations 4–10) can be obtained from Dendritech Inc. (Midland, MI) as methanol solutions. After thorough drying, the solids are weighed and then redissolved in distilled water to produce stock solutions of 0.1% (w/w). Thin films of the dendrimers on mica are prepared by spin coating a solution of a known concentration on freshly cleaved mica surfaces, which are then dried in air at room temperature.

Imaging of Dendrimers on Mica by TM-AFM

The TM-AFM set up and procedure do not differ from the details discussed above in *hands-on example 1* (*Standard tapping/intermittent contact mode set-up*). Care must be taken to operate the AFM with a, minimum free amplitude (A_0) in order to minimize the flattening of the observed macromolecules due to the interaction with the probe tip.

In the series of tapping mode images obtained for dendrimers with different generations (Fig. 3.13), the increase in width and in height of the round features is seen. Obviously the width is convoluted by the tip shape, however, if the same tip is used and remains unaltered (this can be checked by using tip standards as outlined in Chap. 2) a correlation of apparent, i.e. visualized, feature width and true feature width is justified. The results of the study by Tomalia et al. [27] led to the result that pronounced flattening of the higher generation macromolecules occurs. Thus, the conformation of these well-defined model macromolecules can be qualitatively extracted from the TM-AFM data. If de-convolution procedures are applied and the effect of tip-induced flattening is taken into account, truly quantitative information can be obtained.

3.2.2 Lattice Visualization of Crystallized Homopolymers

The crystal structure of crystallized homopolymers can be conveniently visualized in contact mode AFM measurements on oriented samples obtained by, for instance, uniaxial compression, drawing, gel, electro or wet spinning, topochemical

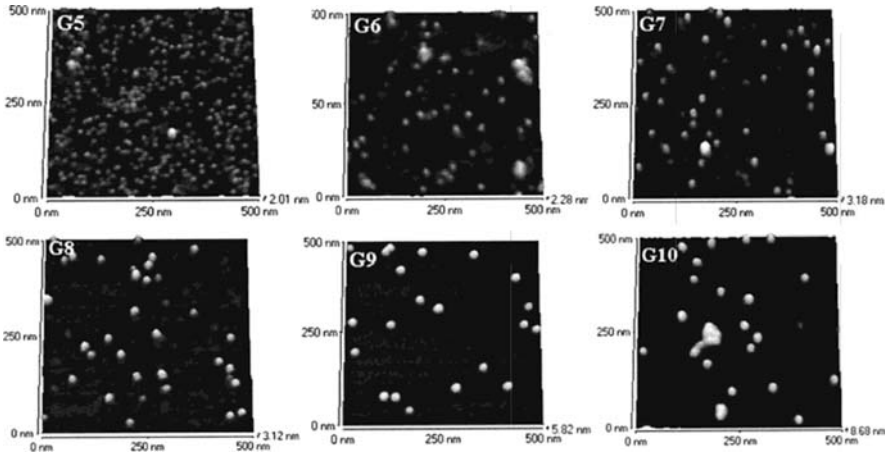

Fig. 3.13 TM-AFM images of PAMAM dendrimer molecules from G5 to G10. Dendrimer molecules (0.001% w/w) are deposited on the mica surface by spin-coating. Reproduced with permission from [27]. Copyright 2000. American Chemical Society

polymerization or friction deposition. From the wide variety of examples we will discuss two typical cases, namely poly(tetrafluoro ethylene) oriented by friction deposition and drawn poly(oxy methylene). Besides the identification of the local polymorphic structure of the crystallized polymer, it is possible in some cases to detect new (minority) crystal structures [28].

Prerequirements for the successful imaging of crystallized homopolymers with molecular (lattice) resolution are (a) flat samples, which expose sufficiently large crystal facets at the specimen surface, and (b) an optimized stable AFM instrumentation. While the crystal structure of a variety of polymers has been visualized at the untreated free surface of (micro)fibrils [29], it may be necessary to expose crystal facets by cleaving the crystal using, for instance, a microtome [see Chap. 2]. We recommend independent AFM experiments in tapping mode or contact mode to verify that the resulting surface is at least locally flat and does not contain extreme height variations, which may adversely affect the tip sharpness.

The AFM equipment must be isolated from vibrations as outlined in Chap. 2 and it must be ensured that the instrument is thermally equilibrated with its environment (see "trick" below). A short-range scanner (short tube scanner with e.g., 1 μm max. scan range) is advisable, although some longer range scanners (10 μm max. scan range) may still be sufficiently accurate and possess sufficiently low noise levels. The use of sharpened AFM tips [see Chap. 2] with low spring constants (0.30–0.02 N/m) is advisable. The samples must be firmly attached to the sample holder disc (if applicable). In order to avoid thermal drift due to the relaxation of double sided-pressure-sensitive adhesive, we suggest using a minute amount of fast curing two-component epoxy glue.

The accurate calibration of the piezo scanner in x and y direction is crucial for obtaining reproducible quantitative data. Since the specimen height affects the

calibration of the scanner [30], the typical calibration standards mica and HOPG must have the *same* height as the polymer specimen. In addition, it should be mentioned that the calibration may fluctuate from day-to-day [31], which requires a recalibration on a daily basis.

Hands-on Example 3

Lattice Visualization of Poly(tetrafluoro ethylene) (PTFE) by CM-AFM

Sample Preparation: Friction Deposition

Thin films of PTFE can be transferred to glass substrates by sliding a block of PTFE over heated glass substrates [32, 33]. The temperature of the precleaned glass substrates should be between 180°C and 220°C. The presence of the transferred layer can be confirmed by a condensation (breath) figure. The glass substrate is then cut to an appropriate size for mounting onto the AFM specimen holder (if applicable). Two component epoxy or cyano-acrylate glues [***caution: cure glue without covering the sample to avoid condensation of reaction by-products on the sample surface***] are recommended for firm attachment. As an alternative to the transferred film the oriented surface of the slider can also be analyzed by AFM [34]. In both cases the orientation direction should be noted by placing a mark on the sample holder disk.

Imaging of PTFE: Contact mode AFM

Standard CM-AFM set-up: *A CM cantilever with a spring constant of ca. 0.3 N/m, or preferably smaller, is inserted into the cantilever holder, the laser is aligned, and the photodiode is moved such that the laser spot is centered. The alignment of the laser must be carried out carefully in order to ensure that the spot is located very close to the end of the cantilever. This can be verified by studying the shape of the reflected laser beam using a piece of paper (Chap. 2).*

The crude approach is carried out stepwise; it is essential that the distance between probe tip and surface is monitored, e.g. by means of an optical eye piece or a CCD camera, to avoid a tip crash. The subsequent computer-controlled approach should start with a small difference voltage in order to minimize the engagement force. This should wait until thermal equilibration has been achieved.

Thermal equilibrium is established by a sufficiently long waiting period. Alternatively, a little trick called "intentional false engagement", will help to thermally equilibrate the set up: Set, the setpoint prior to engaging to a value, which is more negative than the photodiode differential signal, and start the engagement procedure. The piezo will not travel since the setpoint has been reached/has been crossed, however, the piezo will start to scan without actual tip-sample contact. This scanning can be carried out for several hours and helps to warm up the whole AFM to operation temperature. ***CAUTION: This procedure may be risky and may result in***

damage of the piezo scanner in case the computer program crashes, e.g. due to a power outages, which may results in an uncontrolled voltage output from the AFM controller to the scan head. We do not take any responsibility for damages occurring due to this procedure. We note, however, that in 10 years of operation of AFM units we did not have a single piezo scanner damaged owing to this procedure.

Then the engagement procedure is carried out with a standard preset engagement force and a small scan area (e.g. 20 nm × 20 nm) as described in Chap. 2. After successful engagement, the tip is withdrawn once from the surface and the vertical deflection signal of the photodiode is adjusted closer to the specified engagement setpoint. Engagement with this updated setting will result in minimized engagement forces; however, an unintentional false engagement may occur [see Chap. 2]. After successful re-engagement, the operation point is adjusted to minimum imaging forces by reducing the setpoint as far as possible. If the tip suddenly loses track of the surface and the piezo goes out of range, the setpoint has been too negative, so the setpoint must be increased until tip-sample contact is re-established. Subsequently, the imaging forces must be reduced again.

After the sample has been mounted (at an angle of $\sim 15^\circ$ with respect to the slow scan direction), and the crude approach has been carried out, the system is equilibrated for several hours (2–10 h depending on thermal drift). Next, the scan size is stepwise increased, while the gains are optimized accordingly. Images of the transferred PTFE film can be captured at different levels of magnification. For image sizes between ca. 1 and 10 μm a scan rate of several Hz is usually appropriate, for smaller scan sizes the rates may be increased. There should be a fibrillar texture visible along the (marked) orientation direction (see Fig. 3.14 left). The best resolution can be obtained on top of the fibrils. In order to locate the top a stepwise zoom-in procedure can be carried out. The forces should be kept at a minimum at all times.

With a typical scan size of 40×40 nm^2 and smaller, a periodic array of parallel lines becomes visible (Fig. 3.14 right). It may be necessary to re-adjust the gains and scan rate for optimized imaging conditions. Rates of > 10 Hz are advisable and the gains should be set as high as possible *without* obtaining uncontrolled feedback (i.e., oscillations, frequently observed in the vertical direction). If a periodic structure is visualized, three fundamental consistency checks must be performed: (a) does the spacing scale with scan size?, (b) does the structure rotate with changed relative scan angle?; (c) is the spacing independent of scan rate or other parameters? Only if all the checks are positive, the images may correspond to a real surface crystal structure.

The interchain periodicity of 5.6 Å can typically be visualized in all three common CM-AFM imaging modes, height, deflection and friction (latter one shows highest sensitivity with scan angles of 90°, see also Chap. 2) [34–36]. In the literature, some authors have reported that even the helical structure of the PTFE chains can be resolved in some cases [37], however, this is not obvious in the images shown here. For quantitative work, it is essential that the thermal drift is minimized, hence subsequent up and down scans should match and in particular the inclination angles of the periodic structure should be invariant with this capture direction.

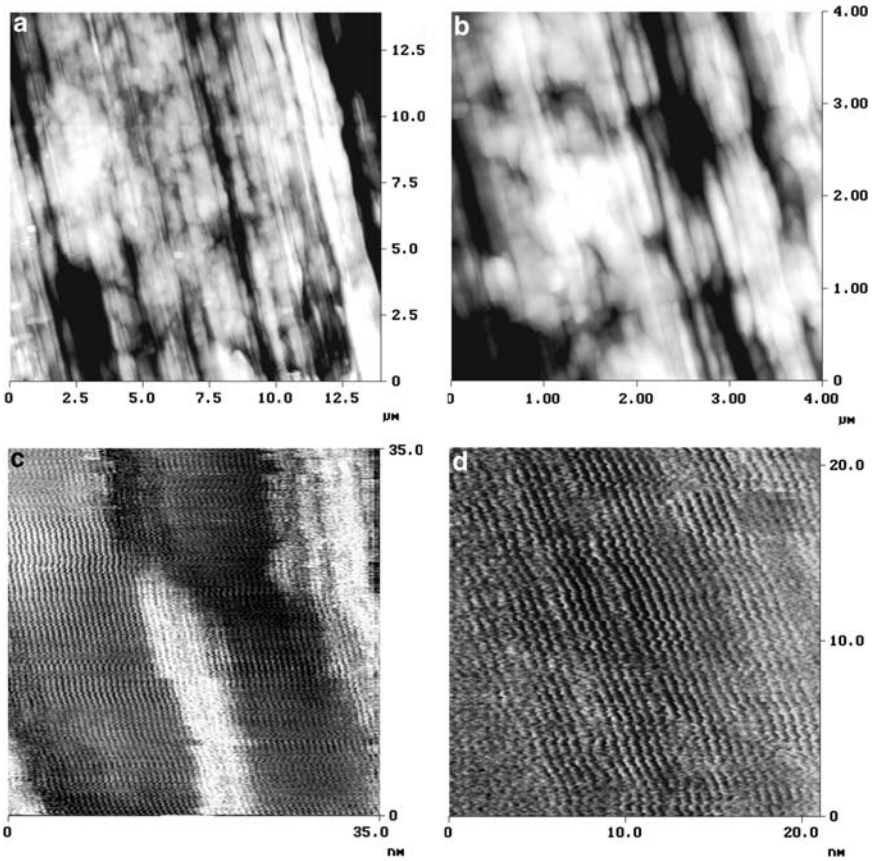

Fig. 3.14 CM-AFM height images (top, *z*-scale: 250 nm) and friction force nanographs (*bottom*) of the surface of a PTFE slider, which has been oriented at a temperature of 220°C, imaged in air. The *parallel lines* correspond to tightly packed PTFE chains oriented in the sliding direction. Reproduced with permission from [34]. Copyright 1998. Elsevier

Hands-on Example 4

Lattice Visualization of Poly(oxy methylene) (POM) by CM-AFM

Sample Preparation: Uniaxial Extension of Extruded Specimens and Cutting

Orientation of commercial POM can be carried out using cylindrical samples which are obtained by extruding POM into a thermostatically controlled form. After the form is filled with the melt, it is removed from the extruder and gradually cooled down in a compression-molding press. Cylindrical specimens are then uniaxially stretched in a tensile test instrument at a temperature of 130°C and a stretching rate

of $\sim$ 5 mm/min. Samples for AFM measurements can be cleaved from these stretched rods either by using a razor blade or preferably by using a microtome with diamond or glass knives. Microtoming (Chap. 2) is preferred over cutting with a razor blade since the alteration of the sample surface and concomitant artifacts are minimized.

Imaging of POM: Contact Mode AFM

The imaging protocol summarized above for PTFE (*hands-on example 3*) remains fully applicable for POM. Imaging at minimized forces F is obviously beneficial to reduce the contact area (which scales in a purely elastic approximation as $F^{2/3}$) and thus to increase lateral resolution, while minimizing sample deformation. The resolution of the exposed POM crystal facet may require a careful adjustment of the relative scan angle, since periodicities are more clearly discernible in a near perpendicular (vertical direction of the image) orientation with respect to the fast scan direction (horizontal direction of the image). Hence, for the two periodicities observed, in, Fig. 3.15, the chain direction (see arrows) should be in an angle of $\sim 45^\circ$ with respect to the fast scan direction in order to visualize *both* periodicities.

In the images shown below, the advantage of investigating uniaxially oriented systems and the necessity to mark the orientation direction precisely are obvious (Fig. 3.15). Since the chain direction is ***not*** a priori known, only the knowledge of this direction enables one to elucidate the structure from an analysis of the periodic features of the AFM images. The quantitative analysis of the structure can be performed by an evaluation of autocorrelation-filtered images or better by analyzing the corresponding 2D FFT (see Chap. 2). In panels (c) and (d) a contact mode AFM height image and the corresponding autocorrelation-filtered image are shown that were acquired on POM crystals obtained by solid state polymerization [39].

3.2.3 Amorphous Polymers

Amorphous polymers can be imaged by AFM in both the glassy state and in the melt. Owing to the occurrence of plastic deformation, CM-AFM is inferior to intermittent contact mode measurements. Using the latter approach, polymers can be imaged in the molten state.

Amorphous polymers are widely applied in many applications, ranging from photoresists for projection lithography to paints and adhesive coatings [40]. For many of these applications, the characterization of defects in thin films and the surface roughness (Chap. 2) are of importance. In general, it is difficult to describe the appearance of amorphous polymer surfaces in AFM images owing to the absence of long-range structural order.

Many examples in the literature show that plastic deformation even of glassy polymers, such as polystyrene, may occur under relatively modest loads in CM-AFM experiments. As summarized in Fig. 3.16. the formation of more or less regularly spaced ridges perpendicular to the fast scan direction is observed. The amplitude of the ridges increases over time (from top to bottom in Fig. 3.16a) and

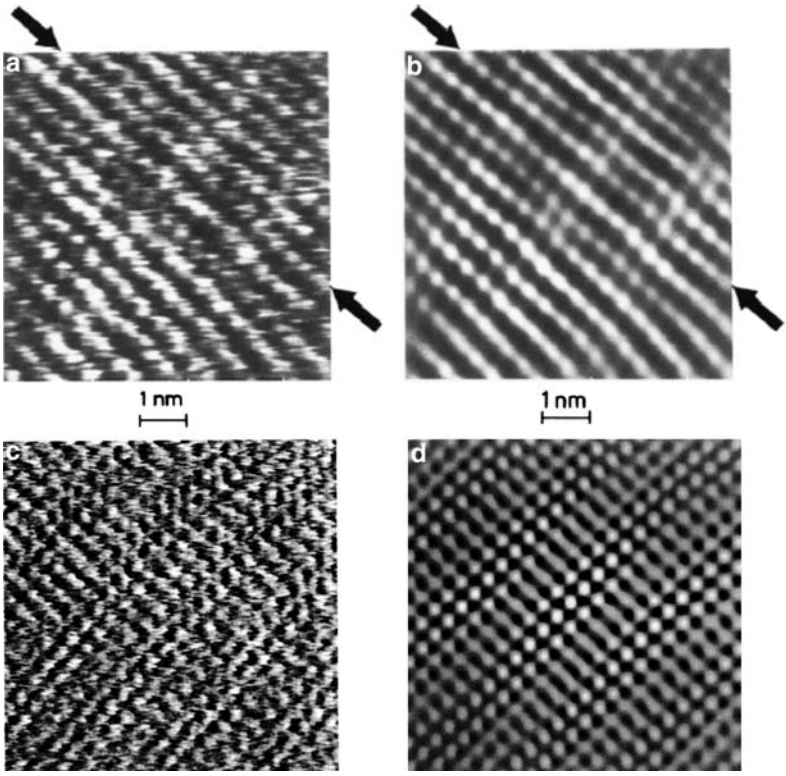

Fig. 3.15 Atomic force microscopy images of poly(oxy methylene) with molecular resolution: (**a**) raw data; (**b**) image obtained from Fourier reconstruction. The arrow indicates the polymer chain direction (image size 7 × 7 nm^2; Reproduced with permission from [38]). Copyright 1992. American Chemical Society. (**c**) AFM height image and (**d**) corresponding autocorrelation-filtered image acquired on POM crystals obtained by solid state polymerization [39]. Reproduced with permission from [39]. Copyright 1994. The Royal Society of Chemistry

it is obvious that instead of analyzing the underlying amorphous polymer, the surface is being modified by the scanning AFM tip (Fig. 3.16b).

Hence it can be concluded that CM-AFM is in many cases a poor choice for imaging the surface morphology of amorphous polymers. Intermittent contact modes, such as tapping mode, are less invasive, since here lateral forces are virtually eliminated and the cantilever-tip assembly is oscillated at relatively high frequencies (on the order of 100 kHz in air). Despite these facts, it must be ensured in *any* experiment that the interaction of the scanned probe and the surface did not lead to a modification of the surface. This can be conveniently done by imaging both a previously scanned and previously unscanned area by zooming out.

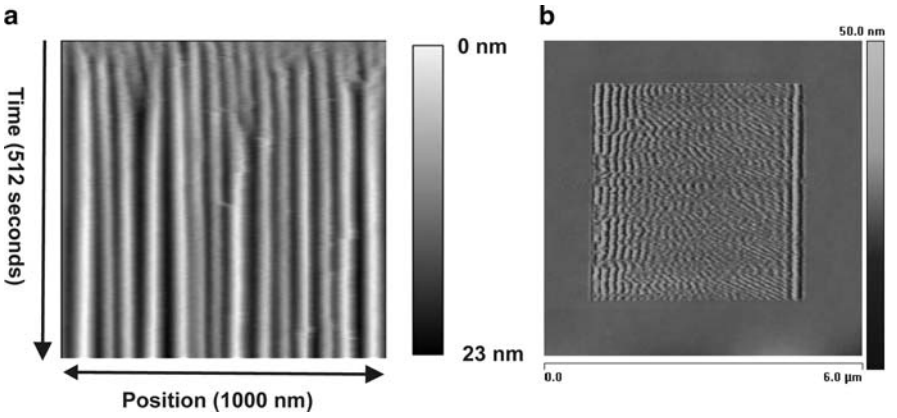

Fig. 3.16 (**a**) Formation of parallel ridges on PS imaged by CM-AFM under a load of 30 nN. The slow scan axis (down scan) was disabled hence the vertical axis corresponds to time. Reproduced with permission from [41]. Copyright 1999. Elsevier. (**b**) Contact mode AFM height image acquired with minimized forces on a PS film scanned previously with high forces

Hands-on Example 5

Imaging of the Surface Morphology of Poly(ethylene terephthalate) (PET) by TM-AFM

Sample Preparation: Quenching from the Melt

Commercial PET films can be melted in a microscopy hot stage ($T_m \sim 260°C$) and are then quenched to liquid nitrogen temperatures by dipping the sample into liquid nitrogen. ***Careful: Do wear suitable safety glasses, lab coat, gloves and further equipment to prevent contact with the liquid nitrogen!*** This procedure efficiently quenches the melt to the amorphous phase ($T_g \sim 75°C$).

TM-AFM Visualization of Amorphous PET Films

The films can be directly glued to the sample holder using double-sided pressure-sensitive adhesive. An equilibration period of ca. 1 h helps to minimize the drift caused by the relaxation of the adhesive. After alignment of the laser and photodiode adjustment (see *hands-on example 1*), the excitation frequency and amplitude are adjusted to ν at 0.85 A_o and 50 nm, respectively. Since the ambient temperature is well below the T_g of PET, we can expect that the surface is not very adhesive, thus this rather small amplitude is sufficient to allow the tip to break away from adhesive interactions with the surface. The engagement procedure and feedback loop adjustment is carried out as described in Chap. 2 and in *hands-on example 1*.

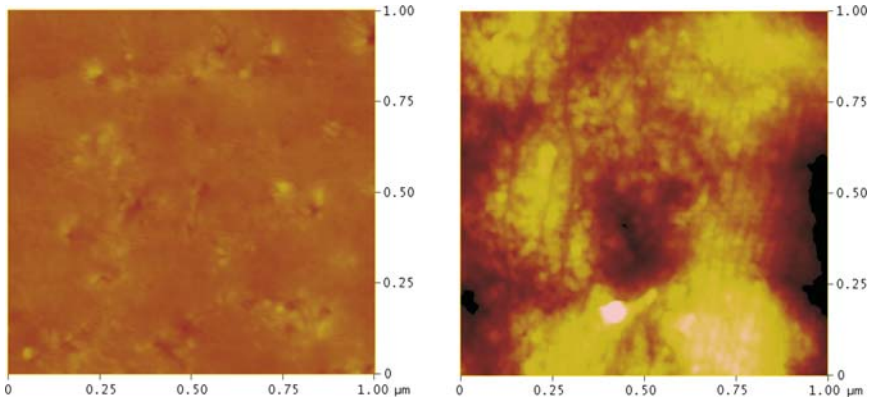

Fig. 3.17 TM-AFM height image of PET quenched from the melt to liquid nitrogen temperature (*left*) and sample crystallized isothermally at 190°C for 10 min (*z* range 14 nm) [42]

A TM-AFM scan of amorphous PET is shown in Fig. 3.17 A in comparison to an isothermally crystallized sample. On the rather smooth surface of the glassy PET, some undulations can be seen. The roughness analysis carried out over the shown scan size of $1.00 \times 1.00\ \mu m^2$ leads to an rms roughness of 0.9 nm (compared to 9.3 nm for the crystallized sample). This former value compares well with rms roughnesses measured on annealed glass or Si wafers (rms roughness: $\sim$ 0.5 nm).

This amorphous sample can be oriented and partially crystallized by uniaxial extension (see Fig. 3.26 for AFM images of the crystal structure of PET at the surface of the observed microfibrils). In contrast to TM-AFM, the surface of the amorphous PET film is modified by CM-AFM, similar to the example of PS discussed above. This observation confirms that CM-AFM imaging of amorphous polymers is not recommended.

Hands-on Example 6

Imaging of Dewetted Perfluoropolyether Lubricant on Hard Disc Surfaces by TM-AFM

Sample Preparation: Dip Coating

Standard computer hard disk surfaces (substrates used in this experiment were industrial hard disk surfaces that have been sputter-coated with nominally 100 Å of hydrogenated amorphous carbon) can be coated by dip coating with nm thin films of perfluoropolyethers, such as Fomblin ZDOL, from solutions in perfluorohexane. For films thicker than several nm dewetting occurs spontaneously over a period of days to weeks due to the autophobic effect [43].

TM-AFM Visualization of Dewetted Drops of Fomblin ZDOL on a HD Surface

The standard settings for tapping mode AFM in air are selected (see *hands-on example 1*). Since the dewetted drops will likely capture the tip, very high amplitudes of the cantilever-tip assembly must be selected ($\sim$ 200 nm). The value of the amplitude can also be adjusted after successful engagement in an area far from a ZDOL drop. For this purpose the setpoint is increased beyond the rms amplitude for free vibration in air (this will result in a retraction of the piezo scanner and an out of contact situation). Now the drive amplitude (energy input into the forced oscillator) can be increased and the setpoint can be lower to some 90% of the new A_0. The gains and scan rates must be carefully adjusted to avoid saw tooth-like oscillations of the feedback loop when the tip is located on top of a drop. Very slow scan rates and high gains help to obtain stable images.

As an example, the TM-AFM image of a ZDOL drop and its cross-section are shown in Fig. 3.18. Considering the sharpness and aspect ratio of the Si tapping mode tip utilized in this experiment, the width can be approximated with some accuracy. However, the height information may not be free of a systematic error: If we recapitulate the imaging mechanism of TM-AFM (constant amplitude image) and in particular the assumption, which allows us to convert the (negative of the) piezo travel in z-direction directly to feature height, we come to the conclusion that the apparent height may be an overestimate. If the drop damps the tip oscillation more than the HD substrate covered with a monolayer of ZDOL, the height of the drop appears too high. On the other hand, the effect of the repulsive forces of the tip, which is tapping on the drop, is unknown. A deformation of the drop as a result of the tapping action may result in an underestimate of the drop height. This example illustrates the necessary careful considerations of contrast mechanisms in the analysis of AFM data.

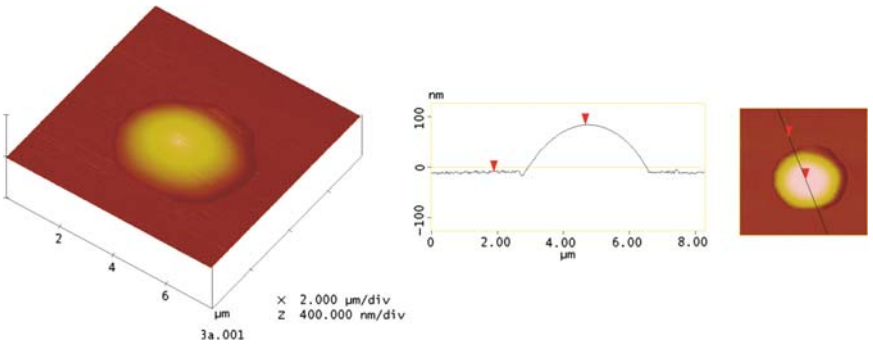

Fig. 3.18 TM-AFM height image (*left*) and cross-section analysis (*right*) of drop of dewetted Fomblin ZDOL on a hard disc surface [44]

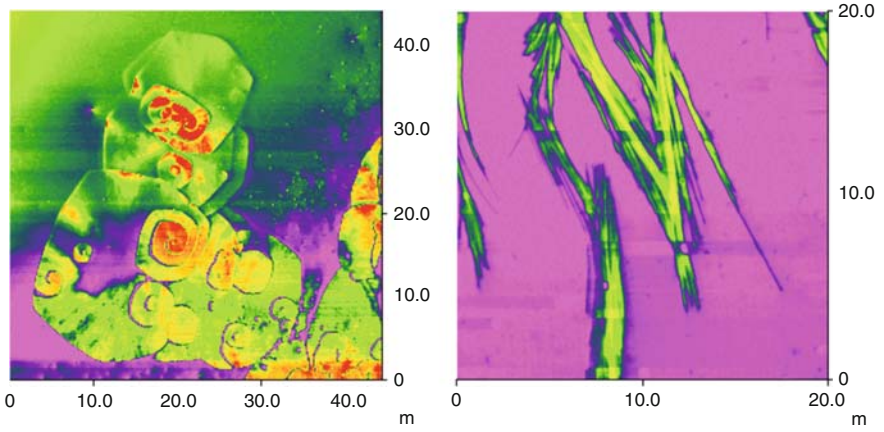

Fig. 3.19 TM-AFM phase images of lamellae in PEO films (film thicknesses *left*: 110 nm, *right*: >2 μm). Reproduced with permission from [45]. Copyright 2003. American Chemical Society

3.2.4 Lamellar Crystals (Crystallized from Solution or Melt)

Semicrystalline polymers may crystallize from solution, as well as from the melt, in the form of chain folded lamellar crystals. The high spatial resolution of AFM enables one to assess lamellar thicknesses from images of these lamellar crystals in edge-on and flat-on orientation. As discussed in this section, images of flat-on oriented lamellae are particularly suitable for a quantitative determination of lamellar thicknesses.

Chain-folded lamellar crystals can be viewed as the intermediate hierarchical level in polymer morphology between macromolecule and higher order multi-crystals aggregates, such as spherulites. Typical lamellar thickness for a given polymer depends on the crystallization temperature and are in a range of typically 10 nm to several tens on nanometers. Owing to the sub-nanometer accuracy of AFM piezo scanners, metrology on this length scale is straightforward. However, the finite size of the AFM probe tip and the concomitant convolution of the AFM data thus obtained must be taken into consideration, when quantitative work is attempted.

In general, it is possible to visualize individual solution-grown lamellae by both CM-AFM and TM-AFM. The same is true for many melt-grown lamellae. Due to the contrast based on the difference in energy dissipation between amorphous and crystalline phases in the TM-AFM phase images, the lamellae can be seen with excellent contrast, and hence, high resolution. Two examples of lamellae of poly (ethylene oxide) (PEO) viewed in flat-on and edge-on projection are shown in Fig. 3.19.

Hands-on Example 7

Solution-Grown Lamellae of POM and PE by CM-AFM

Sample Preparation: Crystallization from Solution

PE and POM lamellar crystals can be prepared by isothermal crystallization following a standard procedure described in the literature [46]: A 0.007% w/w solution of PE in xylene (distilled over Na, filtered through a cellulose membrane filter of 45 µm average pore size) is prepared by dissolving the polymer in boiling solvent. The hot solution is then transferred into a crystallization vessel [47] comprising mica sheets as substrates, immersed in a water bath, which is maintained at the crystallization temperature of 90°C. The mica sheets with the grown crystals are removed from the vessel for further investigation. In the case of POM, the lamellar crystals are obtained from 0.015% (w/w) solution of Delrin (Dupont) in bromo-benzene. The polymer is dissolved in the boiling solvent, and is transferred into the crystallization vessel. The setup is maintained at the crystallization temperature of 136°C in an oil bath. Typical crystallization times are 20 h; the process of retrieving the crystals is the same as for PE.

Imaging of POM and PE Lamellae: Contact Mode AFM

The AFM is set up for a standard CM experiment (*hands-on example 3*). Owing to the size of a typical lamellar crystal, which may exceed micrometers, a large area scanner is selected. After the sample has been mounted, the relative tip position must be adjusted such that a lamellar crystal is within the scan range of the scanner. Following the crude approach, the system is equilibrated for ca. half an hour.

The engagement procedure is carried out with minimized forces as described for *hands-on example 3*. After engagement, the gains and the scan rate must be optimized. While it is advisable to image the lamellae in constant force mode in order to obtain quantitative height information, i.e. lamellar thickness, the error signal of the feedback loop (deflection signal) should also be monitored to help with the adjustment of the gains (for a deflection image of a POM lamella (Fig. 3.20 top).

Faint contrast in the error signal is a good indication for an optimized feedback loop. At the same time the dimension and the habit and possible defects of the crystal, including the fold domain boundaries, are very well visualized. For several polymers including PE [49] and poly(4-methyl-1-pentene) [50], the friction forces measured on the surface of the lamellar crystals obtained from solution are anisotropic (Fig. 3.20 bottom right). This anisotropy is related to the direction of the folds on the crystal surface.

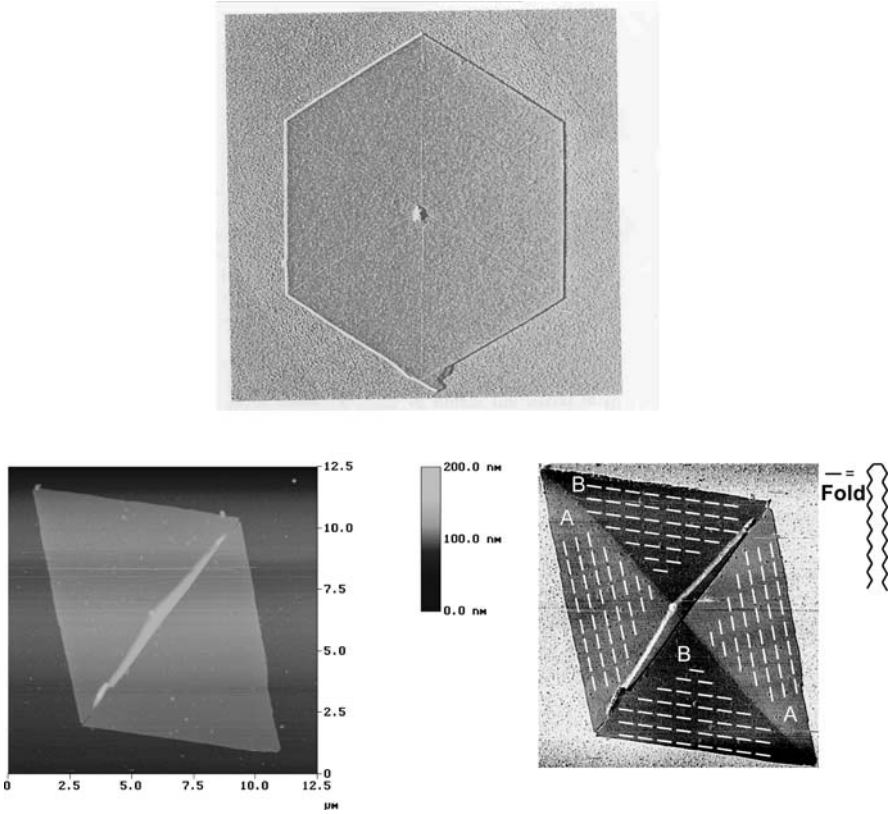

Fig. 3.20 CM-AFM deflection (error signal) image of POM lamella (*top*), height image of a collapsed PE lamella (*bottom left*) and friction image of the same PE crystal including schematic drawing of fold direction (*bottom right*). Reproduced with permission from [46] Copyright 1994. Elsevier and [48]. Copyright 1999. American Chemical Society

Hands-on Example 8

Lamellae in Isotactic Polypropylene (iPP) by TM-AFM

Sample Preparation: Recrystallization from the Melt

Thin films of isotactic or elastomeric [51] polypropylene can be prepared from pellets by melt pressing. For this purpose several iPP or ePP pellets are placed between two sheets of thick aluminum foil and are subjected to pressure in in a hot press (T = 175°C; pressure ca. 1–10 tons). ***Careful: Wear appropriate safety shields and gloves!*** After cooling the sample down to ambient temperature, the foil is unwrapped. If the polymer sticks to the foil, the film can be removed after cooling it down below the glass transition temperature e.g. in liquid nitrogen. ***Careful! For***

safety instructions consult the literature! The film is then placed on a small piece of cleaned cover glass, which is transferred to a microscopy hot stage. Under inert atmosphere (nitrogen or better argon flow) the sample is heated up to 175°C, then cooled to the isothermal crystallization temperature of ca. 120°C–130°C. After holding the sample at this temperature for 6 h the sample is rapidly cooled to below RT.

Imaging of iPP Lamellae in iPP by TM-AFM Phase Imaging and Pulsed Force Mode

Tapping Mode

The PP films on glass are glued to the sample holder using double-sided pressure-sensitive adhesive. The standard TM-AFM procedure (*hands-on example 1*) is followed with v at 0.85 A_o and 150 nm, respectively. The slightly increased amplitude is used in order to ensure sufficient amplitude to overcome the adhesion of the *elastomeric* PP film. For the isotactic samples slightly smaller A_0 is recommended. Prior to engaging, the phase signal is zeroed. The engagement procedure is carried out as described in Chap. 2. After successful engagement the operation point is adjusted to ca. 75% to 65% of A_0. This intermediate tapping condition will ensure stiffness-dominated contrast [52]. Next the scan size is increased stepwise while the gains are optimized accordingly, which corresponds to vanishing contrast in the amplitude image.

Images, such as the one shown in, Fig. 3.21 (left), can be obtained in flat areas of the ePP film. Since intermediate tapping conditions have been chosen (see Chap. 1 and 2 for details), the stiffer phase will appear with a positive phase shift (i.e. bright contrast), while the less stiff phase will appear dark (less positive phase shift). Based on this crude approximation, the elongated *bright* features seen in, Fig. 3.21 can be attributed to edge-on lamellae, while the *dark* matrix can be identified as amorphous phase. A quantitative determination of the lamellar thicknesses of these features

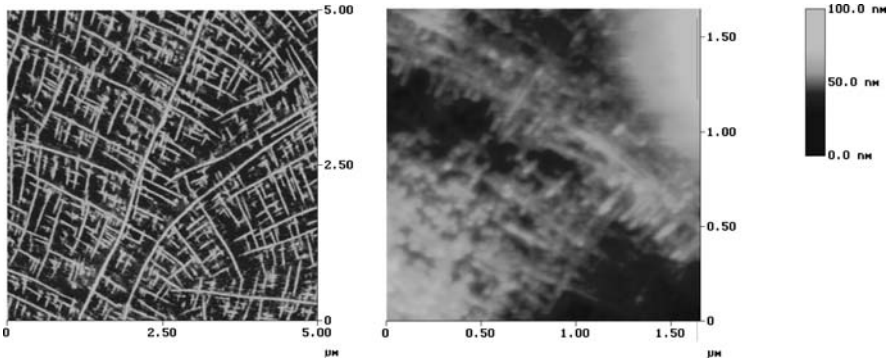

Fig. 3.21 Tapping mode AFM phase image (*left*) and height image (*right*) of cross-hatched lamellae of iPP in elastomeric polypropylene and isotactic PP, respectively. The angles of 80° agree well with the theoretically predicted and experimentally confirmed value [53]. Reproduced with permission from [51]. Copyright 2002. American Chemical Society, and [54]

from high-resolution AFM images is inaccurate due to tip convolution, however, when quantitative deconvolution procedures (Chap. 2) are applied or lamellae are imaged in flat-on projection (see e.g. Fig. 3.20), this measurement is feasible. A qualitatively similar observation can be made for iPP specimens (Fig. 3.21 right). In the height image cross-hatched lamellae at the free surface of the film are clearly identified (compare also CM-AFM data in Fig. 3.30).

Pulsed Force Mode

In the so-called "pulsed force mode" AFM technique developed by Marti and coworkers [56], the sample is modulated sinusoidally (with a frequency ~ 1 kHz) during a conventional contact mode AFM scan. The amplitude of this forced oscillation is chosen large enough for the tip to overcome the adhesive tip-sample interactions. Hence the tip contacts, indents, and breaks free from the surface with a frequency of $\sim$ 1 kHz during scanning (Fig. 3.22). Instead of recording the complete f-d curve, only the four points are captured, i.e. the baseline, the maximum repulsive force, the maximum adhesion force and a point that can be used with the maximum repulsive force to define the slope in the loading regime as a measure of stiffness, respectively. Thus, the simultaneous mapping of sample topography, pull-off forces *and* stiffness at useful scan rates becomes possible.

For pulsed force mode imaging of the PP sample, a modulation frequency in the range of 800 Hz is selected. The cantilever oscillations are adjusted such that the adhesive interactions between tip and surface are overcome, as monitored using an oscilloscope. The modulation must clearly show the snap-off of the tip. Next the four markers are set as shown in Fig. 3.22.

The images shown in, Fig. 3.23 display the simultaneously captured height (left) and stiffness images. The (cross-hatched) lamellae are visualized in both modes.

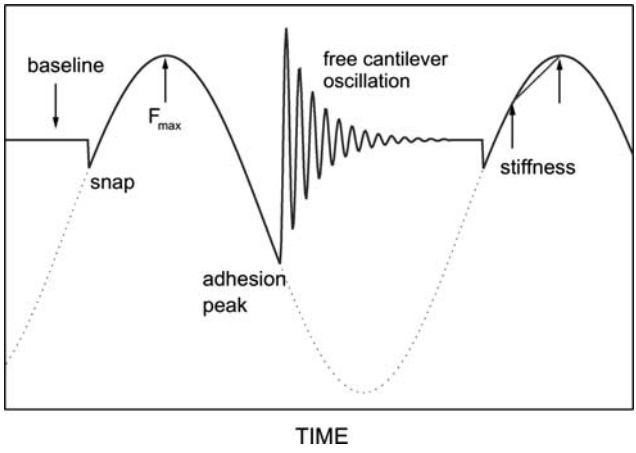

Fig. 3.22 Schematic of the force signal in pulsed force mode AFM. Reproduced with permission from [57]. Copyright 2004. Elsevier

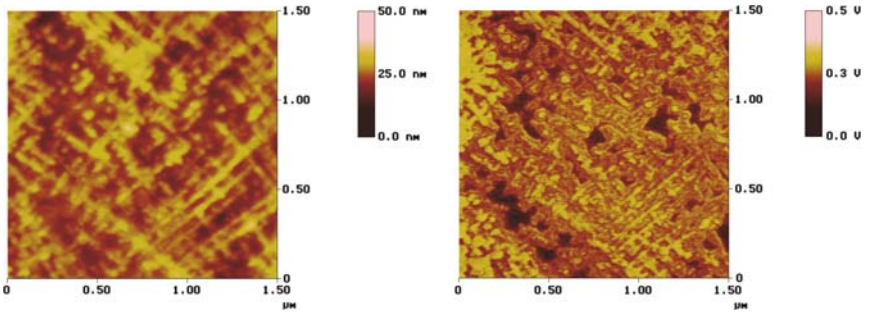

Fig. 3.23 Pulsed force mode AFM height image (*left*) and stiffness image (*right*) of cross-hatched lamellae of iPP. [58]

In addition, the stiffness image reveals areas of different (intermediate) stiffness in between the lamellae.

Hands-on Example 9

Lamellae in Spin-Coated Films of Poly(ethylene oxide) (PEO) by TM-AFM

Sample Preparation: Spin-Coating

Thin films of PEO can be prepared by spin coating filtered (mesh size ca. 0.2 µm) solutions of PEO in chloroform onto precleaned silicon wafers or glass cover slips using a conventional spin-coater (typical concentrations of 1.0–20.0 mg/ml and typical spinning speeds of 2,000–3,000 rpm for 1 min are recommended for film thicknesses between ca. 15 and 300 nm). The cleaning of silicon wafers can be carried out in a plasma cleaner or using oxidizing solutions [59]. The films should be dried for at least 24 h in vacuum to remove residual solvent.

TM-AFM on PEO Lamellae in Spin-Coated Films

The PEO films supported on Si or glass are glued to the sample holder using presssure-sensitive adhesive. The standard TM-AFM procedures are followed (*hands-on example 1*). The excitation frequency and amplitude are adjusted to v at 0.85 A_0 and 130 nm, respectively. The engagement procedure is carried out as described in Chap. 2. After successful engagement, the operation point is adjusted to ca. 75% of A_0. Images of the PEO films can be captured at different scan sizes. For image sizes between ca. 1 and 10 µm a scan rate of 1.0 Hz is usually appropriate, for larger scan the rate should be decreased to 0.5 Hz or below. It is essential to check the quality of the feedback loop by analyzing the amplitude image. Here minimized contrast is beneficial.

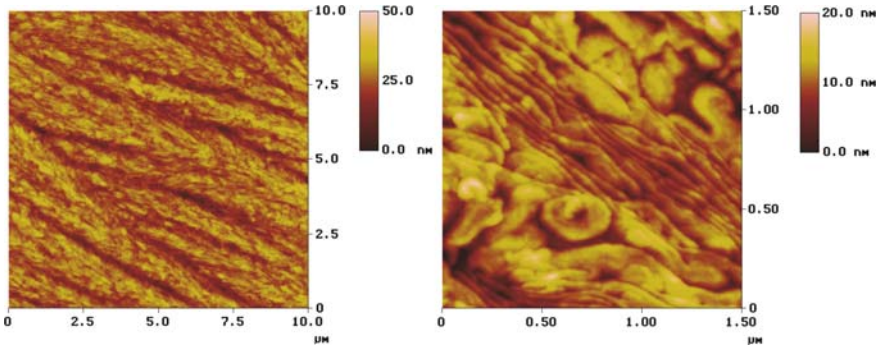

Fig. 3.24 TM-AFM height images of large scale morphology (*left*) and flat on lamellae (*right*) spincoated PEO films on silicon [60]

Two typical TM-AFM height images with different scan sizes are shown in Fig. 3.24. While the low magnification images shows details of a large spherulite with sheaf-like morphology, the high magnification image allows one to differentiate individual lamellae in edge-on and flat-on projection, as well as a growth spiral, which is due to a screw dislocation.

3.2.5 Extended Chain Crystals and Shish-Kebob Structures

Extended chain crystals can be obtained by crystallization under high pressures or under uniaxial extension. So-called shish-kebob structures are frequently observed when crystallizing polymers under orientation, e.g. in stirred solutions and polymer processing from the melt. Similar to lamellae and (micro) fibrils treated in previous chapters, these structures can be routinely visualized and analyzed by AFM.

Extended chain crystals have been implicitly included in the treatment on lattice visualization of crystallized homopolymers. While crystals obtained by crystallization under extension may be imperfect compared to the classical examples of high-pressure crystallization [61], these examples are closer to many applications. The morphology of fibrils and microfibrils of PTFE has been analyzed by CM-AFM (Fig. 3.14). A second example discussed below refers to cold-drawn PET (Fig. 3.17), which is crystallized in extended chain crystals.

Similar to extended chain crystals, the shish-kebob morphology is not observed in samples, which have been subjected to quiescent crystallization conditions. We introduce several examples already in this chapter in order to present a complete cross-section of all levels of structural hierarchy in polymers. Further examples related to oriented crystallization of polymers in practical applications will be the focus of Sect. 3.5.

The imaging of extended chain crystals, as well as the related shish-kebob structures, can be carried out in CM-AFM and TM-AFM. CM-AFM is the preferred method if the lattice structure is to be analyzed in the same experiment; otherwise

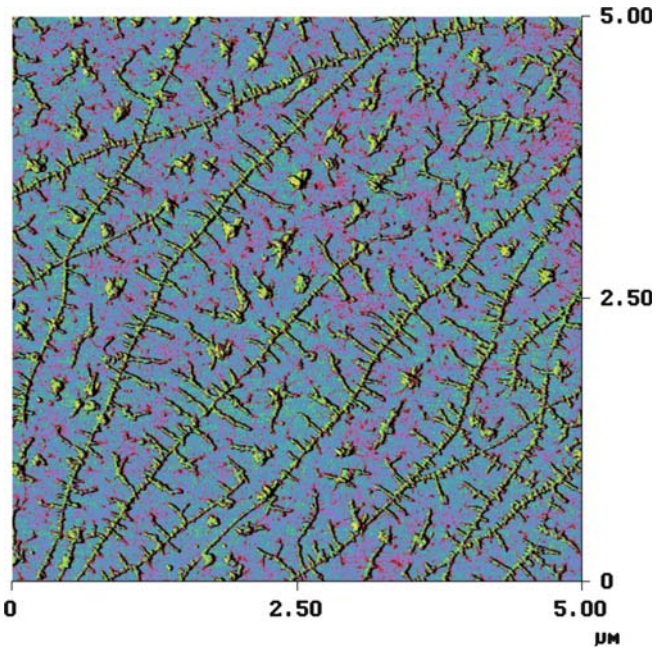

Fig. 3.25 TM-AFM phase image of PP shish-kebob crystals on silicon [62]

TM-AFM is superior due to reduced sample deformation and excellent contrast between amorphous phase and crystal phase in the TM phase images. An example of a, shish-kebob morphology is observed in partially dewetted ultrathin films of polypropylene derivatives grafted onto silicon (Fig. 3.25).

Hands-on Example 10

CM-AFM on Extended Chain Crystals of Cold-Drawn PET

Sample Preparation: Cold Drawing

PET films with a thermal pre-treatment can be uniaxially drawn in a standard tensile tester to draw ratios of 2.0 to 4.0. The observations can be performed at the free surface of these specimens.

CM-AFM on Cold-Drawn PET

The CM-AFM experiment must be carried out with the lowest possible force to avoid plastic deformation of the PET specimens. Therefore a cantilever with a spring constant < 0.1 N/m is advisable. Further, the imaging forces may be reduced by imaging in an atmosphere of dry nitrogen or under a suitable liquid, e.g. ethanol. Here we will focus on imaging in dry nitrogen (glovebox or gas purge hood work equally well, see Chap. 2).

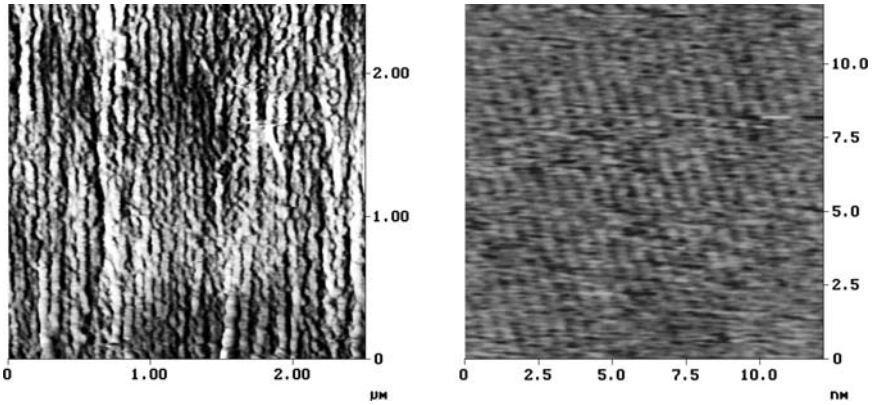

Fig. 3.26 CM-AFM deflection (*left*) and height (*right*) images of cold-drawn PET at different levels of magnification (draw ratio was 2.0). [42]

The AFM is set up for a standard CM experiment (see *hands-on example 3*). The very soft CM cantilever is inserted into the cantilever holder, the laser is aligned, and the photodiode is moved such that the laser spot is centered. Following the crude approach, the system is equilibrated for several hours.

The CM-AFM height image shown in, Fig. 3.26 (left), shows the typical fiber-type morphology of the drawn PET. The surface exposed nanofibrils with a typical diameter of 100 nm for samples with a draw ratio of $\lambda = 2$ and 65 nm for specimens with a draw ratio of $\lambda = 4$. At this modest draw ratio of 2.0, the orientation of the fibrils in the drawing direction is already clearly discernible, though far from being perfect. Upon zooming in and careful re-adjustment of the scan rate (to higher rates, e.g. > 15 Hz) and the gains (to higher values), it is possible to detect patches of PET extended chain crystals (Fig. 3.26 right). The parallel lines correspond to tightly packed PET chains in the typical structure of PET and thus the impact of the drawing can be visualized on a molecular level. The (bc) crystal facet of the known triclinic crystal structure can thus be imaged with molecular (lattice) resolution at the free surface of the films (repeat distance of 5.8 Å in the chain perpendicular direction).

Hands-on Example 11

TM-AFM on Shish-Kebob Morphology in Drawn Polyethylene Copolymers

Sample Preparation: Drawing

Polyethylene-co-octene (DOW) is pressed into films using a hot press ($T = 140°C$, load of $\sim$ 1 ton). The film is stretched after quenching to room temperature and fixed by careful attachment to the AFM sample holder puck by using pressure sensitive adhesive.

TM-AFM on Drawn PE Copolymer

The TM-AFM experiment is carried out with relatively high amplitude since the elastomeric PE-based copolymer is adhesive. Prior to engaging (set-up according to standard TM-AFM procedure in *hands-on example 1*) the phase signal is zeroed. The engagement procedure is carried out as described in Chap. 2. After successful engagement, the operation point is adjusted to ca. 75% to 65% of A_0. This intermediate tapping condition will ensure energy dissipation-dominated contrast [52]. Similar to all other experiments the scan size is stepwise increased, while the gains are optimized as described.

Sporadically, the shish-kebob structures, such as the one shown in Fig. 3.27 can be found. Since intermediate tapping conditions have been chosen (see Chap. 2 for details), the less dissipative phase will appear with a positive phase shift (i.e. bright contrast), while the more dissipative phase will appear dark (less positive phase shift). Clearly the relative contrast of the (crystalline) shish-kebob seen in the TM-AFM phase image is consistent with the simplified theory.

3.2.6 Hedrites and Spherulites

Many polymers crystallize in the form of spherulites. Hedrites, as early stages of development of spherulites, can reveal information about the growth and development of spherulites in time. As shown below, the morphological analysis is often

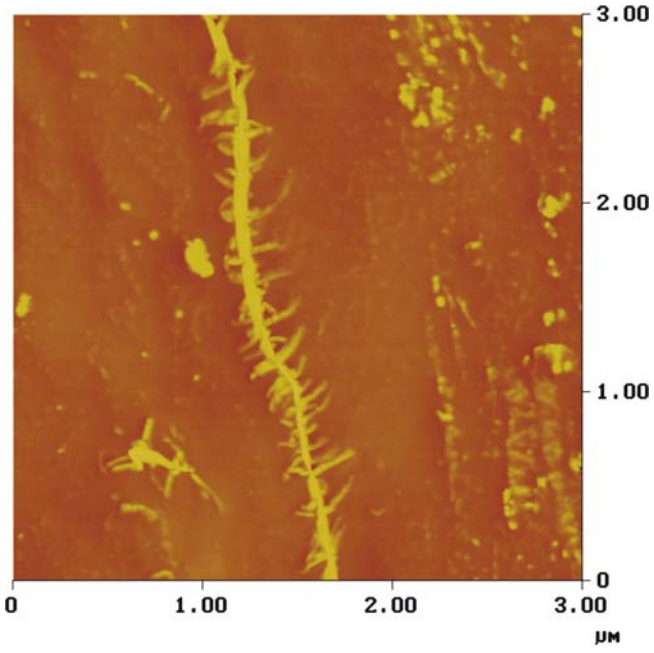

Fig. 3.27 TM-AFM phase image of shish kebob morphology in oriented elastomeric PE [58]

feasible at the free surface of melt-crystallized films; however, also permanganate-etched films of PP can be studied to reveal information in the depth of a specimen.

For the investigation of spherulites and hedrites, but also more generally for morphological investigations of polymers, CM-AFM can be applied for a limited number of samples only. As discussed in before, shear forces between the tip and the soft polymer surface often result in large contact areas, deformation of the material, or even plastic deformation or damage of the specimen. Thus, CM-AFM is usually unsuitable for imaging elastomeric and other low crystallinity materials. If CM-AFM is used, the cantilever spring constant should be chosen as low as possible and forces should be reduced as far as possible by properly adjusting the setpoint. Capillary forces may limit the minimum stable imaging force. In numerous cases imaging in liquid was found to be beneficial.

Hands-on Example 12

Sample Preparation: Melt Crystallization Followed by Etching

Dehydrated calcium pimelate is added (between 0.01 and 0.5 wt %) as the nucleating agent to isotactic polypropylene to produce the β modification of iPP [63]. Following molding between two glass plates at 220°C thin films of the polymer are isothermally crystallized at 140°C–143°C in a microscopy hot stage. After the hedritic structures develop, the samples are quenched to room temperature. Prior to AFM examination, the specimens are etched with a 1% solution of potassium permanganate in a mixture of sulfuric and orthophosphoric acid [64, 65]. This procedure is described in detail in the literature (*Caution: consult the literature for safety precautions!*) and helps to remove preferentially amorphous phase of PP [64]. Thus, unlike in the many other examples discussed in Sect. 3.2, here the interior of a specimen is analyzed after its exposure.

Contact Mode AFM on β-iPP

The etched iPP film is glued to the sample holder using pressure-sensitive adhesive and left for several hours to relax. The standard CM-AFM procedure (*hands-on example 3*) is applied. After successful engagement with minimized forces, the operation point is adjusted to minimum imaging forces with the help of force-distance plots. Next the scan size is stepwise increased while the gains are optimized accordingly. Images of the iPP film can be captured at different levels of magnification. For image sizes between ca. 1 and 10 μm a scan rate of several Hz is usually appropriate. Since the film may be quite rough overall, the scan rate must be reduced when the scan sizes exceed 10 μm in order to protect the probe tip. Figure 3.28 shows a compilation of CM-AFM data acquired on etched β-iPP samples. In particular in panels a and b, the different projections of hedrites showing views observed from the y axis and from the z axis near the center of hedrites crystallized at 140°C, respectively, can be discerned.

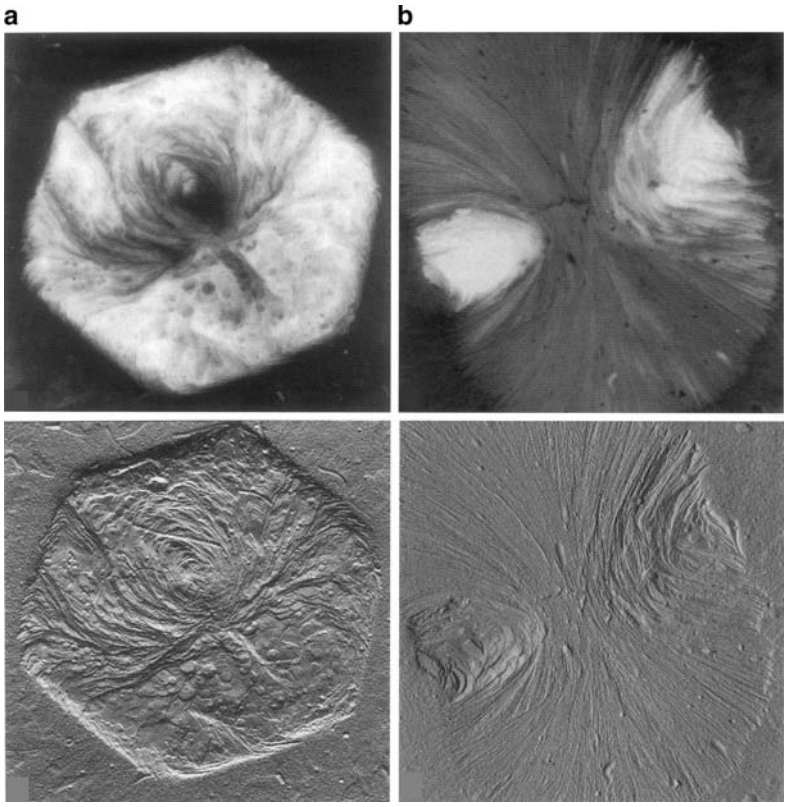

Fig. 3.28 CM-AFM height (top) and deflection (bottom) images showing 6 views observed (a) from the y axis and (b) from the z axis near the center of hedrites crystallized at 140°C. Reprinted with permission of John Wiley & Sons Inc. from [66]. Copyright 2000. John Wiley & Sons Inc.

The determination of lamellar thicknesses of the β-modification of isotactic polypropylene (iPP) by CM-AFM is shown in Fig. 3.29 (c,d). Assuming that the differences in compliance of the lamella and the surrounding phase are negligible, the step height as measured corresponds to the lamellar thickness, or multiples thereof, when lamellae are imaged in flat-on projection (Fig. 3.29, top). Care must be taken to utilize a first order planefit and a flattening of no more than 0-th order. As mentioned, the measurement of lamellar thicknesses from images of lamellar crystals in edge-on projection are complicated due to the need to correct for tip convolution (Fig. 3.29, bottom). As discussed in Chap. 2, this can be achieved by deconvolution of the images. Mean values for lamellar thicknesses can be estimated based on the statistical analysis of numerous images. The histograms for the measured lamellar thicknesses in these β-iPP films are also shown in Fig. 3.29 (right).

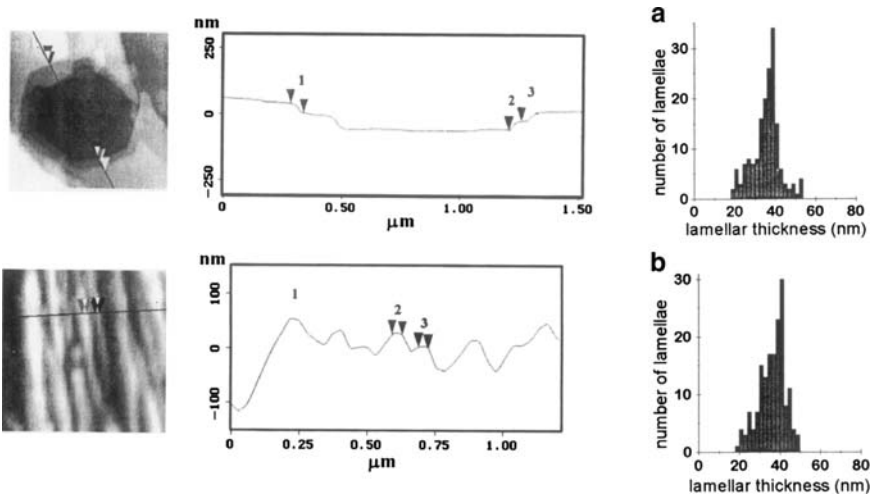

Fig. 3.29 Cross-sectional analyses of β-iPP lamellae (crystallized isothermally in a thick film at 140°C for 1 h and subsequently exposed to $KMnO_4$ etching) viewed in (**a**) flat-on projection (*top*) and (**b**) in edge-on projection (*bottom*) together with corresponding section analyses and histograms of lamellar thicknesses. With kind permission from Springer Science+Business Media from [65]. Copyright (1998).. Springer-Verlag

Hands-on Example 13

CM-AFM on Thin Films of Isotactic Polypropylene (iPP): α-iPP

Melt-Pressing

Thin films of iPP can be prepared by pressing several PP pellets (e.g. commercial Ziegler Natta or metallocene iPP) between two sheets of thick aluminum foil in a hot press ($T = 175°C$; pressure ca. 1–10 tons; ***for safety instructions please consult the hot press manual!***) followed by isothermal crystallization as described in *hands-on example 8*.

Contact Mode AFM of PP Spherulites

The AFM protocol is identical to the experiment on the β-modification (Sect. 3.2.6 A).

Two typical images which depict a spherulite and the dense cross-hatched morphology typical of the α–modification of iPP are shown in Fig. 3.30 (see also Fig. 3.21 for a comparison with TM-AFM data). The presence of cross-hatching is often noted in all common CM-AFM modes, namely height, deflection (error signal), and also friction modes.

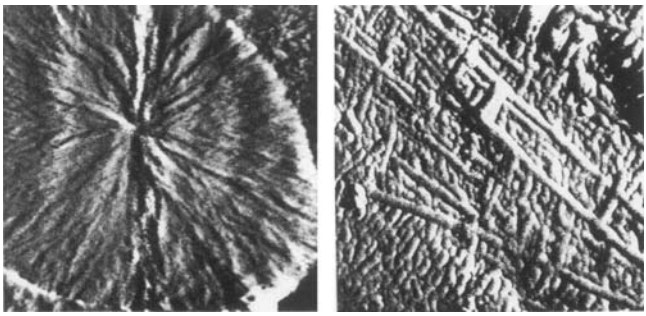

Fig. 3.30 CM-AFM deflection images of spherulite (*left*) and cross-hatched morphology (*right*) found at the surface of melt-crystallized iPP films (image sizes, 15 and 1.0 μm, respectively). With kind permission from Springer Science+Business Media from [55]. Copyright (1993). Springer-Verlag

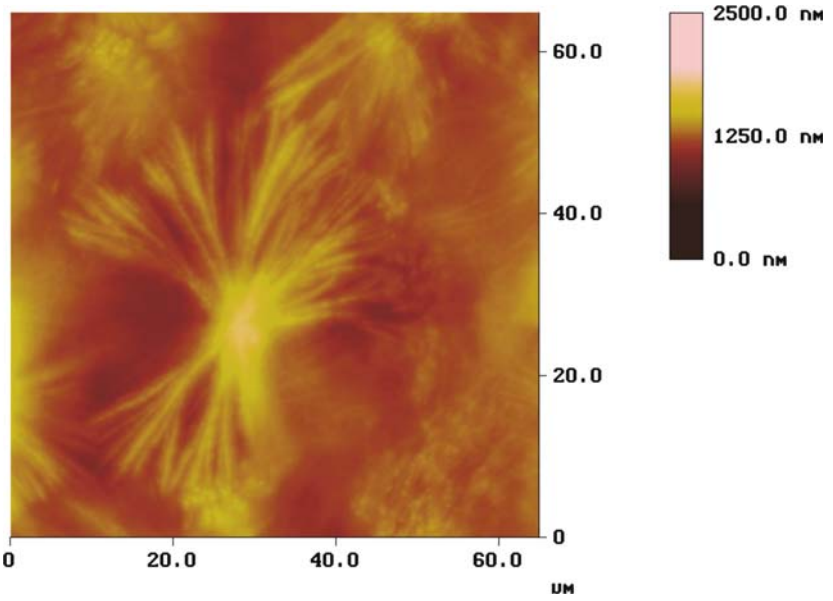

Fig. 3.31 TM-AFM images of unfractionated ePP bulk film crystallized isothermally at 120°C (*left*: height image, z scale from dark to bright 3.5 μm; *right*: phase image). Reproduced from [51] with permission. Copyright 2002. American Chemical Society

Tapping Mode AFM of PP Hedrite

Using the standard TM-AFM procedures (*hands-on example 1*), the same (or similar) specimens PP can be investigated. In Fig. 3.31 we, show images obtained at the free surface of isothermally crystallized ePP [51].

3.3 Biopolymers

3.3.1 Imaging of Biological and Biopolymer Specimens Under Liquid

The imaging of biologically relevant polymers must be performed in most cases under liquids in order to reduce the forces between the scanned probe tip and the sample surface or, more importantly, to ensure that the polymers of interest retain their integrity, shape, and biological function when studied by AFM approaches. This Chapter will provide an introduction to AFM operation under liquid and will elucidate the peculiarities of force microscopy operation in conjunction with a liquid cell. Finally, ex situ and in situ studies of biopolymeric specimens will be highlighted.

Biopolymers can be studied by AFM-related approaches under various conditions [67–74]. While the conventional study of surface-fixated biopolymers in air using contact or tapping mode AFM is feasible in various cases (for a higher order assembly, i.e. a chromosome, see Figure 3.32), AFM operation under liquid has numerous advantages. These advantages will be discussed in detail below. It is important to note already at this point for the practitioner that the operation under liquids is more difficult than operation in air under ambient conditions. Therefore, additional training and experience with the liquid cell are necessary to obtain meaningful data with similar ease as in air.

Studies on biopolymers and biological specimens in air are adequate if their integrity is preserved upon drying and if the corresponding samples are robust enough to withstand the normal forces, and in contact mode AFM also the shear forces, associated with the scanning. While for instance, lipid bilayers may collapse upon drying, polymerized bilayers possess improved stability and imaging in air using contact mode and tapping mode AFM is feasible [76]. Similarly,

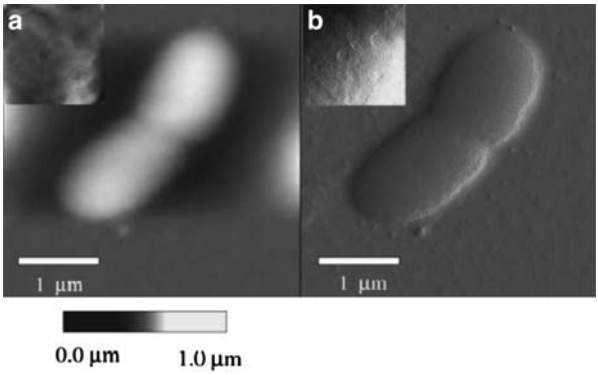

Fig. 3.32 (**a**) Tapping mode AFM image of an untreated native chromosome in air. The surface of the chromosome is smooth with visible centromeres. The inset figures are an enlarged part of the chromosome. Reproduced with permission from [75]. Copyright 2002. Elsevier

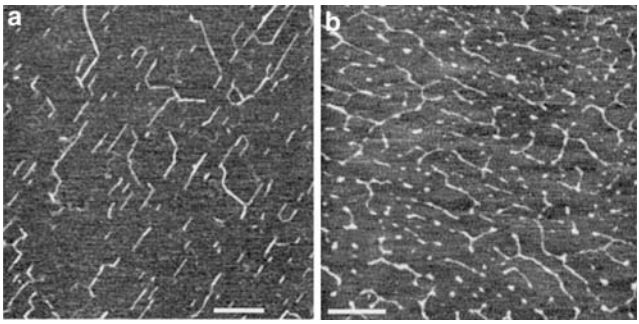

Fig. 3.33 Intermittent contact mode AFM height images acquired in air of purified κ-carrageenan (*left*) and τ-carrageenan (*right*) diluted in water and prepared by aerosol spray deposition (scale bars 200 nm). Reproduced with permission from [78]. Copyright 1999. Elsevier

polysaccharides, such as cellulose [77] or carrageenan [78] (Fig. 3.33), can be deposited onto solid supports and are amenable to AFM investigations under ambient conditions.

As mentioned, in AFM studies of biopolymers the use of a suitable liquid cell is indispensable in many cases. On the one hand, biopolymers or even living cells may be studied *in vitro* under natural conditions (pH, temperature, salt, etc.) and variations of these conditions is often possible during the experiment [71–74], on the other hand excessive normal and lateral forces can be reduced to a minimum, which still allows one to image and study the biopolymeric samples non-invasively [79–81]. Hence we will first provide an introduction to the use of the mentioned liquid cells and then treat contact mode AFM and intermittent contact mode AFM operation under liquid. The procedures and operation principles discussed can of course be readily extended to the study of non-biological polymers (see e.g. Chap. 4).

3.3.1.1 AFM Under Liquid

The typical design of a liquid cell for an AFM with stationary cantilever-tip assembly is shown in Fig. 3.34. A transparent holder made, e.g., of quartz or PMMA replaces the conventional cantilever holder. The liquid fills the indicated volume between the holder and the sample surface, thus, the entire cantilever-tip assembly, including the cantilever chip, is immersed in the liquid. There are two ways of operation: First, it is possible to seal off the mentioned volume by means of a flexible rubber ring (Fig. 3.34); in many cases, it is possible for, e.g., aqueous solution to work *without* the rubber rings (Fig. 3.37) [82–84].

For CM-AFM, soft cantilevers with spring constants between 0.02 N/m and 0.3 N/m are frequently used in liquids, while for intermittent contact modes various possibilities exist. Many researchers have successfully employed contact mode cantilevers (triangular and preferably single beam) with a spring constant between

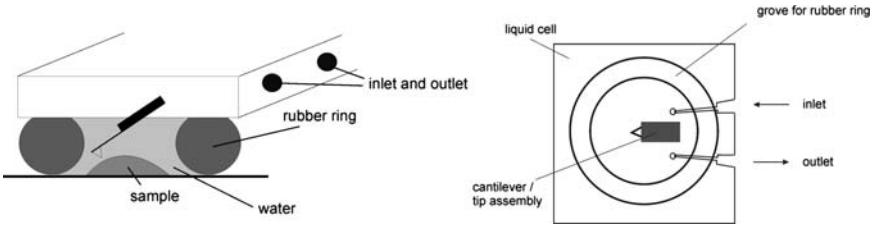

Fig. 3.34 Schematic of AFM liquid cell for AFM with stationary cantilever-tip assembly in side view with rubber ring (*left*) and top view (*right*)

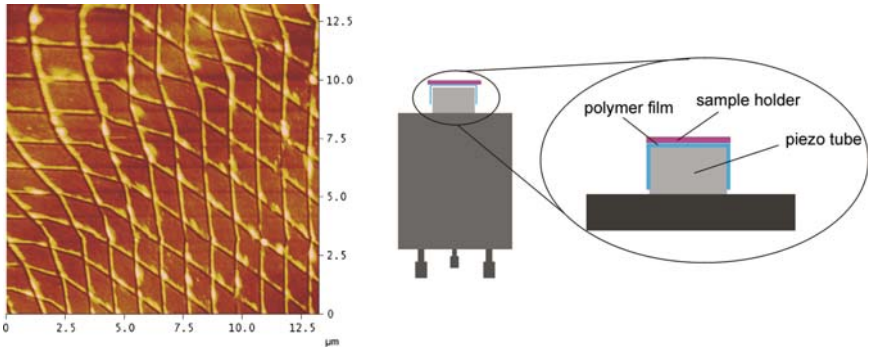

Fig. 3.35 (**a**) AFM height image recorded with a damaged AFM scanner on a calibration grid (*left*); (**b**) schematic of protective coating for piezo scanner (*right*)

0.3 N/m and few N/m, while typical tapping mode AFM probes (k = 20–80 N/m) have also been used with success.

Points of Special Concern and Caution

Before we start to explain the set-up and operation of AFM in liquid environment, we must advise the users to take some important points into consideration. In addition to all the safety precautions and operation procedures of your AFM supplier,[1] some general notes of caution apply to virtually all equipment:

Care must be taken to not spill any liquid onto the piezo transducer since this can cause a local short circuit and thus terminal damage to the piezo (for a typical image recorded with a damaged piezo transducer see Fig. 3.35, left[2]). In order to protect the piezo from accidental liquid spillage, the top of the scanner tube can be wrapped into a very thin polymer film (e.g. Parafilm, American National Can, Neenah, WI). For this purpose, the film is pre-stretched and then gently wrapped over the tube end (see schematic Fig. 3.35, right). It is also clear that the sample size should

[1]For safety precautions see your suppliers manual and warnings.

[2]This piezo transducer was damaged by accidental feed with high uncontrolled voltages, the resulting damage and its manifestation in AFM scans, however, is very similar.

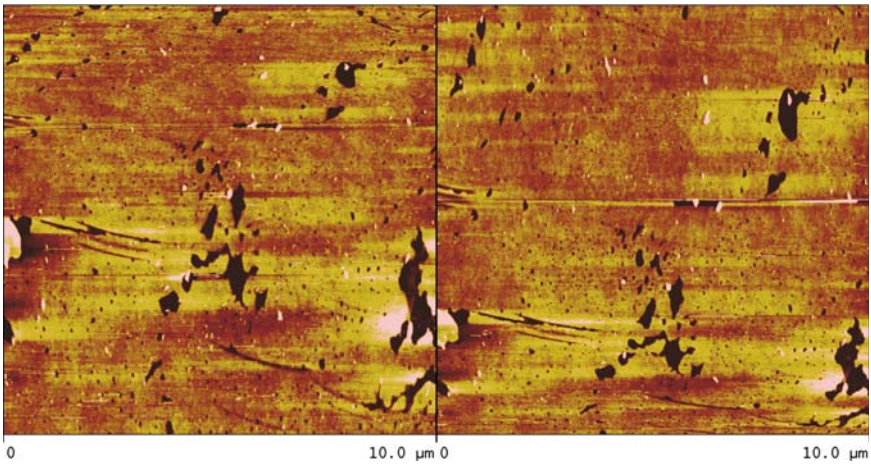

Fig. 3.36 Subsequently captured AFM height images (z-scale 10 nm; *left*: up-scan; *right*: down-scan) of a defective phospholipid bilayer on glass mounted with double-sided pressure sensitive adhesive on the sample holder recorded in water. The distortions of the images due to shear of the adhesive are obvious. Flexing of an improperly mounted rubber ring yields very similar distortions [85]

exceed the lateral size of the rubber ring by several millimeters at least to prevent liquid spillage.

Another requirement for a successful experiment is the secure attachment of the sample to the specimen holder, especially when a rubber ring is used. In this latter case the sample *must* be glued with epoxy (or other fast curing glue, see Chap. 2) to the sample holder puck. Typical double-sided pressure sensitive adhesive does *not* work well. Since the rubber ring is pressed against the sample and the sample moves while scanning, the sample holder-sample connection must be tight. If this connection is not tight, as in the case of most pressure sensitive adhesives, the sample will *not* follow the lateral movements of the piezo transducer correctly. The lightly cross-linked polymer in the adhesive behaves viscoelastically and will constantly be deformed. The result is a distorted image with erroneous distances. In Fig. 3.36. the disparity of subsequently captured up- and down-scans is obvious. While the up-scan shows an apparent elongation of the image in the vertical direction at the bottom and a compressed image in the same direction on the top, the down-scan shows the opposite artifact. As a consequence, the lateral dimensions, as well as the orientation of various defects present in the phospholipid bilayer imaged here differ widely and remain unknown. As for imaging in ambient conditions, up- and down-scans must match in order to obtain reliable metrology data.

3.3.1.2 Mounting the Liquid Cell (Dry Sample)

When the liquid cell is mounted onto a dry sample, the usual protocol for contact or tapping mode AFM can be followed (see Chap. 2 and Sect. 3.2). The laser is aligned

and the tip–sample distance is carefully reduced without bringing the two surfaces too close.

Mounting of Liquid Cell with Rubber Ring

Following the completion of the crude approach procedure, i.e., when the set-up would be ready for engagement in air, the optical head is removed vertically and the rubber ring is carefully placed on the sample. The location should coincide with the location of the groove on the liquid cell into which the rubber ring will be inserted subsequently. Then the optical head is carefully lowered exactly vertically onto the rubber ring such that it (a) stays horizontally leveled at all times, (b) that it does not wiggle, and (c) that the rubber rings slips partially into the groove simultaneously around the complete perimeter. Finally, the optical head is secured and the inlet and outlet tubings are attached.

If the head is not horizontal at all times or wiggles, the rubber ring is pushed too much into the groove on one hand side. This will lead to a leakage in most cases. In addition, the ring (or the glue in case it is not a thermoset) may be sheared and will lead to a pronounced drift due to relaxation of the cross-linked material (compare also Fig. 3.36).

After an equilibration period of several minutes to (preferably) hours, in which the rubber ring and other compliant parts of the system can relax, the cell is filled via a syringe or an external pump with liquid through the attached tubing. Once the cell is filled the tubing is clamped close to the cell to prevent liquid circulation and/or evaporation. Now the whole assembly must be inspected to verify that no leakage of the cell has occurred[3] and that no air bubble may interfere with the measurement (see below). Finally, the reflected laser beam must be directed onto the photodiode (due to refraction the path of the light is altered) by adjusting the mirror. When the differential photodiode signal(s) show stable readings, the experiment can be started. This may take several minutes to even hours, depending on the relaxation and temperature equilibration in the cell [86].

The filling of the cell requires some training, since the filling velocity must be carefully tuned. If the cell is filled too rapidly, the cantilever may be damaged, displaced or a leakage may occur; if the cell is filled too slowly, it is likely that air bubbles are trapped inside. This latter problem must be avoided. For this purpose, the cell, as well as the cantilever incl. chip, must be thoroughly cleaned prior to use (air bubbles frequently adhere to hydrophobic surfaces) and the solvent introduced through the tubing must be degassed (ultrasound bath) and free of visible bubbles. A useful trick is often to place a drop of solution onto the sample *prior to* mounting the liquid cell/optical head.

If an air bubble is trapped in the cell, repeated flushing (both forward and backward) is recommended to remove the bubble. Should this fail, it is usually preferred to remount the cell unless the bubble is not close to the cantilever-tip

[3] In the case of a leakage the set up must be disassembled and carefully dried immediately to prevent damage of the scanner or the electronics.

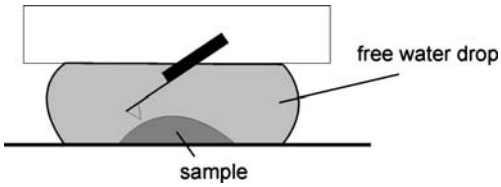

Fig. 3.37 Schematic of AFM operation under liquid without rubber ring. A water drop, which is spanned between liquid cell and sample, encloses the imaged area incl. tip and cantilever completely

assembly. In this latter case, it may be possible to operate the AFM without interference from the bubble.

Mounting of Liquid Cell Without Rubber Ring

AFM operation under liquid without rubber ring works with solvents that possess sufficiently high surface tensions such as glycerol, water, and aqueous solutions. The use of double-sided pressure sensitive adhesive is possible in this case due to the absence of a mechanically coupled connection between sample and liquid cell base. If the AFM is to be operated without rubber rings, the normal crude approach procedure is followed and once the setup would be ready for engagement in air, the optical head is removed vertically. A drop of solution is placed onto the sample (to form a lens) and the optical head is lowered vertically into its rest position and carefully secured. Now the drop of solvent should span the gap between the sample and the liquid cell (Fig. 3.37). If the drop is too small or does not symmetrically span the gap, additional solvent may be added very carefully through the inlet or from the side using a syringe. Care must be taken *not* to spill any liquid! Similarly, to the operation with rubber ring, the assembly must be inspected to verify that no leakage of the cell or air bubble may interfere with the measurement. After the redirection of the reflected laser beam onto the photodiode (see above), the experiment can be started when the differential photodiode signal(s) show stable readings. This may again take several minutes depending primarily on the temperature adjustments in the cell. During the experiment, the solvent may evaporate, so it is advised to monitor the shape of the spanned drop regularly and, if needed, to replenish the solution after withdrawal of the tip from the surface. Obviously, when buffers and salt are used this will lead to a slow drift in salt concentration/ionic strength and the corresponding effects should be considered.

Mounting the Liquid Cell for Experiments in Which the Sample Must Stay Under Liquid at all Times

For many biopolymeric specimens it is of vital interest to keep the specimen covered by water or buffer at all times. For this purpose the rubber ring can be pressed onto the sample supported on e.g. a glass slide under water. The slide and the rubber ring are then taken out of the solution and placed onto a sheet of adsorbent

paper to dry the bottom side of the slide. If necessary, water is refilled into the rubber ring using a syringe. Next the sample is transferred onto the sample holder which is covered with pressure sensitive adhesive. The holder is mounted onto the protected scanner with minimal delay. Then the rubber ring is removed with tweezers and additional water is deposited at the same time onto the sample ensuring that the water spans the distance between the sample and the liquid cell of the AFM after the AFM optical head is put onto the scanner. After a brief equilibration period of typically several minutes in order to obtain a stable photodiode reading, the experiments can be started.

The general procedure is also applicable for liquid cell work *with* the rubber ring. In this case a fast curing epoxy must be used instead of the pressure sensitive adhesive. It is advisable to cure the glue completely before mounting the sample in the AFM.

3.3.1.3 CM-AFM Operation Under Liquid

For the operation of contact mode AFM under liquid there are only few details that differ from operation in air. The imaging forces can often be controlled much more precisely if the adhesion is lower due to the absence of capillary forces. Hence the adjustment of the setpoint requires more attention and can be done with much more precision. The adjustment can be based on acquired force-displacement curves (see below, Fig. 3.39). Setpoint deflection values close to the out of contact deflection yield minimized normal forces [82–84].

Alternatively, the setpoint is lowered during imaging until the tip does no longer track the surface properly. This effect is seen by the appearance of a halo behind elevated objects in the direction of the data collection (Fig. 3.38, left). Then the scan

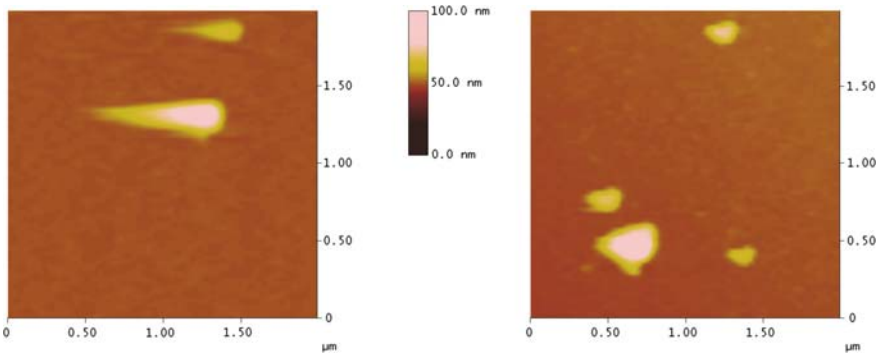

Fig. 3.38 Contact mode AFM height image of egg PC vesicles adsorbed on glass captured with an imaging force of 30 pN (*left*) and 50 pN (*right*). The halo in the fast scan direction (*right to left*) indicates that the tip can no longer track the surface features accurately, when imaging force and noise of the deflection signal become comparable (~30 pN in this case). When the imaging forces are increased to 50 pN, the surface is tracked better. The asymmetry of the features can be explained by tip convolution effects (asymmetry of the probe tip) [87]

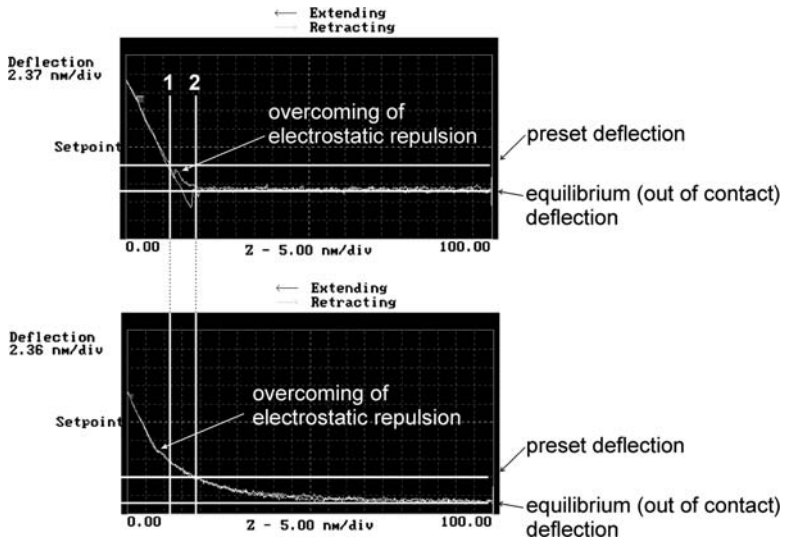

Fig. 3.39 Force-displacement curves captured with silicon nitride tip on glass in buffer (10 mM Tris [pH 8], 100 mM NaCl, top) and ultrapure water (Millipore water (18.4 MW cm), *bottom*). The different range of the electrostatic repulsion, as well as a difference in pull-off force are obvious

rate may be reduced, the gains increased and the force/setpoint slightly increased to achieve proper tracking of the surface (as assessed by inspection of trace and retrace data of individual scan lines; Figure Fig. 3.38, right).

The forces operating between tip and sample in the liquid may be distinctly different from the situation in ambient conditions. As mentioned capillary forces are absent and hence weaker interactions may become significant in liquids. Electrostatic repulsion may also occur between tip and sample, which has an impact on the selection of proper imaging conditions. The situation is exemplified in Fig. 3.39, where force-displacement curves obtained in different media are compared. For the same preset deflection (i.e. setpoint) the z-position corresponds to a different value. At the point where the repulsion is overcome, the tip penetrates through the bilayer.

It is important to realize that such a significant difference in f-d curves may also occur in aqueous medium in areas with different surface charge density [88]. In this situation, a preset deflection (setpoint) value below the hard wall contact (force larger than the force required to overcome the electrostatic repulsion) may lead to artifacts in the constant force (i.e. height) image (Fig. 3.40). This kind of artifact is based on the fact that under these conditions the constant setpoint force corresponds to a different tip–sample distance (similar to the difference between the lines labeled with 1 and 2 in Fig. 3.39).

In the example, shown in Fig. 3.40 egg PC lipid bilayer patches on glass were imaged by contact mode AFM using slightly different forces. For high imaging forces corresponding to hard wall contact (Fig. 3.40, left) the patches appear

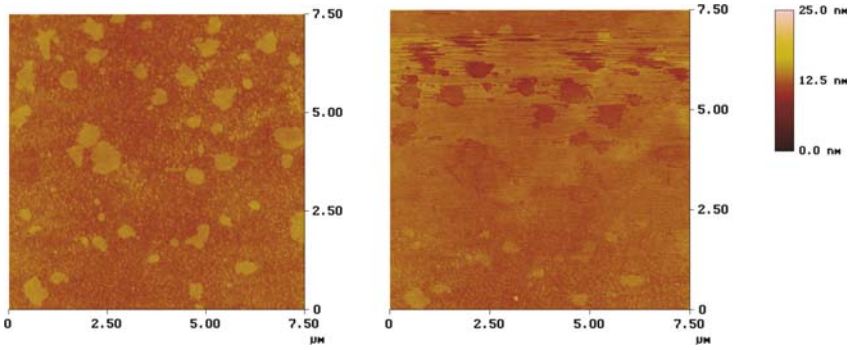

Fig. 3.40 Egg PC bilayer patches on glass imaged in constant force mode CM-AFM in Milli-Q water. The imaging conditions for the image on the right hand side changed during the scan, hence the imaging force was close the transition from the regime of electrostatic repulsion to had wall contact (compare Fig. 3.39) [89]

elevated, while for forces corresponding to nearly the equilibrium deflection of the cantilever in the imaging medium (Milli-Q water), the bilayer patches appear depressed (Fig. 3.40, right).

The observed artifact (negative height of deposited matter) can be explained by considering the locally different electrostatic repulsion, which is sensed by the tip in the latter case. The repulsion on the bare glass is apparently higher than on the bilayer patches, which results in a z-movement of the piezo towards the tip in the bilayer areas to keep the preset force constant. If a normal force that corresponds to hard wall contact (electrostatic repulsion is overcome) is chosen, the correct height differences are measured, assuming that the difference in compliance of the bilayer and the glass are negligible.

Further, considering the viscosity of the medium, high scan rates will sometimes lead to drag forces on the cantilever. A typical trace of these may be seen in force-displacement measurements [90]. Furthermore, the optimized gains (in conjunction with scan rate) will likely have different values for operation in liquid media compared to operation in air.

Sometimes clearly audible feedback may occur during the engagement process or when the deflection of the cantilever is nearly equal to the setpoint. The former problem can lead to a false engagement in the worst case and may be avoided by reducing the gains and increasing the differential offset. In the latter case it is recommended to adjust the setpoint to slightly increased forces.

3.3.1.4 TM-AFM Operation Under Liquid

For TM-AFM operation under liquid, the system is set up similar to the contact mode in liquid. By contrast, the cantilevers used are typically much softer than for operation in air. Often conventional contact mode levers (spring constant of ~ 0.3–few N/m) are used; single beam cantilevers work in some cases better than triangular levers. The tuning of the lever is performed after the crude approach has

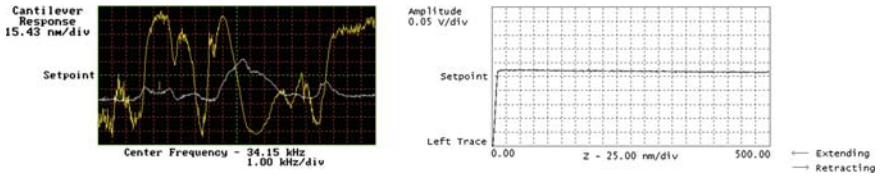

Fig. 3.41 *Left*: Frequency sweep in water (silicon nitride lever); *right*: amplitude distance curve recorded in water on a glass sample

been carried out. Owing to the damping of the forced oscillation by the imaging medium (and thus a low quality factor Q), the resonance curves of a lever in liquid looks rather broad (Fig. 3.41, left). For the operation of the TM-AFM experiment under liquid, the operation (excitation) frequency is tuned to a side of a peak, where the gradient is steep and near constant, i.e., a shoulder of one of the broad peaks.

The amplitude is typically lower in liquid than in air, however, care must be taken that it is sufficiently high that the adhesive interactions experienced by the probe tip are overcome during each cycle of oscillation. After successful engagement, it is therefore advisable to monitor the rms amplitude sum, as well as the deflection, signal during the scanning. If the tip adheres to the surface as a result of strong adhesive forces or too low amplitude of the cantilever to overcome the attraction, the rms amplitude will not show a constant value equal to the setpoint amplitude and the deflection signal may also indicate significant lever bending. These observations indicate that the tapping conditions must be corrected immediately.

Another independent check is the acquisition of an amplitude-displacement curve. To protect the tip, care must be taken that the z-travel is adjusted such that the vibration of the tip/cantilever assembly is not damped completely (Fig. 3.41, right).

It is generally advisable to check how image contrast in height and phase images change as a function of the operation conditions; a number of artifacts related to adhesive interactions, such as contrast inversion, have been reported [91].

3.3.2 Hand-on Examples

Hands-on Example 14

Visualization of Adsorbed Lipid Vesicles and Bilayers

Sample Preparation: Vesicle Fusion

The importance of lipid bilayers, as, near natural environment for, e.g., protein studies by AFM and the model character of these systems for AFM liquid cell work

predestine the visualization of adsorbed lipid vesicles and bilayers for a discussion as first hands-on examples. Vesicles (e.g. egg phosphatidylcholine (Egg PC) purchased from Avanti Polar Lipids (Alabaster, AL)) may be prepared by the extrusion method. As described in detail in [92], chloroform is evaporated from the egg PC under vacuum, and the lipids are allowed to hydrate in standard buffer (10 mM Tris [pH 8], 100 mM NaCl). The resulting multi-lamellar vesicles are subjected to 5 freeze/thaw cycles and then extruded through polycarbonate membranes of 30, 50 or 100 nm pore diameter (Avanti Mini-Extruder).

As substrates, glass coverslips are used, which should be thoroughly cleaned by soaking the substrates in heated detergent solution for at least 20 min, followed by exhaustive rinsing and finally baking at 400°C for 4 h. The substrates are glued to the AFM sample holder using epoxy glue.

Imaging of Vesicles and Bilayers on Glass by CM-AFM in Buffer

The AFM set-up is assembled for operation using the liquid cell in conjunction with a rubber ring; very soft cantilevers with a spring constant of 0.06 N/m are advisable. The set-up is prepared as outlined in detail in Sect. 3.3.1.2 for mounting the dry substrate. Care must be taken that the optical head is placed according to the procedure without shearing the rubber ring. After an equilibration period of 2 h the liquid cell is filled with buffer and is thermally equilibrated. Once the photodiode differential signal show a constant value, the engagement procedure as described in Sect. 3.2 is carried out and images of the glass substrate can be acquired after the feedback loop has been optimized. It should be ensured that subsequent up- and down-scans match and that the f-d curves show no pull-off force exceeding 20–35 pN. Higher pull-off forces indicate a dull tip or contamination on the sample or the tip surface (in this case it will be practically impossible to image the adsorbed vesicles non-destructively). If the set-up is stable, the tip is withdrawn from the surface and the degassed vesicle solution (concentration of $\sim 5 \times 10^{-3}$ mg/mL) can be slowly injected into the AFM liquid cell [93].

The engagement should be carried out with $\sim (100\ \text{nm})^2$ scan size and the minimum imaging force should be determined by reducing the setpoint to the point where the tip loses track of the surface. The force is then increased in small increments until contact is re-established. Then the scan rate may be reduced, the gains increased and the force/setpoint slightly varied to achieve proper tracking of the surface (as assessed by inspection of trace and retrace data of individual scan lines). Finally, the scan size is increased to track adsorbed vesicles. A typical contact mode AFM height image is shown in Fig. 3.42. While the heights (depending on vesicle radius between 10 and 60 nm) measured may be considered as a good approximation of the true feature height, the width of the observed features is an overestimate owing to tip convolution effects. In the case of too large imaging forces (> 60 pN), the vesicles rupture owing to forces exerted by the tip and form a bilayer patch (height ~ 4.5–5.0 nm). High vesicle concentrations lead to the formation of lipid bilayers, which appear homogeneous. Using high imaging forces defects may be introduced on purpose (scratching of bilayer) to be able to assess the layer thickness, as shown in Fig. 3.42. middle and right.

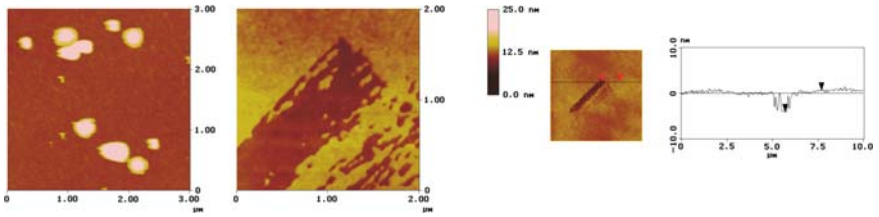

Fig. 3.42 Contact mode AFM height image of (**a**) egg PC vesicles adsorbed on glass at high concentration (*left*) and (**b**) intentionally scratched lipid bilayer (*middle*), and (**c**) section analysis of a scratch, which may be used to elucidate the thickness of the bilayer. Adapted with permission from [93]. Copyright 2004. American Chemical Society

Hands-on Example 15

Visualization of Polymerizable Lipid Bilayers

Sample Preparation: Langmuir-Blodgett, Langmuir Schaefer Transfer, and UV Photopolymerization

Bilayers of the diacetylene phospholipid (1,2-bis(10,12-tricosadiynoyl)-*sn*-glycero-3- phosphocholine) (Avanti Polar Lipids, Alabaster, AL) can be prepared by Langmuir-Blodgett and subsequent Langmuir-Schaefer transfer followed by photopolymerization through a contact mask using UV light (254 nm) in argon-purged oxygen-free water as described in [94, 95]. Since the polymerization may not be completed in all regions, which leads to the stabilization of the bilayer, the sample is mounted in the AFM such that it stays under liquid at all times. The procedure is outlined in Sect. 3.3.1.2. (c) in detail.

Imaging of Photopolymerized Bilayers on Glass by CM-AFM in Water

For large area scans it is advised to use the AFM liquid cell without rubber rings to prevent ring flexing upon large displacements. Hence the AFM set-up is assembled for operation using the liquid cell for operation without a rubber ring. Standard cantilevers with a spring constant of 0.3 N/m are selected.

After the stabilization of the photodiode differential signal, the engagement procedure as described in Sect. 3.2 is carried out and images of the bilayer can be acquired after the feedback loop has been optimized. In Fig. 3.43, the topography of a photo patterned polymeric lipid bilayer is depicted (left) together with a cross-sectional analysis (middle). Using a different photomask and a more complete polymerization, the pattern is stable to exposure to air. As depicted in Fig. 3.43 (bottom, right), conventional intermittent contact mode in air can be utilized to interrogate the structure obtained.

In the following section of hands-on examples for imaging of biopolymers, we discuss a broad range of topics without going into further detail regarding the biological or biomedical relevance of the samples discussed as this is beyond the scope of

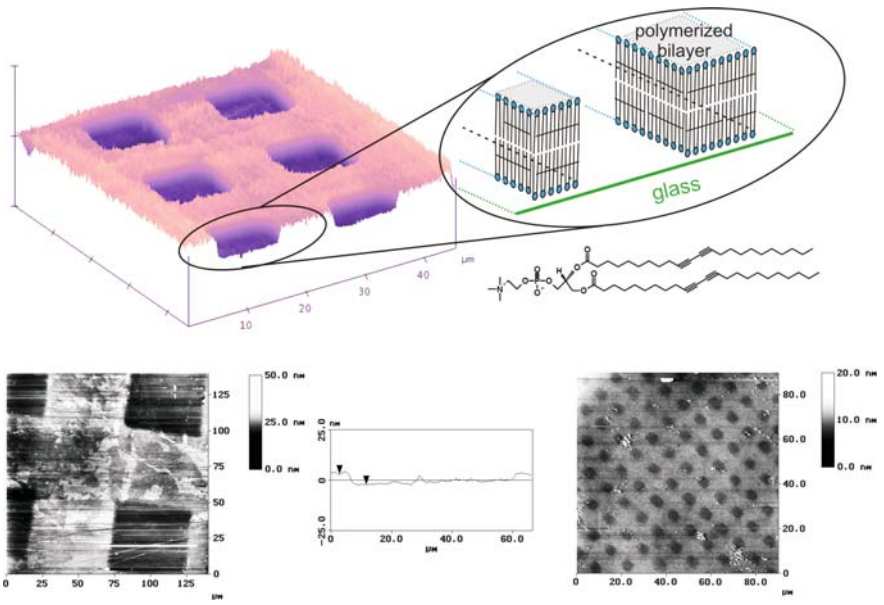

Fig. 3.43 *Top*: 3D plot of contact mode AFM height image obtained under water of photopolymerized lipid bilayer on glass. Reproduced with permission from [95]. Copyright 2007. American Chemical Society. *Bottom*: (*Left*, *middle*) Contact mode AFM height image obtained under water and corresponding section analysis of photopolymerized lipid bilayer on glass; (*right*) TM-AFM height image of photopolymerized lipid bilayer on glass acquired in ambient conditions. Reproduced with permission from [94]. Copyright 2003. American Chemical Society

this book. Instead we try to highlight a range of relevant sample preparation methods, imaging media and representative classes of biopolymeric specimens.

Hands-on Example 16

Visualization of the Tobacco Mosaic Virus

The tobacco mosaic virus was selected as model for complex assemblies involving biopolymers. AFM in selected media helps to clarify the structure of such assemblies under different conditions and eventually may allow one to study details of the biological function in situ.

Sample Preparation: Deposition from Suspension onto Graphite

In this experiment we follow a procedure adapted from work reported by Bittner and coworkers [96]. Graphite (highly oriented pyrolytic graphite (HOPG)) is freshly

cleaved using adhesive tape. Onto this surface, tobacco mosaic viruses are adsorbed by exposure to a 40% DMSO aqueous suspension containing 0.1 mg/mL virions.

TM-AFM Visualization of Tobacco Mosaic Viruses

The TM-AFM set up and general procedures are the same as discussed above (*Standard tapping/intermittent contact mode set-up*). In order to avoid damage of the virus particles imaged, a minimum free amplitude (A_0) is selected. The engagement procedure is carried out as described in Chap. 2. Similar to all other experiments, the scan size is increased stepwise, while the gains are optimized as described. The length and width of the viruses can be independently determined by electron microscopy, thus enabling one to independently verify the AFM data.

As shown in Fig. 3.44, the virus covered HOPG displays elongated rods with a typical height of 18 nm. This height is in excellent agreement with the diameter of the virus, which implies that the adsorption process does not deform the virus. However, the length of the rod corresponds to twice the length of an individual virus (300 nm), hence the visualized rod corresponds to two viruses arranged in a head to tail fashion. The apparent diameter determined as full width at half maximum (fwhm) of 85 nm greatly overestimates the width of the virus. This well-known effect is attributed to tip convolution and can be corrected for if the tip radius is known (e.g. by measurement of a colloidal particle with known diameter. As discussed in [96], the substrate and imaging medium, e.g. acidic solutions, have an impact on the apparent size of the surface attached virus. Owing to interfacial interactions or covalent attachment the shape of the virus may even be altered.

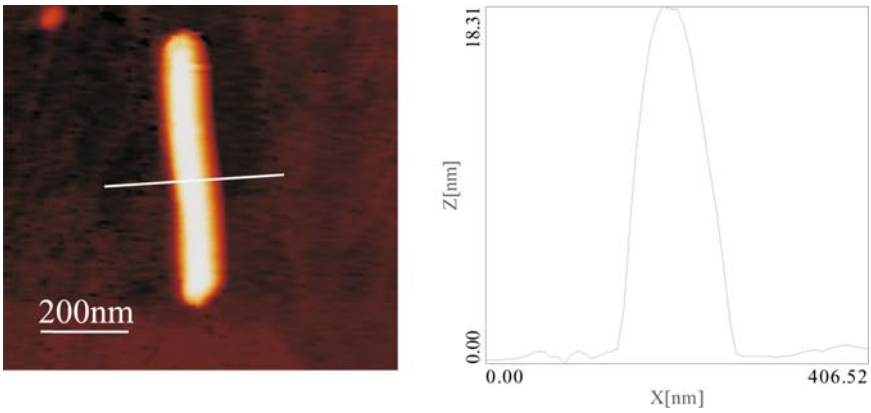

Fig. 3.44 Intermittent contact AFM of two virions in linear arrangement on graphite (reproduced with permission from [96]). The measured height of 18 nm corresponds to the true diameter, while the width (ca. 85 nm (fwhm)) is attributed to the AFM tip shape. Reproduced with permission from [96]. Copyright 2004. American Chemical Society

Hands-on Example 17

Naturally occurring polymeric fibers possess interesting properties and have found widespread use in passive and active applications long before man-made polymers began to flourish. Well-known examples included cellulose, silk, cotton, etc. The AFM investigation of cellulose will be discussed as a prime example for these important natural polymeric fibers.

Cellulose Fibers in Pulp

In pulp and paper research, the localization of surface components of wood fibers is of particular interest. Using AFM approaches, the morphology and origin (native or re-precipitated) of lignin, hemicelluloses and extractives on the pulp surface may be elucidated in combination with other surface science techniques.

Sample Preparation: Cooking and Drying in Air

Pulp samples can be prepared according to [77]. Spruce (Picea abies) is cooked at a liquor-to-wood ratio of 4.5 (supplied by KCL, Finland) at an effective alkali of 5 mol/kg and a sulphidity of 30%. The temperature is raised from 80 to 170°C at 1°C/min and kept at 170°C for various times. For AFM imaging the pulp samples are dried on sample holder disks covered by double-sided adhesive tape.

TM-AFM Visualization in Air

The standard TM-AFM procedure discussed in Sect. 3.2 is used (*Standard tapping/intermittent contact mode set-up*). The image contrast observed in the phase images is sensitive to the free amplitude (A_0). A free, amplitude of ~ 60 nm and a setpoint amplitude/free tapping amplitude ratio of 0.6 typically yield good image contrast. The engagement procedure is carried out as described in Sect. 3.2. Similar to all other experiments the scan size is increased stepwise, while the gains are optimized as described.

In Fig. 3.45 the surface morphology of pulp samples after cooking for 15 and 45 min, respectively, are compared. The TM-AFM phase images provide good contrast and enable one to analyze the changes in surface morphology as a function of cooking time. The transition of a granular surface (15 min) to a more fibrillar morphology (45 min) can be observed. The exposed microfibrils possess a thickness of ca. 20 nm. In [77] the random cellulose microfibril orientation and the loose surface structure in Fig. 3.45 are related to the characteristics of the primary cell wall.

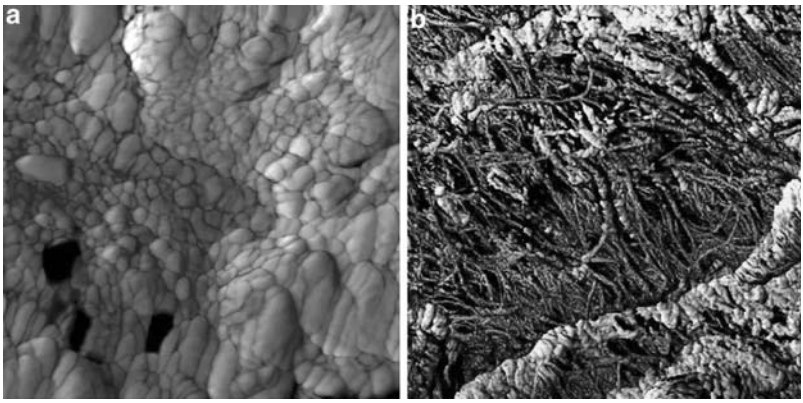

Fig. 3.45 TM-AFM phase images of (**a**) 15 min and (**b**) 45 min cooked spruce kraft pulp sample. Image sizes are (**a**) 2 × 2 μm^2 and (**b**) 2 × 2 μm^2. Reproduced with permission from [77]. Copyright 2003. Elsevier

Hands-on Example 18

Cellulose Microcrystals

Sample Preparation: Deposition onto Chemically Activated Mica Substrates

Cellulose microcrystals extracted from *valonia ventricosa* are prepared according to [97] to yield cellulose suspensions. For AFM, a 5-μl drop of a 100-fold diluted (water) suspension is deposited onto freshly cleaved mica and left to dry under ambient conditions. For imaging under propanol, the samples are deposited onto 3-aminopropyltriethoxysilane–functionalized mica [98].

CM-AFM Visualization in Liquid [99]

The CM-AFM protocol follows closely the standard procedure for imaging in CM in liquids using the rubber rings, as introduced in Sect 3.3. Standard silicon nitride cantilevers with a spring constant of 0.06 N/m are used. The very soft CM cantilever is inserted into the cantilever holder, the laser is aligned, and the photodiode is moved such that the laser spot is centered. Following the crude approach, the system is equilibrated for several hours. The scan rates (typically 10–20 Hz) and the scan angle, are varied to obtain optimum contrast. The images may be captured in constant force mode; however, Miles and co-workers reported the successful use of the deflection images to obtain high-resolution data on cellulose microcrystal surface. When used with the feedback on, the deflection channel provides an image that enhances high spatial frequency information, such as sharp edges.

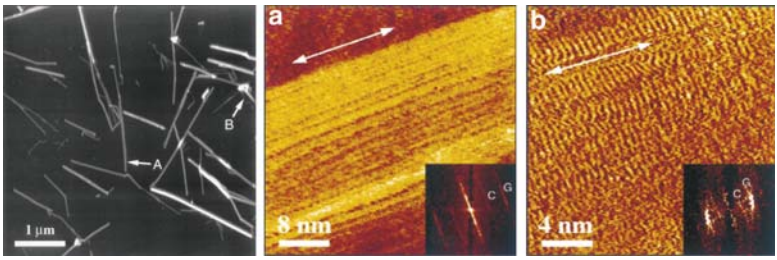

Fig. 3.46 CM-AFM height (*left*) and deflection images (*middle*, *right*) obtained in propanol of the *Valonia* surface. In the height image individual microcrystals as well as aggregates may be seen. The *arrow* indicated by A points to where two crystals are closely joined together, but do not end at the same point. The feature labeled B is an example of a microcrystal with a measured height of less than 5 nm. The double-headed arrows in the deflection images indicate the direction of the crystal (molecular) axis. The inset pictures are FFTs of the image data, where the letters C and G have been placed by the regions of spectral intensity due to the cellobiose (1.04 nm) and glucose (0.52 nm) spacings, respectively. Reproduced with permission from [99]. Copyright 1997. Elsevier

The microcrystals and their orientation can be deduced from low-resolution images as shown in Fig. 3.46 (left). These single crystals possess widths between $\sim$ 20 nm and 100 nm, the height is below 12 nm. In high resolution images (Fig. 3.46 middle and right) the molecular scale arrangement can be assessed, which gives useful insight into local surface crystal structures and opens the possibility to investigate chemical and enzyme degradation at high resolution on these surfaces.

Hands-on Example 19

Polysaccharides: Xanthan Gum

Sample Preparation: Deposition onto Mica and Drying

Following [100] the powdered xanthan sample (Keltrol, Kelco-AIL) is dispersed in water, heated for 1 h at 85°C under stirring. After cooling down to ambient, a 0.1% (w/v) sample is centrifuged at 150,000 g for 3 h at 25°C, followed by storage at 1°C. After bringing the sample to 25°C again, the solution is diluted to 20 µg/mL and a 2 mL droplet is deposited onto freshly cleaved mica. After 10 min drying in air the sample is mounted in the AFM.

CM-AFM Visualization of Xanthan on Mica in Alcohols

CM-AFM imaging of xanthan on mica is carried out following the standard procedure for imaging in CM in liquid (compare in Sect. 3.3.1). 1-butanol or 1, 2-propanediol

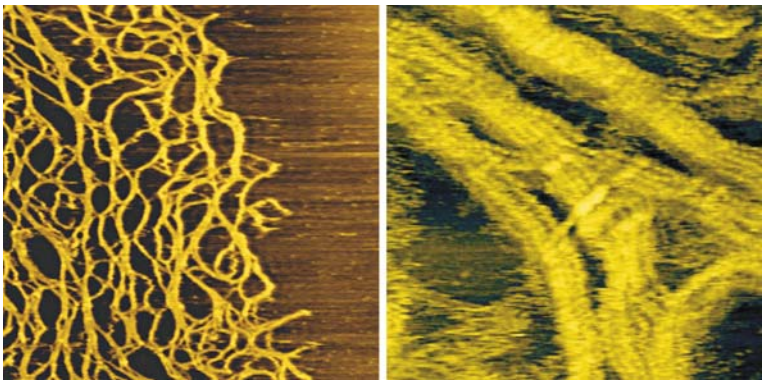

Fig. 3.47 *Left*: AFM image of an entangled network of the polysaccharide xanthan deposited on mica. The image was acquired under butanol (image size: 1.5 × 1.5 μm^2; reproduced with permission from [100]). Copyright 1995. Elsevier. *Right*: High resolution AFM image of several molecules of the polysaccharide xanthan illustrating its helical secondary structure. Scanned under 1,2 propanediol in contact (dc) mode. Scan size: 0.2 × 0.2 μm^2 (reproduced with kind permission of Dr. Andrew Kirby from [101])

are chosen as imaging liquids, because the forces between the silicon nitride tips and the mica substrate are minimized and the alcohols are precipitants for polysaccharides and thus might be expected to inhibit desorption from the mica surface. Silicon nitride cantilevers with a spring constant of $\sim$ 0.3 N/m are used. The CM cantilever is inserted into the cantilever holder, the laser is aligned, and the photodiode is moved such that the laser spot is centered. Following the crude approach, the system is equilibrated for several hours.

After engagement the imaging forces are adjusted to $\sim$ 3–4 nN. Using these forces with carefully optimized feedback loop the network structure of xanthan, as well as the molecular scale structure may be unveiled. The resolution is typically limited by the sharpness of the probe tip, but under optimum conditions, the helical secondary structure can be visualized (Fig. 3.47).

Hands-on Example 20

Collagen

Sample Preparation: Polishing and Wet Chemical Etching

Following [102], sagittal midcoronal sections (thickness of 2 mm) of sterilized teeth are prepared by polishing using a series of SiO_2 papers and a water-based diamond paste to 0.25 µm (Buehler, Lake Blu., IL). The sample surface is cleaned by an ultrasonic treatment in water for 10 s. Wet chemical etching of the specimens in

10 vol% citric acid for 15 s dissolves the mineral in the calcified tissues and leaves the organic phases behind. Finally, specimens are treated with an aqueous solution of 6.5 vol% sodium hypochlorite for different time intervals. Specimens are dehydrated by air-blowing (5 s) and continued drying in air for at least 1 h before imaging.

TM-AFM Visualization in Air

The standard TM-AFM procedure discussed in Sect. 3.2 is used (*Standard tapping/intermittent contact mode set-up*). In order to obtain high-resolution images in air, high-aspect-ratio Si-tips with a radius of 10 nm or less is advised (resonance frequency $\sim$ 300–350 kHz). The engagement procedure is carried out as described in Sect. 3.2. Similar to all other experiments the scan size is increased stepwise, while the gains are optimized as described.

Figure 3.48 shows the fibril organization on the micrometer scale. The fibril possesses a random orientation. Already at this magnification, a periodic pattern on top of the fibril is discernible. For a quantitative analysis, higher resolution images are required. As described in [102], the analysis of the pitch of the periodic pattern can be performed using fast Fourier transform procedures. Dehydration leads to an alteration of the observed structure, thus suggesting the need for studies in liquid

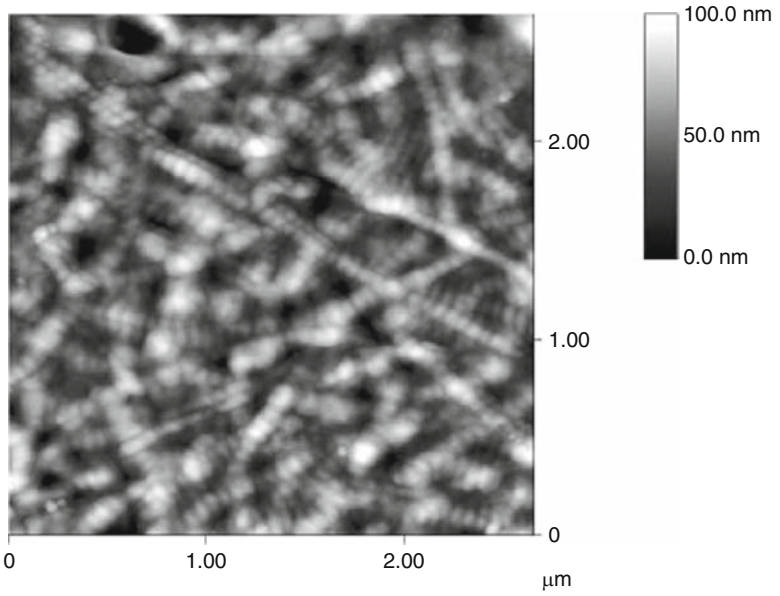

Fig. 3.48 Tapping mode AFM image of dentin collagen fibrils, obtained from demineralized specimen (15 s citric acid) treated with 6.5 vol% $NaOCl_{aq}$ for 130 s and in air, showing the repeat pattern and the random distribution of fibrils in intertubular dentin. Reproduced with permission from [102]. Copyright 2002. Elsevier

media. These can be performed according to the CM-AFM and TM-AFM procedures outlined in the beginning of this Chapter in Hanks balanced salt solutions (for details see [102]).

Hands-on Example 21

Crystallized Protein Layers: Streptavidin

Sample Preparation: 2D Crystallization at the Air-Water Interface

The crystallization of streptavidin is carried out at the air-water interface according to [103]. Lyophilized streptavidin from *Streptomyces avidinii* (Prozyme Inc., San Leandro, CA) is crystallized at a surface pressure of approximately 25–30 mN/m of a Langmuir film prepared from a 10 wt-% mixture of biotin-X-DHPE in DOPC in 2:1 chloroform/methanol at a total concentration of 0.1 mg/mL on a subphase of varying pH. The ionic solutions of 50 mM NaH_2PO_4 in 500 mM NaCl and the pH is adjusted by adding HCl or NaOH. A small aliquot of protein is injected into the subphase through an injection port to a final concentration of 20 µg/mL. The wells are left in the dark in a closed, hydrated environment for at least 4 h before they are transferred to TEM grids. To prepare the crystals for TEM, 50% glutaraldehyde is gently injected into the subphase to a total concentration of 0.5% and left for 3 h. Then a carbon-coated grid is laid on top of the region of interest and lifted from the surface with a piece of Parafilm backing paper (American National Can, Greenwich, CT) as a support. After washing with Milli-Q water, the grid is fixed on an AFM sample holder disk using pressure sensitive adhesive.

TM-AFM Visualization in Air

We use the standard TM-AFM imaging procedure for experiments in air (Sect. 3.2) and sharpened silicon probes. Using an active vibration isolation system (air-table) and a noise isolation compartment, as well as a long equilibration period of several hours, the lattice of the 2D crystal of streptavidin (here grown at pH > 7) can be imaged with molecular resolution. The engagement procedure is carried out as described in Chap. 3.2. Similar to all other experiments the scan size is increased stepwise, while the gains are optimized as described. Since the scan rates of conventional TM-AFM are low, thermal equilibration is a pre-requirement to obtain undistorted images. If the probe tip is sharp enough, true molecular resolution may be obtained, as shown in Fig. 3.49. In the top right hand corner a vacancy in the lattice can be observed, which, is a trustable indication for the presence of true molecular resolution. The lattice imaged in real space agrees with previous reports of streptavidin crystals with a square lattice with C222 symmetry (a = b = 58 Å, $\gamma = 90°$) [104] (Fig. 3.49).

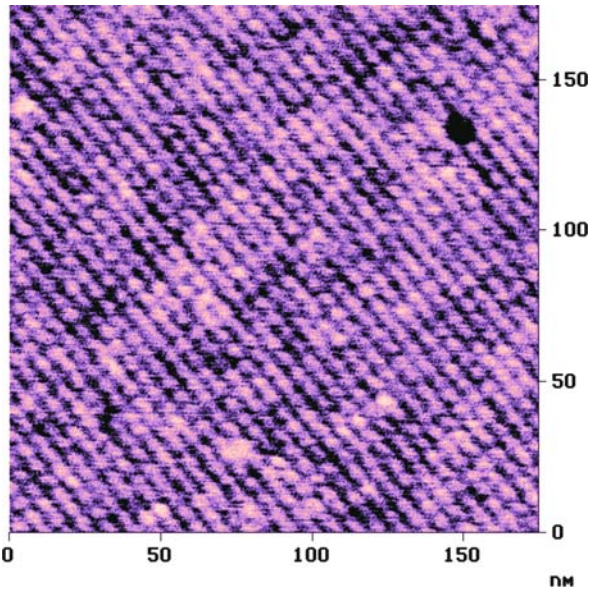

Fig. 3.49 TM-AFM phase image of 2D crystal of streptavidin recorded in ambient conditions [105]

Hands-on Example 22

Lambda DNA

Sample Preparation: Immobilization on Silanized Mica

According to [106], mica substrates are coated with a self-assembled monolayer of (3-aminopropyl)triethoxysilane (APS, United Chemical Technology Co., Bristol, PA). Freshly cleaved mica sheets are immersed in filtered (2 μm cellulose filter) APS solution (APS in distilled-deionized (dd) water, concentration 1% by volume) for ∼5 min and rinsed thoroughly with dd water afterward. DNA solutions of lambda DNA (48,502 base pairs (bp), from GIBCO/LTI, Gaithersburg, MD) with a concentration of 1 ng/mL in dd water are used. Samples are prepared by first depositing a small drop of DNA solution onto a clean glass coverslip, which is then laid on top of the APS-mica. The solution between the two surfaces spreads immediately as the cover glass and the APS-mica come together. After a few minutes, the cover glass is removed and the APS-mica surface is rinsed with dd water thoroughly and blown dried with clean compressed air.

CM-AFM Visualization of immobilized λ–DNA on Mica in Liquid

Standard CM-AFM using a liquid cell filled with Tris buffer solution is carried out with oxide sharpened tips; a cantilever spring constant of 0.1 N/m is used. The engagement procedure is carried out as described in Sect. 3.2. Similar to all

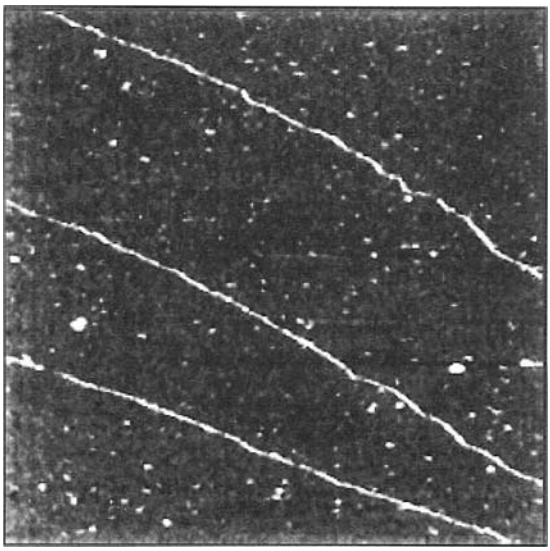

Fig. 3.50 A 2.5 × 2.5 μm^2 AFM image of lambda DNA on APS-modified mica acquired in CM-AFM in Tris buffer. This image was collected in normal contact mode, with loading force of 1 nN, using a Park sharpened tip (cantilever force constant of 0.1 N/m). Reproduced with permission from [106]. Copyright 1996. American Chemical Society

other experiments the scan size is increased stepwise, while the gains are optimized as described. Since the immobilized DNA molecules may suffer damage when the imaging forces are too high (in fact the scission of such DNA molecules has been reported) [106], the imaging forces must be minimized according to the procedure introduced in Sect. 3.2.

Depending on the concentration of DNA used in the sample preparation procedure, the surface coverage can be adjusted. The fixation using the silanization procedure is beneficial in effectively immobilizing the DAN for AFM work. Stability in excess of 5 h has been reported [106] (Fig. 3.50).

Hands-on Example 23

Biocompatible Polymers

The investigation of biocompatible polymers and polymeric coatings is of central importance in many areas, including biomedical applications. The investigation of biomedically relevant and biocompatible polymers can be pursued following the general guidelines for AFM studies on synthetic polymers in the appropriate medium. Here we discuss the application of AFM in testing cell adhesion to biocompatible polymers.

Sample Preparation: Dip-Coating and Exposure to Bacteria

Poly (ethylene oxide)–copoly(propylene oxide) (PEO-PPO) copolymers (Pluronics™) obtained from BASF are applied to polystyrene-coated glass slides by dip coating. For this purpose, aqueous solutions of the Pluronic copolymer (1–2% w/v in double-distilled water) are prepared; samples are dip coated, followed by drying under a flow of dry nitrogen. Aliquots (200 μL) of suspended bacteria (details see [107]) are transferred to sterile 3-[N-morpholino]propanesulfonicacid (MOPS) (50 mM, pH 7.0, 6 mL) (10 mL) in capped bottles. The test surfaces, i.e. glass (1 cm^2), with and without polymer coatings, are then placed in the bottles and incubated with gentle shaking (40 rpm) for 24 h at 37°C. Finally, the slides are rinsed in sterile MOPS (10 mL), and dried for AFM investigation.

CM-AFM Visualization in Air

The AFM is set up for a standard CM experiment (see Sect. 3.2). A very soft CM cantilever (0.03 N/m) is inserted into the cantilever holder, the laser is aligned, and the photodiode is moved such that the laser spot is centered. Following the crude approach, the system is equilibrated for several hours.

The experiment must be carried out with minimized forces and very small scan rates, because the adhering bacteria may be swept away by the scanned tip in case that the feedback loop does not correct the z-position of the piezo sufficiently rapidly.

Adhesion of skin-borne bacteria to the surfaces modified by adsorbed poly (ethyleneoxide)–poly (propyleneoxide) copolymers can be assessed in CM-AFM height images. As seen in Fig. 3.51, cells adhering to the PS-silanized glass slides (a, b) clearly show that these surfaces are unsuitably modified; by contrast, the absence of cell adhesion on the Pluronics modified samples (c,d) demonstrates the efficiency of the surface modification.

3.4 Multicomponent Systems

3.4.1 Materials Contrast in AFM Imaging of Multicomponent Systems

Polymer-based multicomponent systems are abundant in many applications. The properties and performance of particulate-filled systems, such as elastomers and impact modified polymers, and also polymer blends, block copolymers, and fiber reinforced systems, depend to a large extent on the distribution of the components. Hence the local analysis of these distributions down to sub-100 nm length scales (dictated, e.g., by the size of primary filler particles) is of considerable significance. Materials contrast in several AFM approaches offers the possibility to address these issues directly at the surface of specimens or on bulk samples that have been prepared correspondingly.

In addition to its capability of imaging the topography of polymer surfaces with virtually eliminated shear forces, intermittent contact (tapping) mode AFM, can also be useful to probe various surface properties, such as adhesive or surface mechanical properties. Thereby AFM can help to identify and quantify the abundance and distribution of the phases present in multicomponent systems. As shown already

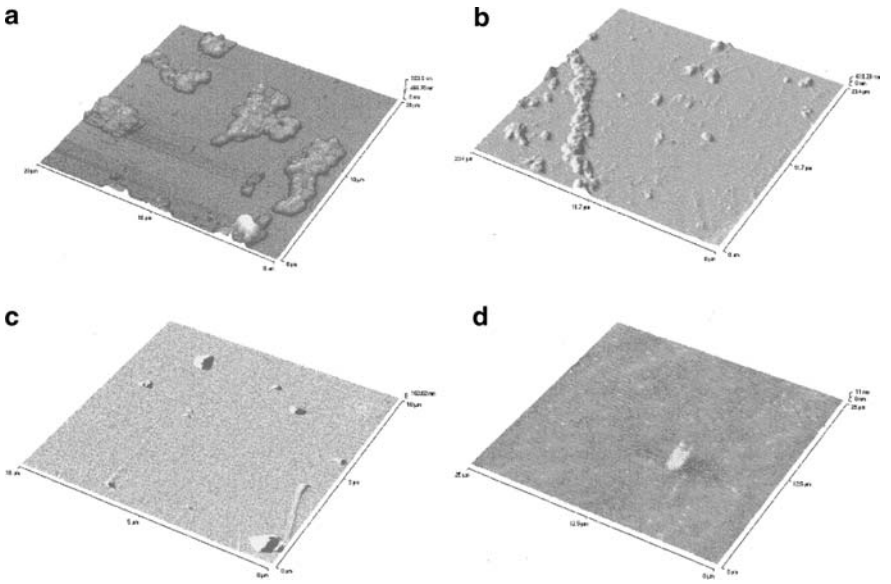

Fig. 3.51 Atomic force micrographs of surfaces after incubation with bacterial cultures for 24 h. (**a**) PS-silanized glass slide, $x = y = 20$ μm, $z = 934$ nm; incubation in *S. marcescens*. (**b**) PS-silanized glass slide, $x = y = 23.4$ μm, $z = 610$ nm; incubation in *S. epidermidis*. (**c**) F127-PS-silanized glass slide, $x = y = 10$ μm, $z = 143$ nm; incubation in *S. marcescens*. (**d**) F127 P S-silanized glass slide, $x = y = 25$ μm, $z = 3.18$ nm; incubation in *S. epidermidis*. Reprinted with permission of John Wiley & Sons from Inc. [107]. Copyright 2002. John Wiley & Sons Inc.

in Sect. 3.2, contrast between different materials or components (phases, such as crystalline and amorphous phase) can be achieved in the so-called intermittent contact mode AFM *phase* imaging mode. The phase relation of the excitation piezo and the vibration of the cantilever in time, yields often useful information on the interaction of tip and sample surface (Fig. 3.52) [108]. The phase angle shift $\Delta\phi$ between excitation oscillation and forced oscillation of the cantilever (Fig. 3.52a) can be described by a simple harmonic [111–113], but also by a more complicated anharmonic [109], treatment of a forced oscillator.

The phase angle shift can be used to obtain contrast due to local differences in *energy dissipation* as a consequence of different surface characteristics related to materials properties. These different properties allow one to differentiate materials with different adhesion [110] or widely different Young's moduli, if these differences are related to differences in energy dissipation [111–115]. Hence the amorphous and crystalline phases in semicrystalline polymers can be clearly differentiated, as discussed in Sect. 3.2, as well as different phases in polymer blends or filled systems (see below). As an example, we show in Fig. 3.52 an intermittent contact AFM phase image of a block copolymer thin film on silicon [116].

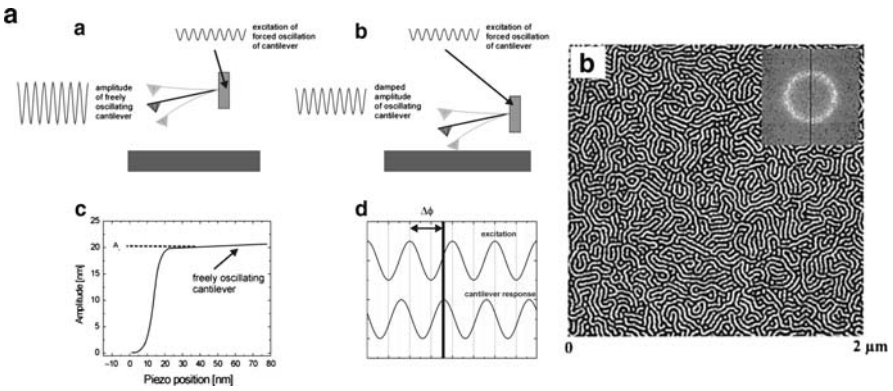

Fig. 3.52 *Left* (**a**): Schematic of intermittent contact mode AFM and phase imaging; *right* (**b**): intermittent contact AFM phase image of a 30 nm thin block copolymer films on silicon [(poly(isoprene)-b-poly(ferrocenyl dimethylsilane), 29 kg/mol/15 kg/mol], which displays a in-plane worm-like surface pattern of poly(ferrocenyl dimethylsilane) in a matrix of poly (isoprene). From the 2D FFT analysis (*inset*) an average repeat period of 33 nm was estimated. Reprinted with permission from [116]. Copyright 2000. American Chemical Society

A principally similarly suitable, albeit not as widely applied technique is the force modulation mode (FMM) AFM. FMM AFM is a contact mode technique that is sensitive to difference in modulus.[117, 118] While the tip/cantilever assembly scans the surface similar to the contact mode, the cantilever is excited by a bimorph to oscillate at a frequency of tens of kHz in FMM AFM. The elastic modulus of the surface can be mapped with high resolution by monitoring the oscillation amplitude. Depending on the corresponding moduli, the contrast in the amplitude image reveals high modulus (i.e. large amplitude) and low modulus (i.e. lower amplitude) are as (Fig. 3.53)[4] [119]. As shown in Figure 3.53, the local modification of a blend of PVC and PC due to irradiation (25 keV Ga ions, which caused subsurface damage) can be differentiated based on the amplitude contrast [120].

Compositional contrast, as well as modulus, can also be assessed by laterally resolved imaging of normal or lateral forces in the contact mode AFM. In the corresponding mapping [121] (see also Chap. 4), force-displacement curves are recorded for each pixel. Subsequently, the pull-off forces, as a measure for adhesion, and the indentation part of the loading curves, to extract/fit the elastic modulus, are evaluated for each pixel. In particular for adhesion mapping, the use of chemically functionalized AFM probe tips [122], has been shown to be a suitable approach to map chemical composition and functional group distributions down to the sub-50 nm scale [123]. The mapping of adhesion, friction, and surface mechanical properties will be treated in more detail in Chap. 4.

[4]A practical limitation for the approach in the field of polymers is the fact that shear forces, similar to contact mode, may cause sample damage or distortion of the underlying morphology.

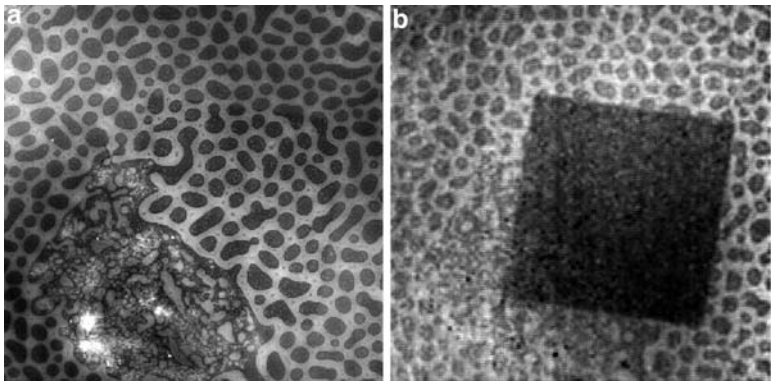

Fig. 3.53 Atomic force microscopy images ($100 \times 100\ \mu m^2$), of a PVC–PC polymer blend: (**a**) topographic image (dark is low and light is high); (**b**) force modulation image showing the material response to deduce elasticity moduli (the image contrast in the FMM image is scaled from dark (low amplitude, low modulus) to bright (high amplitude, high modulus) contrast). The dark islands correspond to PVC. Reprinted with permission of John Wiley and Sons, Inc. from [120]. Copyright 2003. John Wiley & Sons, Inc.

In the so-called "pulsed force mode" AFM technique developed by Marti and coworkers [124], the data acquisition rates are increased. In this mode, as outlined in Sect. 3.2, the sample is modulated sinusoidally (~ 1 kHz) during a conventional contact mode AFM scan to cause that the tip contacts, indents, and breaks free from the surface with a frequency of ~ 1 kHz during scanning. Instead of recording the complete f-d curve, pull-off forces *and* stiffness are acquired parallel to sample topography at useful scan rates that become possible (Fig. 3.54).

It is straightforward to see that the relative surface coverage of the respective phases can be conveniently determined by image analysis, such as bearing analysis, in the illustrative examples shown above (see also Chap. 2). In addition, one can investigate the often crucially important interface region between the phases (Sect. 3.4.5).

3.4.2 Block Copolymers

Defined diblocks, triblock or multiblock copolymers find important applications in the areas of thermoplastic elastomers, data storage technology [126], *and as compatibilizers (e.g. in polymer blends). In thin films these polymers may display different morphologies than in the bulk, which necessitates an accurate analysis.*

Magerle, Krausch and coworkers showed based on AFM data and simulations that the phase behavior at interfaces [127] and in thin films (interphases) [128] can be understood in terms of analogous to those of classic, inorganic crystals. In Fig. 3.55 thin triblock copolymer films of SBS on silicon are shown, which display a rich variety of morphologies depending on the local film thickness [129].

Similar experimental observations were reported by Lammertink and Vancso (Fig. 3.56). In this case, poly-(isoprene)-b-poly(ferrocenyl dimethylsilane) films

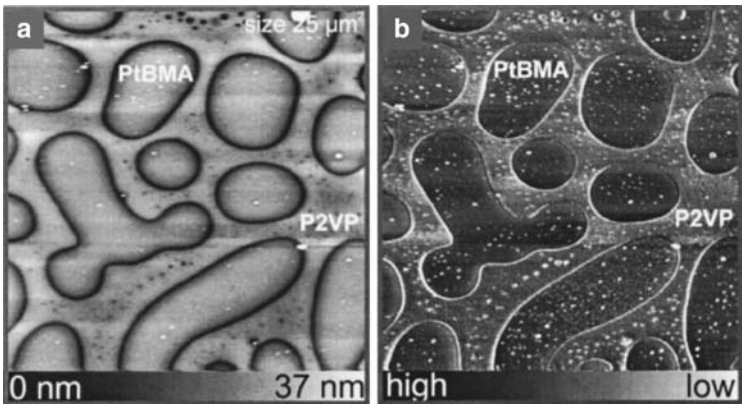

Fig. 3.54 Pulsed force mode measurement on a blend of P2VP and PtBMA spincoated on silicon. The pulsed force mode AFM images clearly distinguish the PtBMA islands from the surrounding P2VP in both topography (**a**) and in adhesion (**b**). (Reprinted with permission from [125]. Copyright 2000. American Institute of Physics)

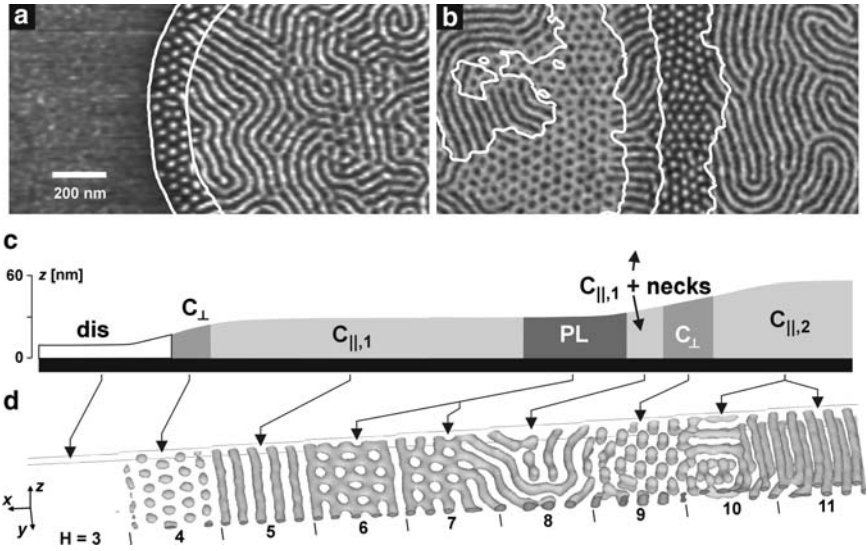

Fig. 3.55 (**a**,**b**) Intermittent contact mode AFM phase images of thin SBS films on silicon substrates after annealing in chloroform vapor. (**c**) Schematic height profile of the phase images shown in (**a**,**b**). (**d**) MesoDyn computer simulation of a $A_3B_{12}A_3$ block copolymer film in one large simulation box with from left to right increasing film thickness. Reprinted with permission from [129]. Copyright 2002 by the American Physical Society

were studied for film thicknesses that were incommensurate with the characteristic domain spacing. These films displayed holes. At the edge of these holes, where the film thickness can be expected to increase gradually, a hexagonal arrangement of

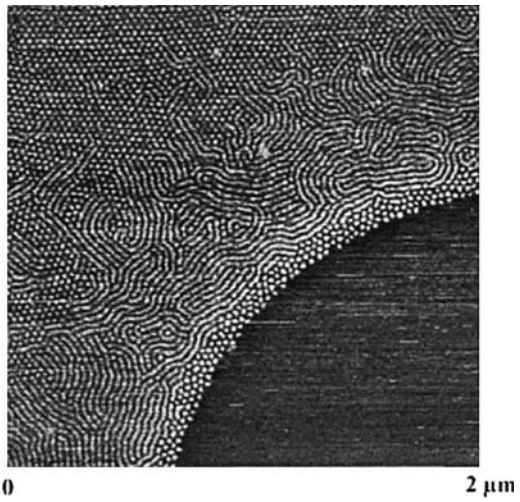

Fig. 3.56 Tapping mode AFM phase image a thin (d_{film} <30 nm) poly(isoprene)-b-poly (ferrocenyl dimethylsilane) (36 kg/mol/12 kg/mol) film displaying different microphase separated morphologies as a function of film thickness. Reprinted with permission from [116]. Copyright 2000. American Chemical Society

the minority component can be observed. An in-plane wormlike morphology can be observed in areas, where the film thickness is higher than the average thickness of the remaining film. Further away from the hole, the hexagonal structure is still present.

Hands-on Example 24

Visualization of Microphase Separated Morphology of Films of Polystyrene-b-polyisoprene-b-polystyrene

Sample Preparation: Solution Casting

Thin films of a commercially available PS-PI-PS triblock copolymer (e.g. from Aldrich, 17% mol PS) can be prepared on freshly cleaved mica[5] by casting from toluene solution, followed by solvent evaporation under ambient conditions, as described in [130]. For this purpose a 30% weight solution of the copolymer is prepared in toluene using a magnetic stirrer. One drop of this freshly prepared

[5]Mica can be conveniently cleaved by placing a piece of pressure sensitive adhesive on top of a planar mica specimen. The tape is carefully peeled off the surface, thus exposing a near atomically smooth, clean surface. In ambient conditions this very hydrophilic surface is rapidly covered with airborne adsorbates.

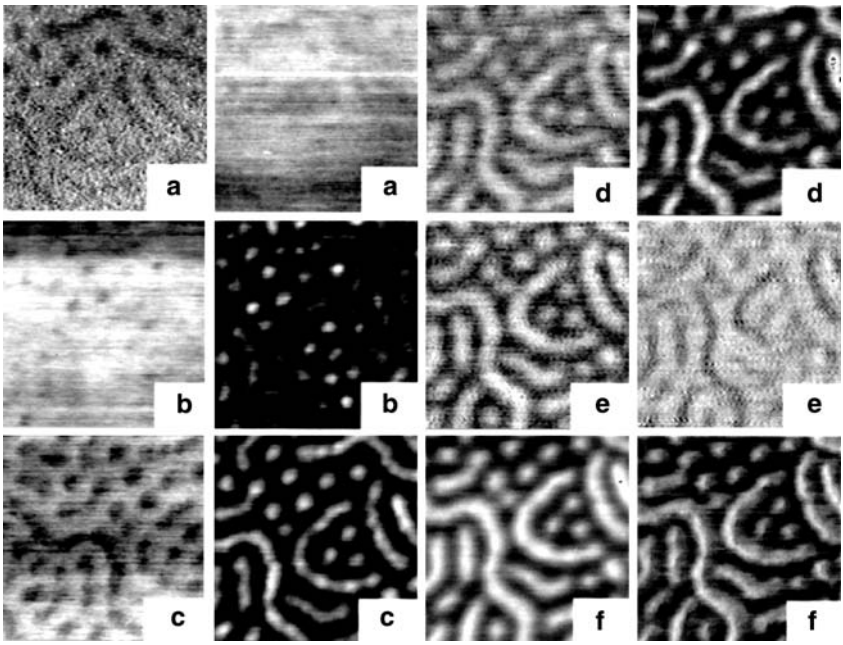

Fig. 3.57 Height (*left*, z-scale 8 nm) and phase (*right*) images (350 × 350 nm^2) of solution cast films of PS-b-PI-b-PS. The data were acquired using the following setpoint ratios A_r: (**a**) 0.99, (**b**) 0.95, (**c**) 0.70, (**d**) 0.50, (**e**) 0.40, (**f**) 0.20. With kind permission from Springer Science+Business Media from [130]. Copyright 1998. Springer

solution is placed on a piece of freshly cleaved mica. The solvent is allowed to evaporate and the films are examined immediately after drying.

TM-AFM Visualization of Microphase Separated Morphology

We use a standard tapping/intermittent contact mode set-up, which is started as described in Sect. 3.2.1. After inserting the TM cantilever into the cantilever holder, the optical head is mounted, the laser is aligned and the resonance peak is analyzed. The operation frequency ν and amplitude A_o are adjusted to ν at 0.85 A_o and 150 nm, respectively. Due to the stickiness of the low T_g isoprene block, this high amplitude is advisable to avoid permanent tip-sample contact/adherence during the scans. Prior to engaging, the phase signal is zeroed. The crude and fine engagement procedures are carried out as described in Chap. 2. After the successful engagement the operation point must be carefully adjusted. As shown in Fig. 3.57, the image contrast depends on the rms amplitude of the free oscillation, but also on the setpoint chosen. For the most faithful imaging of the surface profile it is advised to use minimum imaging forces by increasing the setpoint as close as possible to the rms amplitude of the freely vibrating cantilever. This can be achieved, as mentioned previously, by increasing the setpoint to the point, where the tip can no longer trace

the surface, followed by a slight reduction of the setpoint such that the halo, when traversing elevated objects, vanishes.[6]

The morphology obtained by microphase separation of the PS-PI-PS tri-block copolymer is similar to those investigated in other methods, such as SAXS and TEM. For the particular polymer used, the polystyrene (PS) phase separates into cylinders surrounded by an amorphous polyisoprene (PI) matrix. Since PS is below its T_g and PI is above its T_g at ambient conditions, resulting in very different material properties, contrast can be expected in the phase images. As shown in Fig. 3.57, the microphase separated morphology can be observed, depending on the operation parameters, in both height and phase channels. Typical scan sizes would be larger than those displayed to minimize effects of thermal drift, if the AFM set-up is not yet fully thermally equilibrated.

In this Figure, the dependence of image contrast on the setpoint ratio, also in height mode, are clearly discerned. The variations in the height images are related to the different damping of the cantilever's oscillation, as well as the change of the effective spring constant of the lever owing to tip-sample interactions. The changes in the phase images can be explained qualitatively by the change in energy dissipation for different indentation. For a more in depth treatment, based the work by García et al. [109], we refer to Chap. 1.

The change of relative image contrast renders the assignment of the constituent phases difficult without independent knowledge e.g. about sample composition and hence morphology or independent experimental evidence. Therefore the use of independent AFM measurements, e.g. indentation mapping (force modulation, f-d, A-d curves, see Chap. 2) or electron microscopy measurements are often advisable. In this particular case the phases can be identified based on the knowledge that PS is present in the bulk inside PS cylinders, which are found in some image also in an orientation perpendicular to the film surface.

Hands-on Example 25

Visualization of Microphase Separated Morphology of Hydrolyzed Films of polystyrene-b-poly(tert-butyl acrylate)

Sample Preparation: Spin-coating and Hydrolysis

Thin films of PS_{690}-b-$PtBA_{1210}$ diblock copolymer (e.g. purchased from Polymer Source Company, Dorval, Canada) are prepared by spin coating corresponding polymer solutions in toluene (conc. 10 mg/mL) onto oxygen plasma cleaned silicon wafers.

[6]The setpoint amplitude is adjusted to ~0.9 A_0 to 0.95 A_0. If the tip loses track of the surface during scanning, the setpoint must be slightly reduced. Next the scan size is stepwise increased while the gains are optimized accordingly, which corresponds to vanishing contrast in the amplitude image.

Spinning at 3,000 rpm for 30 s provides films with a thickness of approx. 100 nm. All spin-coated samples are annealed at 135°C for 24 h in vacuum before analysis.

The *tert*-butyl ester groups of the PtBA block can be hydrolyzed under acid conditions by placing them into neat trifluoroacetic acid for 20 min. **CAREFUL !** *Trifluoroacetic acid is very corrosive and should be handled by experienced and properly trained personnel according to published safety rules*. After hydrolysis the films are rinsed three times using Milli-Q water, and are finally dried in a stream of nitrogen.

TM-AFM Visualization of Microphase Separated Morphology

We use a standard tapping/intermittent contact mode set-up, which is started as described in Sect. 3.2.1. The procedures used for imaging are identical to those mentioned for hands-on example 24 except for a, lower amplitude A_o.

Figure 3.58 a and b show AFM topographic and phase images of PS_{690}-b-$PtBA_{1210}$ films (film thickness $\sim$ 90 nm) before hydrolysis. In the height image worm-like domains are observed with a domain spacing of ca. 83 nm. Phase contrast is not so clearly observed, which may be attributed to the glassy character of both blocks of the block copolymer and hence very similar energy dissipation. The mean roughness (R_a), as assessed from 1.0 μm^2 topographical images, is $\sim$ 1 nm.

After hydrolysis of the films, different topographical and phase images are observed, as shown in Fig. 3.58 c and d. Block copolymer microphase separation is more pronounced and the phase images in particular reveal the presence of small features on top of the elevated worm-like features. These observations may be attributed to the fact that the PtBA groups have reacted to polyacrylic acid, which now swells due to uptake of water from the ambient air. The measured roughness increases to $\sim$ 5 nm.

3.4.3 Polymer Blends

Polymer blends find widespread application in various technologies that require materials with a range of properties that are not available with a single component material without synthesizing new polymers. Prominent examples are rubber reinforced thermoplastics in which the microdispersion of a rubber into a brittle polymer matrix provides impact modified materials [132]. *Application areas of blends cover a broad range from biomedical materials to high performance composites in aerospace applications. Also here the analysis, e.g. by means of AFM, of these compositional distributions down to nanometer length scales is of considerable significance.*

In the analysis of polymer blends the identification and subsequently the characterization of the distribution of the components of the blend (surface coverage and dispersion) is of prime interest. The already mentioned materials contrast in various AFM modes provides a straightforward differentiation of, e.g. glassy and rubbery phases (after considering the effect of frequency on the corresponding transition temperatures). As different components in a blend tend to possess different surface

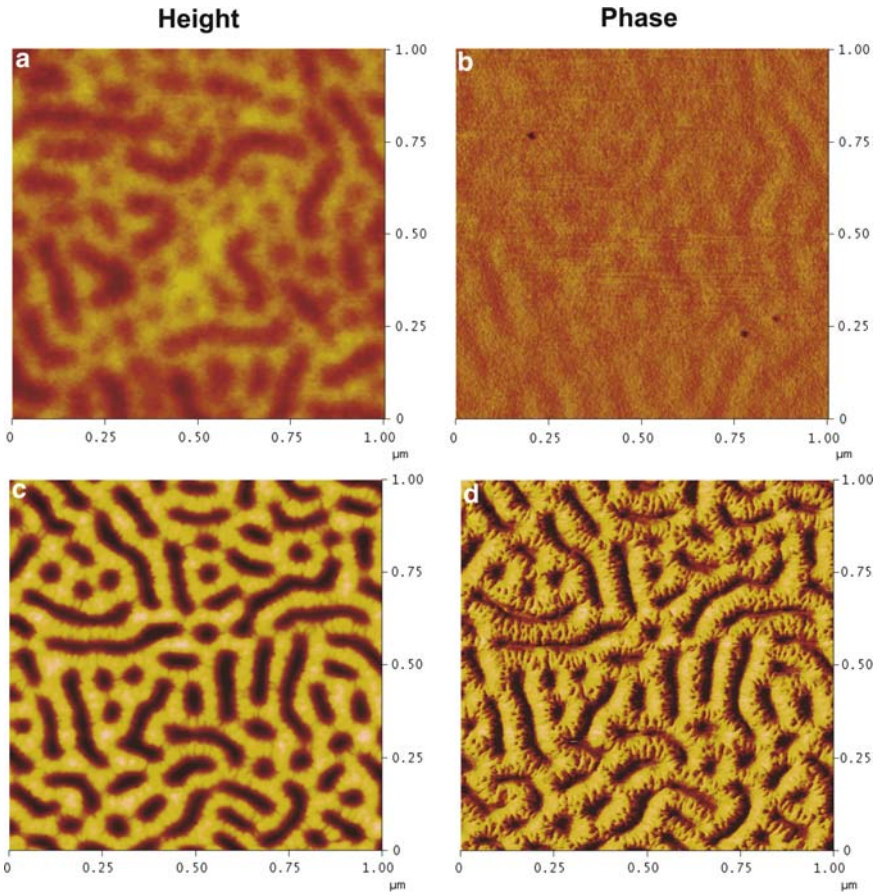

Fig. 3.58 TM-AFM height (*left*) and phase (*right*) images of (**a**, **b**) PS-b-PtBA copolymer film after annealing in vacuum oven, and (**c**, **d**) PS-b-PtBA after hydrolysis in trifluoroacetic acid for 15 min. Reproduced with permission from [131]. Copyright 2005. American Chemical Society

tensions, the free surface of blends is enriched in the component that shows the lower surface tension. In many cases this component forms a skin layer.

The appropriate use of sample preparation procedures to expose the interior (bulk) of a blend of interest is in many cases required. In addition, selective solvent treatments may assist to unequivocally identify the different phase, as illustrated in Fig. 3.59 [133]. In this example, the polystyrene phase in a blend of polystyrene and poly (n-butyl methacrylate) was identified by selective removal of the PS using cyclohexane. Thus the protrusion seen in the height image in panel (a), which are attributed to PS domains, are no longer detectable in panel (b).

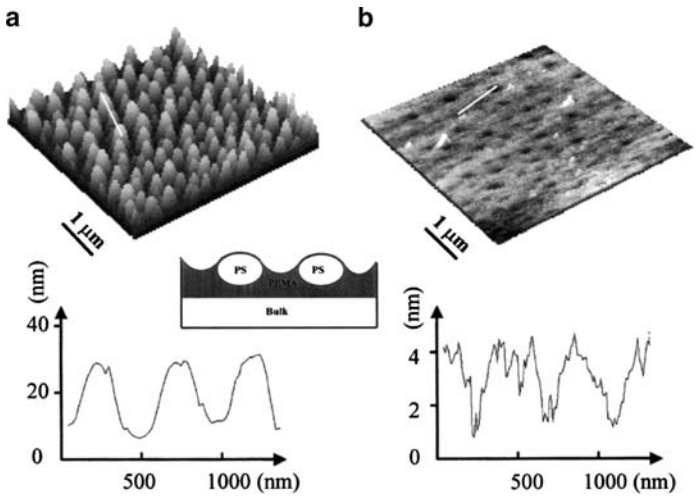

Fig. 3.59 AFM topographic images (*top*) and cross-sectional profiles (*bottom*) of PS/PBMA blend (with 20 wt%PS) thin film before and after being washed by cyclohexane (*inset*: Scheme of phase segregation on PS/PBMA blend (with 20 wt % PS) surface). Reprinted with permission from [133]. Copyright 2002. American Chemical Society

Hands-on Example 26

Identification of Phases in Blends of PMMA and PB

Sample Preparation: Spincoating of Blends

Blends, e.g. 80:20, of poly (methyl methacrylate) (PMMA, weight average molar mass, M_w, of 15,000 g/mol) and polybutadiene (PB, with M_w 420,000 g/mol) (e.g. from Aldrich) are prepared by mixing solutions of a mass fraction of PMMA of 0.02 in toluene and mass fraction of PB of 0.02 in toluene in a ratio of 8:2 followed by spin-coating onto pre-cleaned silicon wafers. Following the spinning, the samples are treated for 24 h at ambient temperatures under vacuum to remove residual solvent. Pieces of the blend-covered silicon wafer are glued to the sample holder disc and inserted into the AFM.

Imaging of Blend of PMMA and PB by TM-AFM

Using the standard TM-AFM procedures (3.2.1), the free surface of the blend thin films can be investigated. Owing to the softness and adherent properties of the PB phase, it is advisable to increase the rms amplitude of the free cantilever oscillation sufficiently.

A typical dual height and phase image of a PMMA–PB 80–20 blend is shown in Fig. 3.60. The height differences observed are small, typically only few nanometers

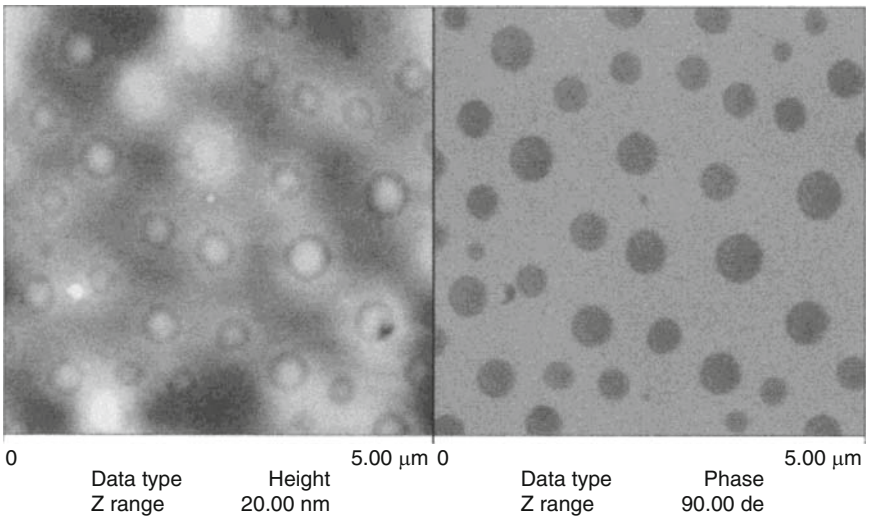

Fig. 3.60 (**a**) Tapping mode AFM height image (*left*) and phase image (*right*) for PMMA – PB 80 – 20 blend after 24 h of ambient conditioning [134]. Contrast variations are 20 nm from *white to black* for the height images and 90° from *white to black* for the phase image. Reprinted with permission from [134]. Copyright 2000. American Chemical Society

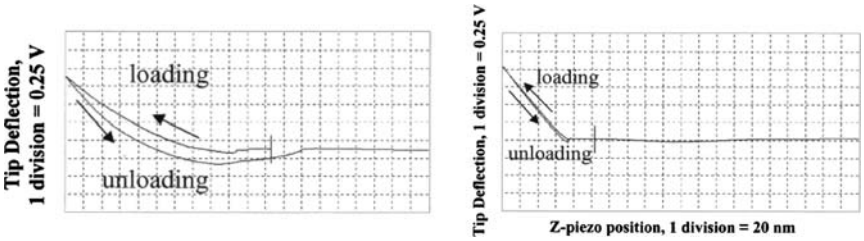

Fig. 3.61 Force curves for (**a**) the PB-rich matrix and (**b**) the PMMA-rich domain for a 20:80 blend sample after 24 h of ambient conditioning and 107 h of annealing. Reprinted with permission from [134]. Copyright 2000. American Chemical Society

peak to valley heights. The phase image shows circular areas with darker image contrast, which corresponds to a pronounced phase lag of the circular areas compared to the matrix. This contrast is consistent with a pronounced energy dissipation in the rubbery phase.

The phase, which can be identified based on the stiffness contrast and the relative abundance of the particular phase, show additionally pronounced differences in force-displacement measurements (Fig. 3.61). Force curves were obtained with the tip probing the regions of interest in the blend films. While a more elaborate analysis of the f-d curves (Sect. 4.3 in Chap. 4) provides information

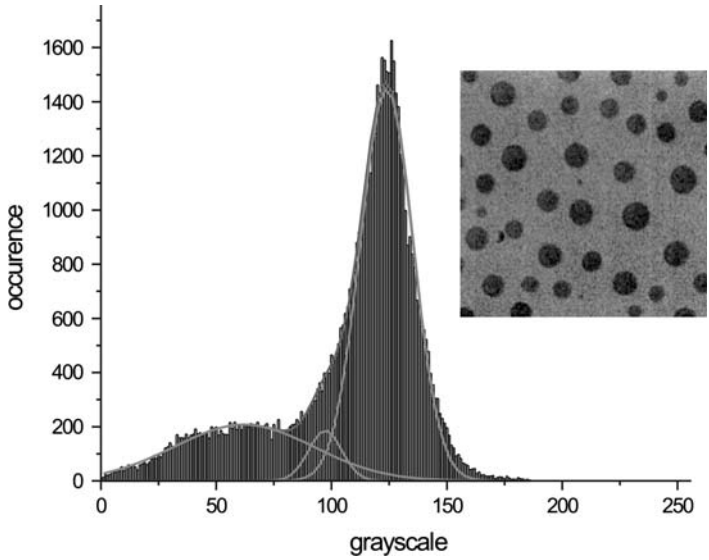

Fig. 3.62 Statistical analysis of the tapping mode AFM phase image (5 × 5 μm^2) for PMMA – PB 80 – 20 blend after 24 h of ambient conditioning [134] shown as *inset*. The distribution of pixel values can be deconvoluted into three components (the corresponding curves have been superimposed on the histogram), thus reflecting the presence of the two distinct phases and a contribution that may originate from possible from tip convolution (or an intermediate phase) at the phase boundaries

about the modulus values [134], the PMMA and PB phases can be qualitatively identified based on their different indentation and adhesion behavior. The slope of the contact region is larger (in fact ∼ 1.0) for the glassy PMMA, while the PB shows a significant hysteresis. This hysteretic f-d behavior is partially related to viscous flow of the PB.

The composition of a blend can be analyzed using a statistical analysis of the height of phase images. This can be done by calculating a histogram of the pixel values for the corresponding image) also referenced to, e.g., the highest pixel value of an image, "bearing analysis", described in detail in Chap. 2). As illustrated for the phase image shown in Fig. 3.60 one obtains a distribution of pixels with particular values of the phase signal. In this binary blend we observe a multimodal distribution that can be analyzed by peak fitting procedures to estimate the relative coverage (i.e. the composition at the exposed surface). In this case one can calculate, using standard image processing software the relative coverages (for a list of shareware, see Part III). For the image shown below, one observes a coverage of ∼26% for the minority component (dark phase contrast) and ∼69% for the majority component (bright phase contrast). An area of approximately 5% is occupied by a third contributor, which may be related to the domain boundaries (Fig. 3.62).

Hands-on Example 27

Identification of Phases in Blends of Impact Polymers by FMM

The identification of phases in polymer blends can be accomplished in force modulation mode (FMM) AFM. Using FMM AFM the relative moduli (a convolution of storage and loss moduli) are mapped on the specimen surface. The rms amplitude of the FMM cantilever, driven in an oscillatory fashion, reflects directly the modulus of underlying polymer specimen. In the blend discussed below three phases can be differentiated.

Sample Preparation: Cryomicrotoming (Cryofacing)

For cryofacing, the samples (an impact copolymer (ICP) composed of a polypropylene (PP) matrix with high-ethylene (60 wt.%) ethylene–propylene copolymer (EP) domains, available, e.g. from: ExxonMobil) are microtomed using a glass knife at a temperature of –150°C. Instead of analyzing the microtomed slices, the bulk specimen with the freshly exposed (cryofaced) surface will be analyzed. Moisture condensation can be avoided if samples are allowed to warm to ambient temperatures in a dessicator filled with nitrogen [135]. Cryofaced specimen should be transferred to the AFM sample holder disk with minimal delay.

Imaging of a Ternary Blend by FMM AFM

For the FMM AFM experiments, rectangular Si cantilevers (225 μm long, 30 μm wide, approx. force constant of 0.4 to 1 N/m) are inserted into the FMM cantilever holder. The cantilever is tuned as described in the manual of the AFM. Typical excitation frequencies for these cantilevers using the integrated bimorph are ∼11 kHz. Subsequently, the AFM is adjusted according to the standard contact mode AFM protocol (see Sect. 3.2.2).

The tip is thus engaged similar to contact mode AFM. Scan rates of 1 Hz and low imaging forces are advisable to minimize possible impact of lateral forces. During each scan line the tip periodically indents the sample surface. From the feedback loop correction for the z-component for each pixel a topography (height) image is obtained; the simultaneously recorded rms cantilever amplitude provides a stiffness map [117].

As shown in Fig. 3.63, FMM AFM allows one to differentiate among the three phases present in the sample, i.e., the EP, PE, and PP phases [135]. While these phases can already be discerned based on a comparison of topographic AFM images and TEM data, force modulation mode AFM provides a clear modulus-based differentiation: EP as the softest phase shows the lightest contrast, followed by the crystalline PE phase and the PP with increasingly darker contrast reflecting the decreasing extent energy dissipation. These data are very much in agreement with TEM data. Yet it has been noted that no staining or thin

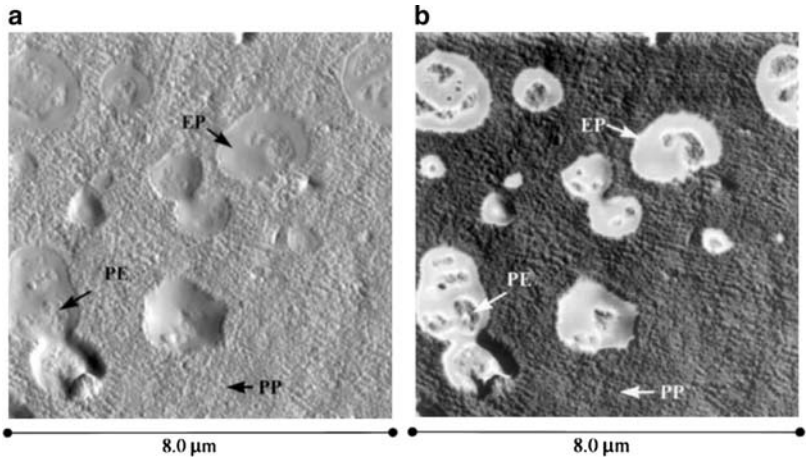

Fig. 3.63 Micrographs of an impact copolymer (ICP) composed of a polypropylene (PP) matrix with high-ethylene (60 wt.%) ethylene–propylene copolymer (EP) domains: (**a**) topography image of the cryogenically faced ICP. The presence and morphology of the three polymeric phases are indicated by the topography. (**b**) Force modulation image of the cryogenically face ICP (the image contrast in the FMM image is scaled from bright (low amplitude, low modulus) to dark (high amplitude, high modulus) contrast). A pronounced modulus contrast associated with the three polymers is observed. Reprinted with permission of John Wiley & Sons, Inc. from [135]. Copyright 1997. John Wiley & Sons, Inc.

sectioning is required for AFM analyses, thus making sample preparation more convenient.

3.4.4 Filled Polymer Systems

Polymers, as well as elastomers, are reinforced by the addition of small filler particles. The performance of rubber compounds (e.g. strength, wear resistance, energy loss, and resilience) can be improved by loading the rubber with particulate fillers. Among the important characteristics of the fillers, several aspects can be successfully interrogated by AFM approaches. For instance, the particle and aggregate size, the morphology, and in some cases the surface characteristics of the filler can be assessed.

In semicrystalline polymers, fillers may act as reinforcement, as well as nucleation agents. For example in PP, nanoscale silica fillers may nucleate the crystallization resulting in spherulites that show enrichment in particles in the center of the spherulite (Fig. 3.64). For a quantitative analysis of, e.g., filler sizes and filler size distributions, high resolution imaging is necessary and tip convolution effects [137–140] must be corrected for. The particles shown below are likely aggregates of filler particles considering the mean filler size of 7 nm [136].

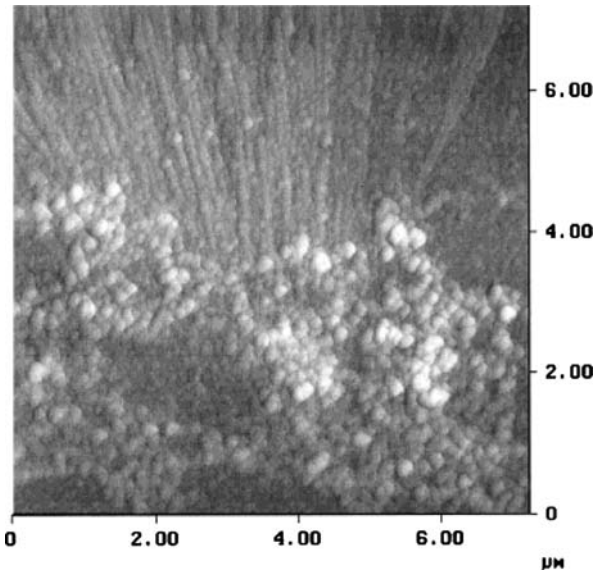

Fig. 3.64 Tapping mode AFM height image of $KMnO_4$-etched nano-SiO_2/PP: Reprinted with permission of John Wiley & Sons, Inc. from [136]. Copyright 2001. John Wiley & Sons, Inc.

Hands-on Example 28

Distribution of Filler Particles in Elastomers by TMAFM

It is well known that the reinforcing potential of fillers can only be realized if a good dispersion of the filler is achieved. Traditionally, various carbon blacks have been used as fillers, more recently (modified) silica particles are being increasingly utilized. As shown below, the filler distribution can be directly assessed by AFM.

Sample Preparation: Cutting and Pressing

Particulate filled EPDM rubber can be produced via conventional mixing procedures as described in [141]. Pure precipitated silica (Ultrasil® VN3) and silica modified with a commerically available organosilane (Si 69), as well as carbon black (N 550) are employed as fillers.[7] Unvulcanized samples for AFM observation are prepared by cutting small pieces of the compounds using a scalpel knife [(cryo)

[7]The EPDM rubber used was Keltan® 512, produced by DSM Elastomers. Pure precipitated silica (Ultrasil® VN3) and silica modified with the organosilane (Si 69), as well as carbon black (N 550) were employed as fillers. Masterbatches without curing additives were mixed in a Shaw K1 Mark IV intermeshing mixer of DSM Elastomers Europe BV. Mixing was stopped once the compounds reached a temperature of ca. 110° C. The mixing conditions are given in below. Masterbatches without curing additives were mixed in a Shaw K1 Mark IV intermeshing mixer of DSM Elastomers Europe BV. Mixing

microtoming is more time consuming, but leads to better results, see Chap. 2] and by pressing them between two glass slides in order to flatten the surface. The samples are left to relax at least for 24 h in ambient conditions. Afterwards they are glued onto AFM sample holders.

Intermittent Contact Phase Imaging of Filler Distributions

We use the standard TM-AFM procedures (3.2.1) for the investigation of the filler distribution. To enhance the phase contrast, the AFM is operated at moderately high amplitude (150 nm) and a setpoint ratio of ~0.7. The height images display large scale corrugations which are a result of the cutting process and subsequent relaxation of the material. However, close inspection of the height images shows some evidence of particles on the surface. These particles are seen in superior contrast in the phase image, as the topographic variations do not interfere.

The size of the filler aggregates can be determined by evaluating the cross-section of the particles in cross-sectional plots of the phase images. The results are then plotted as histograms. In the analysis shown, large aggregates with sizes larger than 300 nm were not included in the statistical analysis. The histograms show a broad distribution of grain sizes, the maximum, however, coincides with the expected primary particles size (Fig. 3.65).

was stopped once the compounds reached a temperature of ca. 110° C. The mixing conditions are given in further below.

Ingredients (phr)	1	2
Kelton® 512	100	100
ZnO	3	3
Stearic acid	1	1
Ultrasil®VN3	50	–
Si 69	4	–
Sunpar® 2280	30	30
MBT	–	–
TMTD	–	–
Sulfur	–	–
N 550	–	50
Mixer acquisition	1	2
Load factor (%)	54	54
Power max (kW)	50	49
Power end (kW)	40	37
Tbatch max (oC)	113	108
Tbatch end (oC)	112	107
E motor (MJ/m3)	7	6
E water (MJ/m3)	56	−7
Mix time (sec)	312	205

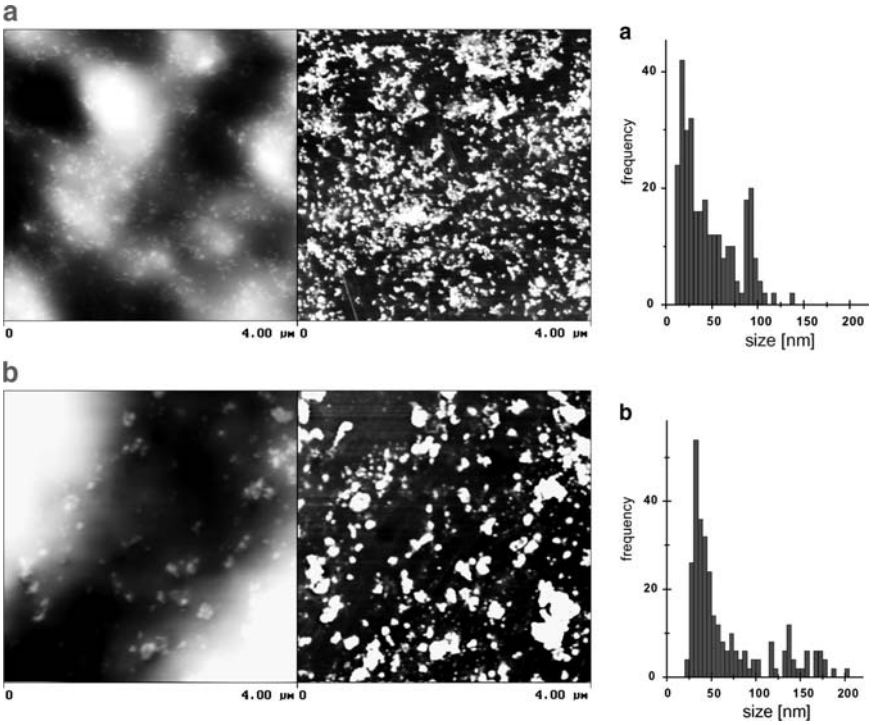

Fig. 3.65 *Left*: TM-AFM images (*left*: height, *right*: phase) showing the filler microdispersion in the unvulcanized compounds. (**a**) unvulcanized EPDM filled with modified silica (Compound 1) (z-scale: height, 310 nm, phase, 30°); (**b**) unvulcanized EPDM filled with carbon black (Compound 2) (z-scale: height, 365 nm, phase, 35°). *Right* (**c**), (**d**): filler distributions as determined from the analysis of the phase images (**a**) and (**b**) Reproduced with permission from reference [141]. Copyright 1999. American Chemical Society

Hands-on Example 29

Distribution of Filler Particles in Rubbers by PF mode AFM

Sample Preparation: Microtoming

Natural rubber (polyisoprene, PI) mixed with 1.8 PHR DCP for chemical cross-linking and 15 PHR carbon black N660 (Degussa AG, Hürth, Germany) with a primary particle diameter of 67 nm [142] is microtomed at low temperatures to provide ~ 10 µm thin slices with smooth sample surfaces. These slices are mounted on metallic sample holder discs using pressure sensitive adhesive.

Pulsed Force Mode Imaging of Filler Distributions

We use the standard pulsed force mode-AFM procedures (Sect. 3.2.4) for the investigation of the filler distribution. A contact mode AFM cantilever with a spring

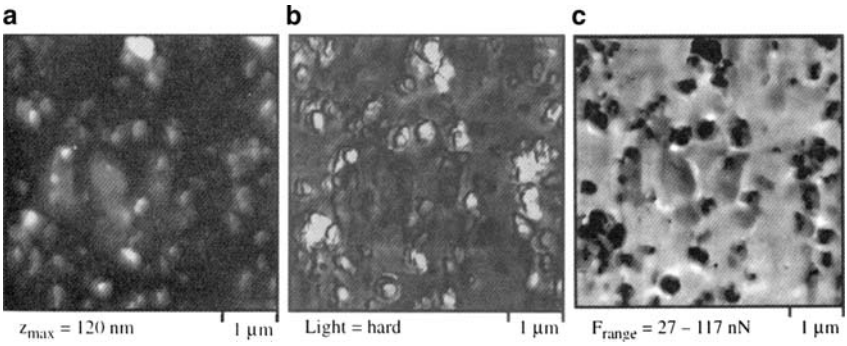

Fig. 3.66 Pulsed force mode AFM images of carbon black filled rubber: (**a**) height, (**b**) stiffness, (**c**) adhesion image. Reproduced with permission from [142]. Copyright 1998 American Chemical Society. The image contrast in the images (**a**. height, **b**. stiffness, **c**. pull-off force) have been scaled from dark (low values of property) to bright (high values of property) contrast

constant of ~0.5 to 1.0 N/m is inserted into the cantilever holder. The laser alignment and crude approach are carried out as described for contact mode AFM (3.2.2). For pulsed force mode, a modulation frequency in the range of 800–1,200 Hz is selected and the cantilever oscillations are adjusted such that the adhesive interactions between tip and surface are overcome, as monitored using an oscilloscope. The modulation must clearly show the snap-off of the tip. Next, the four markers are set according to the general procedure outlined in Sect. 3.2.4.

By appropriate selection of the markers for stiffness and adhesion, it is possible to differentiate the rubbery matrix (low modulus, high adhesion) and the filler particles (high modulus, low adhesion). As shown in Fig. 3.66, elevations in the height image corresponds well with areas of higher stiffness and lower adhesion. The carbon black particles can be observed in a non-homogeneous distribution at the surface of this microtomed specimen.

3.4.5 Interfaces and Interphases in Composites

Glass fiber reinforced polymers and resins have found widespread application as light weight construction materials. In addition, the properties of interfaces and interphases play a crucial role in determining the ultimate mechanical and other properties in these and related applications. Since the corresponding length scales can be on the far sub-micrometer level, a more detailed insight requires local analysis techniques which provide materials contrast.

Intermittent contact mode phase imaging is, similar to force modulation and pulsed, force mode, sensitive to differences in materials properties. In Fig. 3.67 (a), the stiffness difference between glass and a polymer-based matrix gives rise to excellent image contrast. In addition, the different components of the polymer blend can be recognized (compare schematic in Fig. 3.67 (b)).

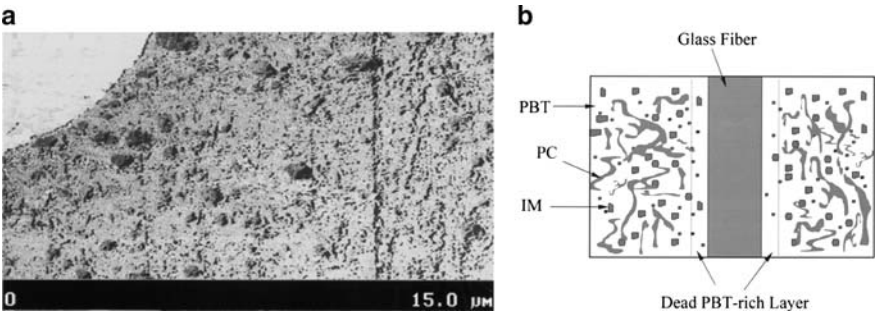

Fig. 3.67 (**a**) AFM phase images of (**a**) (PBT/GF)/IM; (**b**) Schematic representation of the phase structure of the (PBT/GF)/IM/PC composites. Reproduced with permission from [143]. Copyright 2001. Elsevier

In a recent study, the interphases for different fiber/polymer matrix systems were investigated. By using phase imaging the differences in local mechanical property variation in the interphase of glass fiber reinforced epoxy resin (EP) and glass fiber reinforced polypropylene matrix (PP) composites could be unraveled. As shown in Fig. 3.68, the glass fiber, the interphase and the PP matrix can be differentiated based on their surface mechanical properties as assessed qualitatively by TM phase imaging.

Hands-on Example 30

Morphology of Transcrystallized Isotactic PP Induced by Pulling of a Carbon Fiber

Sample Preparation: Melt-Crystallization, Sectioning and $KMnO_4$ Etching

A single high modulus carbon fiber is placed between two isotactic polypropylene (iPP) films [(iPP) of injection-molding grade (e.g. Tipplen H-523, Tisza Chemical Works Ltd, Hungary, with $M_w = 5.2 \times 10^5$ g/mol, melt flow index of 4 g/10 min at 230°C and 21.2 N load] and is melted at 220°C for 5 min. After remelting the sample at 220°C in a hot stage, the specimen is quickly cooled (at a rate of ca. 8°C/min) to the isothermal crystallization temperature T_c of $\sim$ 125°C. The carbon fiber was then pulled manually as described in [145]. The interface of the fiber/iPP composite is exposed by $KMnO_4$ etching [146].[8]

[8]Caution! Consult appropriate literature and ensure that safety regulations are being followed. Strong oxidants and acids are used. *Conditions*: 0.7 % w/v of potassium permanganate in a mixture of sulfuric acid (95-97%, Merck) and phosphoric acid (85%, Aldrich) in the volumetric ratio of 2:1. Specimens are etched in 0.7 % w/v of the permanganic solution at room temperature typically over 5 h. The etched

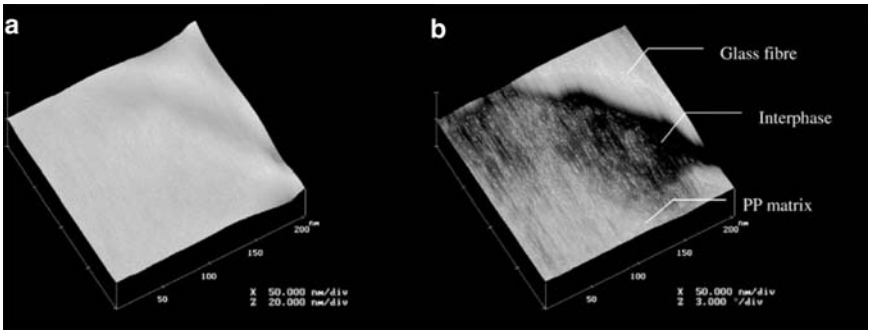

Fig. 3.68 AFM 3D (**a**) topographic and (**b**) phase images of interphase in APS/PU sized glass fibre/PP matrix composites. With kind permission from Springer Science+Business Media from [144]. Copyright 2001. Springer Verlag

Imaging of Fiber-Polymer Interface and Interphase using Contact Mode AFM

The etched iPP film is glued to the sample holder using pressure-sensitive adhesive and left for several hours to relax. A large area scanner (100 μm) and soft cantilevers ($k_c \sim 0.1$ N/m) are used and the standard CM-AFM procedure (3.2.2) is applied. After successful engagement with minimized forces, the operation point is adjusted to minimum imaging forces with the help of force-distance plots. Next the scan size is stepwise increased while the gains are optimized accordingly. Images of the iPP film can be captured at different levels of magnification. For image sizes between ca. 10 and 100 μm a scan rate of several to 1.0 Hz is usually appropriate. Since the film may be quite rough overall the scan rate must be reduced when scan ranges exceed 10 μm in order to protect the probe tip.

In the contact mode AFM height images the fiber (Fig. 3.69 a), as well as different morphological iPP features can be discerned. The appearance of these features close to the fiber is consistent with α-row nuclei, while the emanating lamellar features can be attributed to β-phase lamellae, in conjunction with optical microscopy observations [147]. The fine details discernible even at this level of resolution thus provide important insight into the interphases present. Higher resolution measurements, also by means of using intermittent contact mode AFM, enable one to obtain an even more detailed insight.

samples are washed with a diluted sulfuric acid in the volume ratio of 2:7 in distilled water, which is cooled to near the freezing point with ice to prevent the heat of dilution of the original acids from affecting the sample surface. This solution is subsequently decanted. The samples are then washed with hydrogen peroxide (35%) to reduce any remaining manganese dioxide or permanganate. The final step is to wash the sample(s) several times with distilled water, and finally with acetone.

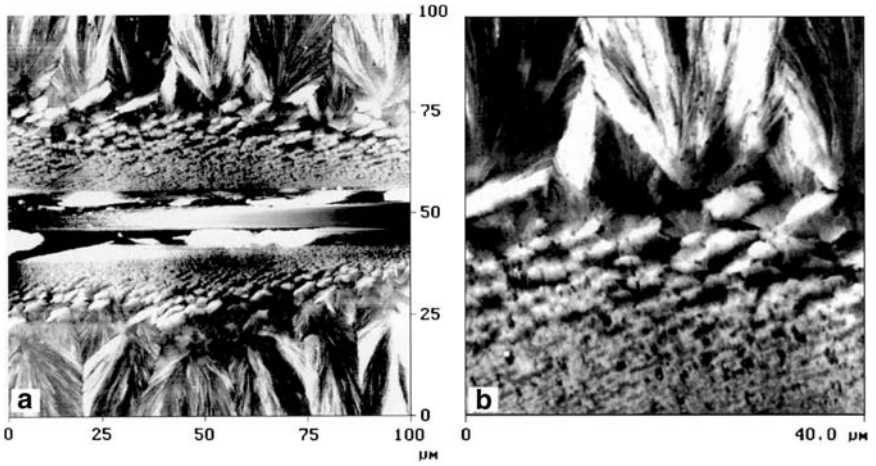

Fig. 3.69 (**a**) AFM height image of the alpha beta-cylindritic columnar morphology of transcrystallized isotactic PP induced by pulling of a carbon fiber. The lamellar growth occurs during epitaxial crystallization on bundles of extended isotactic PP chains, which form during shearing of the polymer matrix by fiber pull. (**b**) Close up scan in region displaying α-row nuclei (*bottom*) and β-phase lamellae (*top*). Reprinted with permission from [147]. Copyright 1997. Steinkopff Verlag

3.5 Polymers in Applications: Effects of Processing and Processes

3.5.1 Polymers in Applications

Single or multicomponent polymer systems are applied in very diverse fields ranging from commodity plastics to high performance functional materials. In many of these applications, the surface morphology and properties are, key to the desired performance. Since various classes of polymers are being subjected to a wide range of processes during manufacture and processing, the impact of the type of polymer, as well as the processing, on morphology, properties and thus ultimately performance if appropriate sample preparation methods are applied. In this chapter, some key examples are treated in detail to provide an overview of representative cases that are met by the practitioner.

In the context of polymers in industrial applications a number of key issues can be identified that are amenable to direct investigation and analysis by AFM approaches. From the preceding chapters the potential of probe microscopic techniques to conveniently visualize for instance surface (or bulk) morphologies and filler distributions has become obvious. Different classes of polymer materials, such as for instance thermoplastics, latexes, porous materials for membranes or thin films are subjected to different types of processing and treatments. The impact of all these modifications and the dependence on the process parameters can hence be closely monitored and in many cases quantitatively characterized by AFM.

As an illustrative example, we begin with well known spatial variations in morphologies on specimens of semicrystalline polymers as a consequence of (1) rapid, nonisothermal cooling from the melt and (2) forces exerted on the polymer during processing (deformation and orientation). Variations in temperature (and pressure) and contact with a counter surface may result in different morphologies along the surface of the polymer sample, but also in the surface's normal direction. The changes in morphology of melt-processed polyolefins from the surface into the bulk of the polymer product (in this case an extruded HDPE pipe [148]) is a good example (Fig. 3.70). Here the HDPE was subjected to differences in temperature as a consequence of the local temperatures in the production process (the outer specimen surface was water-cooled). Since the temperature differences present lead to altered

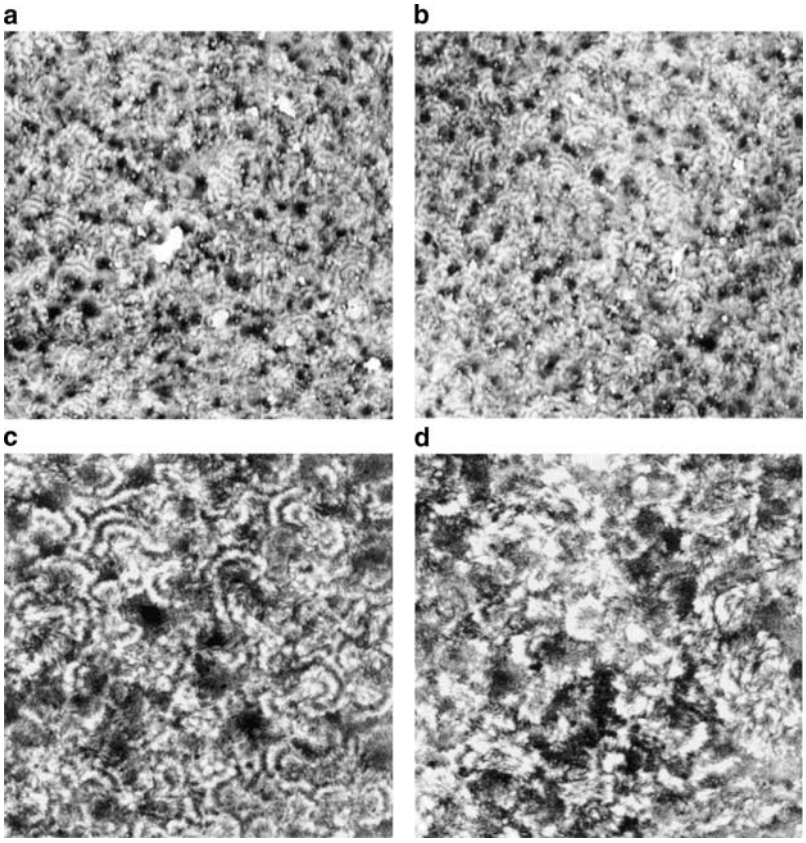

Fig. 3.70 CM-AFM height images of the cross-section of etched specimens transverse to the extrusion direction of extruded HDPE pipes: (**a**) cooled edge; (**b**) midway between the cooled edge and the middle; (**c**) middle; (**d**) non-cooled edge. In all images, the cooling direction is from the *bottom to the top*. Scan size: $40 \times 40\ \mu m^2$. Gray scale for the feature heights: *black* = 0.0 nm; *white* = 1.20 µm. Reprinted with permission of John Wiley & Sons, Inc. from [148]. Copyright 1997. John Wiley & Sons, Inc.

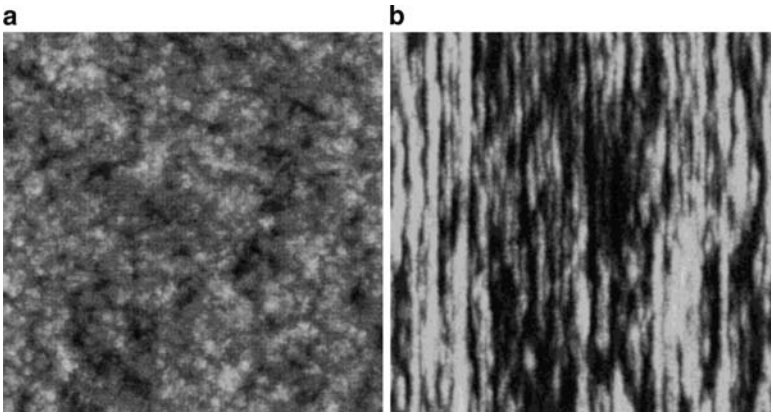

Fig. 3.71 Intermittent contact mode AFM height of (**a**) an un-stretched blown film of hexene linear low density polyethylene and (**b**) a film that was placed under stress (in the vertical direction) leading to an extension of 250%. Image dimensions are 20 × 20 μm^2. Reprinted with permission of John Wiley & Sons, Inc. from [149]. Copyright 2002. John Wiley & Sons, Inc.

crystallization conditions, they cause structural differences in the material which can result in variations in orders of magnitude of the mechanical characteristics of PE. While skin–core morphologies are usually observed in injection-moulded plastics, the pipes studied by Trifonova et al. showed a gradual morphology transition. The size of the banded spherulites, which are well known for PE, clearly varied.

Similarly, the re-orientation effects due to tensile forces in post-blowing tensile deformation can be unraveled down to sub-micrometer length scales in such materials (Fig. 3.71).

3.5.2 Polymer Processing

During polymer processing non-isothermal crystallization conditions, mechanical deformation, and shear forces may alter the morphology and orientation of polymers both at the surface and in the bulk. In addition, orientation effects of semi-crystalline polymers that crystallize in contact with solids are considered.

Altered interfacial morphologies as a result of shear, temperature gradients or contact with a wall (or filler) material are encountered in various applications, as mentioned. The application of AFM to such polymer-related questions in practice and the choice of the imaging mode and contrast mechanisms follow closely with the guidelines and general recommendations of the previous chapters. The AFM techniques discussed are applied to ‘real’ samples and, apart from general considerations regarding primarily the roughness of the samples, there are no fundamental differences.

One example is the toughening of HDPE by rubber or calcite particles. To address this issue, the morphology and orientation of polyethylene in thin films

crystallized non-isothermally in contact with calcite and rubber substrates has been investigated by Kowalewski and co-workers [150]. The contact mode AFM deflection images in Fig. 3.72 display the changes in morphology of these films as a function of film thickness (and hence distance to the interface) after non-isothermal crystallization.

A preferentially and a sheaf-like aggregation with random in-plane orientation are observed for the thinner films (thicknesses of 0.1, 0.2 and 0.4 μm in panels a–c). By contrast thick films (0.6 μm and thicker, panel d) show a morphology that resembles the well known (bulk) spherulitic form with a banded structure, characteristic of linear polyethylene crystallized from the melt at moderately high undercooling.

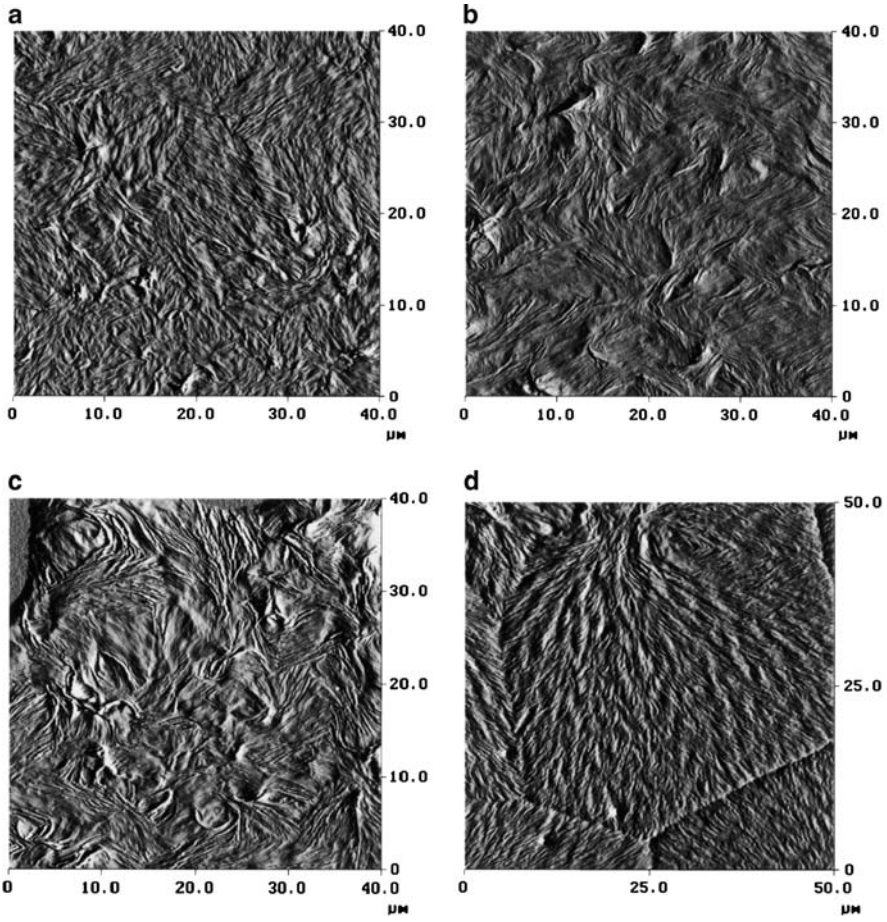

Fig. 3.72 Contact mode AFM deflection images of thin films of HDPE crystallized on calcite surface with the film thicknesses of: (**a**) 0.1, (**b**) 0.2, (**c**) 0.4 and (**d**) 0.6 μm. Reproduced with permission from [150]. Copyright 1999. Elsevier

Opdahl and Somorjai studied the surface deformation and surface elastic properties of stretched polyethylene in a device depicted in Fig. 3.73. It was found that the surface textures of both HDPE and LDPE changed and that the nodular structures present at the surface lengthened in the direction of the stretch and contracted perpendicular to the stretch at various elongations. This resulted in a roughening of the surface.

Hands-on Example 31

AFM Imaging of Processed Polymers (1): Blown Films of High Melt Strength Polypropylene (hmsPP)

Sample Preparation: Microtoming and permanganate etching

In this example we follow the procedures reported by Hiltner, Baer and co-workers [152]. Pellets and blown thin films of hmsPP (The Dow Chemical Company) are investigated. The hmsPP discussed below is a modified impact resin with 16 wt% of an ethylene–propylene rubber (EPR). To reveal the morphology in the machine or extrusion direction (MD) and in the transverse or blow-up direction (TD), pieces of film are sandwiched between two sheets of partially cured embedding media (SPI-PON 812) from Structure Probe Inc. and are cured at 75°C for 10 h under light pressure. Partial curing prevents diffusion of the embedding media into the films. The embedded specimens are trimmed with a diamond band saw, polished, and microtomed with a glass knife at a sample temperature of –50°C and knife temperature of –40°C with a cutting rate of 2 mm/s. Pellets of hmsPP were compression molded at 230°C and microtomed for examination in the AFM.

To reveal the morphology normal to the film surface (ND), films are etched with a 0.7 wt% solution of potassium permanganate in a 2:1 (v/v) mixture of concentrated sulfuric acid and 85% orthophosphoric acid [153]. Specimens are etched for 2–4 h until the thickness is reduced by 40–60%. Etching preferentially removes the amorphous phase thereby revealing the lamellar morphology. Finally, the etched and microtomed specimens are rinsed with methanol and blown dry with compressed air or nitrogen.

TM-AFM Visualization of the Morphology

We use a standard tapping/intermittent contact mode set-up, which is assembled as described in Sect. 3.2.1. After inserting the TM cantilever into the cantilever holder, the optical head is mounted, the laser is aligned and the resonance peak is analyzed. The operation frequency and amplitude are adjusted to v at 0.85 A_o and 100 nm, respectively. Prior to engaging, the phase signal is zeroed. The crude and fine engagement procedures are carried out as described in Chap. 2 and Sect. 3.2. After the successful engagement the operation point must be carefully adjusted to maximize the contrast between the EPR and PP phases present (compare

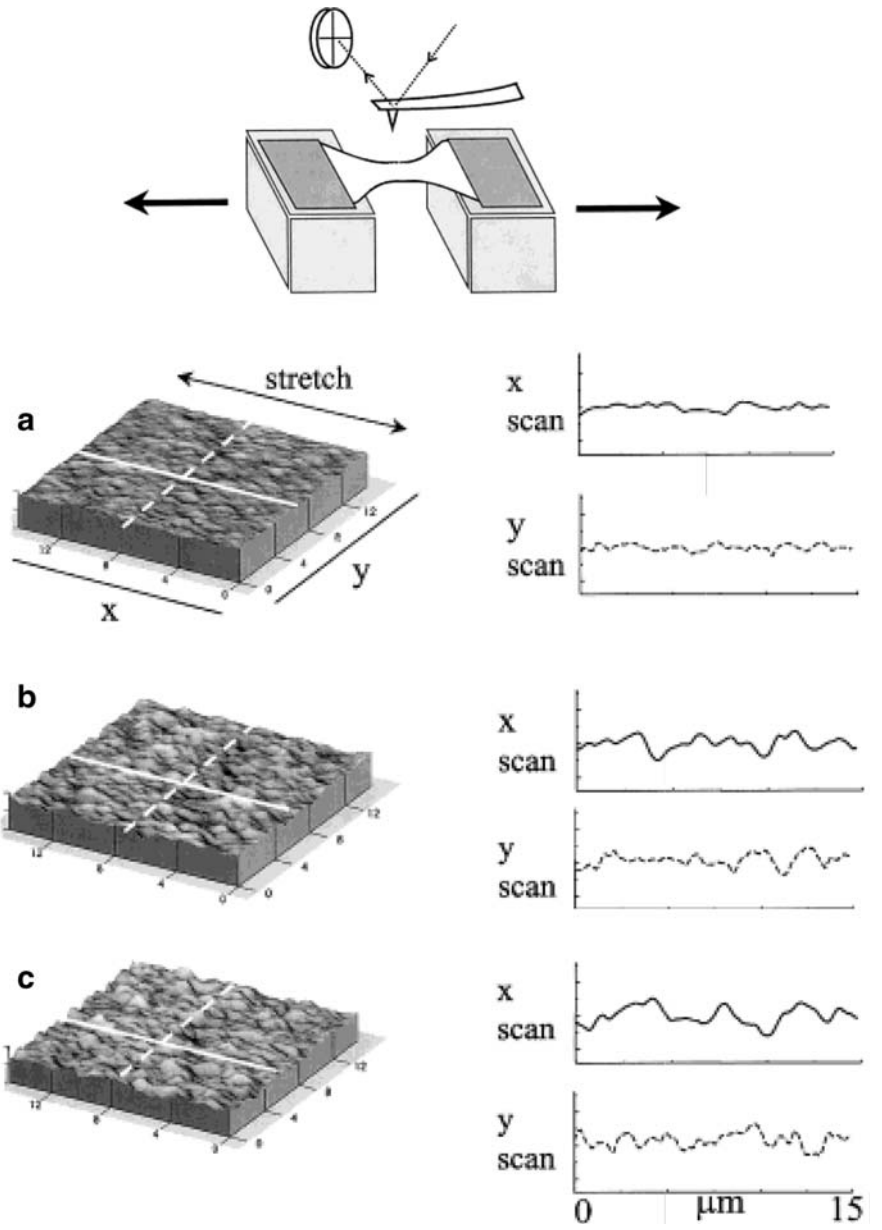

Fig. 3.73 *Top*: Schematic of the combined AFM – stretching experiment and *bottom*: (15 μm)^2 AFM images of LDPE at (**a**) 7.5% elongation, (**b**) 17.5% elongation, and (**c**) 27.5% elongation. Reproduced with permission of John Wiley & Sons, Inc. from [151]. Copyright 2001. John Wiley & Sons, Inc.

Sect. 3.4.2). The use of hard tapping conditions with an amplitude setpoint A/A_0 ratio of 0.5 is suggested.

In the intermittent contact mode phase images shown in Fig. 3.74 a clear contrast between the constituent phases can be observed both for the compression-molded hmsPP (panel a), as well as for the blown film (in the machine and transverse direction in panels band c, respectively). The soft EPR phase appears with dark phase contrast indicating that a substantial amount of energy is dissipated in this phase compared to the PP phase. The EPR particles measure 1 μm or smaller in diameter dispersed in the polypropylene matrix. The horizontal lines and the occasional vertical streaks in the images are artifacts of microtoming.

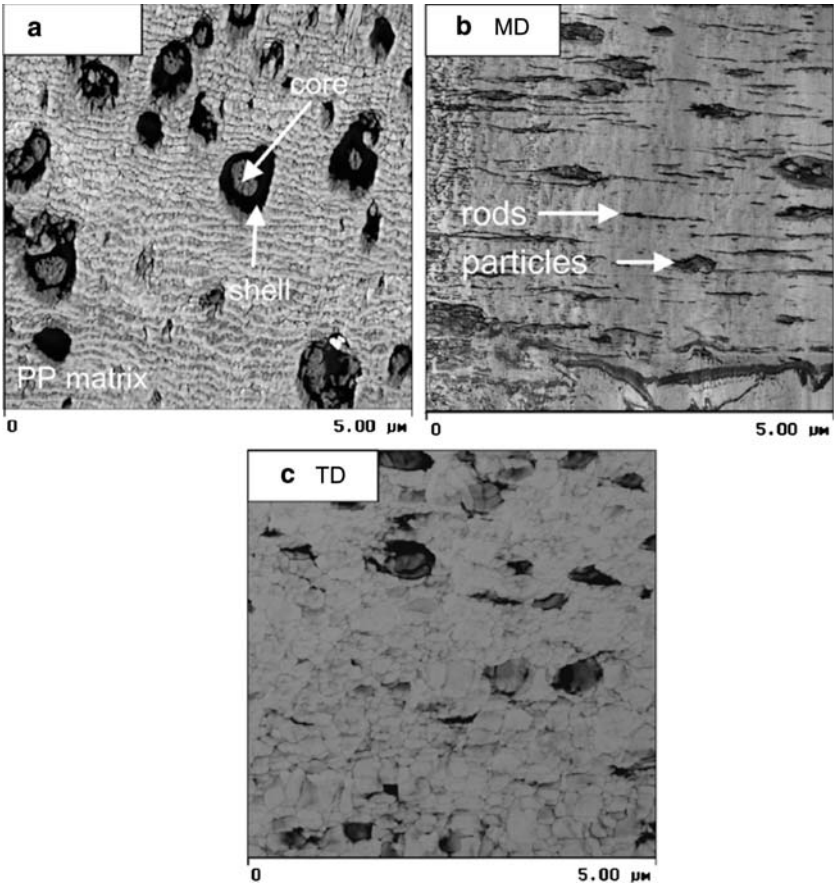

Fig. 3.74 Intermittent contact mode AFM phase images obtained with an amplitude setpoint ratio of 0.5 on (**a**) compression molded high melt strength polypropylene and microtomed sections of hmsPP blown film in the (**b**) machine direction (MD), and (**c**) the transverse direction (TD). Reproduced with permission from [152]. Copyright 2002. Elsevier

The oriented structure of hmsPP *blown* films is revealed in AFM phase images of cross-sections microtomed parallel (MD) and perpendicular (TD) to the extrusion direction. The softer EPR phase is recognized as large elongated domains (particles) and as very thin dark streaks (rods) aligned in the extrusion direction, panel b (MD view). Baer and co-workers attribute the large particles to particles that contain hard granular subparticles of crystallizable EPR, whereas the elongated rods comprise exclusively soft amorphous material. In the transverse view circular EPR domains and small patches are observed which are attributed to cross-sections of the large domains and cross-sections of the dark streaks detected in the MD view, respectively (panel c). These data lead to the overall conclusion that the EPR phase is present in blown hmsPP films in the form of elongated particles that contain the crystalline fractions and as long thin rods that consist of amorphous chains.

Hands-on Example 32

AFM Imaging of Processed Polymers (2): Surface Roughness and Haze

Sample Preparation

The free surfaces of blown PE films (blends of linear low density and high density polyethylene, First Brands Cooperation Canada) and calendered iPP films (isotactic polypropylene films, SOLVAY ELTEX P KL 177) [154] are investigated in the following examples using (1) contact mode AFM and (2) intermittent contact mode AFM. The direct imaging of the surface topography and the analysis of the surface roughness is possible in both AFM modes. Naturally, care has to be taken in the contact mode to limit the imaging forces to a minimum to avoid sample deformation.

CM-AFM Visualization of the Morphology

The AFM is set up for a standard CM experiment (Sect. 3.2.2). To be able to address the morphology and roughness on various lateral length scales, a large area scanner is selected. After the sample (film firmly attached to the sample puck with double sided sticky tape) has been mounted, care has to be taken to note the relative orientation of cantilever and characteristic film directions (e.g. the machine direction).

The engagement procedure is carried out with minimized forces as described in Sect. 3.2.2. After engagement, the gains and the scan rate must be optimized. It is advisable to image the films in constant force mode with minimized forces in order

to obtain quantitative height information, i.e. to prevent compression of soft areas of the film.

TM-AFM Visualization of the Morphology

We use a standard tapping/intermittent contact mode set-up, which is assembled as described in Sect. 3.2.1. After inserting the TM cantilever into the cantilever holder, the optical head is mounted, the laser is aligned and the resonance peak is analyzed. The operation frequency and amplitude are adjusted to v at 0.85 A_o and 100 nm, respectively. Prior to engaging the phase signal is zeroed. The crude and fine engagement procedures are carried out as described in Chap. 2 and Sect. 3.2. After the successful engagement the operation point is carefully adjusted to minimize the force exerted by the AFM tip. Very light tapping conditions with an amplitude setpoint A/A_0 ratio of 0.9 are used (compare Sect. 3.4.2).

Representative AFM height images are shown in Fig. 3.75. For the blown PE films (panel a), CM-AFM unveils lamellar features, which are oriented predominantly in the transverse direction. The roughness analyses of these films have been reported to yield useful insight into the origin of optical properties. In particular, the results showed that the haze, defined as percentage of transmitted light that deviates more than 2.5° from the incident beam when passing through a sample, is related predominantly to surface roughness and can be reduced by changing the processing conditions [155].

For the processed iPP films, TM-AFM reveals clearly the nearly vertically oriented marks of the calendering rolls on the polymer films, as well as the

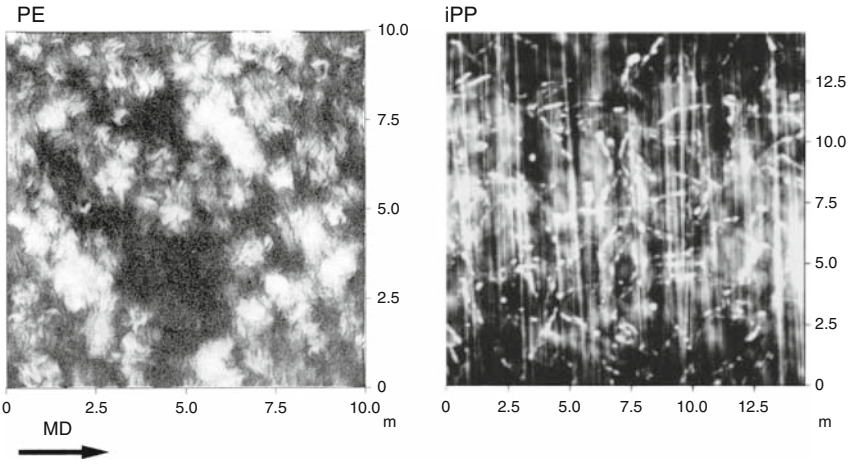

Fig. 3.75 (**a**) AFM height image of the outside surface of a blown PE blend film. Reprinted with permission of John Wiley & Sons, Inc. from [155]. Copyright 1996. Society for Plastic Engineers. (**b**) TM-AFM height image of calendered iPP film displaying marks of the calendering rolls in approx. vertical direction. Reproduced with permission from [154]. Copyright 1998. American Chemical Society

incorporated filler particles. The surface roughness of the films will affect, similar to the example of blown PE films, the haze, as well as the gloss (defined as reflected intensity of light compared to that of a standard) of these films.

Hands-on Example 33

Deformation of Block Copolymers

Sample Preparation: Solution Casting

Thin films with a thickness of $\sim$ 50 μm of a commercially available PS-PB-PS triblock copolymer (e.g. from BASF, 74% PS, 26% PB) are prepared by solution casting from a 3% solution in toluene onto TEFLON™-foil, which is placed in a pre-cleaned petri-dish. The solvent is slowly evaporated over a period of $\sim$ 2 weeks. Residual solvent is then removed and films are annealed under reduced pressure in a vacuum oven at 120°C (48 h). Finally, the films are removed from the support and are uniaxially stretched at a constant strain rate of $\sim$ 0.1 s^{-1} beyond the yield point at room temperature. AFM investigations are carried out on prestretched samples that are mechanically clamped or fixated by double-sided sticky tape onto the AFM sample holder.

TM-AFM Visualization of Deformed Microphase Separated Morphology

We use a standard tapping/intermittent contact mode set-up, which is assembled as described in Sect. 3.2.1 with an operation frequency of v at 0.85 A_o and an, amplitude of 100 nm. To avoid the situation in which the tip is trapped on the sticky surface and to achieve appreciable contrast, this intermediate amplitude is advisable to avoid permanent tip-sample contact/adherence during the scans.

As shown in Fig. 3.76, the microphase separated morphology can be clearly resolved in the unstretched state (panel a), as well as in the stretched state (panels b-d). The rubbery PB phase shows under the imaging conditions chosen, a dark contrast (pronounced phase lag), while the glassy PS phase in this lamellar morphology appears with a bright phase contrast [157]. The deformation of the heterogeneous block copolymer film depends on the local morphology. While randomly oriented lamellae display a chevron fold-like morphology at the high deformation utilized [158, 159], lamellae oriented perpendicular to the drawing direction (denoted by the arrows, σ) show a widening of the spacing compared to the unstretched state.

Lamellae that display a parallel orientation with respect to the drawing direction show morphological changes that are in accordance with the deformation mechanism termed hard layer sliding [160]. In this mechanism the PS lamellae are assumed to slightly slip towards each other without noticeable deformation. In addition, PS lamellae may be fractured into smaller domains, which are ordered in series to yield a lamellar type structure again.

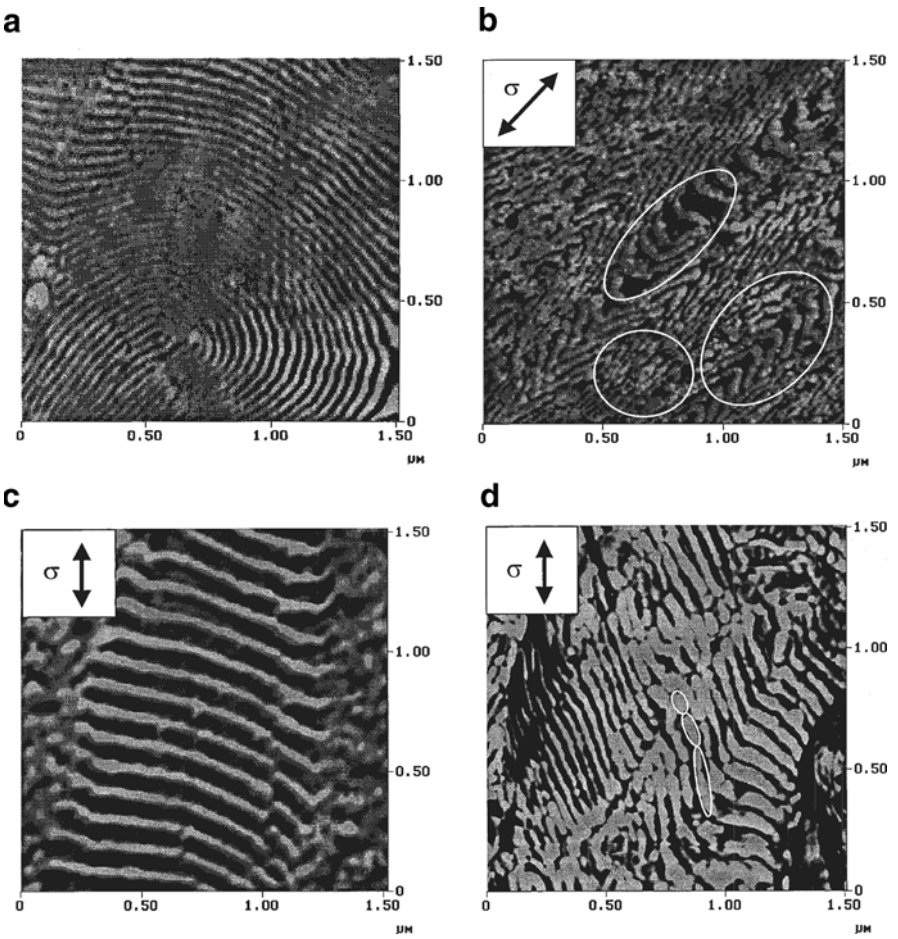

Fig. 3.76 Intermittent contact mode AFM phase images of (**a**) undeformed and (**b–d**) uniaxially deformed film of SBS. Reprinted with permission from [156]. Copyright 2002. Wiley-VCH

3.5.3 Polymer Surface Modifications

Polymer surface modifications are omnipresent in applications where the surface properties of materials with favorable bulk properties are insufficient. By altering the surface characteristics using physical or chemical modification the desired surface properties may be achieved. Such treatments are required e.g. to enhance printability of films, the adhesion of paints, metal or other coatings, biocompatibility, protein resistances/reduced biofouling, etc. The diverse approaches met in practice include, among others, wet chemical and gas phase chemistry, plasma or corona, UV/ozone and flame treatments. In most cases surface chemical modification reactions take place that alter the surface energy in a desired way. For example,

by increasing the surface tension of a polymer the wettability and adhesion of inks and adhesives is improved. The modification processes may also result in a surface roughening and restructuring. Due to the dynamic nature of many polymer films, reorientation phenomena, which contribute to ageing and concomitantly limited shelf life of modified polymer surfaces, have been observed.

In addition to the characterization of the lamellar arrangement in processed polymers, as discussed above, AFM is useful to analyze changes in surface morphology and roughness owing to surface treatments. For example, Vancso and coworkers reported on an early AFM study of the surface morphology of commercial polymer films. The effects of various oxidizing treatments and of metallization of PP have been unraveled. In this study the thickness and orientation of the exposed lamellae were determined [161].

Related illustrative examples are flame and corona treatments, which find widespread industrial application [162]. Here an oxidizing flame and a high voltage, high frequency electrical discharge are applied e.g. to non-polar polymer films, respectively. As a result molecular bonds on the surface of the non-polar polymer are broken. These broken bonds recombine with free radicals generated in the discharge (or by reaction with oxygen) and form polar groups on the film surface. The effect of

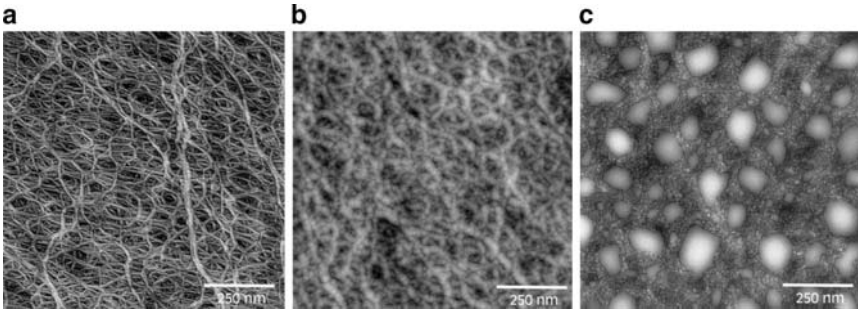

Fig. 3.77 TM-AFM height images of (**a**) an untreated polypropylene web, (**b**) a flame-treated PP film and (**c**) a corona treated PP film. Reproduced with permission from [162]. Copyright 2003. Plenum Publishing

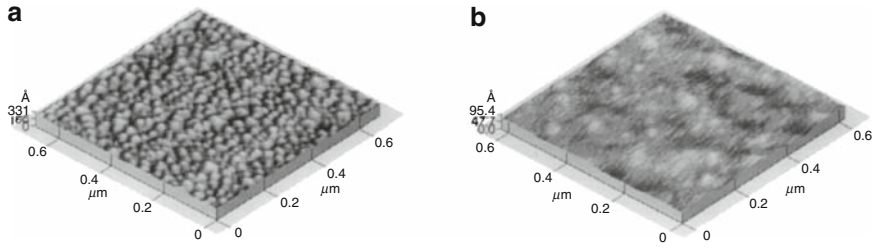

Fig. 3.78 AFM height images of gold clusters on a TMC-polycarbonate film acquired (**a**) before and (**b**) after annealing above T_g. Reproduced with permission from [164]. Copyright 2000. Elsevier

flame and corona treatments on the morphology of polypropylene films is shown in Fig. 3.77.

A second already mentioned application is the metallization of polymer films. As shown in Fig. 3.78, is the thermal treatment of a TMC-polycarbonate film onto which gold metal clusters were deposited [164]. Upon annealing above T_g, the metal particles are in parts sunken into the softened film, thereby reducing the surface roughness. It was also concluded that the embedded clusters were covered with a thin polymer layer.

Hands-on Example 34

Surface Oxidized Polypropylene by Oxyfluorination

For the last 50 years, corona discharges and flame are the most widely used pretreatment methods for polymer films in industry. The corona discharge treatment is generally used for the pretreatment of polyolefin films whereas the flame treatment is used for thicker sections. Corona treatments are effective in modification of the surface chemistry of polyolefins, among others, but often result in properties that quickly erode with storage time. A possible approach to improve shelf life is the use of plasma treatments, such as helium and ammonia plasmas [165], or processes, such as the treatment with a N_2, F_2, and O_2 gas mixture at elevated temperatures ("oxyfluorination") [166]. This surface modification leads to the formation of a variety of functional groups at the surface of iPP, such as carbonyl groups, fluorocarboxylic acids, peroxides, hydroxyl groups, ether groups (recombination of two radicals via an epoxy bridge), and acid fluoride groups that hydrolyze slowly in contact with atmospheric moisture to form carboxylic acids [167–170].

In the example we elaborate here, we focus on oxyfluorinated iPP (e.g. oxyfluorinated isotactic polypropylene films, SOLVAY ELTEX P KL 177 obtained from SOLVAY ALKOR-DRAKA Snc.). In principle, corona treated iPP films can be utilized similarly well. The freshly oxidized films are cut into small 1×1 cm^2 sized samples and are inserted quickly after mounting to the metallic sample puck (using a minute amount of a fast curing epoxy).

TM-AFM Visualization of Surface Morphology

We use a standard tapping/intermittent contact mode set-up, which is assembled as described in Sect. 3.2.1, see also hands-on example 31. The operation frequency and amplitude are adjusted to v at 0.85 A_o and 100 nm, respectively.

The surface topology is best tracked by utilizing a high setpoint amplitude ratio (close to $\sim$ 0.9). Care must be taken that the tip does not lose track of the surface when traversing elevated features, such as the ridges (marks of the calandering rolls) or filler particles that may have been pulled out of the film during processing (Fig. 3.79). Halos in the phase or amplitude images in the fats scan direction indicate the inadequate tracking of the ample surface. The setpoint is then too close to the

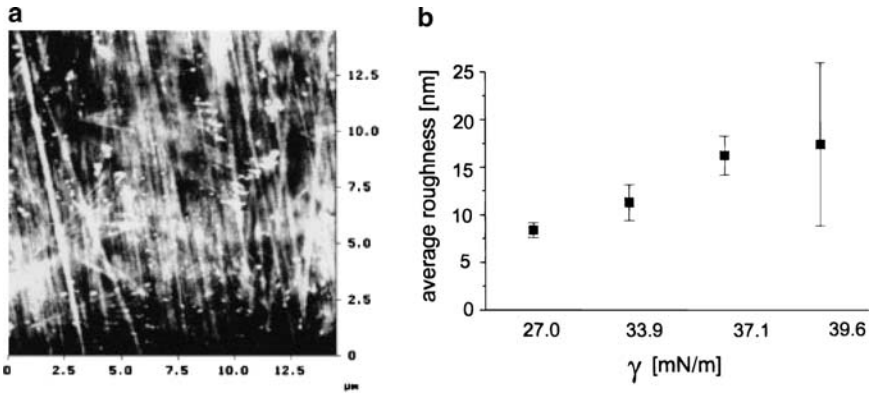

Fig. 3.79 (**a**) TM-AFM height image of an oxyfluorinated iPP film (surface energy 33.9 mN/m, as determined by contact angle measurements with a range of liquids) and (**b**) roughness for iPP films with various surface energies obtained by different degrees of plasma treatment. Reproduced with permission from [154]. Copyright 1997. American Chemical Society

freely oscillating lever; hence we slightly reduce the setpoint. Different treatment times and conditions may lead to a different degree of oxidation and surface restructuring, as can be analyzed in quantitative roughness analyses (panel b). The untreated iPP film has been shown in Fig. 3.75b.

Hands-on Example 35

Flame Treatment of LDPE

A second relevant example is the surface oxidation of polyolefins, such as LDPE, which is carried out frequently for thick specimens using an oxidizing flame treatment. For instance, while untreated LDPE surfaces are non-polar and thus fairly hydrophobic, flame-treated LDPE possesses a much higher surface energy and therefore improve the binding of these surfaces with other substances, such as adhesives, printing inks, paints, and various metal surfaces.

In this hands-on example we follow closely a recently published procedure [171]. Additive free LDPE films (with a thickness of 0.2 mm, e.g. obtained from DSM, Geleen, the, Netherlands) is cut into pieces of ca. 1×1 cm^2 prior to treatment. To remove contaminants, the samples are refluxed in dichloromethane for 30 min, followed by a rinse with ethanol and drying in a stream of nitrogen immediately prior to use. For the flame treatment a mixture of natural gas and air are combusted by a nozzle type burner (using a typical flow rate of the mixture of natural gas and air of ca. 12.3 cm^3/s and an equivalence ratio, which is defined as the stoichiometric oxidizer: fuel ratio divided by the actual oxidizer: fuel ratio of ca. 0.93). The LDPE

films are repeatedly pulled across the tip of the flame at a distance of ca. 0–1 mm with a speed of ca. 0.5 m/s. The flame cone length is ca. 1 cm so that the exposure time of the film to the flame is about ca. 0.02 s. In order to increase the oxidation at the surface, repeated cycles of the flame treatment can be carried out. Too long exposure to the high temperature flame will cause destruction of the films.

TM-AFM Visualization of Surface Morphology

The operation and adjustment of the TM-AFM are identical to the procedures discussed in example 34 (oxyfluorinated iPP).

Figure 3.80 shows several AFM height images of untreated as well as flame-treated LDPE films. The untreated LDPE (panel a) displays a clearly visible lamellar surface structure, indicative of the presence of spherulites throughout the film. After the flame treatment of the surface, the LDPE film became somewhat smoother and exhibited round-shaped features which formed a nodular structure (Fig. 3.80b-e). The large nodular features were 0.5–1.0 μm in diameter, and the number of larger features increased for prolonged treatment times. These water soluble low molecular weight oxidized materials, which were generated as products of oxidation and chain scission of the LDPE surface, thus agglomerated into small topographical mounds that were visible in the AFM micrographs. Upon rinsing these materials are no longer traceable (Fig. 3.80 (f)).

3.5.4 Latexes and Paints

Polymer latex particles play a major role in coatings and paint industry. The size distributions in multicomponent formulations as well as the drying of paints and the coalescence of particles into a continuous protective film are topics that have been frequently investigated by AFM approaches. AFM provides direct access to the visualization down to the individual particle level and, as discussed in Sect. 4.3 in Chap. 4, to the assessment of the mechanical properties.

Lepizzera et al [172] reported in an early publication on the deformation of latex particle films, as detected by AFM. Films made from core/shell latex particles that possess a soft shell and a hard core exhibited a continuous phase composed of the shell polymer in which the hard cores formed long-range hexagonal orderings. Upon elongation of the films (for small draw ratios), linear necklaces of core particles, perpendicular to the elongation direction, were observed at the surface of the films (Fig. 3.81).

3.5.5 Membranes and Porous Films

A limitation of AFM approaches in the study of porous materials is the limited ability of the scanned probe tip to penetrate and probe into smaller pores. This is illustrated in Chap. 2 (Fig. 2.23). Clearly, ultrasharp, high aspect ratio probe tips comprise an improvement in this respect. While carbon nanotube functionalized tips are not yet of widespread availability, conventional TM probes are preferred over CM probes because of the different opening angles (compare Chap. 2). In addition,

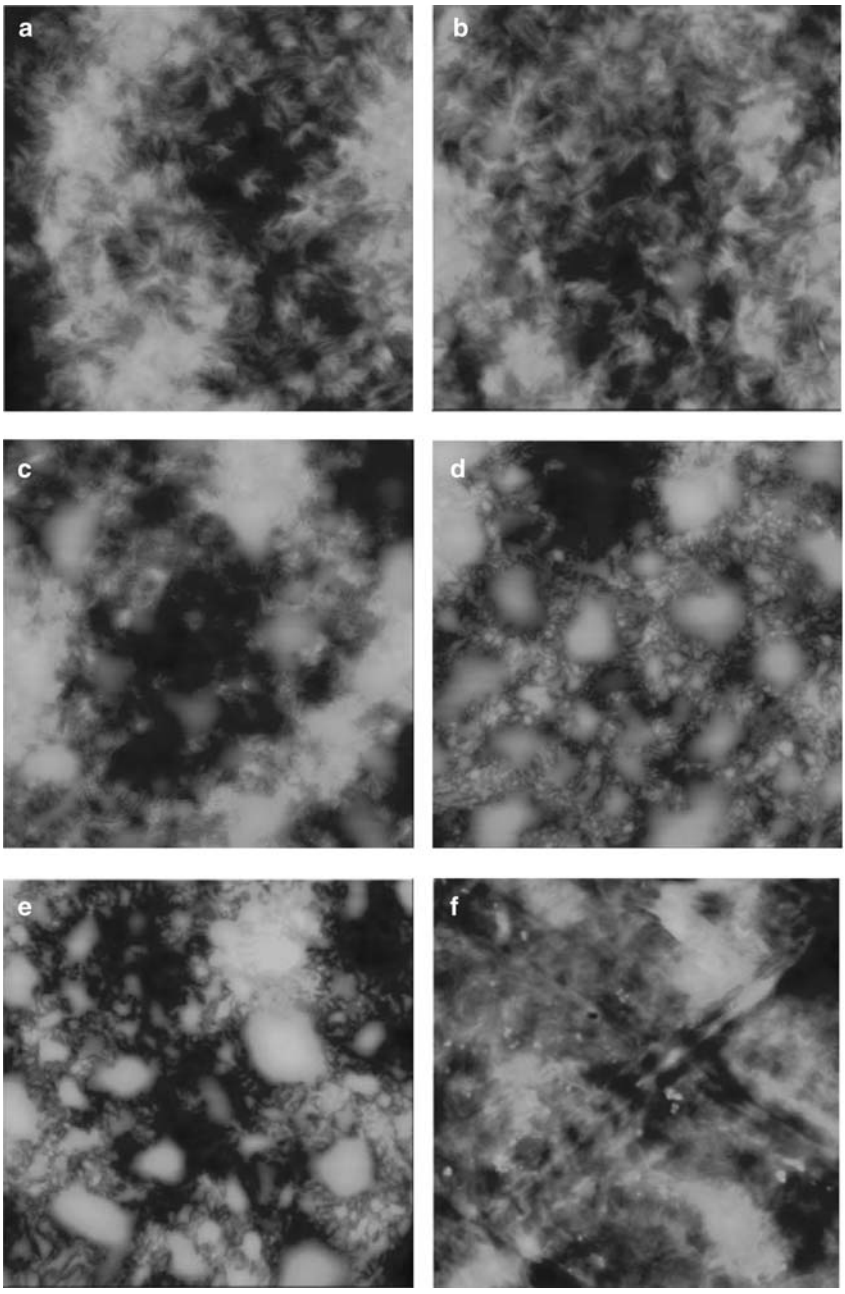

Fig. 3.80 Tapping mode AFM height images (z-scale 300 nm) of (**a**) untreated LDPE; (**b**) LDPE treated 5 times; (**c**) LDPE treated 50 times; (**d**) LDPE treated 100 times (**e**) LDPE treated 200 times; and (**f**) LDPE treated 200 times and subsequently rinsed. The scan size was $5 \times 5\ \mu m^2$. Reproduced with permission from [171]. Copyright 2007. Elsevier

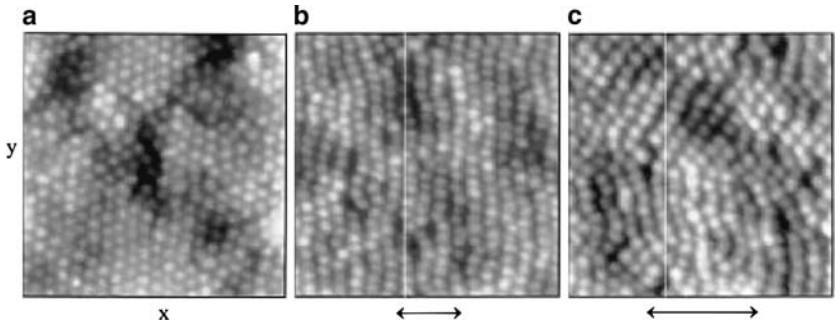

Fig. 3.81 TM-AFM height images of core-shell latex films in different states of elongation: (**a**) undeformed film; (**b**) film with an elongation below 1.05; (**c**) film with an elongation equal to 2 ± 0.2. Film elongation is along the *x*-axis, as indicated by the *double arrows*. Size of the images: 4 × 4 μm^2. Reproduced with permission from [172]. Copyright 1997. American Chemical Society

one must keep in mind that the z-scale displayed in AFM height is exaggerated most of the time. Thus relatively shallow depressions or undulations of the surface, which may give rise to a more or less faint color scale contrast, are often erroneously attributed to "pores". A careful cross-sectional analysis of the lateral width, the depth, and sidewall angles of the convoluted AFM images may help to successfully identify true pores.

The potential of AFM approaches to characterize membranes and porous materials (of limited surface roughness) is demonstrated in the work of Sirijarokul et al. [173]. Track-etch PET membranes with controlled gradients of pore size and density along the length of the membrane were analyzed by scanning electron microscopy and TM-AFM. In the top-view AFM micrographs the differences in pore size for the two conditions (different wavelengths for irradiation were employed) used in the experiments is obvious. The pore size and the local arrangement can be conveniently analyzed (Fig. 3.82).

In addition to the assessment of pore sizes and quality control, AFM provides direct access to the dynamic changes of smart pores, for instance pores that are equipped with a stimulus-responsive coating. Iwata et al. reported on the pH control of pore opening and closing of poly (acrylic acid) (PAA) -functionalized pores, as shown in Fig. 3.83. [174] The pores of two different membranes are closed, as seen by CM-AFM, at high pH due to the deprotonation of the PAA coating and concomitant expansion of the polymeric layer into the opening of the pore.

3.5.6 Defects and Failure Analysis

A final area of direct practical relevance for AFM on polymers is the analysis of defects and failure mechanisms. In fact this application is natural owing to the direct visualization of surface structures and morphologies of polymers and polymer products and therefore it is omnipresent.

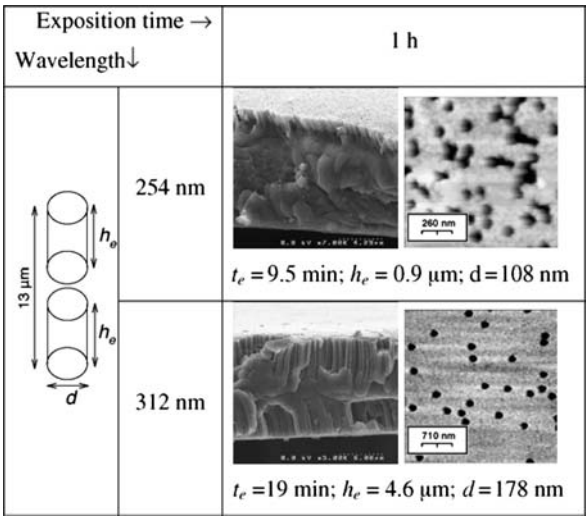

Fig. 3.82 Pore creation through 13 µm thick PET membranes exposed to 254 and 312 nm wavelengths for 1 h. Ion beam of ^{58}Ni with incident energy: 10.7 MeV/u (1 h, 254 nm); 9.1 MeV/u (15 h, 254 nm). Etching occurs at the both faces, d is the pore diameter measured with AFM (surface image) and h_e is the depth of etching penetration through the membrane measured with SEM (cross-section image) and t_e = etching time. Reproduced with permission from [173]. Copyright 2007. Elsevier

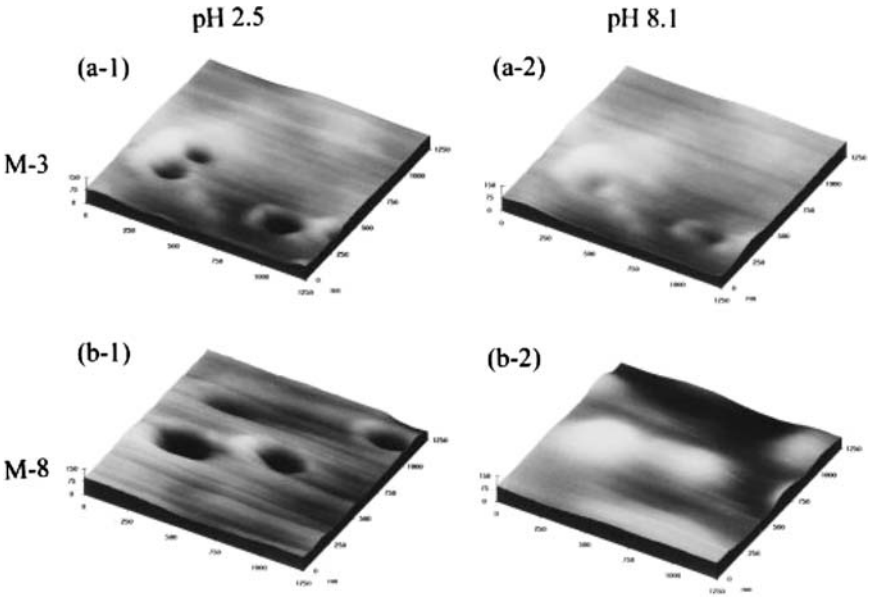

Fig. 3.83 CM-AFM height images (acquired at constant load of 1 nN in buffered solution) in 3D projection of porous membranes with PAA coating visualized at different pH. Reproduced with permission from [174]. Copyright 1998. American Chemical Society

Examples, which have in parts already been explicitly mentioned, are defects, such as marks of processing equipment on polymer films, filler particles that were removed from the polymer matrix, irregular ordering and pinholes in latex assemblies, or altered morphologies due to mechanical deformation and concentration of stresses, among others.

Defects and failure of polymers during tensile deformation, such as cracks, have been studied by Bhushan and coworkers in metal particle (MP) tapes [175]. MP tapes are magnetic tapes that consist of a polymeric substrate, generally PET with a thin magnetic coating of magnetic particles dispersed in a polymer binder. As depicted in Fig. 3.84, a crack that develops perpendicular to the loading direction is detected in situ in TM-AFM scans that were acquired using a custom-built stretching device.

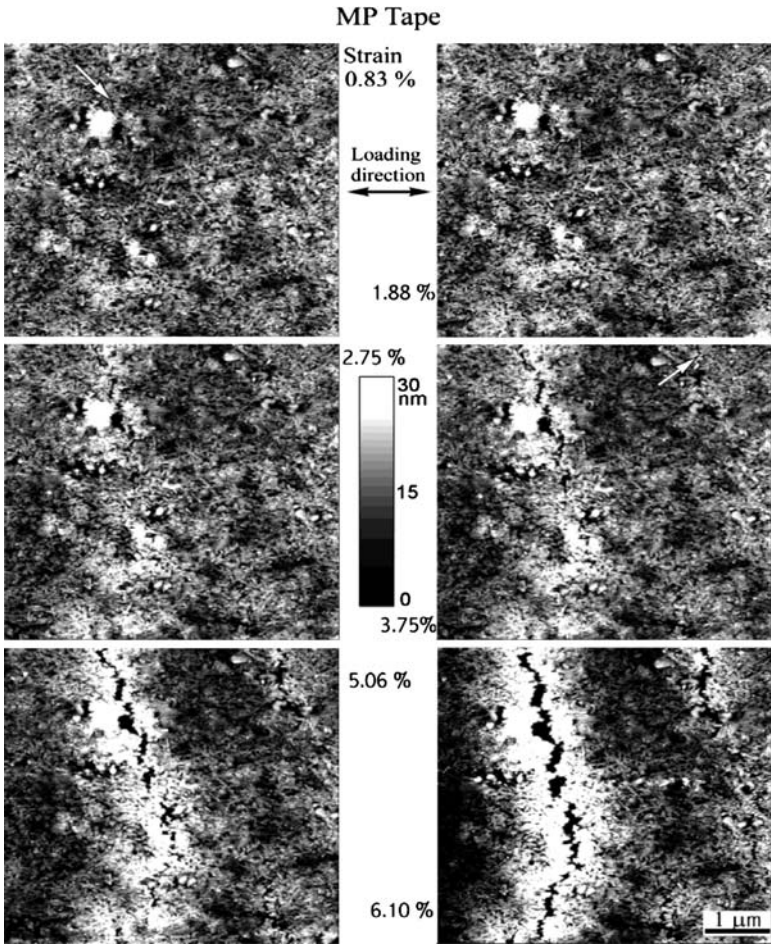

Fig. 3.84 TM-AFM height images of a PET-based MP tape at different strain values between 0.83 and 6.10%. Reproduced with permission from [175]. Copyright 2001. Materials Research Society

Hands-on Example 36

AFM Imaging of Rubbed Polyimide [176]

Polyimide films that are unidirectionally rubbed with cloth are widely used as alignment layers in the liquid crystal display industry. These aligned films orient contacting liquid crystals into monodomains over large areas. Since device quality and the degree and perfection of the alignment of the liquid crystals are closely related, the underlying process and also the defect structure found are of great interest.

In the example reported by Russell and coworkers, the poly(amic acid) diethyl ester of biphenyltetracarboxylicdianhydride–*p*-phenylenediamine (BPDA–PDA) is used (30,000 g/mol). Thin films are prepared by spincoating from solutions in 1-methyl-2-pyrrolidinone (NMP) onto various substrates, including freshly cleaved mica. The films are imidized in an oven at 300°C for 1 h (heating ramp: 300°C at a rate of 1°C/h) under flowing nitrogen and then cooled to room temperature at a rate of 1°C/h. Finally, the films are rubbed by first placing them face down on a velour cloth with a load between 1 and 20 g/cm^2 (see Fig. 3.85, panel a), as described by Russell and coworkers [176], and pulling out the velour unidirectionally beneath the film at a rate of 30 cm/min for a distance of 30 cm.

TM-AFM Visualization of Surface Morphology

We use a standard tapping/intermittent contact mode set-up, which is assembled as described in Sect. 3.2.1 (see also hands-on example 31). The operation frequency and amplitude are adjusted to v at 0.85 A_o and 100 nm, respectively. The surface is tracked most accurately by utilizing a high setpoint amplitude ratio (close to $\sim$ 0.9). Care must be taken that the tip does not lose track of the surface when traversing elevated features, therefore the phase (and the amplitude) signal is carefully monitored. Halos in the fast scan direction that are devoid of contrast (i.e. show a constant phase shift or amplitude response), are indicative of absent tip–sample interaction. In this case the setpoint can be lowered slightly.

The AFM data shows spherically appearing polyimide islands for the pristine film, which are randomly arranged (Fig. 3.85, panel b). No preferred orientation or anisotropy is detected. By contrast, the oriented film (panel c) shows clearly some degree of orientation of the morphological features observed. In (c) two stripes of chained islands, along two slightly different directions (indicated by black arrows), adjacent to patches of random islands (indicated by white arrow) are unveiled. In addition, a marked scratch can be observed in the upper right-hand corner.

In panel (d) a strikingly different type of defect structure is encountered, the so-called tears. It should be noted that these correspond to much larger defects (compare the scan size). In the work of Russell and coworkers it was found that three types of failure were present in the rubbed polyimide films, namely scratches, tears, and strings of islands, all of which are aligned along the rubbing direction. Local overshearing of the film was held responsible for the observed formation of

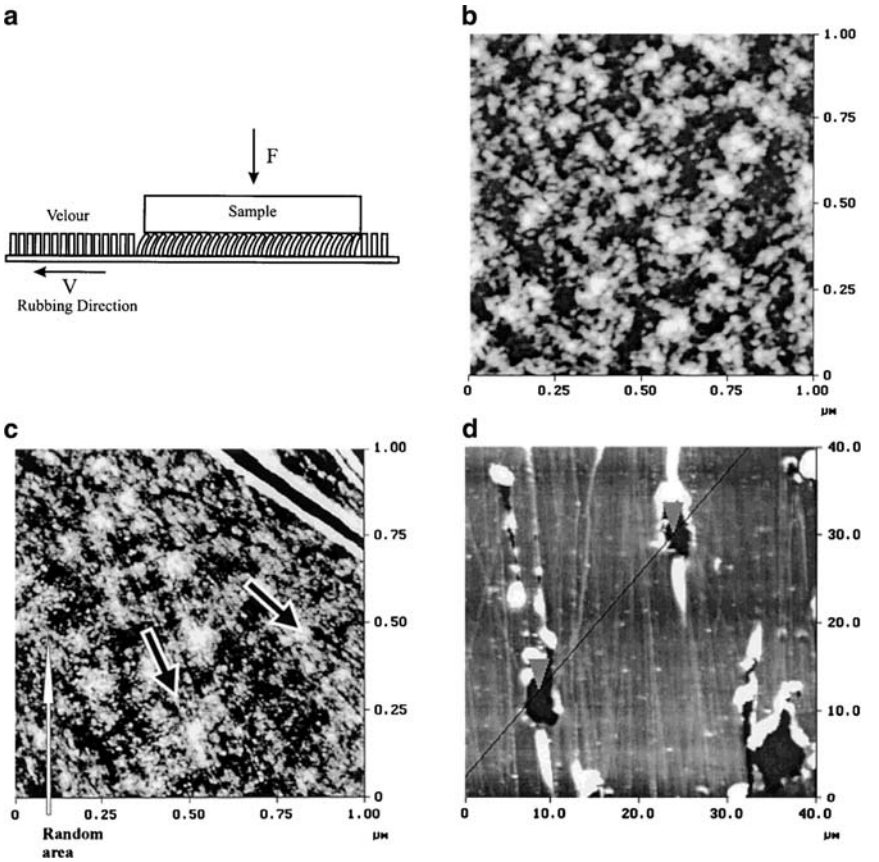

Fig. 3.85 (**a**) Schematic of the polyimide rubbing process; TM-AFM height images (z-scale 3 nm) of (**b**) the pristine polyimide film, and (**c**) and (**d**) a rubbed film. The rub direction in (**c**) was from *upper left to lower right*, in (**d**) vertical. Reprinted with permission of John Wiley & Sons, Inc. from [176]. Copyright 2001. John Wiley & Sons, Inc.

tears. In particular, the presence of tears and scratches may inhibit liquid crystal alignment.

References

1. Osswald TA, Menges G (1995) Materials science of polymers for engineers. Hanser-Gardner, Cincinnati
2. Balnois E, Stoll S, Wilkinson KJ, Buffle J, Rinaudo M, Milas M (2000) Macromolecules 33:7440–7442
3. Baer E, Hiltner A, Keith HD (1987) Science 235:1015–1022
4. Odian G (1991) Principles of polymerization, 3rd edn. Wiley, New York

5. Kumaki J, Kawauchi T, Okoshi K, Kusanagi H, Yashima E (2007) Angew Chem Int Ed 46(28):5348–5351
6. Sperling LH (2001) Introduction to physical polymer science, 3rd edn. Wiley, New York
7. Strobl G (2000) Eur Phys J E 3:165–183
8. G. Reiter, J.-U. Sommer (eds) (2003) Polymer crystallization: obervations, concepts and interpretations (Lecture Notes in Physics). Springer, Berlin
9. Khoury F, Passaglia E (1976) Treatise on solid state chemistry, vol 3. In Hannay NB (ed) Crystalline and noncrystalline solids, Chap 6. Plenum, New York
10. Wunderlich B (1973/1976/1980) Macromolecular physics. Academic, New York (Vol. 1: 1973; Vol. 2: 1976; Vol. 3: 1980)
11. Allen SM, Thomas EL (1999) The structure of materials. Wiley, New York
12. Schultz JM (2001) Polymer crystallization: the development of crystalline order in thermoplastic polymers. Oxford University Press, Oxford
13. Sawyer LC, Grubb DT, Meyers GF (2008) Polymer microscopy: characterization and evaluation of materials, 3rd edn. Springer, Berlin
14. Woodward AE (1988) Atlas of polymer morphology. Hanser, Munich
15. Woodward AE (1995) Understanding polymer morphology. Hanser, Munich
16. Cantor CR, Schimmel PR (1980) Biophysical chemistry. W.H. Freeman, San Francisco
17. Sawyer LC, Jaffe M (1986) J Mater Sci 21:1897–1913
18. Lakes RS (1993) Nature 361:511
19. Cheng J, Deming TJ (2001) J Am Chem Soc 123(38), 9457–9458
20. Hansma HG (2001) Annu Rev Phys Chem 52:71
21. Sheiko SS, Möller M (2001) Chem Rev 101:4099
22. Kumaki J, Nishikawa Y, Hashimoto T (1996) J Am Chem Soc 118:3321
23. Uchida E, Ikada Y (1997) Macromolecules 30:5464
24. Schönherr H (1999) Ph.D. thesis, University of Twente
25. Samori P, Ecker C, Gössl I, de Witte PAJ, Cornelissen JJLM, Metselaar GA, Otten MBJ, Rowan AE, Nolte RJM, Rabe JP (2002) Macromolecules 35:5290
26. Pfau A, Schrepp W, Horn D (1999) Langmuir 15:3219
27. Li J, Piehler LT, Qin D, Baker JR Jr., Tomalia DA, Meier DJ (2000) Langmuir 16:5613
28. Snétivy D, Vancso GJ, Rutledge GC (1992) Macromolecules 25:7037
29. Vancso GJ, Snétivy D, Schönherr H (1998) In Ratner BD, Tsukruk V (eds) Scanning probe microscopy of polymers, Chap. 4. ACS Symposium Series vol 694, pp 67–93
30. Snétivy D, Vancso GJ (1993) Langmuir 9:2253
31. Schönherr H, Ringsdorf H, Jaschke M, Butt H-J, Bamberg E, Allinson H, Evans SD (1996) Langmuir 12:3898
32. Pooley CM, Tabor D (1972) Proc R Soc Lond A 329:251
33. Wittman JC, Smith P (1991) Nature 352:414
34. Schönherr H, Vancso GJ (1998) Polymer 39:5705
35. Hansma H, Montamedi F, Smith P, Hansma PK, Wittman JC (1992) Polymer 33:647

36. Vancso GJ, Förster S, Leist H (1996) Macromolecules 29:2158
37. Magonov SN, Kempf S, Kimmig M, Cantow HJ (1991) Polym Bull 26:715
38. Snétivy D, Vancso GJ (1992) Macromolecules 25:3320
39. Snétivy D, Yang HF, Glomm B, Vancso GJ (1994) J Mater Chem 4:55
40. Frank CW, Rao V, Despotopoulou MM, Pease RFW, Hinsberg WD, Miller RD, Rabolt JF (1996) Science 273:912
41. Pickering JP, Vancso GJ (1999) Appl Surf Sci 148:147
42. Schönherr H, Pearce R, Vancso GJ unpublished data
43. Kim HI, Mate CM, Hannibal KA, Perry SS (1999) Phys Rev Lett 82:3496
44. Schönherr H, Bailey LE, Frank CW unpublished data
45. Schönherr H, Frank CW (2003) Macromolecules 36:1188–1198
46. Vancso GJ, Nisman R, Snétivy D, Schönherr H, Smith P, Ng C, Yang H (1994) Coll Surf A 87:263
47. Bassett DC, Keller A (1962) Philos Mag 7:1553
48. Vancso GJ, Schönherr H (1999) In Microstructure and microtribology of polymer surfaces. In Tsukruk VV, Wahl KJ (eds), ACS Symposium Series vol 741, Chap. 19, pp 317–335
49. Smith PF, Nisman R, Ng C, Vancso GJ (1994) Polym Bull 33:459
50. Pearce R, Vancso GJ (1998) Polymer 39:6743
51. Schönherr H, Wiyatno W, Pople J, Frank CW, Fuller GG, Gast AP, Waymouth RM (2002) Macromolecules 35:2654
52. Magonov SN, Elings V, Whangbo M-H (1997) Surf Sci 372:L385
53. Lotz B, Wittmann JC (1986) J Polym Sci Polym Phys 24:1541
54. Schönherr H, Waymouth RM, Frank CW unpublished data
55. Schönherr H, Snétivy D, Vancso GJ (1993) Polym Bull 30:567
56. Krotil HU, Stifter T, Waschipky H, Weishaupt K, Hild S, Marti O (1999) Surf Interface Anal 27:336
57. Kresz N, Smausz J, Kokavecz T, Hopp B, Cset M, Hild S, Marti O (2004) Thin Solid Films 453–454:239–244
58. Schönherr H, Waymouth RM, Frank CW unpublished data
59. Schönherr H, Feng CL, Shovsky A (2003) Langmuir 19:10843–10851
60. Schönherr H, Frank CW unpublished data
61. Wunderlich B (1973/1976/1980) Macromolecular physics. Academic, New York (Vol. 1: 1973, Vol. 2: 1976, Vol. 3: 1980)
62. Schönherr H, Waymouth RM, Frank CW unpublished data
63. Varga J, Schulek-Toth F, Pati Nagy M Hungarian Patent 209132, April 29, 1992
64. Olley R (1986) Sci Progr Oxf 70:17
65. Trifonova D, Varga J, Vancso GJ (1998) Polym Bull 41:341
66. Trifonova-van Haeringen D, Varga J, Ehrenstein GW, Vancso GJ (2000) J Polym Sci B Polym Phys 38:672
67. Ikai A (1996) Surf Sci Rep 26:263–332
68. Morris VJ, Wilde PJ (1997) Curr Opin Colloid Interface Sci 2:567–572
69. Castner DG, Ratner BD (2002) Surf Sci 500:28–60
70. Reich Z, Kapon R, Nevo R, Pilpel Y, Zmora S, Scolnik Y (2001) Biotechnol Adv 19:451–485

71. Marti O, Amrein M (1993) STM and SFM in biology. Academic, London
72. Lindsay SM The scanning probe microscope in biology. In Bonnell D (ed) Scanning tunneling microscopy and related techniques. Wiley, New York
73. Jena B, Horber JK (2002) Atomic force microscopy in cell biology, methods in cell biology, vol 68. Academic, London
74. Morris J, Gunning AP, Kirby AR (1999) Atomic force microscopy for biologists. Imperial College Press, London
75. Sun YC, Arakawa H, Osada T, Ikai A (2002) Appl Surf Sci 188:499–505
76. Morigaki K, Baumgart T, Offenhäusser A, Knoll W (2001) Angew Chem Int Ed Engl 40:172–174
77. Gustafsson J, Ciovica L, Peltonen J (2003) Polymer 44:661–670
78. McIntire TM, Brant DA (1999) Int J Biol Macromol 26:303–310
79. Burnham NA, Colton RJ, Pollock HM (1993) Nanotechnology 4:64
80. Cappella B, Dietler G (1999) Surf Sci Rep 34:1
81. García R, Pérez R (2002) Surf Sci Rep 47:197
82. Drake B, Prater CB, Weisenhorn AL, Gould SAC, Albrecht TR, Quate CF, Cannell DS, Hansma HG, Hansma PK (1989) Science 243:1586–1589
83. Weisenhorn AL, Hansma PK, Albrecht TR, Quate CF (1989) Appl Phys Lett 54:2651
84. Weisenhorn AL, Maivald P, Butt H-J, Hansma PK (1992) Phys Rev B 45:11226
85. Schönherr H, Morigaki K, Frank CW, Knoll W unpublished data
86. Owing to the unsymmetrical coating of the typically used cantilevers, these will bend as a result of different surface tensions [Raiteri R, Butt H-J (1995) J Phys Chem 99:15728–15732] or thermal expansion coefficients
87. Schönherr H, Johnson JM, Frank CW, Boxer SG unpublished data
88. Dufrene YF, Barger WR, Green JBD, Lee GU (1997) Langmuir 13:4779–4784
89. Schönherr H, Johnson JM, Frank CW, Boxer SG unpublished data
90. Hoh JH, Engel A (1993) Langmuir 9:3310–3312
91. Van Noort SJT, Van der Werf KO, De Grooth BG, Van Hulst NF, Greve J (1997) Ultramicroscopy 69:117
92. Johnson JM, Ha T, Chu S, Boxer SG (2002) Biophys J 83:3371–3379
93. Schönherr H, Johnson JM, Lenz P, Frank CW, Boxer SG (2004) Langmuir 20:11600–11606
94. Morigaki K, Schönherr H, Frank CW, Knoll W (2003) Langmuir 19:6994–7002
95. Morigaki K, Schönherr H, Okazaki T (2007) Langmuir 23:12254–12260
96. Knez M, Sumser MP, Bittner AM, Wege C, Jeske H, Hoffmann DMP, Kuhnke K, Kern K (2004) Langmuir 20:441–447
97. Revol J-F, Bradford H, Giasson J, Marchessault RH, Gray DG (1992) Int J Biol Macromol 14:170–172
98. Lyubchenko YL, Jacobs BL, Lindsay SM (1992) Nucleic Acids Res 20:3983–3986
99. Baker AA, Helbert W, Sugiyama J, Miles MJ (1997) J Struct Biol 119:129–138
100. Kirby AR, Gunning AP, Morris VJ (1995) Carbohydr Res 267:161–166

101. http://www.ifr.ac.uk/spm/gallery_image.lasso?ID=39, copyright permission: Dr. Andrew Kirby, Institute of Food Research, Norwich Research Park, Colney, Norwich NR4 7UA, UK
102. Habelitz S, Balooch M, Marshall SJ, Balooch G, Marshall GW Jr (2002) J Struct Biol 138:227–236
103. Ratanabanangkoon P, Gast AP (2003) Langmuir 19:1794–1801
104. Hemming SA, Bochkarev A, Darst SA, Kornberg RD, Ala P, Yang DSC, Edwards AM (1995) J Mol Biol 246:308–316
105. Schönherr H, Ratanabanangkoon P, Frank CW, Gast AP unpublished data
106. Hu J, Wang M, Weier H-UG, Frantz P, Kolbe W, Ogletree DF, Salmeron M (1996) Langmuir 12:1697–1700
107. Marsh LH, Coke M, Dettmar PW, Ewen RJ, Havler M, Nevell TG, Smart JD, Smith JR, Timmins B, Tsibouklis J, Alexander C (2002) J Biomed Mater Res 61:641–652
108. Whangbo M-H, Magonov SN, Bengel H (1997) Probe Microsc 1:23
109. García R, Pérez R (2002) Surf Sci Rep 47:197
110. Noy A, Sanders CH, Vezenov DV, Wong SS, Lieber CM (1998) Langmuir 14:1508
111. Bar G, Thomann Y, Whangbo M-H (1998) Langmuir 14:1219
112. Bar G, Thomann Y, Brandsch R, Cantow H-J, Whangbo M-H (1997) Langmuir 13:3807
113. Bar G, Brandsch R, Whangbo M-H (1997) Langmuir 14:7343
114. Leclère Ph, Lazzaroni R, Brédas JL, Yu JM, Dubois Ph, Jérôme R (1996) Langmuir 12:4317
115. Pickering JP, Vancso GJ (1996) Polym Bull 40:549
116. Lammertink RGH, Hempenius MA, Vancso GJ (2000) Langmuir 16:6245–6252
117. Maivald P, Butt H-J, Gould SAC, Prater CB, Drake B, Gurley JA, Elings VB, Hansma PK (1991) Nanotechnology 2:103
118. Chi L-F, Anders M, Fuchs H, Johnston RR, Ringsdorf H (1993) Science 259:213
119. Chen JT, Thomas EL (1996) J Mater Sci 31:2531
120. Gilmore IS, Seah MP, Johnstone JE (2003) Surf Interface Anal 35:888
121. Mizes HA, Loh K-G, Miller RJD, Ahuja SK, Grabowski EF (1991) Appl Phys Lett 59:2901
122. Frisbie CD, Rozsnyai LF, Noy A, Wrighton MS, Lieber CM (1994) Science 265:2071
123. Schönherr H, Hruska Z, Vancso GJ (2000) Macromolecules 33:4532
124. Krotil HU, Stifter T, Waschipky H, Weishaupt K, Hild S, Marti O (1999) Surf Interface Anal 27:336
125. Krotil HU, Stifter T, Marti O (2000) Rev Sci Instrum 71:2765
126. Guarini KW et al. (2003) International electron devices meeting technical digest. IEEE, Piscataway, NJ, pp 541–544
127. Rehse N, Knoll A, Konrad M, Magerle R, Krausch G (2001) Phys Rev Lett 87:035505

128. Magerle R (2000) Phys Rev Lett 85:2749
129. Knoll A, Horvat A, Lyakhova KS, Krausch G, Sevink GJA, Zvelindovsky AV, Magerle R (2002) Phys Rev Lett 89:035501
130. Pickering JP, Vancso GJ (1998) Polym Bull 40:549–554
131. Feng CL, Vancso GJ, Schönherr H (2005) Langmuir 21:2356–2363
132. Timothy J Cavanaugh A, Russo P, Bruce E Nauman (1996) Chemtech 26(8):32–27
133. Chen C, Wang J, Woodcock SE, Chen Z (2002) Langmuir 18:1302–1309
134. Raghavan D, VanLandingham M, Gu X, Nguyen T (2000) Langmuir 16:9448–9459
135. Galuska AA, Poulter RR, McElrath KO (1997) Surf Interface Anal 25:418–429
136. Zhang MQ, Rong MZ, Zeng HM, Schmitt S, Wetzel B, Friedrich K (2001) J Appl Polym Sci 80:2218–2227
137. Allen MJ, Hud NV, Balooch M, Tench RJ, Siekhaus WJ, Balhron R (1992) Ultramicroscopy 42:1095
138. Van Cleef M, Holt SA, Watson GS, Myhra S (1996) J Microsc Oxf 181:2
139. Tabet MF, Urban FK (1997) J Vac Sci Technol B 15:800
140. Nie HY, Walzak MJ, McIntyre NS (2002) Rev Sci Instrum 73:3831
141. Trifonova D, Schönherr H, van der Does L, Janssen PJP, Noordermeer JWM, Vancso GJ (1999) Rubber Chem Technol 72:862–875
142. Hild S, Rosa A, Marti O (1998) ACS Symp Ser 694:110–128
143. Wang K, Wu J, Zeng H (2001) Composites Sci Technol 61:1529–1538
144. Mäder E, Gao SL (2001) J Adhesion Sci Technol 15(9):1015–1037
145. Varga J (1992) J Mater Sci 27:2557
146. Olley R (1986) Sci Progr Oxf 70:17
147. Vancso GJ, Liu G, Karger-Kocsis J, Varga J (1997) Colloid Polym Sci 275:181
148. Trifonova D, Drouillon P, Ghanem A, Vancso GJ (1997) J Appl Polym Sci 66:515–523
149. Drummond KM, Shanks RA, Cser F (2002) Appl Polym Sci 83:777–784
150. Bartczak Z, Argon AS, Cohen RE, Kowalewski T (1999) Polymer 40:2367–2380
151. Opdahl A, Somorjai GA (2001) J Polym Sci B Polym Phys 39:2263–2274
152. Chang AC, Tau L, Hiltner A, Baer E (2002) Polymer 43:4923–4933
153. Olley RH, Bassett DC (1982) Polymer 23:1707–1710
154. Schönherr H, Hruska Z, Vancso GJ (1998) Macromol 31:3679–3685
155. Smith PF, Chun I, Liu G, Dimitrievich D, Rasburn J, Vancso GJ (1996) Polym Eng Sci 36:2129
156. Huy TA, Adhikari R, Michler GH, Radusch H-J (2002) Macromol Symp 184:153–173
157. Garcia R, Perez R (2002) Surf Sci Rep 47:197
158. Cohen Y, Albalak RJ, Dair BJ, Capel MS, Thomas EL (2000) Macromolecules 33:6502
159. Pakula T, Saijo K, Kawai H, Hashimoto T (1985) Macromolecules 18:1294

160. Huy TA, Adhikari R, Michler G (2003) H Polymer 44:1247–1257
161. Vancso GJ, Allston TD, Chun I, Johansson LS, Liu G, Smith PF (1996) Int J Polym Anal Charact 3:89
162. Strobel M, Jones V, Lyons CS, Ulsh M, Kushner MJ, Dorai R, Branch MC (2003) Plasm Polym 8:61–95
163. Moreno A, Baer E (1983) In Hiltner A (ed) Structure-property relationships of polymeric solids. Plenum, New York
164. Zaporojtchenko V, Strunskus T, Behnke K, Bechtolsheim C, Thran A, Faupel F (2000) Microelectron Eng 50:465–471
165. Shahidzadeh N, Arefi-Khonsari F, Chehimi MM, Amouroux J (1996) Surf Sci 888:352–354
166. Hruska Z, Lepot X (2000) J Fluorine Chem 105:87
167. Volkmann T, Widdecke H (1989) Kunststoffe 79:743
168. Kranz G, Lüschen R, Gesang T, Schlett V, Hennemann OD, Stohrer WD (1994) Int J Adhes Adhes 14:243
169. Adcock JL, Inoue S, Lagow RJ (1978) J Am Chem Soc 100:1948
170. Shinohara H, Iwasaki M, Tsujimura S, Watanabe K, Okazaki S (1992) J Polym Sci A 10:2129
171. Song J, Gunst U, Arlinghaus HF, Vancso G (2007) J Appl Surf Sci 253:9489–9499
172. Lepizzera S, Scheer M, Fond C, Pith T, Lambla M, Lang J (1997) Macromolecules 30:7953–7957
173. Sirijarukul S, Balanzat E, Vasina EN, Dejardin PJ (2007) Membr Sci 296:185–194
174. Iwata H, Hirata I, Ikada Y (1998) Macromolecules 31:3671–3678
175. Bobji MS, Bhushan B (2001) J Mater Res 16:844–855
176. Devlin CLH, Glab SD, Chiang S, Russell TP (2001) J Appl Polym Sci 80:1470–1477

4 Polymer Surface and Interface Properties and (Dynamic) Processes

Abstract

The application of AFM in its various modes for studies of polymers has been discussed in the previous chapters with a particular focus on imaging. It is clear that apart from "static" microscopy, AFM offers access to quantitative surface and interface properties. In addition, the family of techniques can be applied to a wide range of dynamic phenomena and processes as outlined in this chapter.

The surface and interface properties addressable by AFM comprise, among others, adhesion and friction, as well as surface mechanical properties. By analyzing these properties on a more relevant length scale, it is in many cases possible for the practitioner to identify the link between microscopic and macroscopic behavior. Similarly important are the dynamic phenomena we encounter in polymers; ranging from the intrinsic thermal behavior to dynamic interactions of polymers with their environment. This is best illustrated in local thermal analysis by advanced AFM approaches and in local property mapping. As shown in Fig. 4.1a, the surface melting temperature of poly(ethylene terephthalate) was determined using a local scanned probe with an integrated heating device. Upon heating the probe that is in contact with the PET surface, the film thermally expands, which can be deduced from the increase in the deflection signal of the AFM cantilever. At the surface melting point, the AFM probe starts to penetrate into the polymer film. As shown, the local surface melting point was found to be 235°C. A second illustrative example is presented in Fig. 4.1b. The sequence of AFM images shown reveals the growth of daughter lamellae of elastomeric polypropylene nucleated on mother lamellae. This process leads eventually to the crosshatched morphology typical for iPP [2].

4.1 Adhesion

Repulsive and attractive forces between a given polymer surface and a probe tip can be measured in contact mode AFM with high accuracy and with high spatial resolution. In these so-called force−displacement measurements, introduced in

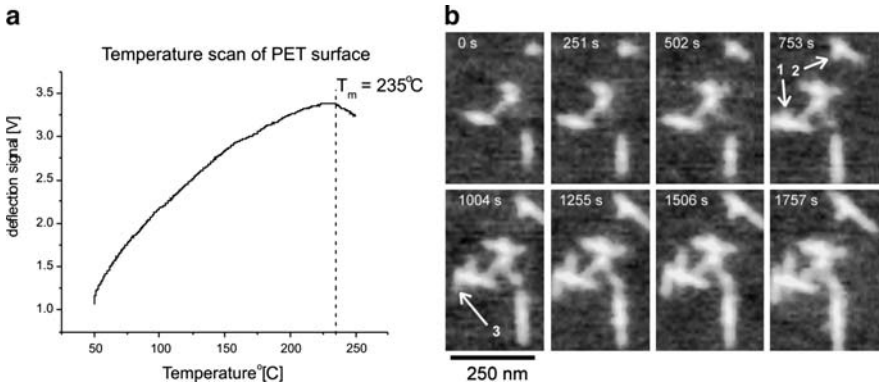

Fig. 4.1 (**a**) Temperature scan recorded on a PET film using a heatable AFM probe [1]. (**b**) TM-AFM images captured during the crystallization of an elastomeric PP film. The arrows point at homo-epitaxial nucleation events; the subsequent growth of lamellar crystals proceeds with different rates. While lamellar patches 1 and 3 grow steadily, patch 2 remains dormant for at least 500 s before growing slowly. Reprinted with permission from [2]. Copyright 2003. American Chemical Society

Chap. 2, altered surface tensions of surface-treated polymers are directly accessible. In addition, laterally resolved maps of adhesive interactions are useful to investigate heterogeneous samples, such as multicomponent systems, or to record local functional group distributions. For quantitative AFM work, calibration procedures for the cantilever spring constant and the AFM detection system become important. In addition, the use of modified tips will be discussed as a means to enhance the applicability of AFM for chemically sensitive imaging.

In force−displacement measurements, the sample is moved up and down (in and out of contact with the tip) at a fixed position (x, y) (compare also Chap. 2). The resulting force−distance plot (force−displacement curve) displays the bending of the cantilever as a result of tip−sample interaction forces. The interpretation of forces curves has been discussed in detail, e.g., by Cappella and Dietler [3] and by Butt and co-workers [4].

Neglecting the effect of surface roughness, the adhesion force F_a between a spherical particle of radius R and a flat surface of the same material in an inert atmosphere is

$$F_a = -4\pi R\gamma_{SV} \tag{4.1}$$

but in an atmosphere containing a condensable vapor, the above equation is replaced by

$$F_a = -4\pi R(\gamma_{LV}\cos\theta + \gamma_{SL}) \tag{4.2}$$

where, γ_{SV}, γ_{LV}, and γ_{SL} are the solid−vapor, liquid−vapor surface energies (surface tensions) and the solid−liquid interfacial energy, respectively, while θ denotes the contact angle of the liquid on the surface. The first term of (4.2) is due to the Laplace pressure of the meniscus and the second is due to the direct adhesion of the two contacting solids with the liquid. Unfortunately, real surfaces are not smooth as assumed for above-mentioned equations. Butt and co-workers have recently shown that only minute roughness on the nanometer length scale may have profound effects on the adhesion force in the presence of liquid condensing in the micro- or nano-contact between tip and surface. Hence, truly quantitative force microscopy experiments are most often carried out in inert liquid media.

In the limits of established contact mechanics models, including those developed by Johnson–Kendall–Roberts (JKR) [5] or by Derjaguin, Muller, and Toporov (DMT) [6], the measured forces are a function of the chemical identity of the contacting surfaces (via the work of adhesion W_{12} that depends on the surface and interfacial free energies involved). In addition, we need to consider the nature of the medium, the radius of the AFM tip, and also temperature and loading rate.

For the interactions between a sphere with radius R and a planar surface, a general equation relating contact area A and load L has been derived by Johnson, Kendall, and Roberts (4.3).

$$A^{3/2} = \pi^{3/2} R/K\{L + 3\pi R W_{12} + [6\pi R W_{12} L + (3\pi R W_{12})^2]^{1/2}\} \tag{4.3}$$

where, K denotes the reduced modulus $\frac{1}{K} = \frac{3}{4}\left(\frac{1-\nu_1^2}{E_1} + \frac{1-\nu_2^2}{E_2}\right)$ and W_{12} denotes the work of adhesion.

The work of adhesion W_{12} can be expressed as a function of the surface free energies of the tip (γ_1), the sample γ_2, and the corresponding interfacial free energy γ_{12} (4.4).

$$W_{12} = \gamma_1 + \gamma_2 - \gamma_{12} \tag{4.4}$$

For the contact area at pull-off one obtains

$$F_{Pull-off} = -3/2\,\pi R W_{12} \tag{4.5}$$

whereas the DMT theory affords:

$$F_{Pull-off} = -2\,\pi R W_{12} \tag{4.6}$$

Thus, the different surface free energies γ_i can, in principle, be experimentally determined based on AFM pull-off force measurements if the surface free energy of the tip is varied in a controlled manner. These equations form the basis for the so-called chemical force microscopy (CFM) approach and allow one to discriminate between different materials [7].

Qualitative force measurements are straightforward; however, for quantitative experiments, the calibration of cantilever spring constants and the AFM detection

system is required. As introduced in Chap. 2, the calibration of the normal spring constant involves (1) the calibration of the sensitivity of the optical deflection detection system and (2) the calibration of the cantilever spring constant using, e.g., the thermal noise or the reference lever method. In addition, force measurements in ambient conditions are complicated by the effect of capillary forces. As alluded to above, water condenses rapidly in the nanocontact between AFM tip and sample surface and creates a water meniscus. This meniscus results in forces that pull tip and surface strongly together. To avoid the contribution of these capillary forces in adhesion (and also friction) measurements, quantitative force measurements are most often carried out in an appropriate imaging liquid using a liquid cell (see Sect. 3.3 in Chap. 3).

An interesting aspect should be mentioned at this point. AFM tips, which are typically covered by oxidic layer on the tip material silicon or silicon nitride, can be functionalized to expand the range of interactions probed and to facilitate imaging with chemical contrast.[1] In the already briefly mentioned methodology termed "chemical force microscopy" (CFM), differences in long and short range forces are exploited for imaging under improved force conditions [8, 9] or "chemical imaging" [10]. This is achieved via (a) the control of the tip chemical composition by selective deposition of various materials or preferably the assembly of a functionalized monolayer (Fig. 4.2), [12] thus via control of γ_{tip} (see (4.4) for $\gamma_1 = \gamma_{tip}$), and (b) control of the medium. The chemical contrast necessary for imaging is achieved by exploiting the spatial (or temporal) variations of tip−sample forces in quantitative measurements.

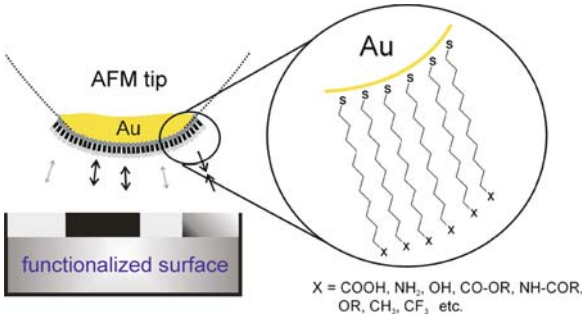

Fig. 4.2 Schematic of alkanethiol monolayer-modified gold-coated AFM tip used for CFM and interactions between exposed functional groups on the contacting surfaces (*right*; chemically modified AFM tip and functionalized surface. Different functionalities, and interactions are indicated by different gray scales and arrows, respectively). For details on the self-assembled monolayer-based tip functionalization, see text (adapted/reproduced with permission from [11])

[1]This oxide layer is covered with a several nanometer thick layer of airborne contaminants, typically hydrocarbons and siloxanes, which lower the surface tension quite substantially. This contamination layer can be removed by plasma treatments, wet chemical cleaning, etc.

An established and widely employed approach relies on the formation of self-assembled monolayers (SAM) of end-functionalized organothiols or disulfides, on gold-coated AFM tips [13]. This approach allows one to vary the composition and properties of these molecularly thin, covalently immobilized coatings [14–16]. The metal coating on the AFM probe tip (Ti or Cr primer plus Au) leads to increased tip radii. However, compared to other modification approaches, this drawback is counterbalanced by the broad range of functional groups that can be introduced. An alternative for the SAM formation on Au-coated tips is the direct functionalization of silanol groups present on oxidized silicon or silicon nitride tips using trichlorosilane or triethoxysilane chemistry [17–20]. These reactive silane derivatives form chemically stable SAMs via robust Si−O−Si bridges as a consequence of condensation reactions. In practice, the analysis of the deposited monolayer in the relevant area at the very tip apex is impossible. Hence, the method of choice must be very reliable. In this respect, the thiol−gold chemistry has advantages over the also mentioned silane chemistry because of the absence of unwanted side reactions, such as uncontrolled cross-linking in the deposition medium, and because of the reduced number of defects.

4.1.1 Practical Adhesion Mapping

Practical adhesion mapping can be performed in the so-called force–volume (FV) mode. In this mode, f-d curves are acquired for each pixel. Thus, information is obtained on attractive forces before the tip contacts the surface, indentation in the contact region (see Sect. 4.3), adhesive interactions, and the dissipated energy (as area under the f-d curve, compare Fig. 4.3).

In the FV approach the deflection data are sliced and sorted in deflection values that are larger and smaller than some arbitrarily chosen value. Hence, this mode displays the deflection values with respect to a reference point, which is different from true pull-off forces. For instance, f-d curves displaying a large hysteresis may show a strongly negative (deflection = force) value in the FV image, which may erroneously imply large pull-off forces (for an illustrative example see hands-on example 38).

The data shown below, in Fig. 4.4, illustrate the richness of local information that can be extracted. On a micropatterned surface of organic molecules exposing hydrophobic -CH_3 and hydrophilic -COOH groups at the film surface (prepared by microcontact printing [23]), the border region of the printed pattern was investigated in AFM-FV measurements. F-d curves were acquired pixel-per-pixel and provided information of local tip-surface interactions as shown in panels a and b. Here, the difference in pull-off force between the two chemically distinct regions and the tip is clearly pronounced.

Advanced off-line analysis software can help to access the statistical and the lateral distribution of the pull-off forces (panels c and d, respectively). The corresponding data, e.g., magnitude of the pull-off force, displayed in a 2D adhesion map (Fig. 4.4d) show that the border region is indeed characterized by a gradually changing, mixed chemical composition. The corresponding composition gradient can thus be mapped. Similarly, the statistically treated data yield a bimodal distribution of the pull-off forces (Fig. 4.4c).

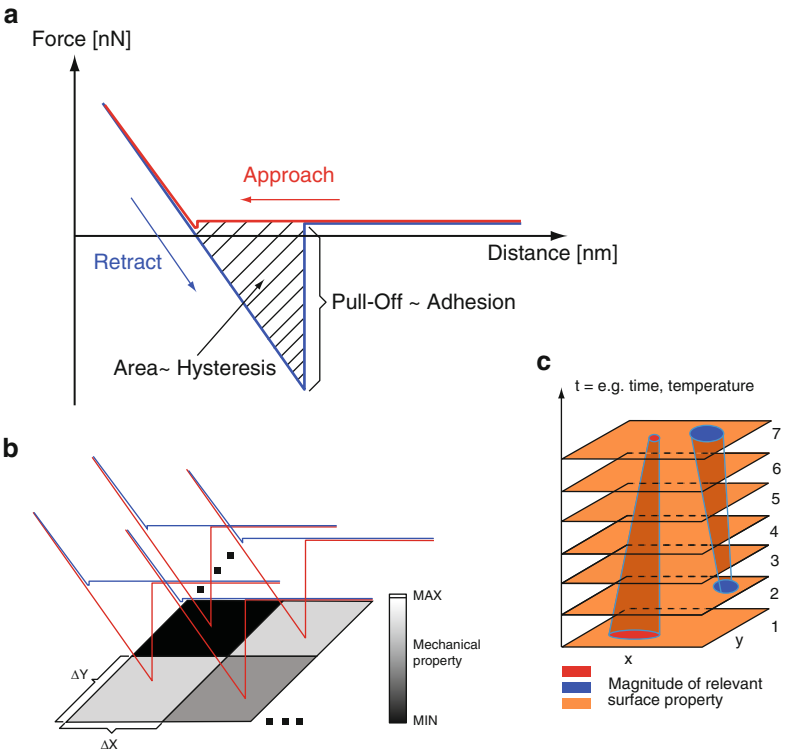

Fig. 4.3 (**a**) Schematic f-d curve with all important parameters that are assessed. (**b**) Pixel by pixel mesh of data recorded in FV imaging. (**c**) Slices through stacks of f-d data may reveal temporal changes of particular surface properties. Reprinted with permission from [21]. Copyright 2005. Wiley-VCH

Hands-on Example 37

Solution-Grown Lamellae of PE on Mica by FV

Sample Preparation: Crystallization from Solution

The sample preparation is described in detail for hands-on example 7. Lamellar PE crystals are obtained on atomically flat mica sheets, which are glued onto metallic sample holder pucks using a minute amount of epoxy glue.

Contact and Force Volume Mode AFM Visualization of the Morphology

The AFM is set up for a standard CM experiment (Sect. 3.2 in Chap. 3). A large area scanner and a cantilever with small spring constant ($k \sim 0.05$ N/m) are selected. After the sample has been mounted, the relative tip position must be adjusted such

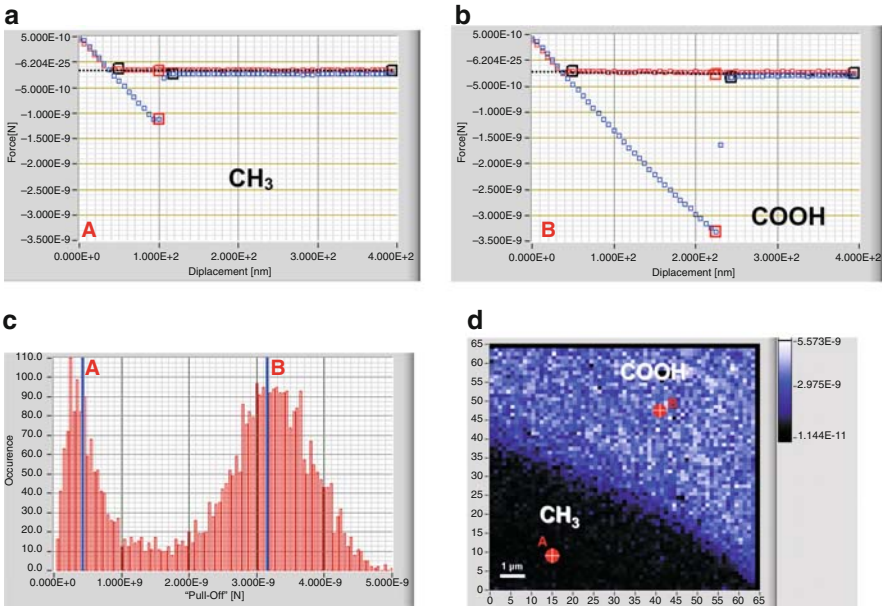

Fig. 4.4 F-d curves recorded with a silicon nitride tip in ambient on (**a**) CH_3 and (**b**) COOH terminated areas of a patterned SAM model surface. (**c**) Pull-off force histogram calculated from 4096 individual f-d curves. (**d**) Corresponding quantitative pull-off force map [22]

that a lamellar crystal is within the scan range of the scanner. Following the crude approach, the system is equilibrated for ca. half an hour.

The engagement procedure is carried out with minimized forces as described in Sect. 3.2 in Chap. 3. After engagement, the gains and the scan rate must be optimized. Once a lamellar crystal has been located in constant force mode, an image is recorded. We zoom into a very small scan area of 50 nm $\times$ 50 nm in a region where no PE lamella is located. Subsequently, f-d curves are acquired in the force spectroscopy mode of the AFM. To prepare for FV imaging, the sensitivity of the optical detection system is calibrated as described above. The maximum upward deflection of the lever is then limited by selecting a trigger option (relative to the out of contact line) to several nN (Fig. 4.5).

Subsequently, the scan size is increased as much as is required to image the entire crystal. Then a FV scan is started using a z ramp rate of $>$ a few Hz. An array of 64 $\times$ 64 points^2 (4,096 consecutive force–distance measurements) is acquired to provide an FV image of the hydrophobic PE crystal on the more hydrophilic mica. Because of the high surface energy of (clean) mica and the sample preparation procedure, which involves hydrophobic solvents, the mica surface will be covered with a thin contamination layer. Nevertheless, the adhesive properties differ markedly and the crystal can be visualized as shown in Fig. 4.6b. This FV image is scaled

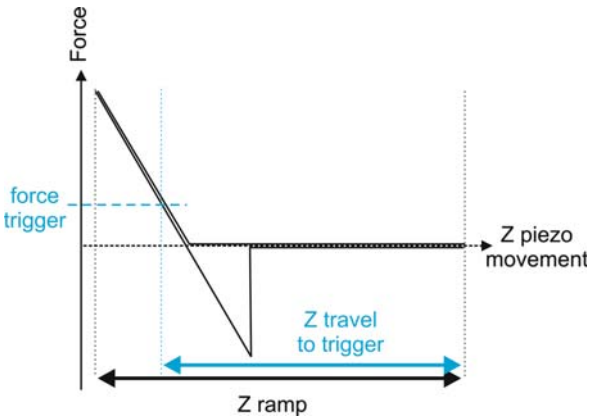

Fig. 4.5 Schematic of f-d curve that is captured with fixed z-ramp and f-d curve captured with a set force trigger that limits the z piezo movement to the pre-set force (*deflection value*). The corresponding (*reduced*) z travelling to trigger provides in FV image the "height" information for each pixel. The FV height images are thus different from a scanned constant force height image as no lateral forces act in the FV mode

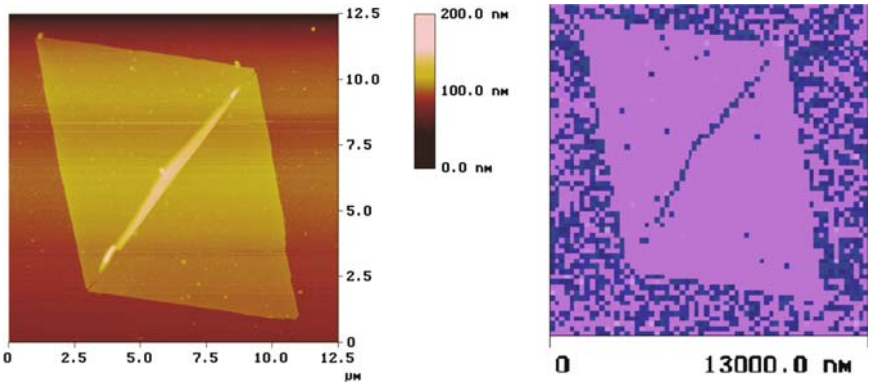

Fig. 4.6 CM-AFM (**a**) height and (**b**) FV image of a collapsed PE lamella (color scale: *dark*: −80 nN, *bright*: −50 nN pull-off force). Since the measurement was carried out in air, the forces are dominated by capillary forces. Reproduced with permission from [24]. Copyright 1999. American Chemical Society

according to the convention that adhesive forces possess a negative sign. Thus, mica is much more adherent than the PE crystal. The diagonal ridge that is a consequence of the well-known collapse of the crystal during deposition and drying on the mica substrate shows up in the FV image as a high adhesion area. It is obvious that this observation is an artefact that is caused by variations in contact area in the elevated part of the crystal.

4.1.2 Correlation of Adhesion Forces and Effects of Surface Treatments

The methodologies introduced above offer a unique possibility to assess and in some cases follow in situ the effect of surface treatments and reactions on sub-micrometer length scales. The distribution of surface forces can be related to distributions of functional groups, even though the cross-talk of topographic effects should not be underestimated. As already indicated in Fig. 4.6b, and as shown in Fig. 4.7, the AFM tip may contact the surface to be analyzed not only near the apex, but also on its flank, which results in an increased contact area and increased magnitude of the pull-off force. Thus, the contact area and pull-off forces are increased along the side of the electro-spun polymer fiber shown in the figure below. In addition, the JKR (or DMT) model may no longer be applicable as the assumption of a sphere–flat interaction may no longer be valid.

For flat samples, the extent of surface modification reactions can be conveniently followed. For the iPP films analyzed in Sect. 3.5 in Chap. 3, the roughness variations due to surface modification were minimal. Thus, crosstalk in the force analysis shown in Fig. 4.8a (acquired using unmodified Si_3N_4 tips in ethanol) subsequent to oxyfluorination is minimized.

In these experiments, individual f-d curves were recorded at various locations of each film using the same tip (i.e., the tip radius is assumed to remain constant). Subsequently, the pull-off forces were evaluated off-line and were plotted in a histogram. The pull-off forces were observed to increase with the extent of oxy-fluorination and the concomitant increase in surface energy (shown as values of surface tension). Using different tip functionalities and media on oxidized iPP and

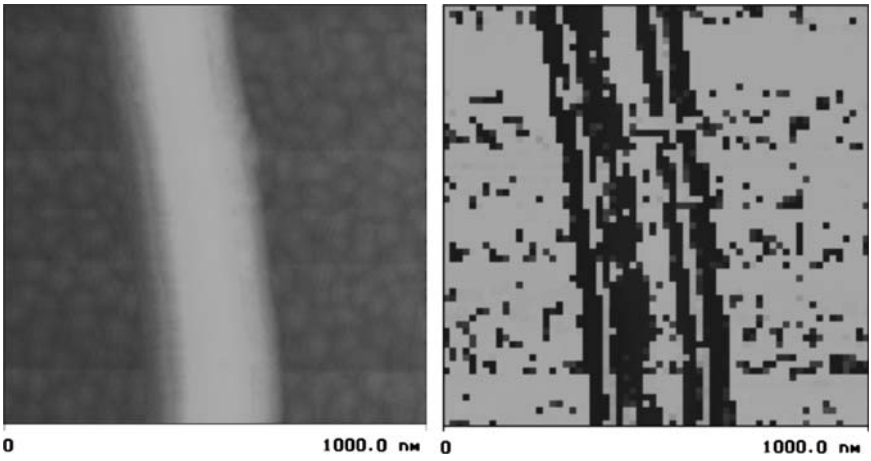

Fig. 4.7 FV height (*left*) and force images (*right*) of electrospun fiber of PVA on SAM of octadecanethiol. The data was acquired with unmodified AFM tips in air. The gray scale denotes: bright (*low forces*) to dark (high forces), −4 nN to −30 nN. With kind permission from Springer Science+Business Media [25]. Copyright 2005. Springer-Verlag

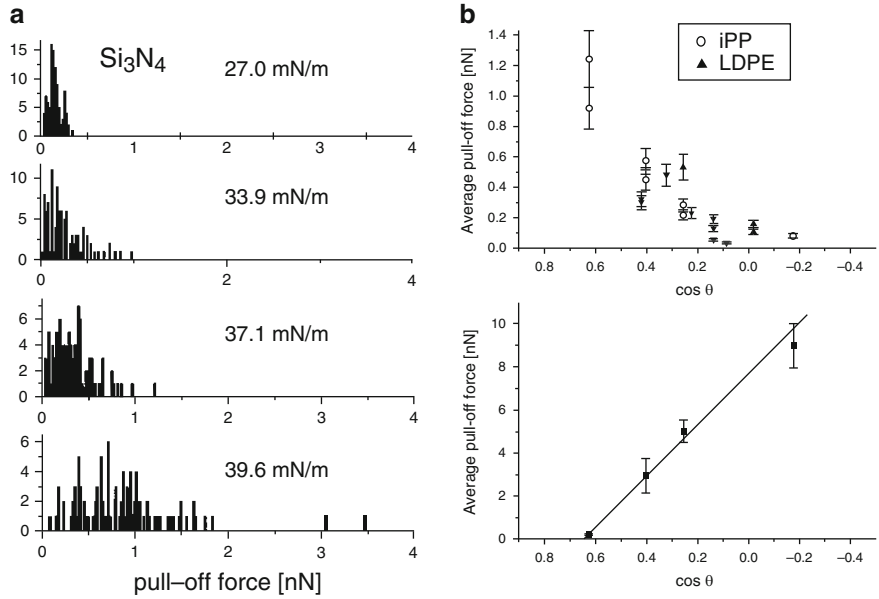

Fig. 4.8 (**a**) Histograms of pull-off force values obtained with an unmodified Si_3N_4 tip on untreated and oxyfluorinated iPP films in ethanol. The total surface free energy γ of the polymer film is shown. (**b**) Mean values of pull-off force measured with COOH-terminated tips on modified polyolefin surfaces (iPP, isotactic polypropylene; LDPE, low-density polyethylene) in ethanol (*top*) and with OH-terminated tips on oxyfluorinated iPP in water (pH 3.8, *bottom*) as a function of cos θ (contact angle measured with water). (Reprinted in part/adapted with permission from [26, 27]. Copyright 1998, 2000, American Chemical Society.)

LDPE films, a consistent trend between forces and surface energy (as assessed by water contact angle measurements) was established (Fig. 4.8b).

Hands-on Example 38

Surface Treatment of PDMS

Sample Preparation: Spin-coating and UV Ozone Treatment [28]

Sylgard 184 (Dow Corning) is prepared by mixing the precursors Sylgard 184A/Sylgard 184B at a ratio of 10:1 by mass followed by degassing in a vacuum oven at room temperature. The PDMS is spin-coated onto oxygen plasma cleaned glass cover slides using a Spincoater model P6700 (Specialty Coating Systems, Inc.). Subsequently, the films are cured at 120°C overnight. Some of the PDMS samples are oxidized by UV/ozone treatment in a UV/ozone cleaner (Ultra-Violet Products PR-100) generating a nominal ozone steady-state concentration of 55 ppm for 30 and 60 min resulting in water contact angles of $\sim$103° and $<$30°, respectively.

FV Measurements

The AFM FV measurements are carried out in contact mode using 11-mercapto-1-undecanol monolayer functionalized gold-coated probe tips (these functionalized probes are commercially available, see Appendix, or can be prepared according to the literature [10]). All measurements are performed in Milli-Q water using a liquid cell without O-ring (see Sect. 3.3 in Chap. 3). The use of very soft cantilevers with a nominal spring constant of ∼0.06 N/m is advisable.

First, the sensitivity of the optical detection system is calibrated. Hence, the set-up is prepared with a neat, pre-cleaned glass slide as sample, as outlined in detail in Sect. 3.3 in Chap. 3 for mounting the dry substrate. A drop of solution is placed onto the sample and the optical head is lowered vertically into its rest position and carefully secured. Once the photodiode differential signal shows a constant value, the engagement procedure as described in hands-on example 3 is carried out. However, to avoid shear forces between tip and sample the scan size is set to 0.0 nm.

After engaging on the surface, f-d curves are acquired in the force spectroscopy mode of the AFM. The maximum upward deflection of the lever is then limited by selecting a trigger option (relative to the out of contact line). Next the tip is withdrawn from the surface and the glass slide is exchanged for a PDMS-coated glass slide. After repeating the engagement procedure, f-d curves are recorded and all parameters (ramp size, pixel resolution, etc.) are optimized before starting an FV scan. To be able to record the FV scan in useful experimental time scales, the z ramp rate must be set to values > a few Hz. Subsequently, arrays of 64×64 points^2 (4,096 consecutive force−distance measurements) are acquired on different locations, using scan sizes of 0.5×0.5 μm^2 or 1.0×1.0 μm^2. The maximum load applied to the samples should be limited to 1−2 nN using a force trigger.

In partially oxidized PDMS samples (30 min UV−ozone treatment, contact angle ∼103°), the surface is often found to be covered with elevated drop-like features. These can be observed, e.g., in conventional TM-AFM images. Using the force data extracted from captured FV images using a custom software [28], 2D maps of FV height, pull-off force ("adhesion"), and dissipated energy ("hysteresis") can be displayed and representative f-d curves can be selected, as shown below. The areas around the elevated droplet-like structures display a sharply defined pull-of event and low hysteresis. Despite the very similar pull-off force, the drops, by contrast, show pronounced hysteresis, which can be understood by interpreting the f-d curves (Fig. 4.9, lower right panel). After reaching the point of maximum negative force (adhesion) the tip does not detach instantaneously from the surface. Upon further withdrawing the sample from the tip, the adhesive force monotonically decreases, which is fully consistent with the formation of a liquid bridge of low molar mass siloxanes between partially oxidized PDMS and the tip.

The effect of the surface treatment for longer UV−ozone treatment times (60 min, water contact angle <30°) in terms of adherence and the laterally inhomogeneous distribution of pull-off forces provide evidence for the successful and complete oxidation of the previously hydrophobic PDMS surfaces. Upon storage in ambient conditions, one can observe that the forces gradually increase in heterogeneity with

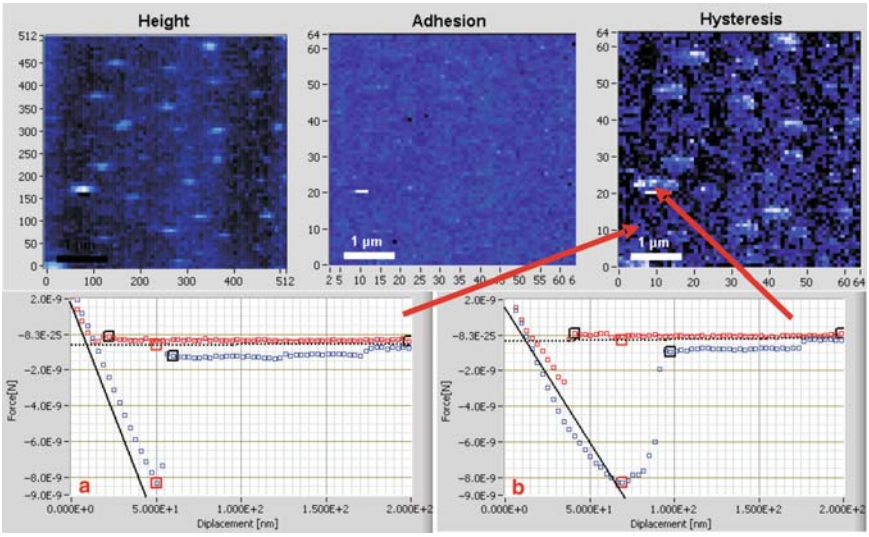

Fig. 4.9 CFM of "droplets" appearing with time after 30 min of UV/ozone exposure: (**a**) height, (**b**) maximum adhesive forces, and (**c**) adhesion hysteresis. The color scales indicate the height [bright (0 nm) to dark (10 nm]; maximum adhesive force [dark (6 nN) to bright (l7 nN)]; and hysteresis [dark (0.2×10^{-17} J) to bright (1.2×10^{-17} J)]. (d) Representative force-distance curves. Adapted with permission from [28]. Copyright 2004. American Chemical Society.

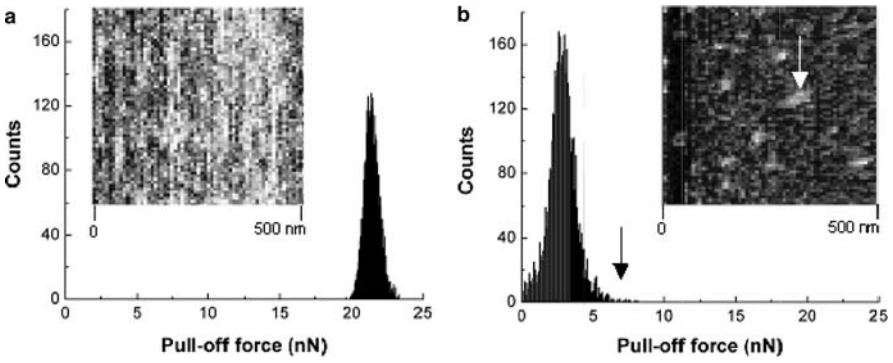

Fig. 4.10 Histograms of the pull-off forces and corresponding adhesion images of (**a**) unexposed PDMS and oxidized PDMS after (**b**) 0.1 day after exposure to 60 min of UV/ozone. In the adhesion images, the color scales are individually scaled from dark (low pull-off) to bright (high pull-off). Reproduced with permission from [28]. Copyright 2004. American Chemical Society

recovery time. The force histograms and adhesion maps shown in Fig. 4.10 indicate that the recovery is heterogeneous in nature as islands with high pull-off forces appear relatively soon after the treatment.

For these and similar measurements, it is advisable to utilize the same tip for each set of samples as the tip radius is one parameter that determines the magnitude of pull-off force for a given tip chemistry−sample pair under identical experimental conditions. In addition, one should verify that the tip has not changed because of wear or contamination by recording data for the first sample after finishing an entire series.

Hands-on Example 39

Force Titrations of Flame-Treated LDPE

Sample Preparation: Flame-treatment [29]

LDPE films are flame-treated (50×, 100×, and 200×) according to hands-on example 35.

FV Measurements

FV images are acquired analogously to hands-on example 38 in liquid environment using soft gold-coated CM cantilevers modified with 11-mercapto-1-undecanol to render the adhesive forces pH independent. To ensure rapid exchange of the solution to vary the pH of the solution, a closed liquid cell system comprising an O-ring is used (compare Sect. 3.3 in Chap. 3). When filling the liquid cell, care has to be taken not to entrap air bubbles in the cell or the tubing. The pH of the solution is varied by preparing solutions with different pH and identical ionic strength. To avoid the possible specific interaction of phosphate based ions in buffers, solutions are prepared with aqueous HCl and NaOH (using commercial kits for acid–base titrations); NaCl is added to keep the ionic strength essentially constant. The actual pH values must be checked with a conventional pH meter immediately before and after the experiments (Table 4.1).

The AFM tip is engaged with zero scan size. Following the acquisition of f-d curves and the calibration of the sensitivity of the optical detection system, FV scans (500 × 500 nm) are recorded at a z ramp rate of > a few Hz. The maximum load applied to the samples should be limited to 1−2 nN.

In such surface treated samples, the surface ionization state can be analyzed by calculating the average pull-off forces from FV scans on various flame treated samples as a function of the solution pH. Thus, FV data are captured for different

Table 4.1 Details to prepare solutions for CFM force titrations

pH	2	3	4	5	6	7	10
HCl(M/L)	0.01	0.001	0.0001	0.00001	0.000001	0	0
NaCl(M/L)	0	0.01	0.01	0.01	0.01	0.01	0.01
NaOH (M/L)	0	0	0	0	0	0	0.0001

pH values of the buffered medium. Care has to be taken that the volume of liquid passed repeatedly through the cell is sufficient to rinse out the previous buffer. Hence, it is clear that one should start at neutral pH and stepwise increase (or in a separate series decrease) the pH value. It is advisable to utilize the same tip for each set of samples as the tip radius is one parameter that determines the magnitude of pull-off force for a given tip chemistry–sample pair under identical experimental conditions in the JKR limit. In addition, one should verify that the tip has not changed because of wear or contamination by recording data for the first sample after finishing an entire series.

The FV data acquired are analyzed as sketched in the examples above. The pull-off force values for each f-d curve are estimated and a histogram of forces for each pH and treatment condition is calculated. In Fig. 4.11 some normalized force titration curves (average pull-off force as a reference of value at pH 4 versus pH) on flame treated LDPE are shown. These titration curves display a typical sigmoidal shape, while the untreated polymer exhibited by contrast an almost constant pull-off force over the entire pH range.

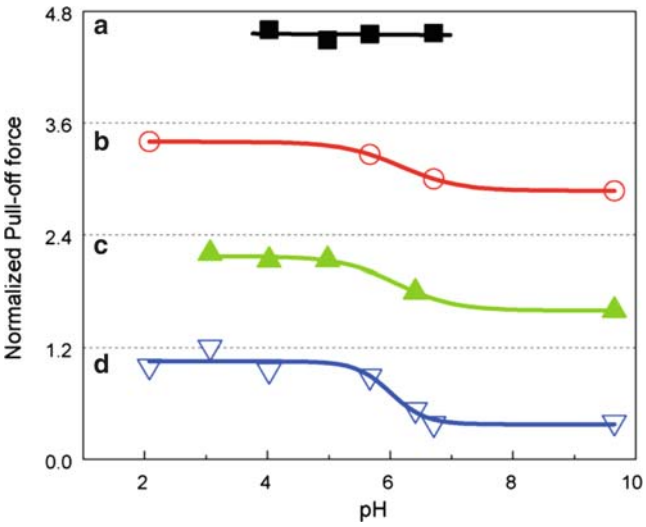

Fig. 4.11 Normalized force titration curves showing the adhesive force between hydroxyl functionalized tips and flame treated LDPE films as a function of the solution pH. The average pull-off force at pH 4 was set as a reference for each sample. The solid lines have been added as guides to the eye. (**a**) Untreated LDPE. (**b**) LDPE flame-treated 50 times. (**c**) LDPE treated 100 times. (**d**) LDPE treated 200 times. Reproduced with permission from [29]. Copyright 2007. Elsevier

Hands-on Example 40

Force Mapping of Polymer Blends

The acquisition of f-d data in a pixel-per-pixel fashion, as discussed so far in this chapter, is intrinsically slow compared to friction imaging (4.2) since the tip must be lifted out of contact for each pixel. In liquids, the corresponding viscous drag forces limit data acquisition to rates of typically few pixels per second, thus, an image of 64 × 64 pixels takes on the order of 8−12 min. For high-resolution work, thermal and instrumental drift may therefore become problematic in some cases. Similarly, the enormous amount of data in FV mode renders this mode inefficient. Pulsed force mode AFM may be an alternative in this context (compare Sect. 3.2 in Chap. 3). Instead of digitally recording the complete f-d curve, only the four points are captured, the baseline, the maximum repulsive force, the maximum adhesion force, and a point that can be used with the maximum repulsive force to define the slope in the loading regime, respectively.

Sample Preparation: Spin-coating [30]

A 3: 1 solution of P2VP (M_w = ca. 300,000 g/mol) and PtBMA (M_w = ca. 850,000 g/mol) in THF is spincoated on pre-cleaned silicon substrates at 3,000 rpm for 1 min followed by drying in vacuum. The silicon sample is attached to the sample disc using pressure sensitive adhesive.

Pulsed Force Mode Measurements

For pulsed force mode imaging, a stiff contact mode lever ($k_N \sim 0.6$ N/m) is selected. A modulation frequency in the range of 800 Hz is selected and the cantilever oscillations are adjusted such that the adhesive interactions between tip and surface are overcome, as monitored using an oscilloscope. The modulation must clearly show the snap-off of the tip. Next the four markers are set according to the general procedure outlined in Sect. 3.2 in Chap. 3.

Pulsed force mode scans on the thin film of the phase separated blend of P2VP and PtBMA show pronounced contrast in two imaging modes, i.e., height and adhesion, while the stiffness suffers to some extent from artefacts. In a new mode called combined dynamic X mode SFM, these problems are overcome [30].

The differences in adherence, as seen in the pulsed force adhesion image, between the AFM tip and the high surface energy P2VP on the one hand and the tip and the lower surface energy PtBMA on the other hand are well pronounced. Since the tip periodically interacts with the two constituent phases and since the properties of polymers are in general rate-dependent, a change in the modulation frequency may change the relative contrast (Fig. 4.12).

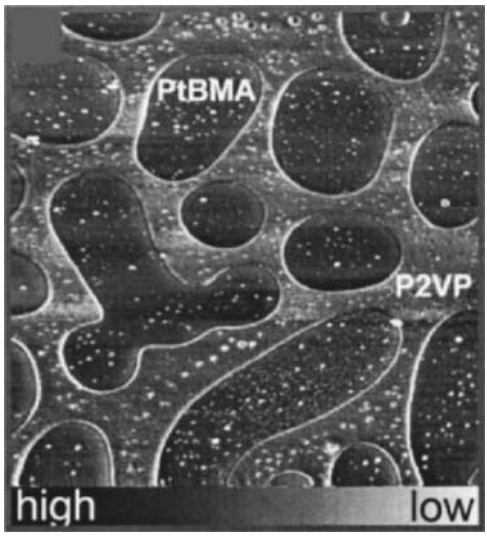

Fig. 4.12 Pulsed force mode measurement on a thin film of a blend of P2VP and PtBMA. The pulsed force mode AFM adhesion image (5 × 5 μm) clearly distinguishes the PtBMA islands from the surrounding P2VP. (Reprinted with permission from [30]. Copyright 2000. American Institute of Physics.)

4.2 Friction

The measurement of friction forces, in particular on multicomponent systems, may provide a rapid, qualitative insight into the distribution of the components and may be useful to map local functional group distributions. For quantitative friction mode AFM work, calibration procedures for the lateral spring constant and the AFM detection system become crucial. These calibration approaches are more demanding than the one described in Sect. 4.1, but because of recent progress in calibration standard development can be successfully tackled.

As outlined in Chap. 2, friction forces can be measured simultaneously with topography imaging in constant force contact mode AFM. In order to maximize the sensitivity of friction force measurements, the sample is scanned at an angle of 90° with respect to the long axis of the cantilever. The torsion of the cantilever around its long axis is measured with a 4-quadrant photodiode. A representative example for the corresponding output of the photodiode signal is shown in Fig. 4.13. The so-called friction loop displayed there allows one to calculate the friction force from the difference between the trace and retrace lines multiplied by 0.5. In order to improve the statistics, one typically acquires a complete scan simultaneously for both relative scan directions (trace and retrace) and calculates the mean friction forces from the corresponding difference image. This procedure also eliminates the effect of topography, unless the scan lines of trace and retrace

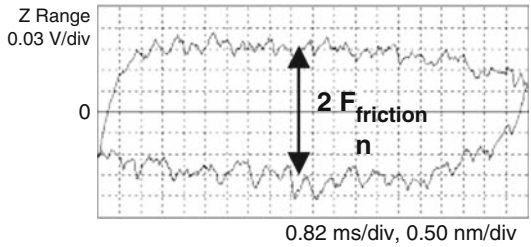

Fig. 4.13 Friction loop (friction signal [V] vs. scanned distance [nm] plot) measured perpendicular to the polymer chain direction of oriented polyethylene with a -CF_3 modified tip. [31]

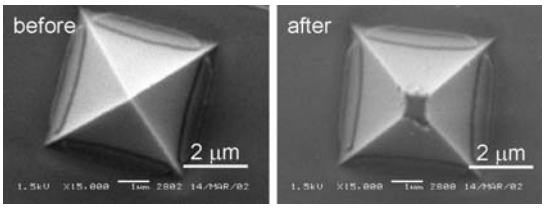

Fig. 4.14 SEM images of an unused and a worn CM AFM tip

do not match well. In this case, the scan line shift must be corrected prior to the subtraction in the AFM software.

The *quantitative* measurement of friction forces is complicated by the geometry in case of triangular shaped cantilevers, variations of photodiode sensitivity, the dependence of the photodiode output signal on laser alignment, and the difficulty of accurate calibration of the lateral force spring constant. The wedge calibration method using a specially designed calibration standard can circumvent these problems, as shown in Chap. 2.

In practice, friction mode AFM relies on the assessment of lateral/shear forces. These forces may damage the sample, as already mentioned. It is also possible that the tip may wear, which needs to be taken into account when data are analyzed and interpreted (Fig. 4.14).

Friction force imaging with chemical contrast, also using modified AFM tips, is (concerning imaging technique and data acquisition) similar to conventional friction force or lateral force imaging in contact mode AFM. The image contrast can be predicted if we assume that adhesive interactions are dominant. The magnitude of the friction force is proportional to the contact area A, which can be calculated as a function of work of adhesion following, e.g., (4.3). Based on this equation, a local increase in work of adhesion leads to an increase in magnitude of the measured friction force.

Sinniah et al. [32] showed that AFM tips functionalized with various alkanethiols can be utilized to differentiate polyamide-rich regions from poly(ethylene glycol)-rich regions in a segmented block copolymer in water (Fig. 4.15). In this case, the friction forces observed with the more hydrophobic methoxy-terminated tips on the polyamide-rich domains exceed the forces measured on the PEG-rich domains. Using amide-terminated tips, the contrast is significantly reduced, which implies imaging with predictable contrast.

Since dynamic friction of polymers has a large contribution from internal viscoelastic dissipation, plots of the friction force, determined, e.g., by AFM, vs. f_o are qualitatively similar to plots of tanδ vs. f_o. Hence, by measuring dynamic friction forces under well-controlled conditions, the dynamics of a given polymer can be directly probed at the free surface of a sample specimen. Thereby surface vs. bulk properties can be probed as well as confinement effects.

For example, enhanced macromolecular mobility was observed at the surface of polystyrene films [33]. In 200 nm thick films of monodisperse PS on silicon, measurements of the lateral force (under a constant applied load of 10 nN) vs.

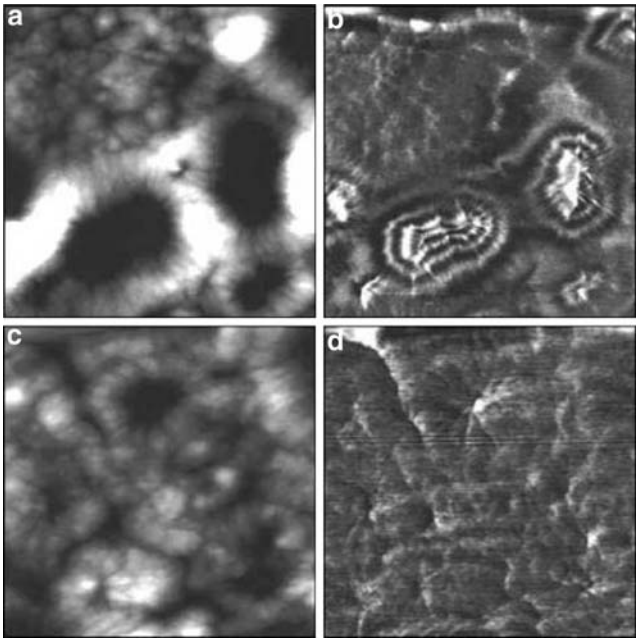

Fig. 4.15 Solvent-exclusion contribution to image contrast is demonstrated with scanning force data acquired on a co-block-polyethylene glycolpolyamide (Nylon-12) surface (PEBAX 1,074), prepared by melting/resolidification. (**a**) Topographic image in water, methoxy tip termination (15 × 15 μm^2); (**b**) friction LFM image in water, methoxy tip termination (15 × 15 μm^2); (**c**) topographic image in water, amide tip termination (7.5 × 7.5 μm^2), (**d**) friction image in water, amide tip termination (7.5 × 7.5 μm^2). (Reprinted with permission from [32]. Copyright 1996. American Chemical Society.)

temperature at a given scan rate indicated that the surface T_g of the PS films was markedly lower than the corresponding bulk T_g over the entire molecular weight range. The surface T_g was determined from the maximum observed in friction force vs. temperature plots (Fig. 4.16 a). In addition, the apparent activation energy of the surface segmental motion in PS was determined as 230 ± 10 kJ/mol, which is significantly smaller than the reported bulk value that ranges from 360 to 880 kJ/mol (Fig. 4.16b, c).

Polystyrene and other materials have been reported to be plastically deformed at temperature even below T_g (compare, e.g., Sect. 3.2 in Chap. 3); thus, such experiments are most likely carried out beyond the elastic contact limit and surface damage may prevail.

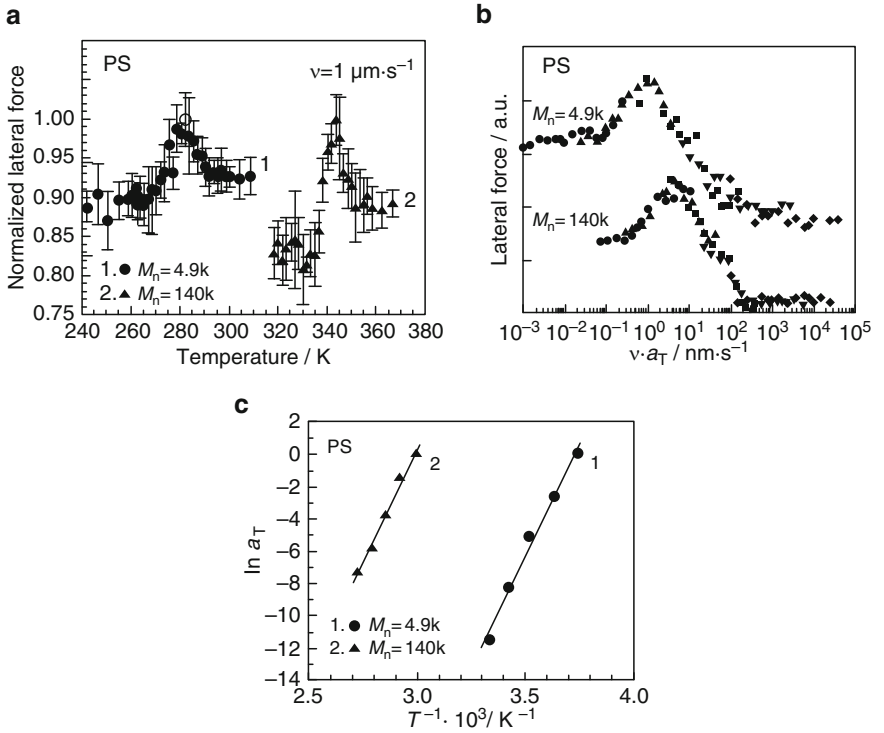

Fig. 4.16 (**a**) Typical lateral force/temperature curves at a given scanning rate. Curves for PS with M_n = 4,900 or M_n = 140,000 at a scanning rate of 1 μm s^{-1} are displayed. The bulk T_g values measured by DSC are 348 and 376 K, respectively. (**b**) Master curves of the scanning rate/lateral force relationship for PS films drawn from each curve in panel a. Reference temperatures of 267 and 333 K have been used for PS with M_n = 4,900 and for PS with M_n = 140,000, respectively. (**c**) Semi-logarithmic plots of a_T versus the reciprocal absolute temperature (T^{-1}) for PS films with M_n = 4900 or M_n = 140,000. (Reprinted with permission from John Wiley & Sons, Inc. [33]. Copyright 2004. John Wiley & Sons, Inc.)

Hands-on Example 41

Sub-T_g Transitions in PMMA

Sample Preparation: Spin-coating

Bare Si(100) wafers with native oxide layer are cleaned prior to spin coating by rinsing them thoroughly with chloroform and ethanol, followed by an oxygen-plasma treatment (30 mA, 60 mTorr) using a Plasma Prep II plasma cleaner (SPI Supplies, West Chester, PA) for 10 min. Films of poly(methyl methacrylate) (PMMA, Aldrich, Mw = 120,000 g/mol) with thickness of ~125 nm are prepared by spin coating filtered solutions in toluene (conc. 5 wt-%) onto freshly cleaned oxidized Si(100) substrates (Spin Coater P6700, Specialty Coating Systems, Indianapolis, IN). The PMMA films obtained are then annealed at 150°C under vacuum for 12 h.

Friction Force AFM

Quantitative friction analyses on freshly prepared PMMA films are carried out using Si and Si_3N_4 probes with small tip radii of ~20 nm. Prior to the measurements the probes are cleaned by immersion in and rinsing with chloroform followed by drying in a stream of nitrogen. Friction force−velocity measurements (scan size of 500 nm) are performed with an AFM that allows for variable velocity [34] temperature and climate control (<5% relative humidity (RH) and temperatures between −3°C and 26°C) via the flow of pre-thermostatted nitrogen gas of controlled humidity through an environmental chamber (see also Sect. 4.4). The calibration of the cantilevers is performed using the method described above. The dimensions of the cantilevers and tip radii can be obtained by scanning electron microscopy or by scanning a tip calibration grating (Chap. 2).

Friction data in the form of friction loops are captured at a constant load for various scan rates (that are converted to velocity taking the scan size into consideration) and sizes at room temperature and at 5°C. The friction force as half width of the friction loop is calculated and then plotted against velocity.

Typical friction force data obtained at a constant load are shown in Fig. 4.17 (*left*). In these experiments, the applied load should be limited to <1 nN to ensure that the surface of the film to a depth of ≤2 nm is probed and that wear of the glassy PMMA film can be excluded. A clear maximum is observed that shifts to higher velocities with increasing temperature, in accordance with the time−temperature superposition principle [36]. From the master curve of friction force vs. velocity data for PMMA (shifted by a_T to the reference temperature of 25°C) an activation energy of 35 kJ/mol can be estimated.

The observed peak was assigned to the β-relaxation of PMMA, which is the result of the rotation of the $-(CO)OCH_3$ side groups around the C−C bonds linking the side groups to the main polymer chain [37]. The value of the corresponding activation energy of ~35 kJ/mol is significantly lower than the bulk value (71–96 kJ/mol) determined by mechanical and dielectric methods [38].

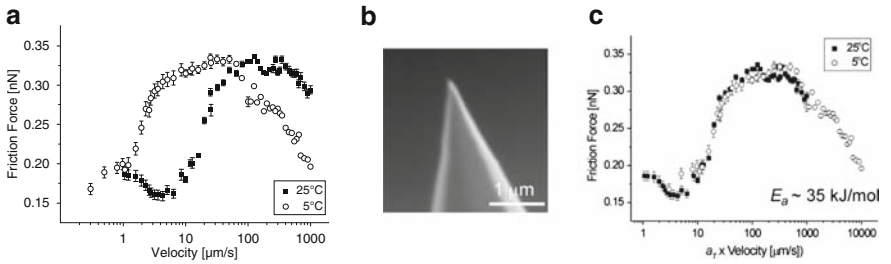

Fig. 4.17 (**a**) Semi-log plot of friction force vs. velocity for PMMA film on oxidized silicon (thickness 125 nm) measured with an oxidized silicon tip (R = 20 nm) in nitrogen atmosphere (<5% RH) at various temperatures: 25°C and 5°C. A load of 0.2 nN was maintained constant during the measurements. The error bars indicate the standard deviation of the data analyzed for a given velocity (n = 150). (**b**) SEM image of the Si tip with radius R = 20 nm. (**c**) Master curve constructed according to the time-temperature superposition principle (With kind permission from Springer Science+Business Media [35]. Copyright 2008 Springer)

Furthermore, the frequency of the β-relaxation is significantly higher (10^6 Hz) than the frequency detected in bulk measurements (10–100 Hz) at room temperature. Both the higher frequency and lower activation energy indicate greater free volume and correspondingly higher mobility at the polymer surface.

Hands-on Example 42

Friction Forces on Oxidized PS [39]

Sample Preparation: Spin-coating and UV Oxidation

PS films are prepared by spin-coating polystyrene (280 kDa, Sigma Aldrich) from 1% w/v chloroform solutions onto freshly cleaved mica (1 cm^2 area) substrates. These films are placed in a standard UV-ozone reactor for 20 and 40 s [9]. Si_3N_4 cantilevers with integrated tips are precleaned in the UV-ozone chamber and are enriched with surface hydroxyl groups by immersion in 0.5 M NaOH for 20 min, in 0.1 M HCl for 10 min, and in 0.5 M NaOH for 10 min (in this order).

Friction Force AFM

Lateral force microscopy (LFM) is performed simultaneously with topographical imaging in contact mode using V-shaped Si_3N_4 cantilevers with a nominal spring constant of 0.06 N/m. All lateral force data are acquired under Milli-Q water. We use the open cell configuration (see Sect. 3.3 in Chap. 3). To ensure meaningful comparisons of friction data acquired on different films, the same tip must be used for all the films tested.

Data are captured in trace and retrace at a constant load (∼ 40 nN) for differently treated films. Secondly, the load is varied by stepwise changing the setpoint (f-d

curves must also be recorded to be able to correlate setpoint and load). For improved statistics, it is suggested to capture friction images instead of loops and to calculate the difference image instead of the half width of individual friction loops.

Oxidized PS films exhibit substantially higher friction than untreated films when imaged with hydroxyl-terminated Si_3N_4 tips in water. The higher frictional forces and coefficients measured for the oxidized surfaces using these tips are due to hydrogen bonding between the polar hydroxyl groups of the tip and the oxygen

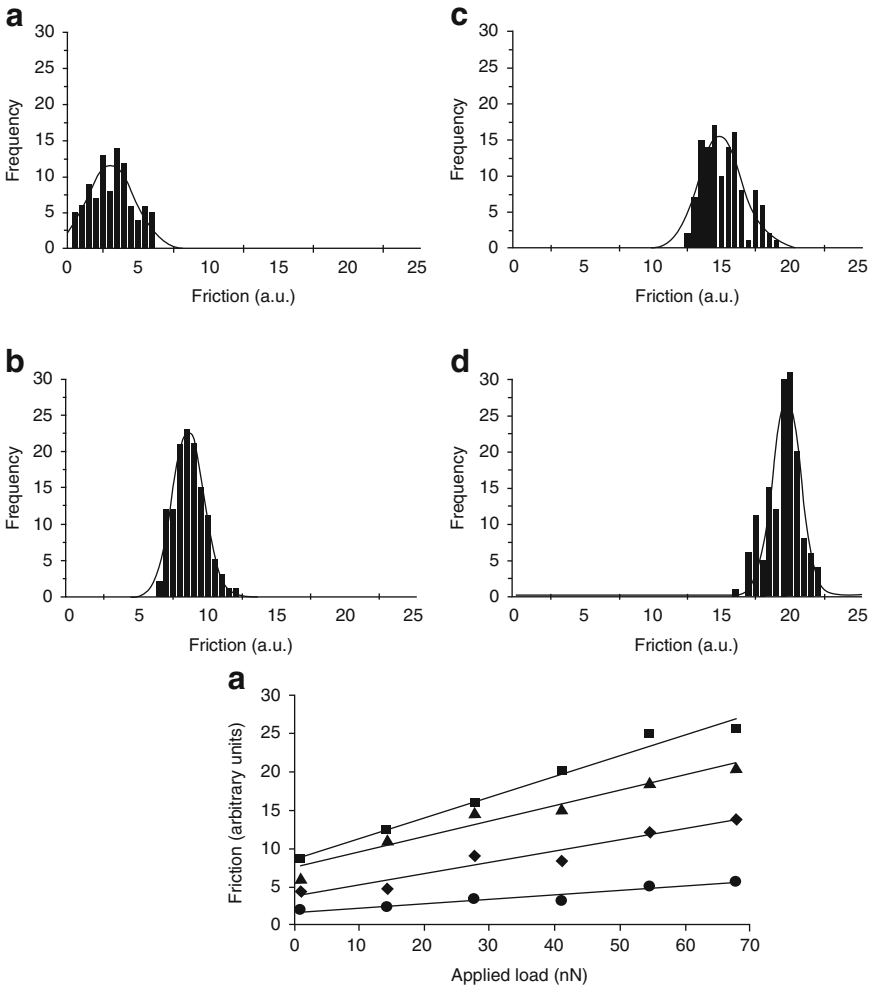

Fig. 4.18 *Top*: Histogram of friction forces acquired at a constant load of 42 nN for PS films subjected to UV-ozone for (**a**) 0s, (**b**) 20s, and (**c**) 40s. *Bottom*: Plots of friction force versus applied load data recorded for untreated and UVO-treated PS films. The vertical arrow denotes increasing treatment time. Reproduced with permission from [39]. Copyright 2000. American Chemical Society

functional groups of the PS surfaces. These data are fully in line with reported XPS data that provide evidence for the introduction of polar species at the film surfaces via the formation of C−O, C = O, and O−C = O functional groups [39].

The friction force vs. load plots provide access to the friction coefficient of the particular tip−polymer sample combination. As illustrated in Fig. 4.18 (*right*), the friction coefficients increase with increasing degree of surface oxidation.

4.3 Surface Mechanical Properties

Apart from repulsive and attractive forces between a given polymer sample surface and an AFM tip, surface mechanical properties can be measured in contact mode AFM. This requires the acquisition of force–displacement curves and their conversion into force−indentation curves. The subsequent analysis is based on theoretical models and provides access to surface elastic moduli, among others. Since the AFM tip is typically very sharp, moduli can be obtained with high spatial resolution.

Indentation force measurements utilize the indentation part of a force–displacement curve (Fig. 4.19). In the case of a non-compliant sample surface, the SFM tip does not indent the sample and hence the deflection vs. piezo position curve in the contact region has a slope of 1.0. For compliant samples, the slope is <1.0 and can be used to obtain the elastic modulus of the sample by fitting the measured

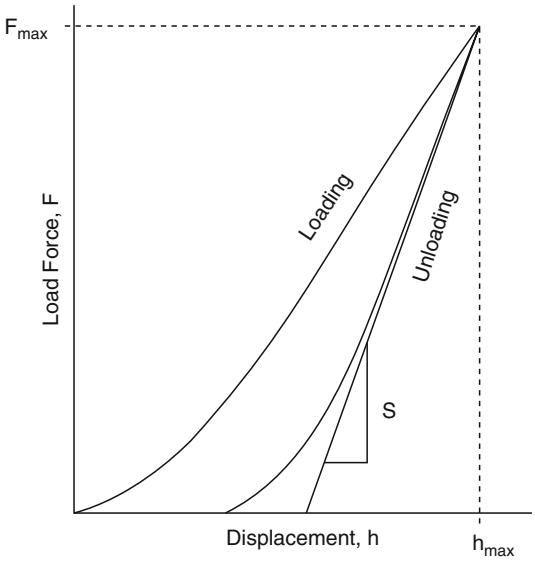

Fig. 4.19 Schematic force − displacement curve obtained in a nanoindentation experiment. The tip is pressed into the sample with a load force F to a maximum displacement h_{max}. The tangent of the unloading curves at h_{max} represents the stiffness S. (Reprinted with permission from [44]. Copyright 2006. Elsevier)

indentation to a suitable model. Knowledge of the tip shape/geometry and elastic constants of the tip is required to obtain the desired materials properties. There have been many different approaches discussed in the corresponding literature.

Van Landigham et al. reviewed nanoindentation of polymers, [40, 41] including a summary of the most common analyses of load-indentation data. Chief among these methods is an analysis of indentation load-penetration curves according to the Oliver-Pharr method. [42] This method is based on relationships developed by Sneddon for the penetration of a flat elastic half space by different probes with particular axisymmetric shapes (e.g., a flat-ended cylindrical punch, a paraboloid of revolution, or a cone) [43]. More recently, Withers and Aston discussed indentation in the context of plasticity and viscoelasticity [44].

For details on the experimental procedures and analyses, including pitfalls, the reader is referred to the mentioned reviews and in particular the work in [73, 74]. We treat below a simplified case. In practice, it is found that the application of these methods to polymers often leads to overestimates of moduli compared to bulk measurements. This deviation and other effects have been largely attributed to neglected *viscoelastic* effects [45].

One of the most simple approaches to analyze indentation measurements is based on Hertz theory. We discuss below an example reported by the Radmacher group on gelatin films (Fig. 4.20) [46].

The slope of a force curve on an infinitely stiff substrate is by definition one; thus, the deflection equals the piezo z travel. In measurements of soft samples, the deflection is reduced by the indentation δ. Thus, employing the cantilever force constant k (which must be chosen appropriately in AFM indentation measurements), Hooke's law can be written as

$$F = kd = k(z - \delta) \tag{4.7}$$

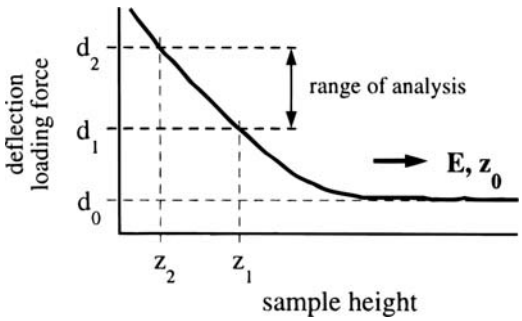

Fig. 4.20 Force curve on a gelatin film. The parameters necessary for data analysis are depicted in the graph: the zero deflection (force) d_0 and the range of analysis defined by two data points (d_1, z_1) and (d_2, z_2). The analysis provides independently the contact point z_0 and the Young's modulus E. (Reprinted with permission from [46]. Copyright 2000. American Chemical Society)

The Hertz model, extended by Sneddon to other geometries provides a relation between load force F and the indentation δ (with Young's modulus E, Poisson ration ν, and the half opening angle of the indenting cone α).

$$F = (2/\pi)[E/(1-\nu^2)]\delta^2 \tan(\alpha) \tag{4.8}$$

The average of the approach and retract curves determined experimentally are fitted with the Hertz model; the combination of the two equations above yields

$$z - z_0 = d - d_0 + \frac{k(d-d_0)}{2/\pi)[E/(1-\nu^2)]^2 \tan(\alpha)} \tag{4.9}$$

The two unknowns, z_0 and E, are determined independently from each other by taking two deflection values and their z values as shown in Fig. 4.21. Radmacher et al considered the range of deflection values chosen as the range of analysis.

Interestingly, for thick gelatin films (>1 micron) the Hertz model matches the data well (here E > 20 kPa). For thinner films, a disagreement between the model and the experimental data has been observed and it is attributed to the effect of the underlying substrate (Fig. 4.21).

These data indicate that, under certain circumstances, the limitations of AFM indentation experiments have to carefully considered. This is particularly true, if quantitative data are sought.

For the practitioner, indentation measurements provide insight into essential dynamic processes of hardening of paints and coating, among others. In addition,

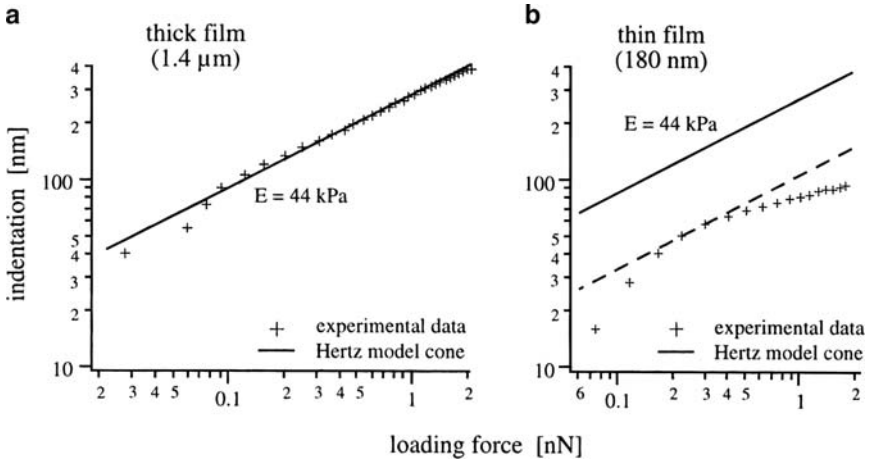

Fig. 4.21 Log−log plots of indentation vs. loading force data for (**a**) thick and (**b**) thin gelatin films. In panel (**b**) a higher modulus was used as well (*dashed line*), but here also the data cannot fit the whole range of the data. (Reprinted with permission from [46]. Copyright 2000. American Chemical Society)

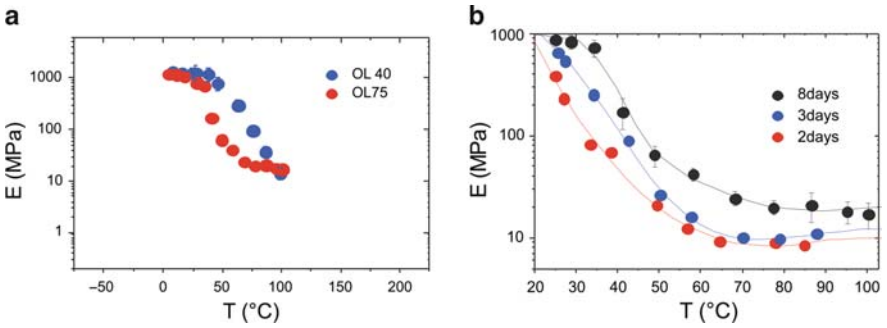

Fig. 4.22 Elastic moduli vs. temperature obtained by AFM nanoindentation measurements on various alkyd-based coatings: (**a**) effect of oil number; (**b**) time evolution of modulus after application of the coating. (Reprinted with permission from [47].)

the surface mechanical properties that play a role in surface deformation, damage, etc. can be related to compositional variations or differences in processing. As illustrated in Fig. 4.22, two different alkyd resins were probed by AFM indentation measurements at various temperatures (see Sect. 4.4). The surface elastic modulus shows a typical dependence on temperature. In accordance with bulk dynamic mechanical analyses, it is also observed that the two materials differ substantially. These differences are attributed to different chemical composition of the alkyd resin (the so-called oil length, which is defined as 100 times the weight of the oil divided by the weight of the alkyd). In panel (b), the time evolution of the modulus is shown. Such data thus help to establish composition/structure−property relationships and to understand the underlying dynamic processes that occur in coatings.

In addition to indentation curves, the residual imprints after the application of a defined load force can be images using intermittent contact mode AFM. This is shown below for indentation tests performed on PE, in which the size of the imprint was shown to be reduced to the level of individual lamellae (Fig. 4.23).

Hands-on Example 43

Nanoindentation of Homopolymers

Sample Preparation: Microscopy Hot Stage Processing

Commercially available poly(carbonate) (PC, $M_w \approx 40$ kg/mol),) iPP ($M_w \approx 500$ kg/mol) as well as poly(propylenglycole) (PPG) rubbers synthesized according to reference [48, 49] are used. The PC samples are prepared using a microscopy hot stage by pressing a pellet of polymer between a clean glass slide and a Teflon-film protected glass slide at temperatures of 260°C, followed by rapid quenching to room temperature. IPP samples are prepared similarly by melting the sample at 180°C,

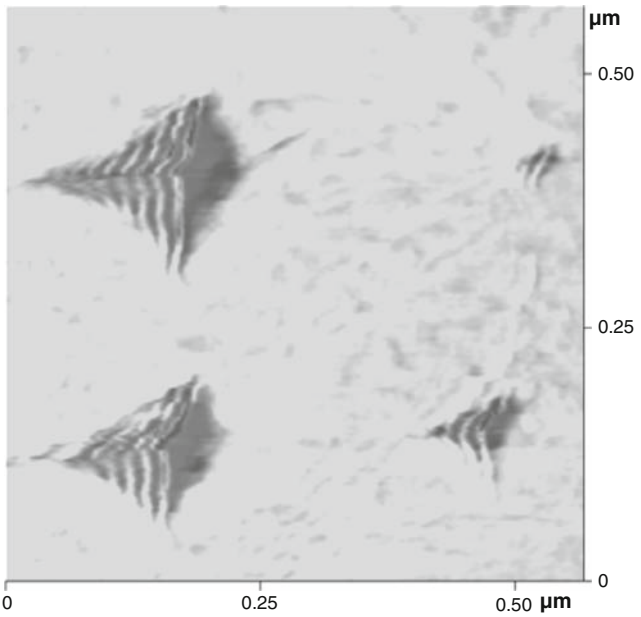

Fig. 4.23 TM-AFM phase image of the residual indentation imprints on a PE sample after four indentations in the applied load range 0.6–4.8 µN. Single lamellae can be tested through indentations performed at tiny loads as well as several lamellae at larger loads. (Reprinted with permission from [73]. Copyright 2006. American Chemical Society)

followed by cooling with a defined cooling rate to room temperature. After cooling the samples, the Teflon film/glass slide is removed and the supporting glass slide is glued with epoxy onto the metallic sample holder disc.

Indentation Measurements

The AFM is set up according to the standard CM-AFM procedure (Sect. 3.2 in Chap. 3). However, in order to be able to probe the moduli of the polymers used, the use of a stiff cantilever is required. Hence, a TM-cantilever (nominal cantilever elastic constant of 30 N/m) is inserted into the cantilever holder. A rough calibration of the photodiode sensitivity can be performed using a separate lever from the same wafer in f-d measurements. To protect the cantilever and the sample from damage, we engage with 0 nm scan size. After successful engagement, force-displacement plots are recorded and the slope of the contact part of the curve is calibrated. After disengaging, the cantilever is exchanged, the laser stage position is adjusted as required, and the tip is engaged on a polymer sample with 0 nm scan size. Again f-d curves are recorded at pre-defined off-set locations using different force trigger values (compare Sect. 4.1.1). It is advisable to re-calibrate the exact photodiode sensitivity after performing the indentation measurements on the polymers, as the cantilevers are not identical and the laser stage may have been moved such that the path of the laser light has been altered.

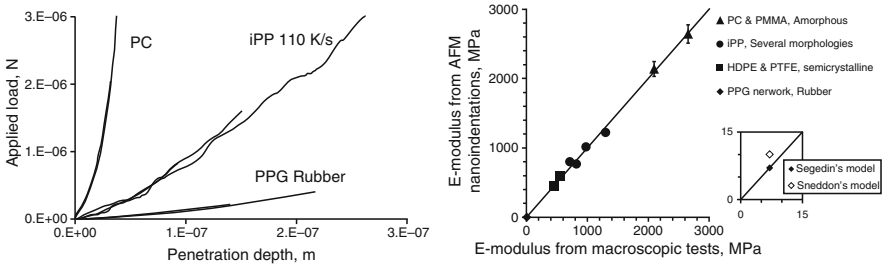

Fig. 4.24 *Left:* AFM force curves at three different maximum loads on three homogeneous polymer samples: PC, iPP, and a PPG rubber. Data from measurements with lower maximum loads are depicted with thicker lines. *Right:* Comparison of the elastic moduli obtained by AFM nanoindentation and application of the Sneddon's elastic contact model [43], with macroscopic moduli obtained from bulk tensile testing. (Reprinted with permission from [43]. Copyright 2006. American Chemical Society)

Typical force – penetration depth curves can be obtained, as shown in Fig. 4.24, together with a comparison of nanoindentation and bulk mechanical tests. Using the approaches as reported by Tranchida et al. a good correspondence between surface and bulk values of the Young's modulus can be achieved.

Hands-on Example 44

Recovery After Nanoindentation of HDPE

Sample Preparation: Microscopy Hot Stage Processing

Research grade HDPE (Mw ≈ 280,000 g/mol) is pressed between a clean glass slide and a Teflon-film protected glass slide at temperatures at 170°C in a nitrogen-flushed microscopy hot stage. The film is slowly cooled to 100°C and kept at that temperature under nitrogen flow for 3 h. After cooling the samples to room temperature, the top slide and the Teflon film are removed and the sample supported on the glass slide is glued with epoxy onto the metallic sample holder disc.

Indentation Measurements and Imaging of Indents

Before indenting the sample, the AFM is set up for standard TM-operation, as described in Sect. 3.2 in Chap. 3. The operation frequency and amplitude are adjusted to ν at 0.85 A_o and 150 nm, respectively. This amplitude is sufficient to avoid permanent tip-sample contact/adherence during the scans. It is advisable to note the rms amplitude (see below).

Then the AFM is switched to CM-operation, which may require a slight adjustment of the photodiode position. The indentation measurements are carried out at specified location (using the offset function of the scan menu) as detailed in hands-on example 43.

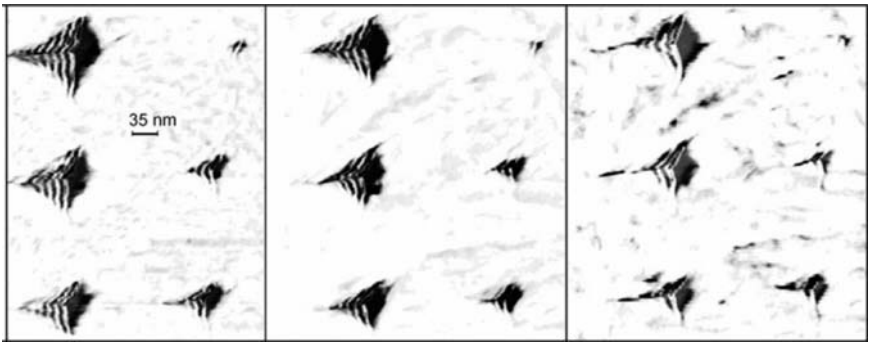

Fig. 4.25 AFM phase images of the residual imprints in HDPE unveil the complex morphology evolution for nanoindentations performed at 0.7, 1.4, 2.1, 2.8, 3.5, 4.1 μN from top right clockwise respectively after 6 (**a**), 400 (**b**), and 1,400 (**c**) min. (Reprinted with permission from [74]. Copyright 2006. American Chemical Society)

Immediately after indenting the sample at various locations with preset loads, the AFM is withdrawn and switched to TM-operation. The differential deflection signal is zeroed by readjusting the photodiode and the rms amplitude is compared to the value obtained before engaging in CM. If the amplitude is too low, the tip may have been damaged or contaminated. In this case, it is a good idea to further withdraw the tip from the sample and re-tune the cantilever. When the appropriate rms amplitude is obtained, the tip is engaged and height images are captured with relatively high scan rates (∼5 Hz) to unveil the short-term recovery behavior. At later stages the scan rate may be reduced to 2 Hz (Fig. 4.25).

Images like these reveal that the recovery after 24 h for HDPE is substantial; however, complete recovery is not observed [74]. Interestingly, the dynamics of the recovery depends on the indentation rate, but not the magnitude of the applied load, which points at viscoelastic processes that play an important role in particular low loading rates (Fig. 4.26).

4.4 Thermal Properties and Thermal Transitions

The thermal properties of polymers are important for many applications. Therefore, direct probing of polymers on the micro- and nanoscale may provide important insight for the practitioner. One can differentiate several thermal options for AFM: visualization of dynamic processes and quantification of thermal properties and transitions. While heatable probes that offer nanoscale resolution have only recently become available,[2] *temperature control stages are available in many commercial devices. However, simple devices can also be built according to the requirements. In the most common set-ups, the sample is heated from below by some heating device.*

[2]Anasys Instruments Inc.

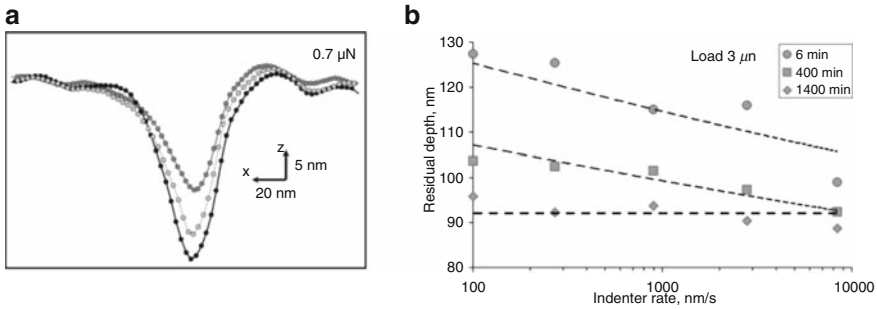

Fig. 4.26 (**a**) Evolution of the indent profile in HDPE, few minutes after the indentation with an applied load of 0.7 μN (*black*), 400 min (*light gray*), and 24 h (*dark gray*); (**b**) Recovery dynamics of imprints obtained from nanoindentations performed with a load of 3 μN and different loading rates. Fast indentations result in low residual depth and low recovery, while slow nanoindentations result in larger indentation depths that recover more rapidly, thereby implying that viscoelastic effects are important during both the nanoindentation and the recovery processes. (Reprinted with permission from [74]. Copyright 2006. American Chemical Society)

For stand alone-type AFMs any hot stage may be used, while for tube scanner design, miniature hot stages can be built.

When operating an AFM with heater accessory, care must be taken in any configuration to shield the heat-sensitive piezoelectric scanners from the heat generated by the hot stage [50]. Here, we show a schematic of a hot stage similar to the one used by the Schwarz group [51], which is based on a Peltier element (Fig. 4.27, *left*). The spacer is inserted to thermally isolate the scanner. The small Peltier element is powered by a conventional DC power supply; grounding of the sample puck may be necessary. Other approaches utilize miniature resistive heating elements [51–57].

Miniaturized coolers can be obtained also by using the Peltier element in reverse polarity as thermal device; however, in this case, the excess heat at the bottom side must be dissipated. Debowski and Vancso reported on a simple water-cooled device that allows one to operate the AFM at temperatures of $\leq 15°C$ [53].

A temperature calibration can be carried out by measuring melting points of substances with known melting points or by analyzing amplitude, resonance frequency–temperature curves in TM AFM. In the absence of an active or passive tip temperature control, it is important to carry out this calibration with the AFM tip being almost in contact with the sample surface to take heat transfer to the holder etc. into account. Additional monitoring of the surface temperature by a small thermocouple is strongly recommended for all experiments. For thicker films, the radiative heat transfer from sample to tip may cause a significant temperature depression in the area imaged and must be taken into account for quantitative work. This effect is exemplified in Fig. 4.27 (*right*). Depending on the materials' thermal conductivities and the temperature difference between surface and cantilever/tip, this temperature depression may be significant, i.e., $>2°C$, for films thicker than a few micrometers.

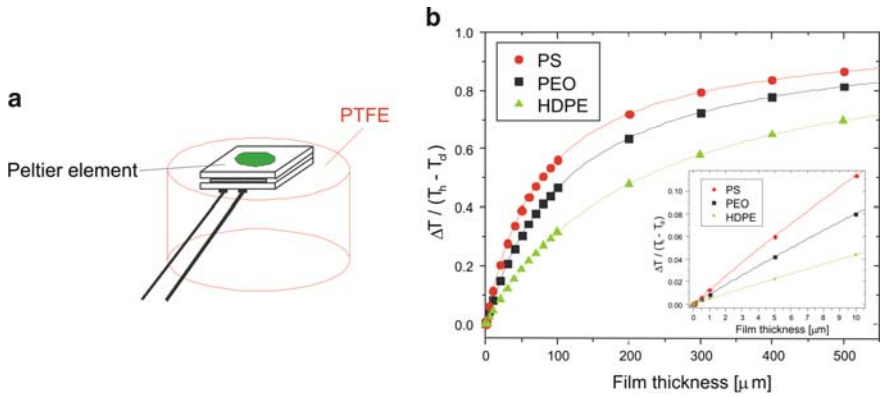

Fig. 4.27 Typical design for AFM hotstage (*left*), and effect of tip/cantilever on true sample surface temperature in air (*right*). Here the differential of sample surface temperature (i.e., temperature overestimate) normalized to the temperature differential between cantilever and true surface temperature is plotted as function of film thickness for typical polymers according to the experimental data and heat transfer modeling described in [52] (*right*). The thermal conductivities of PS, PEO, and HDPE are 0.14 W/(K m), 0.205 W/(K m), and 0.39 W/(K m), respectively. Reproduced with permission from [52]. Copyright 2002. American Chemical Society

Real-time studies of polymer melting and crystallization with nanometer resolution have become possible using suitable hot stages and intermittent contact AFM modes [54–57].While there are numerous approaches to build simple, yet effective heating devices (see above), more recently various sophisticated commercial hot stages have become available. These allow one, if the cantilever is being heated, to interrogate thermal transitions also at temperatures much higher than 100°C [58]. Very recent reports include the study of the crystallization and melting of poly(trimethylene terephthalate) at temperatures above 200°C [59]. In the examples discussed in the hands-on section, we limited ourselves to examples for which the temperatures are low enough to avoid possible damage to the piezo scanner.

The lateral forces associated with CM-AFM make this mode less interesting for *in situ* hot stage work. If a polymer melt is scanned in TM-AFM, the free amplitude of the resonating lever must be higher (sometime three to four times higher) than for conventional experiments in air in order to overcome the adhesive interactions. In addition, intermediate tapping conditions provide stable imaging conditions. It is necessary to retune the cantilever periodically as the resonance frequency may shift as the cantilever heats up. Temperatures higher than ca. 90°C require the use of a glovebox and dry/inert atmosphere to prevent condensation of moisture or low molar mass species from the polymer (additives, degradation products etc.) on the tip and cantilever. In some cases, heatable cantilevers or the use of a pre-heated inert gas stream directed at the cantilever must be used to circumvent these problems.

Using *in situ* hot stage AFM, the melting and crystallization of thin polymer films can be followed in real-time. Thus, melting temperatures, crystallization kinetics, and as mentioned before lamellar thicknesses can be directly measured. Unique for this approach is the high lateral resolution (in the nanometer range) which allows one to address issues of nucleation, as well as early stages of polymer crystallization, lamellar branching, etc. To illustrate the use of hot stage AFM, a series of AFM micrographs obtained *in situ* on a 128 nm thick film of PEO on oxidized silicon at various temperatures are depicted in Fig. 4.28. The series shows the development of lamellar crystals and the action of screw dislocations. These images are frames 1, 5, and 9 of a continuous real-time movie of 33 images. From a series of real-time captured images like these, the linear growth rates can be easily calculated by plotting the dimensions of the lamellae against elapsed time. For the specific case of thin films of PEO, the AFM data acquisition is limited to lamellar growth rates of ca. 0.5–1.0 μm/s.[3] The corresponding (linear) growth rate data, as well as the lamellar thicknesses determined from cross-sectional plots, can further be compared to crystallization theories (Fig. 4.29). In the particular case of PEO, the crystallization kinetics was fitted with the Gibbs-Thomson equation, the Hoffman-Lauritzen theory, and the Hoffman-Weeks treatment in order to extract the equilibrium melting points and surface free energies of the fold surfaces. A quantitative agreement with POM studies on bulk PEO was found [52, 60].

In the f-d/indentation measurements discussed in the previous sections, one can also analyze the part of the curves corresponding to tip–sample contact as a function of sample temperature and loading rate (∼frequency). At the glass transition temperature, the modulus will change by several orders of magnitude. Hence, the T_g in

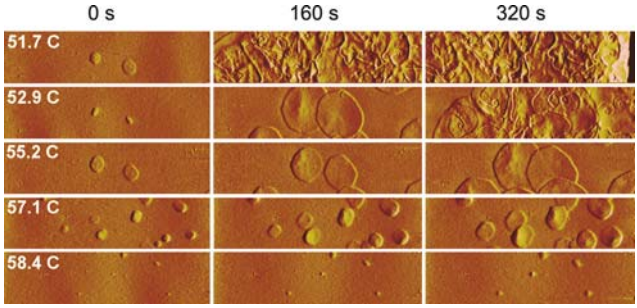

Fig. 4.28 Snap shots of the crystallization of PEO in a 128 nm thick film at different crystallization temperatures and times as unveiled by *in situ* hot stage AFM. The temperatures were (from top to bottom) 51.7, 52.9, 55.2, 57.1, and 58.4°C. The image width is 30 μm. Reproduced with permission from [52]. Copyright 2002. American Chemical Society

[3]This estimate is based on the growth of a lamellar crystal over the distance of a typical scan size of 20 μm within the time elapsed to capture six subsequent images using the following parameters: resolution = 128 pixels/line, 16 lines scanned, scan rate = 2.5–5.0 Hz.

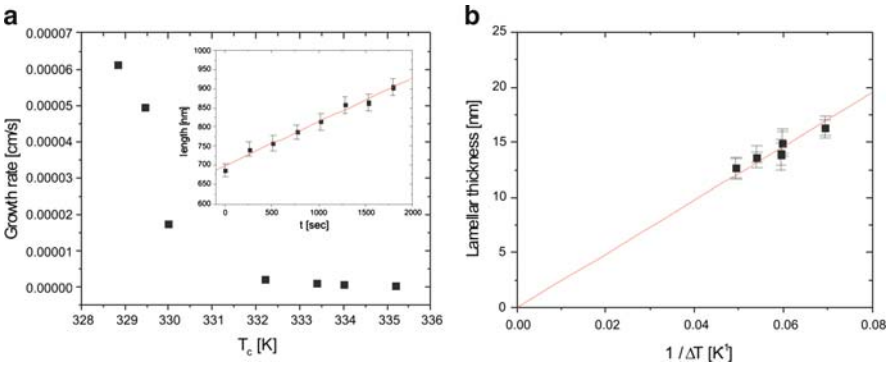

Fig. 4.29 (**a**) Lamellar growth rates for PEO as function of crystallization temperature T_c (inset: lamellar dimensions vs. crystallization time) and (**b**) lamellar thickness plotted against inverse undercooling. The linear fit of the lamellar thickness vs. inverse undercooling plot with the boundary condition (0,0) yields a satisfactory result. Adapted with permission from [52]. Copyright 2002. American Chemical Society

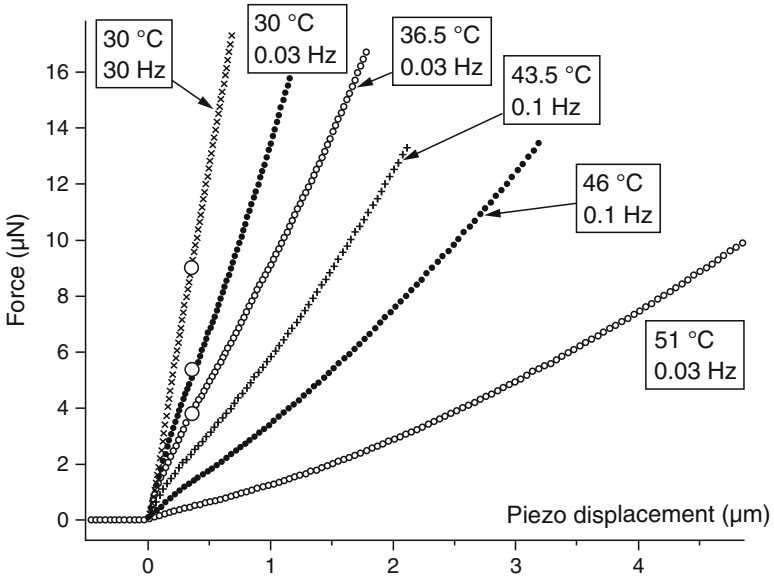

Fig. 4.30 Approach parts of the f-d curves recorded on poly(n-butyl methacrylate) samples at various rates and temperatures. The different slopes of the indentation curves represent different moduli of the polymer (T_g = 22°C) (reproduced with permission from [61]. Copyright 2005 American Chemical Society)

polymer films and its possible dependence on various factors, including film thickness, relative humidity (with water as a plasticizer), etc. can be quantitatively captured, as shown in the example below (Fig. 4.30).

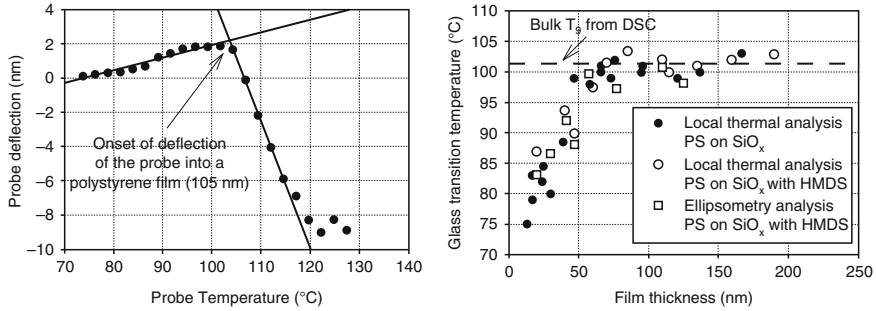

Fig. 4.31 Left: Plot of the thermal probe deflection vs. temperature measured on a 105 nm thick film of PS on a hydrophobized substrate; right: Values of T_g determined for PS ultrathin films on various substrates (reproduced with permission from [62]). Copyright 2000. American Chemical Society

The progressively decreasing slopes of the f-d curves captured on poly(n-butyl methacrylate) samples with decreasing rates and increasing temperatures are a measure for the modulus as a function of rate and temperature. As T_g is crossed, the modulus decreases significantly, which was assessed in this example at the free surface of a polymer sample.

The effect of film thickness on T_g can also be determined by measuring the surface softening temperature of corresponding polymer films using a heated AFM-like tip in scanning thermal probe microscopy. Scanning thermal probe microscopy probes the change in film modulus via the cantilever deflection induced by the thermal probe. As shown in Fig. 4.31, the cantilever deflects markedly when the PS film softens and hence, the onset of the T_g can be assessed. Systematic studies showed that PS on SiO_2 exhibits an altered T_g for film thicknesses below ~50 nm.

Hands-on Example 45

Crystallization and Melting of PEO by Hotstage Contact Mode AFM

Sample Preparation: Solution Casting

We follow examples published by Pearce and Vancso [63] and Beekmans, van der Meer, and Vancso [64]. High molar mass poly(ethylene oxide) (PEO) (Mw = 2,000,000 g/mol), e.g., from Aldrich, is purified by dissolving in chloroform followed by precipitation into hexanes. Samples can be prepared by casting films from (2%) chloroform solutions directly onto a thin Cu foil that is mounted on the heater surface using a minute amount of pressure-sensitive adhesive.

Contact Mode AFM Visualization of the Morphology at Different Temperatures

Owing to the high molar mass of the PEO utilized, contact mode imaging is feasible. Applying the AFM imaging procedure summarized in hands-on example 46, TM-AFM can also be employed. For CM-AFM, a moderately stiff Si_3N_4 cantilever – tip assembly (k = 0.3–0.4 N/m) is chosen in order to find a good compromise between probe torsional stiffness (lateral forces) and vertical deflection at different temperatures due to the bimetal effect (the gold coating and the underlying nitride possess different thermal expansion coefficients). Thermal expansion of the polymer film mandates the use of a scanner that possesses sufficient z-travel (5 μm or more). If a commercial AFM hot stage is used, please refer to the particular settings and instructions of the supplier. Below we sketch how to construct a simple home-based heating element.

A home-built hotstage can be based on a Peltier element (e.g., MELCOR HOT2.0–18-F2A, Melcor, Trenton, NJ) connected to a suitable dc power supply. The heating device is attached to a Teflon spacer, which is glued with to an AFM sample disk. Since the sample possesses increased specimen height, the lateral calibration of the scanner must be adjusted by performing a calibration using a standard with the same height. This can be easily realized by gluing several metallic sample pucks together. The surface temperature of the Peltier element is monitored by a small thermocouple (e.g., IRCO-001 thermocouple J-type, diameter 0.001 in., Omega, Stamford, CT, connected, e.g., to a Fluke 51 K/J thermometer, John Fluke Inc., Everett, WA).

As mentioned before, the piezo scanner must be kept at low temperatures to avoid damage; hence, the Teflon spacer must be thick enough. The calibration of the device, using materials with known melting points (long chain fatty acids) and also the thermocouple should be complemented by measurements of the sample puck temperature. As PEG melts in the range of 60−70°C, a typical device, as sketched in Fig. 4.27, is used that does not damage the piezos if operated appropriately.

The PEO film is heated first to a temperature at which melting can be observed in an optical microscope (with crossed polarizers) or using a CCD camera supplied in AFMs with top-view optics. Then the temperature is lowered to 45°C and the film is allowed to crystallize.

For subsequent CM-AFM imaging, the standard CM-AFM procedure (Sect. 3.2 in Chap. 3) is applied. After successful engagement, the operation point is adjusted to minimum imaging forces with the help of force−distance plots. Next, the scan size is stepwise increased while the gains are optimized accordingly. Scan rates of one to several Hz can be utilized. Because of slight variations in temperature that may lead to cantilever bending (bimetal effect) or thermal drift, the setpoint should be periodically adjusted. If the tip does no longer follow the surface appropriately (after the setpoint value has been decreased), the value must be slightly increased. In addition, the thermal drift and expansion of the film mandate that the z-center position is closely monitored; before the piezos reach their maximum extension/retraction, the stepper motor should be used to correct for the expansion.

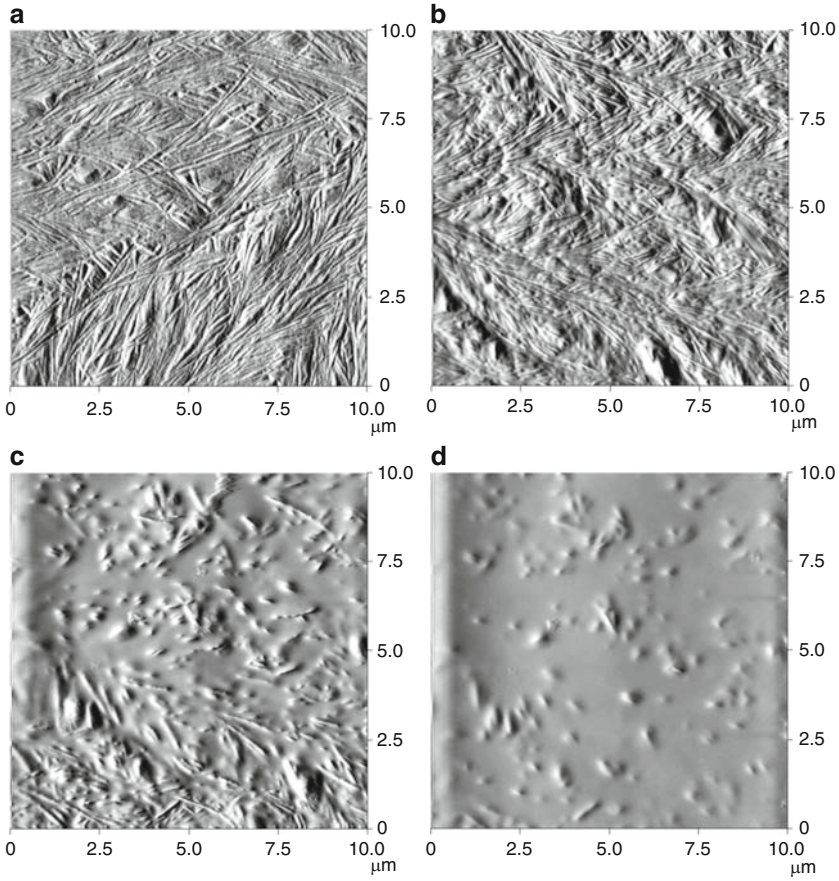

Fig. 4.32 (**a**–**d**) CM-AFM deflection images captured during the melting process of PEO. Image (A) was captured at room temperature, while (**b**–**d**) were captured at 67°C (after 32 min) and time intervals of 8 and 11 min at 70°C. Reproduced with permission from [64]. Copyright 2002 Elsevier

Next the temperature is raised slowly while images are continuously captured. The melting process can be monitored in situ, as shown in the deflection images in Fig. 4.32.

The melting can be followed at the level of individual lamellae, but it should be taken into account that the AFM scanning is relatively slow compared to the processes, depending on the temperature. In general, it is observed that different areas possess different melting points and/or kinetics.

Upon lowering the temperature of the hot stage, crystallization may set in as shown in Fig. 4.33. Again, lamellae are observed in edge-on orientation in the area where two spherulites impinge. In such crystallization experiments, it has been revealed that the growth of lamellae does not proceed homogenously.

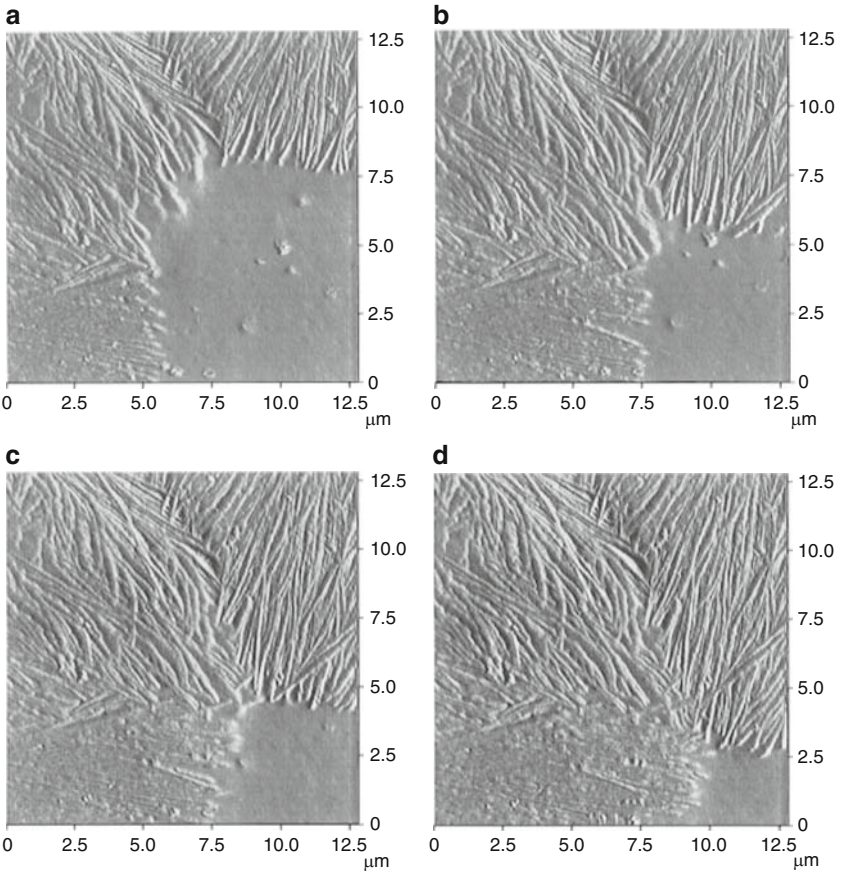

Fig. 4.33 CM-AFM deflection images of lamellae at the edge of PEO spherulites growing at 57°C. The elapsed time between successive images is 3 min. Reproduced with permission from [54]. Copyright 1997. American Chemical Society

Hands-on Example 46

Crystallization of PCL by Hotstage TM-AFM

Sample Preparation: Solution Casting

We follow an example published by Beekmans and Vancso [65]. PCL with a molar mass of 55,000 g/mol (e.g., Aldrich) is purified by precipitation from chloroform solution into methanol. Films are cast from 3% solutions in chloroform on cleaned glass slides at 50°C followed by drying in air at the same temperature, and in vacuum at room temperature for 1 day. The sample is mounted to the AFM hot

stage as described above; as glass is being used as the substrate material, the calibration of the hot stage is altered.

Tapping Mode AFM Visualization of the Melting Behavior

Isothermal crystallization experiments are performed by melting the PCL in the AFM apparatus at 100°C for 10 min, followed by quenching to the desired crystallization temperature. Care must be taken that the AFM tip is not accidentally in contact with the polymer film and is engaged only after reaching the desired temperature.

We use a standard tapping/intermittent contact mode set-up, which is started as described in Sect. 3.2 in Chap. 3. The operation frequency and amplitude are adjusted *to* ν at 0.85 A_o and 200 nm, respectively. Because of the stickiness of the polymer melt, this high amplitude is advisable to avoid permanent tip–sample contact/adherence during the scans. Immediately prior to engaging, the phase signal is zeroed. The crude and fine engagement procedures are carried out as described in Chap. 2. After the successful engagement, the operation point must be carefully adjusted.

The sequence of AFM tapping mode phase images shows an edge-on view near the center of a growing hedrite. Somewhat different lamellar projections (closer to flat-on) are observed, e.g., in Fig. 4.34 C and D, which indicate a tilt of the crystal with respect to the surface. Images captured in time-laps series can provide unique

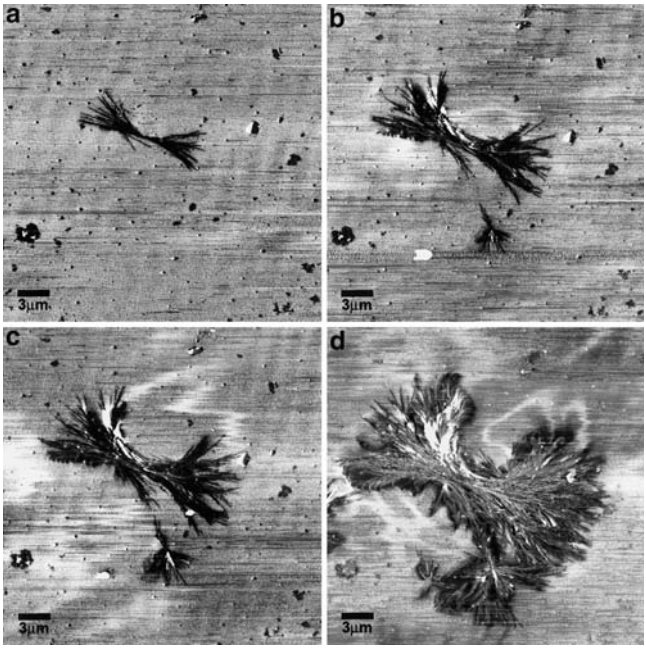

Fig. 4.34 (**a**–**d**) AFM phase images of a PCL hedrite growing at 56°C; the images in (**b**), (**c**), and (**d**) correspond to elapsed times of 244, 290, and 551 min, respectively, with respect to the image in (**a**). Reproduced with permission from [65]. Copyright 2000 Elsevier

insight into the dynamics of the processes that had previously been inferred from quenched samples.

4.5 Swelling and Solvent Effects

Polymer surfaces that are subjected to different environmental conditions are frequently met by the practitioner. The understanding of swelling and solvent effects is key to the selection of materials in many applications, where polymers are used in contact with liquid media. Using AFM liquid cells, the underlying effects can be directly investigated.

An illustrative example for solvent polymer interactions is the solvent induced crystallization of polycarbonate. Amorphous PC was reported to crystallize when in contact with butyl acetate vapor. Figure 4.35 shows a 2D spherulite grown almost to a fully round envelope. These spherulites resemble spherulites grown from the melt. With an AFM, the growth can be in principle followed in real time down to the nanometer level.

More advanced high performance materials, such as tailored stimulus responsive polymeric materials, can also be investigated in great detail using AFM approaches. The well-known responsive poly(*N*-isopropyl acrylamide) (PNIPAM)-based polymers and gels show a reversible coil to globule transition at the so-called lower critical solution temperature (LCST). The transition is also observed for end-grafted

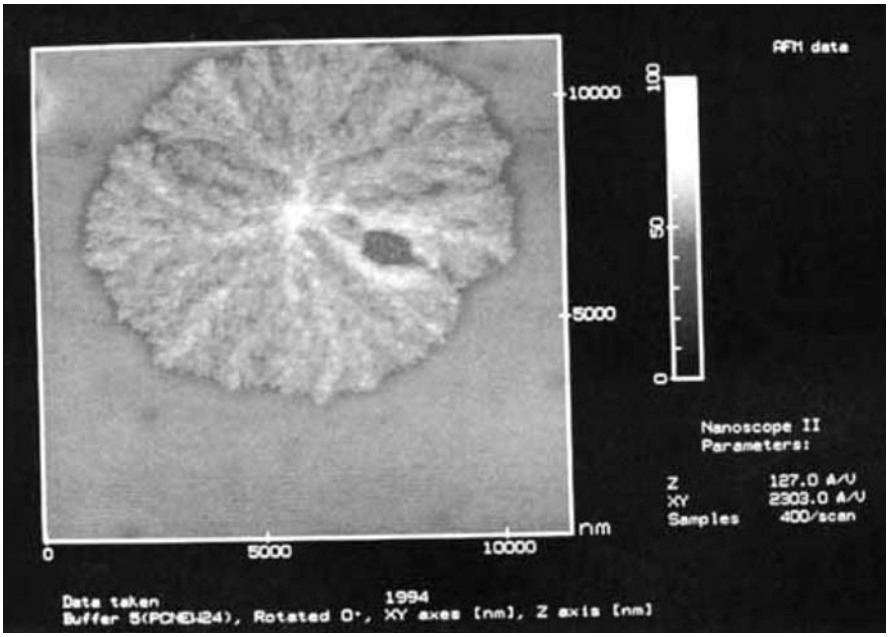

Fig. 4.35 Contact mode AFM image of semicrystalline PC surrounded by an amorphous film. The solvent-induced crystallization process results in spherulitic growth. Reprinted with permission of John Wiley & Sons, Inc. [66]. Copyright 1996. John Wiley & Sons, Inc.

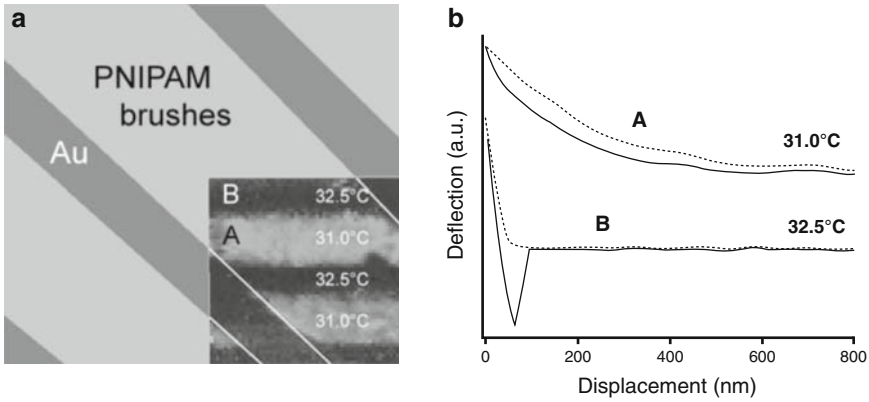

Fig. 4.36 (**a**) The area captured shows a 40 μm × 40 μm section exhibiting a schematic of the structure of the surface-grafted polymer platform. The bottom right is an experimental AFM force–volume image (20 × 20 μm) of the grafted PNIPAM chains in water. The grayscale in the AFM image corresponds to areas of high (*dark*) and low (*bright*) adherence. The temperature was cycled between 31.0 and 32.5°C. (**b**) Force–displacement curves for the two regimes, captured on the polymeric features, reveal the hydrogel-like repulsive interactions and the pronounced adhesion experienced by the tip at temperature below and above the LCST, respectively. Reproduced with permission from [67]. Copyright 2007. Wiley-VCH

polymer chains that have been grown from surface-immobilized monomers. The example shown below comprises a micro-patterned polymer brush surface on which PNIPAM areas are exposed that, upon increasing the temperature, show collapse of the polymer chains. The AFM data were acquired in situ in FV mode under modulated temperature. The power of local proximity probe techniques is evident from the detailed information on the local layer collapse, as seen in panel (a) of Fig. 4.36 as well as the f-d data shown in panel (b), which capture the interactions between tip and polymer layer.

Hands-on Example 47

Swelling of Polymer Films Ex Situ

Sample Preparation: Spin-coating

Polymer films, e.g., poly(*N*-hydroxysuccinimidyl methacrylate) (PNHSMA) [68], are prepared by spin-coating polymer solutions in a suitable solvent (here DMSO with a typical concentration between 10 and 20 mg/ml) onto clean silicon wafers. To remove traces of the solvent, the films are dried in vacuum for several days. Some of the sample is immersed in PBS buffer for swelling time of 100 min, followed by rapid drying of the surface in a gentle stream of nitrogen. For the determination of

the film thicknesses by profilometry, the film is removed by scratching the samples using sharp tweezers (width of scratch between 15 and 30 μm). Films that were in contact with buffer must be analyzed with minimal delay.

Intermittent Contact Mode AFM

We use a standard tapping/intermittent contact mode set-up, which is set up as described in Sect. 3.2 in Chap. 3. The operation frequency and amplitude are adjusted to ν at 0.85 A_o and 150 nm, respectively. Because of the softness and stickiness of the swollen polymer film, this high amplitude is advisable to avoid permanent tip–sample contact/adherence during the scans. Immediately prior to engaging, the phase signal is zeroed. The crude and fine engagement procedures are carried out as described in Chap. 2. After the successful engagement, the operation point must be carefully adjusted.

The captured AFM height images are subjected to a first-order plane fit (that takes only the film plane into account) followed by a cross-section analysis. As shown in the cross-sectional plots in Fig. 4.37, the polymer film remains homogeneous also after swelling in aqueous buffer (pH = 7.4, ionic strength = 0.15 M).

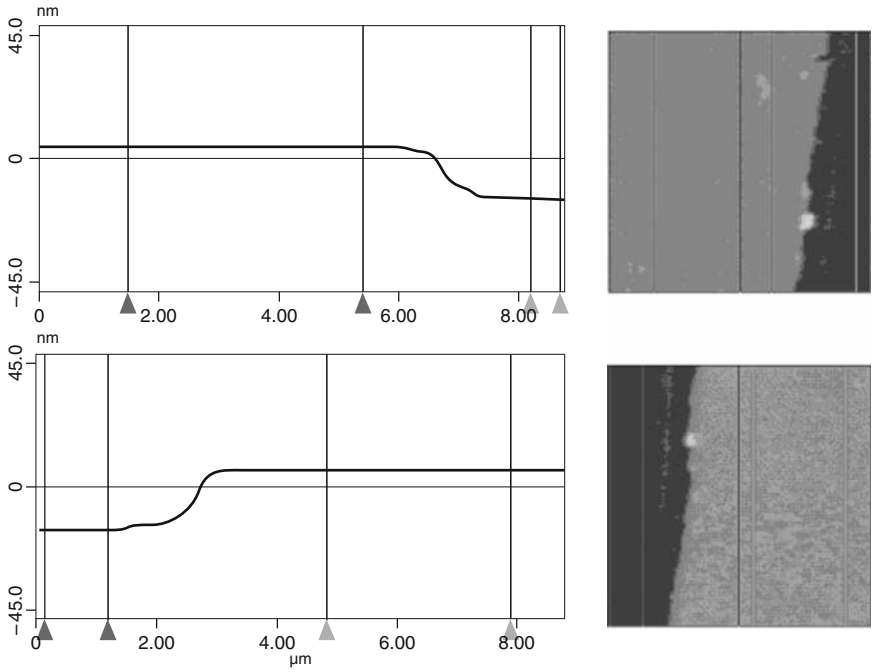

Fig. 4.37 (**a**) AFM height image of PNHSMA film and corresponding step height analysis before treatment in buffer (the step height indicated by the markers is 19.0 nm); (**b**) AFM height image of PNHSMA film after swelling in buffer solution for 100 min and corresponding step height analysis (the step height indicated by the markers is 21.3 nm). All AFM data were acquired in air. Reproduced with permission from [68]. Copyright 2005. American Chemical Society

The analysis of the data shown indicates that the film thickness increases by 2.3 nm, when the film was in contact with buffer over a period of 100 min. The mean increase in film thickness due to swelling of 2.1 ± 0.1 nm for films with dry thicknesses between 12 nm and 40 nm indicates solvent penetration only in the topmost region of the films and hence the water uptake.

For films that strongly interact with the underlying substrate, one can observe the swelling in situ also using a liquid cell and following the guidelines of Sect. 3.3 in Chap. 3.

4.6 Chemical Reactions, Degradation, and Erosion

Surface or bulk chemical reactions, including erosion and degradation are important aspects of polymeric systems. These processes can be desired, as is the case for surface modification reactions to increase, e.g., biocompatibility or drug delivery applications, while other processes are unwanted, such as ageing, degradation in harsh environments, or erosion. AFM approaches offer a unique possibility to study these processes in many cases under realistic conditions and thereby help identify the underlying mechanisms.

Local reactions take place, for instance, in unconventional lithography approaches. Here, the surface of a polystyrene-*block*-poly(*tert*-butyl acrylate) (PS_{690}-*b*-$PtBA_{1210}$) block copolymer film comprising reactive *tert*-butyl ester moieties at the film surface (skin layer of ∼8 nm thickness) is locally hydrolyzed by a reactant (trifluoro acetic acid) that is delivered by a soft elastomeric stamp, as shown in Fig. 4.38. Thus, the surface is locally modified to yield poly(acrylic acid), which possess higher friction forces than the unreacted *tert*-butylester region.

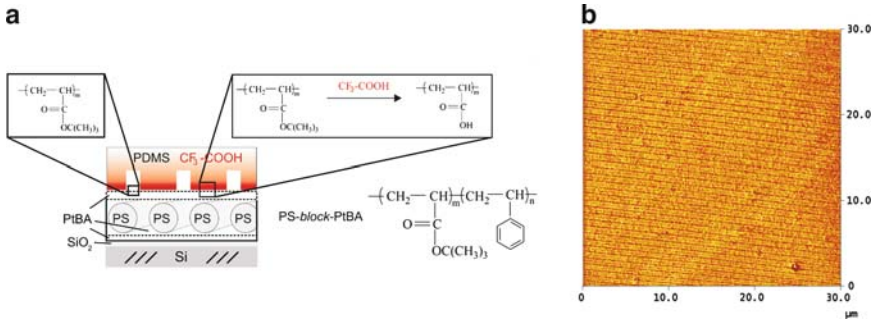

Fig. 4.38 (**a**) Schematic of the patterning via soft lithography on a block copolymer film. (**b**) AFM friction image acquired on a PS_{690}-b-$PtBA_{1210}$ film after local hydrolysis by reactive μCP. Reproduced with permission from [69]. Copyright 2007. Wiley-VCH

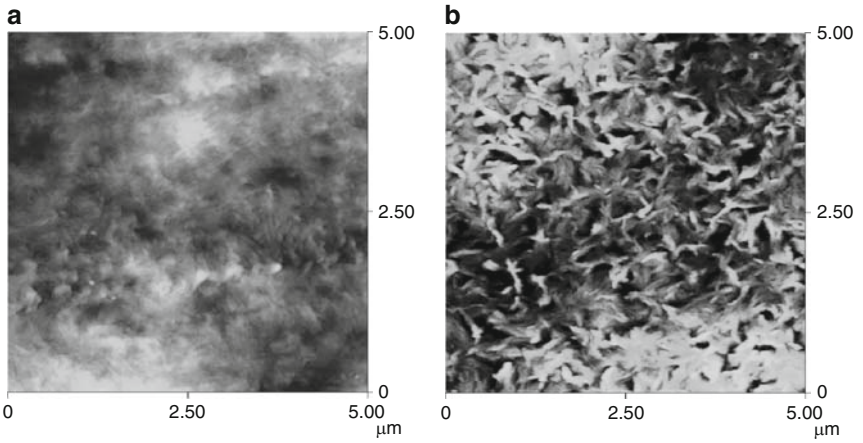

Fig. 4.39 Tapping mode SFM height images (z-scale dark to bright 300 nm) of (**a**) untreated and (**b**) chromic acid treated LDPE sample. Reprinted with permission of John Wiley & Sons, Inc. [75]. Copyright 1998. John Wiley & Sons, Inc.

A second illustrative example is the oxidation and surface erosion of LDPE in chromic acid. This wet chemical treatment introduces different functional groups at the surface (>50% carboxylic acid groups) and produces a very dynamic surface. For example, upon heating in air or argon, the carboxylic acid groups are shown to become buried in regions of the interface which cannot be probed by contact angle measurements. Subsequently, the acid groups can be recovered by heating the LDPE samples in boiling water. In contrast to the oxyfluorination (Sect. 3.5 in Chap. 3), the chromic acid oxidation is concomitant with pronounced etching of sample surface. This can be imaged by TM-AFM (Fig. 4.39).

Hands-on Example 48

Degradation and Erosion of Biodegradable Polymers [70]

Sample Preparation: Spin-coating

Thin films of a blend of poly(sebaic acid) and PLA (Polysciences) on glass are prepared by spin-coating from 1 w/v % solutions in chloroform onto cleaned glass slides. The glass slides are glued with epoxy to the metallic sample holder disc.

Contact Mode AFM Visualization of the Morphology

The initial measurement is performed in Milli-Q water using a liquid cell with O-ring (see Sect. 3.3 in Chap. 3). The use of very soft cantilevers with a nominal

spring constant of ~0.06 N/m is advisable. It is important to remember to lower the optical head vertically into its rest position without shearing the rubber ring too much. After the optical head has been carefully secured, the set-up is equilibrated for 1 h before filling the liquid cell with Milli-Q water. Only after images of the intact film have been acquired, the water is exchanged by aqueous NaOH solution of pH 12.4. *Careful: do not spill NaOH solution onto the housing of the AFM as this surface may corrode*.

Once the photodiode differential signal shows a constant value, the engagement procedure as described in Sect. 3.2 in Chap. 3 is carried out. After engaging on the surface, f-d curves are acquired in the force spectroscopy mode of the AFM and minimum imaging forces are selected. The in situ images in Fig. 4.40 show the degradation of a 50–50% blend of PSA and PLA.

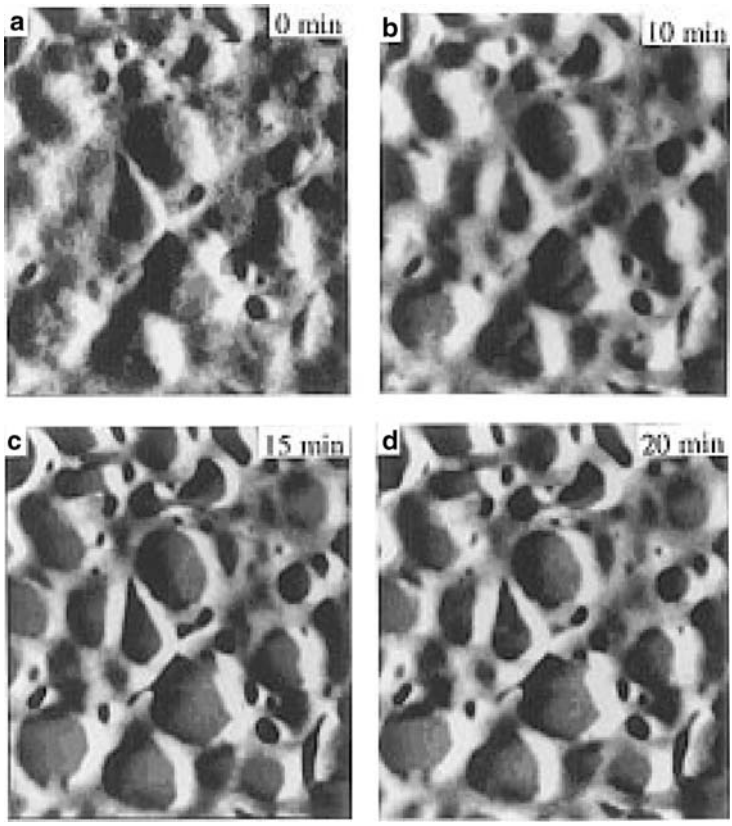

Fig. 4.40 CM-AFM images of degradation of a 50–50% blend of PSA and PLA (scan size 10 × 10 μm). Reproduced with permission from [70]. Copyright 1996. American Chemical Society

Hands-on Example 49

Enzymatic Degradation of Polymers [71]

Sample Preparation: Spin-coating

High molecular weight poly(trimethylene carbonate) PTMC ($Mn \sim 300$ k g/mol, $Mw/Mn \sim 1.46$), synthesized, purified, and characterized as described in reference [72] is dissolved in chloroform (3 mg/mL). Thin films are prepared by spin-coating these solutions on cleaned Si wafers at 3,000 rpm (film thickness obtained 25−50 nm). Film thicknesses can be determined by AFM imaging using the scratch method described in Chap. 2 (see also above, hands-on example 47). The enzymatic reaction takes place in situ in the liquid cells filled with lipase solutions (lipase from *Thermomyces lanuginosus* (EC3.1.1.3, minimum 50,000 units/g purchased from Sigma, U.S.A.) at 37°C for 30 s, 1 min, and 2 min, respectively.

Contact Mode AFM Visualization of the Morphology

Contact mode AFM is performed with soft contact mode levers (spring constant of ca. 0.1 N/m) in situ in lipase solution in the open cell configuration (no O-ring); compare Sect. 3.3 in Chap. 3. The tip is first brought very close to the surface of the film, as can be judged by optical inspection using a top-view CCD camera. To ensure optimum imaging conditions, the surface can be scanned in water. For this purpose the optical head is taken off the AFM, two drops of pure Milli-Q water are added, and the optical head is placed on the scanner. Subsequently, the photodiode position is adjusted and after a stable differential signal is obtained, the tip is engaged on the surface. Then the tip is withdrawn twice. After demounting the optical head, the water is carefully sucked up by using paper tissue and two drops of

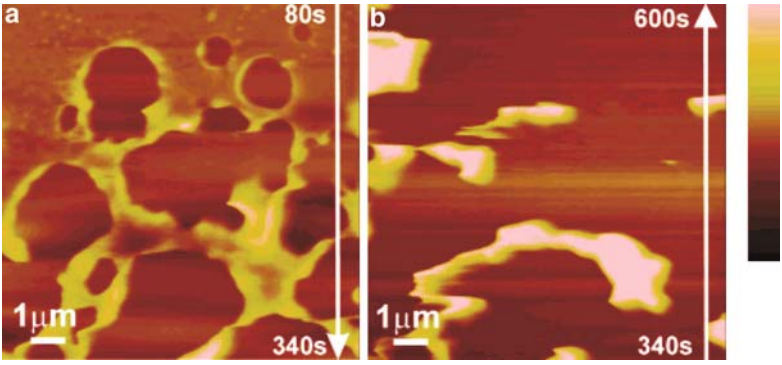

Fig. 4.41 Contact mode AFM height images (the z-scale covers 200 nm) of PTMC film during enzymatic erosion. The images were captured between 80 and 340s and 340 and 600s after start of the hydrolysis, respectively. The arrows indicate the scan direction. Reproduced with permission from [71]. Copyright 2005. American Chemical Society

lipase solution are placed on the polymer film. The head is mounted immediately and within 1 min the photodiode position is corrected such that the tip can be engaged. It is necessary to carry out the experiments rapidly, because the surface erosion process in the lipase solution is a fast process. Thus, images with a scan size of 10 μm are captured immediately; if necessary, the forces are adjusted to the minimum stable force setting.

Figure 4.41 shows two images captured 80 and 600 s after adding the lipase solution. The initially homogeneous, nearly defect-free film shows round depressions, which widen during the first scan shown. After 600 s the film has been in parts eroded and remaining parts of the film can be distinguished.

References

1. Duvigneau J, Schönherr H, Vancso GJ unpublished data
2. Schönherr H, Waymouth RM, Frank CW (2003) Macromolecules 36:2412–2418
3. Cappella B, Dietler G (1999) Surf Sci Rep 34:1–104
4. Butt HJ, Cappella B, Kappl M (2005) Surf Sci Rep 59:1–152
5. Johnson KL, Kendall K, Roberts AD (1971) Proc R Soc Lond A 324:301
6. Derjaguin BV, Muller VK, Toporov YP (1975) J Coll Interface Sci 53:314
7. Frisbie CD, Rozsnyai LF, Noy A, Wrighton MS, Lieber CM (1994) Science 265:2071
8. Alley RL, Komvopoulos K, Howe RT (1994) J Appl Phys 76:5731
9. Howald L, Lüthi R, Meyer E, Güthner P Güntherodt HJ Z Phys B (1994) 93:267
10. Noy A, Vezenov DV, Lieber CM (1997) Annu Rev Mater Sci 27:381
11. Schönherr H (1999) Ph.D. thesis. University of Twente, The Netherlands
12. Laibinis PE, Whitesides GM (1992) J Am Chem Soc 114:1990
13. Dubois LH, Nuzzo RG (1992) Ann Rev Phys Chem 43:437
14. Ulman A (1991) An introduction to ultrathin organic films: from Langmuir-Blodgett to self-assembly. Academic, New York
15. Ulman A (1996) Chem Rev 96:1533.
16. Schreiber F (2000) Prog Surf Sci 65:151
17. Sagiv J (1980) J Am Chem Soc 102:92
18. Maoz R, Sagiv J (1984) J Coll Interface Sci 100:465
19. Ito T, Namba M, Buhlmann P, Umezawa Y (1997) Langmuir 13:4323
20. Headrick JE, Berrie CL (2004) Langmuir 20:4124
21. Schönherr H, Feng CL, Tomczak N, Vancso GJ (2005) Macromol Symp 230:149–157
22. Tomczak N, Schönherr H, Vancso GJ unpublished data.
23. Kumar A, Biebuyck HA, Whitesides GM (1994) Langmuir 10:1498
24. Vancso GJ, Schönherr H (1999) In: Tsukruk VV, Wahl KJ (eds) Microstructure and microtribology of polymer surfaces, ACS Symposium Series 741, p 317–335, American Chemical Society
25. Vancso GJ, Hillborg H, Schönherr H (2005) Adv Polym Sci 182:55–129

26. Schönherr H, Hruska Z, Vancso GJ (1998) Macromolecules 31:3679
27. Schönherr H, Hruska Z, Vancso GJ (2000) Macromolecules 33:4532
28. Hillborg H, Tomczak N, Olah A, Schönherr H, Vancso GJ (2004) Langmuir 20:785
29. Song J, Gunst U, Arlinghaus HF, Vancso GJ (2007) Appl Surf Sci 253:9489–9499
30. Krotil HU, Stifter T, Marti O (2000) Rev Sci Instrum 71:2765
31. Schönherr H (1999) Ph.D. thesis. University of Twente, The Netherlands
32. Sinniah SK, Steel AB, Miller CJ, ReuttRobey JE (1996) J Am Chem Soc 118:8925
33. Kajiyama T, Tanaka K, Takahara A (2004) J Polym Sci Polym Chem 42:639
34. Tocha E, Stefański T, Schönherr H, Vancso GJ (2005) Rev Sci Instrum 76:083704
35. Schönherr H, Tocha E, Vancso GJ (2008) In: Samori P (ed) Topics in current chemistry, vol 285, p 103
36. Aklonis JJ, MacKnight WJ (1983) Introduction to polymer viscoelasticity. Wiley, New York
37. Gedde UW (1999) Polymer Physics. Kluwer, Dordrecht
38. McCrum NG, Read BE, Williams G (1967) Anelastic and dielectric effects in polymeric solids. Wiley, London
39. Ton-That C, Campbell PA, Bradley RH (2000) Langmuir 16:5054–5058
40. Raghavan D, van Landingham M, Gu X, Nguyen T (2000) Langmuir 16:9448
41. van Landingham MR, Villarrubia JS, Guthrie WF, Meyers GF (2001) In: Tsukruk VV, Spencer ND (eds) Scanning probe microscopy of polymers. ACS Symp. Series, 694, p 15, American Chemical Society
42. Oliver WC, Pharr GM (1992) J Mater Res 7:1564
43. Sneddon IN (1965) Int J Eng Sci 3:47
44. Withers JR, Aston DE (2006) Adv Coll Interface Sci 120:57–67
45. Aime JP, Elkaakour Z, Odin C, Bouhacina T, Michel D, Curely MJ, Dautant A (1994) Appl Phys Lett 76:754
46. Domke J, Radmacher M (1998) Langmuir 14:3320–3325
47. Marton B, Vancso GJ unpublished data
48. Steeman PAM, Nusselder JJH (1995) Polym Gel Networks 3:159
49. Bos HH, Nusselder JJH (1994) Polymer 35:2793
50. Hobbs, JK, Miles, MJ (2001) Macromolecules 34, 353
51. Sikes HD, Schwartz DK (1997) Science 278:1604
52. Schönherr H, Bailey LE, Frank CW (2002) Langmuir 18:490–498
53. Debowski M, Vancso GJ (2000) Probe Microsc 2:11–19
54. Pearce R, Vancso GJ (1997) Macromolecules 30:5843
55. Pearce R, Vancso GJ (1998) Polymer 39:1237
56. Hobbs JK, McMaster TJ, Miles MJ, Barham PJ (1998) Polymer 39:2437
57. Schultz JM, Miles MJ (1998) J Polym Sci B Polym Phys 36:2311
58. Ivanov DA, Magonov S (2003) In: Sommer JU, Reiter G (eds) Polymer crystallization: observations, concepts and interpretations, Springer, Berlin, pp 98–129

59. Ivanov DA, Bar G, Dosiere M, Koch MHJ (2008) Macromolecules 41: (23),9224
60. Marentette JM, Brown GR Polymer 1998, *39*, 1405
61. Cappella B, Kaliappan SK, Sturm H (2005) Macromolecules 38:1874–1881
62. Fryer DS, Nealey PF, de Pablo JJ (2000) Macromolecules 33:6439–6447
63. Pearce RE, Vancso GJ (1997) Macromolecules 30:5843–5848
64. Beekmans LGM, van der Meer DW, Vancso GJ (2002) Polymer 43:1887–1895
65. Beekmans LGM, Vancso GJ (2000) Polymer 41:8975–8981
66. Harron HR Pritchard RG, Cope BC, Goddard DTJ (1996) Polym Sci B Poly Phys 34:173–180
67. Benetti EM, Zapotoczny S, Vancso GJ (2007) Adv Mater 19:268–271
68. Feng CL, Zhang Z, Förch R, Knoll W, Vancso GJ, Schönherr H (2005) Biomacromolecules 6:3243–3251
69. Feng CL, Embrechts A, Bredebusch I, Schnekenburger J, Domschke W, Vancso GJ, Schönherr H (2007) Adv Mater 19:286–290
70. Davies MC, Shakesheff KM, Shard AG, Domb A, Roberts CJ, Tendler SJB, Williams PM (1996) Macromolecules 29:2205–2212
71. Zhang Z, Zou S, Vancso GJ, Grijpma DW, Feijen J (2005) Biomacromolecules 6:3404–3409
72. Zhang Z, Grijpma DW, Feijen J Macromol Chem Phys (2004) 205:867–875
73. Tranchida D, Piccarolo S, Soliman M (2006) Macromolecules 39:4547–4556
74. Tranchida D, Kiflie Z, Piccarolo S (2007) Macromolecules 40:7366–7371
75. Schönherr H, Vancso GJ (1998) J Polym Sci B Polym Phys 36:2483

Appendices

A. AFM manufacturers

Veeco Metrology Inc.
AFMs/SPMs
112 Robin Hill Road
Santa Barbara, CA 93117, USA
http://www.veeco.com/

Asylum Research Inc.
6310 Hollister Ave
Santa Barbara, CA 93117, USA
http://www.asylumresearch.com/

JPK Instruments AG
Bouchéstrasse 12
Haus 2, Aufgang C
12435 Berlin, Germany
http://www.jpk.com

Agilent Technologies
http://nano.tm.agilent.com

Pacific Nanotechnology
3350 Scott Blvd., #29
Santa Clara, CA 95054, USA
http://www.pacificnanotech.com/

Nanosurf AG
Grammetstrasse 14
4410 Liestal, Switzerland
http://www.nanosurf.com/

WITec Wissenschaftliche
Instrumente und Technologie GmbH
Hörvelsinger Weg 6
D-89081 Ulm, Germany
http://www.witec.de/

NDT MDT
NT-MDT Co.
Post Box 158
Building 317-A
Zelenograd, Moscow 124482, Russia
http://www.ntmdt.com

Park Systems Corp.
KANC 4F, Iui-Dong, 906-10
Suwon 443-270, Korea
Homepage: www.parkAFM.co.kr
http://www.parkafm.com

Seiko / S II Nanotechnologies Inc.
http://www.siint.com/en/products/spm/probe_microscope.html

JEOL (Germany) GmbH
Oskar-von-Miller-Str. 1A
D-85386 Eching b. München, Germany
http://www.jeol.de

Novascan Technologies, Inc.
Sales, Production and R&D
131 Main Street
Ames, IA 50010, USA
http://www.novascan.com

RHK Technology
1050 East Maple Road
Troy, MI 48083, USA
http://www.rhk-tech.com

Ambios Technology, Inc.
100 Pioneer Street, Suite A
Santa Cruz, CA 95060, USA
http://www.ambiostech.com/atomic_force_microscope.htm

Nanoscience Instruments, Inc.
9831 S. 51st Street
Suite C119
Phoenix, AZ 85044, USA
http://www.nanoscience.com

Omicron
NanoTechnology GmbH
Limburger Str. 75
65232 Taunusstein, Germany
http://www.omicron.de

SURFACE IMAGING SYSTEMS (S.I.S.)
Rastersonden- und Sensormesstechnik GmbH
Kaiserstrasse 100 (Technologiepark Herzogenrath, TPH)
D-52134 Herzogenrath, Germany
www.sis-gmbh.com/

Nanotec Electronica S.L.
Centro Empresarial Euronova 3
Ronda de Poniente
Edificio 12, planta 2ª, oficina C
E28760 Tres Cantos (Madrid), Spain
www.nanotec.es

NanoInk, Inc.
8025 Lamon Ave., Skokie, IL 60077, USA
http://www.nanoink.net/

Nanofactory Instruments AB
Chalmers Science Park
41288 Göteborg, Sweden
http://www.nanofactory.com/

B. Probe Tip manufacturers / vendors

NANOSENSORS
Rue Jaquet-Droz 1
Case Postale 216
CH-2002 Neuchatel, Switzerland
http://www.nanosensors.com/
www.nanosensors.com/

Veeco Probes
3601 Calle Tecate
Suite C
Camarillo, CA 93012, USA
http://store.veeco.com/

NT-MDT Co., P.B. 158, building 317 A
Zelenograd,
Moscow 124482, Russia
http://www.ntmdt-tips.com
www.ntmdt-tips.com

NanoAndMore GmbH
Spilburg Bld. A1
Steinbühlstrasse 7D-35578 Wetzlar, Germany
http://www.nanoandmore.com/

Atomic Force F&E GmbH
Hauptstrasse 161 DE-68259 Mannheim, Germany
http://www.atomicforce.de/
www.atomicforce.de/

Olympus
www.probe.olympus-global.com

Innovative Solutions Bulgaria Ltd.
48, Joliot Curie Str.1113 Sofia, Bulgaria
http://www.budgetsensors.com
www.budgetsensors.com

Advanced Diamond Technologies Inc.
429 B Weber Road
286, Romeoville, IL 60446, USA
http://www.thindiamond.com

MIKROMASCH
Akadeemia tee 21 E12618 Tallinn, Estonia
http://www.spmtips.com/

Novascan Technologies, Inc.131 Main Street
Ames, IA 50010, USA
http://www.novascan.com

Nanotools GmbH
Reichenbachstraβe 33D - 80469 München, Germany
http://www.nano-tools.com/

Applied NanoStructures, Inc.
1700 Wyatt Drive, Suite 12
Santa Clara, CA 95054, USA
http://appnano.com

Nanoscience Instruments, Inc.
9831 S. 51st Street,
Suite C119
Phoenix, AZ 85044, USA
http://www.nanoscience.com

SmartTip B.V.
Chemical and magnetic force probes
PO Box 347
7500 AH, Enschede, The Netherlands
info@smarttip.nl
www.smarttip.nl

C. SPM software

Scanning Probe Image Processor (SPIP)
Image Metrology A/S
http://www.imagemet.com/
http://reg.ssci.liv.ac.uk

ImageSXM
http://www.liv.ac.uk/~sdb/ImageSXM/

NIH Image
http://rsb.info.nih.gov/nih-image/

WSxM
http://www.nanotec.es/

Gwyddion
http://gwyddion.net/

FemtoScan Online
http://www.nanoscopy.net/en/Femtoscan-D.php

PUNIAS (Protein Unfolding and Nanoindenation Analysis Software)
http://site.voila.fr/punias

Carpick Lab's Software Toolbox
http://nanoprobenetwork.org/welcome-to-the-carpick-labs-software-toolbox

ImageJ
http://rsbweb.nih.gov/ij/

TrueMap and TrueSurf
http://www.truegage.com

MountainsMap SPM Image
http://www.digitalsurf.fr/en/spm.html

D. Web-based resources

Spm@spmlist.di.com
Nanoprobe Network (http://nanoprobenetwork.org)

Index

D

E

F

G

H

I

J

K

L

M

N

O

P

Q

R

S